Plasma-enhanced CVD growth of cubic and hexagonal diamond silicon nanowires with liquid-solid mixed catalysts for photovoltaic applications

Weixi Wang

▶ **To cite this version:**

Weixi Wang. Plasma-enhanced CVD growth of cubic and hexagonal diamond silicon nanowires with liquid-solid mixed catalysts for photovoltaic applications. Material chemistry. Institut Polytechnique de Paris, 2021. English. NNT : 2021IPPAX014 . tel-03297142

HAL Id: tel-03297142

https://theses.hal.science/tel-03297142

Submitted on 23 Jul 2021

HAL is a multi-disciplinary open access archive for the deposit and dissemination of scientific research documents, whether they are published or not. The documents may come from teaching and research institutions in France or abroad, or from public or private research centers.

L'archive ouverte pluridisciplinaire **HAL**, est destinée au dépôt et à la diffusion de documents scientifiques de niveau recherche, publiés ou non, émanant des établissements d'enseignement et de recherche français ou étrangers, des laboratoires publics ou privés.

INSTITUT POLYTECHNIQUE DE PARIS

ÉCOLE POLYTECHNIQUE

IP PARIS

NNT : 2021IPPAX014

Thèse de doctorat

Plasma-enhanced CVD growth of cubic and hexagonal diamond silicon nanowires with liquid-solid mixed catalysts for photovoltaic applications

Thèse de doctorat de l'Institut Polytechnique de Paris
préparée à École polytechnique

École doctorale n°626
École doctorale de l'Institut Polytechnique de Paris (ED IP Paris)
Spécialité de doctorat : Physique de la matière condensée

Thèse présentée et soutenue à Palaiseau, le 1 Juin 2021, par

Weixi Wang

Composition du Jury :

Maria Tchernycheva Directrice de recherche, Université Paris-Saclay (– C2N)	Président
Vincent Sallet Chargé de recherche, Université Paris-Saclay (– GEMaC)	Rapporteur
Antonin Fejfar Professeur, Czech Academy of Sciences (– LNSM)	Examinateur
Martien den Hertog Chargée de recherche, CNRS (– Institut Néel)	Examinateur
Jean-Luc Maurice Directeur de recherche, École polytechnique (– LPICM)	Directeur de thèse
Martin Foldyna Chargé de recherche, École polytechnique (– LPICM)	Co-Directeur de thèse
Pere Roca i Cabarrocas Professeur, École polytechnique (– LPICM)	Invité

PLASMA-ENHANCED CVD GROWTH OF CUBIC AND HEXAGONAL DIAMOND SILICON NANOWIRES WITH LIQUID-SOLID MIXED CATALYSTS FOR PHOTOVOLTAIC APPLICATIONS

DISSERTATION

Submitted to the École Doctorale of Institut Polytechnique de Paris

in Partial Fulfillment of the Requirements for the Degree of

DOCTOR OF PHILOSOPHY

in Physics

at

École polytechnique

By

Weixi Wang

Supervised by

Dr. Jean-Luc Maurice

Dr. Martin Foldyna

Prof. Pere Roca i Cabarrocas

Spring 2021

Acknowledgements

Having finished the whole thesis, I found the most difficult part to write is the acknowledgements. Among all the people I am grateful for helping me during my PhD, I have been most fortunately blessed by my research supervisors: Jean-Luc Maurice, Martin Foldyna, and Pere Roca i Cabarrocas.

Jean-Luc has brought me to the complex but wonderful world of TEM. I admire his professional skills and depth of thinking in the field of TEM. I am lucky to learn from such a knowledgeable and patient expert. He is always ready to help with the experiments and to answer my questions. I have not only learned about equipment operations, data analysis, but also accumulated knowledge on material science and physics. During the writing of my manuscript and papers, he gave me very professional academic guidance. He corrected my writings word by word, table to table, figure to figure. I have learned a lot from the valuable comments and suggestions. I treasure this experience as one of the most important trainings from my PhD.

I cannot remember how many days I did experiments with Martin. He is always eager to have the first-hand results of my experiments. Discussions with him gave me everyday inspiration. His meticulously guided me through my PhD, especially on giving scientific presentations and writing papers. He is strict with every sentence in every single slide, teaching me how to make a good story. He has been not only an advisor guiding my research, but more like a good friend helping me in many aspects professionally and personally throughout my PhD. I really miss the days before the pandemic that we had lunch and coffee every day, which made me relaxed and happy outside the experiments.

I am impressed not only with Pere's fruitful academic results but also with his efficiency. I usually receive his quick reply with valuable comments on my writings the next day early in the morning. He also regularly gave face-to-face discussions with me about my results and gives me very helpful suggestions. Meanwhile, he is teaching, doing experiments, participating meetings and supervising interns, PhDs, and

postdocs…He invites us to have barbecue every year in his big garden with beautiful trees, flowers, and vegetables. I marvel at his enthusiasm for scientific research and for life.

I must also extend a big thank to our colleagues who contributed to this work. Ileana Florea trained me how to operate on TEM equipment Nan'eau and helped me make many nice TEM images and EDX results, which are the key of this thesis; Thanks to Dmitri Daineka, Jacqueline Tran, Cyril Jadaud, Jean-Charles Vanel, and Jérôme Charliac for giving me training and solving problems of the thermal evaporator, SEM, PECVD, and the sputtering machine; Thanks to Maria Tchernycheva and Tiphaine Mathieu-Pennober from C2N for their kind help with the EBIC experiments; I would like to also thank to our NW group members, Eric Ngo, Chaoqi Wang, Letian Dai, Maria Mendez, Mutaz Al-Ghzaiwat, and Lukas Halagacka, for their help with my experiments.

I would like to thank Maria Tchernycheva, Vincent Sallet, Martien den Hertog, and Antonin Fejfar for accepting to be my jury members.

I have had the best time in my life in France up till now, and my older daughter Xingxian has been the best part of it. You have accompanied me almost my entire PhD. I am most happy when I come back home from work and see your lovely face. My second daughter Xingfa was just born in this spring. You are like a blooming flower that brings us new hope.

Special thanks to my mother-in-low and my mother, who travelled to France to help with the grandchildren. My PhD would have become much more difficult without you look after my baby when I work on my research. You have done more than enough.

I would like to reserve this last paragraph for my husband, Zhengyu Zhang, whose love and devotion have encouraged me throughout my PhD. Meeting you is the luckiest thing that ever happened to me, and I will enjoy this fortune for the rest of my life to see our kids grow up and to see the oceans and the stars with you.

Abstract

Silicon nanowires (SiNWs) are attracting an increasing attention due to their unique one-dimensional geometry with properties suitable for different optoelectronic applications. Recently, small diameter NWs (below 10 nm) have become the target due to predicted quantum size effects. Moreover, small diameter SiNWs with hexagonal diamond crystalline structure, which are predicted to have a direct bandgap that can be tuned by the diameter control, have been synthesized directly in a PECVD reactor. This thesis is dedicated to fabricating small diameter SiNWs with hexagonal phase using PECVD. The analysis on the previous work at LPICM has shown that hexagonal SiNWs were not obtained with a single Sn catalyst. We have demonstrated SiNW growth using evaporated SnCu mixed catalysts with a controlled composition for the first time, which leads to a core-shell structure on the top of SiNW with a crystalline Cu_3Si core and a Sn-rich shell most probably liquid during the growth. The SiNWs have been grown through a combined VLS and VSS growth process. We have investigated the influence of the catalyst composition and PECVD conditions on the SiNW growth systematically and achieved ultra-dense (5.7×10^{10} /cm^2) and ultra-thin silicon quantum nanowire arrays with average crystalline diameter of around 4 to 5 nm and with a narrow distribution. TEM observation showed that hexagonal phase can be obtained with a substrate temperature between 385 and 447 °C, and within a SiH_4 partial pressure range from 0.026 to 0.068 mbar, on a Cu TEM grid, and on (100) Si wafer substrates using different SnCu compositions. The hexagonal phase appeared statistically rarely (usually with a yield of around 5 – 6%), with no particular growth condition except for the small diameter (with crystalline diameters from 4.0 to 7.2 nm). By replacing Sn with In element with similar properties in a mixed catalyst with Cu, dense SiNW arrays with an average diameter of 10.5 nm have been obtained, among which we found a hexagonal SiNW with crystalline diameter of 5 nm. In addition, the use of AuCu mixed catalysts has led to faster SiNW growth rate when compared to pure Au catalyst. Therefore, using mixed catalysts allows for a control of SiNW diameter (narrower distribution), length (growth rate), and density that cannot be obtained by using pure metal

catalysts. Finally, PIN radial junction solar cells based on ultra-dense and thin SiNWs synthesized with SnCu and InCu co-catalysts have been fabricated successfully.

Keywords: small diameter SiNWs, PECVD, TEM, hexagonal phase, mixed catalyst

Résumé

Les nanofils de silicium bénéficient d'une attention accrue du fait de propriétés uniques liées à leur géométrie unidimensionnelle, propriétés qui intéressent différentes applications en opto-électronique. Récemment, des nanofils de très petit diamètre (inférieur à 10 nm) ont été l'objet de plusieurs études, car leurs propriétés prédites témoignent d'intéressants effets de confinement quantique. De plus, la structure hexagonale-diamant a été observée dans ce type de nanofils, et les calculs prédisent qu'ils auraient alors un gap direct, ajustable par contrôle du diamètre. Ces nanofils de silicium hexagonal ont été synthétisés lors d'une précédente étude au LPICM, dans un réacteur de dépôt chimique en phase vapeur assisté par plasma (PECVD). Le travail présenté ici a pour but la fabrication par PECVD de nanofils de très petit diamètre, avec la phase hexagonale diamant. Notre analyse des précédents travaux menés au LPICM montre que le catalyseur utilisé alors – nominalement de l'étain – comprenait en réalité un part de cuivre venant du substrat – une grille en cuivre de microscopie électronique en transmission (TEM). Nous avons donc démarré cette thèse par l'étude de catalyseurs mixtes SnCu de composition contrôlée. Ce type de catalyseur acquiert lors des traitements préliminaires une structure de type « cœur-coquille ». Lors de la croissance, le cœur devient du Cu_3Si cristallin tandis que la coquille demeure un eutectique riche en étain, très certainement liquide à la température de croissance. Ce mode de croissance combine donc VLS (vapeur-liquide-solide) et VSS (Vapeur-solide-solide). Nous avons étudié de manière systématique l'influence de la composition du catalyseur et des conditions PECVD sur la croissance. Nous avons ainsi obtenu des tapis ultra-denses (5.7×10^{10} /cm^2) de nanofils ultrafins (4-5 nm de diamètre cristallin). Nos observations TEM montrent que la phase hexagonale est présente, dans cette gamme de diamètres, pour toutes les conditions de croissance testées (température de 385 à 447 °C, pression de SiH_4 de 0,026 à 0,068 mbar, sur grille TEM en Cu comme sur Si (100) et avec des catalyseurs de compositions en Sn et Cu variables). La phase hexagonale apparaît cependant avec une relativement faible probabilité (typiquement de 5 à 6%), sans condition de croissance particulière si ce n'est la faible taille (les valeurs des diamètres cristallins des nanofils hexagonaux sont entre 4.0 et 7.2 nm). En remplaçant l'étain par l'élément In, qui a des propriétés

similaires, dans le catalyseur mixte avec Cu, nous obtenons également des réseaux denses de nanofils de Si, avec toutefois des diamètres plus grands pour une épaisseur de catalyseur égale. Dans un réseau de diamètre moyen de 10.5 nm, nous avons trouvé un nanofil de Si de 5 nm de diamètre avec une structure partiellement hexagonale. Nous avons également essayé le catalyseur mixte AuCu qui a donné des vitesses de croissance accrues, par rapport à l'Au pur. À l'issue de l'ensemble de ces expériences, nous pouvons affirmer qu'utiliser des catalyseurs mixtes, plutôt que des catalyseurs de métaux purs, permet un meilleur contrôle : du diamètre des nanofils (en autorisant des diamètres plus petits dans des distributions étroites) ; de leur longueur (par la vitesse de croissance), et de leur densité. Pour finir, nous avons fabriqué des cellules solaires à jonction radiale en silicium amorphe hydrogéné sur ce type de petits nanofils très denses, dopés p cette fois, synthétisés à partir des catalyseurs SnCu and InCu. Ces premières cellules apparaissent fonctionnelles.

Mots clés: nanofils de silicium de petit diamètre, PECVD, TEM, Si hexagonal, catalyseur composé

Contents

List of figures

List of tables

Table of acronyms and abbreviations

a-Si:H	hydrogenated amorphous silicon
BF	bright field
BSE	backscattered electron
Cg	Corning glass
c-Si	crystalline silicon
CVD	chemical vapor deposition
DFT	Density Functional Theory
EBIC	electron beam induced current
EDX	energy dispersive X-ray spectroscopy
EQE	external quantum efficiency
fcc	face-centered cubic
FET	field-effect transistors
FF	fill factor
FFT	fast Fourier transform
HAADF	high-angle annular dark-field
HRTEM	high-resolution transmission electron microscopy
ITO	Indium tin oxide
LED	light-emitting diode
MBE	Molecular beam epitaxy
NP	nanoparticle
PECVD	plasma enhanced chemical vapor deposition
QCM	quartz crystal microbalance
RF	radio frequency
RJ	radial junction
SADP	selected-area diffraction pattern
sccm	standard cubic centimeters per minute
SEM	scanning electron microscopy
SiNW	silicon nanowire
STEM	scanning transmission electron microscopy
TEM	transmission electron microscopy
VLS	vapor liquid solid
VSS	vapor solid solid

Chapter 1. Introduction

1.1. **Why studying silicon nanowires**

The design, development and understanding of synthetic materials, with at least one dimension below 100 nm, have been driving a broad range of research in the scientific community for a number of years given the potential of such materials to substantially impact many areas of science and technology. In particular,1D nanowires (NWs), with diameters reaching to the molecular or quantum regime, have been the focus of research for two decades and today remain at the forefront of both scientific research and developing nanotechnologies. The underlying principles for synthesis of one-dimensional materials have been investigated in different contexts for almost half a century as significant challenges existed in developing the critical understanding to control (i) diameters to the deep nanoscale dimensions as well as (ii) structure and composition in the axial and radial coordinates as necessary for the synthesis of materials with designed and tunable functionality. There are also many applications where 1D NWs can be exploited, including (i) functional nanostructure materials, (ii) novel probe microscopy tips, (iii) nanoelectronics, (iv) nanophotonics, (v) quantum devices, (vi) energy storage devices, (vii) energy conversion systems, (viii) chemical and biological sensors, and (ix) nano-bio interfaces [Hu, 1999, Lieber, 2011].

In contrast to other classes of 1D nanostructures, such as carbon nanotubes, semiconductor NWs can be rationally and predictably synthesized in single crystal forms with all key parameters controlled, including chemical composition, diameter, length, doping and electronic properties. Thus, semiconductor NWs represent one of the best-defined classes of nanoscale building blocks [Zhang, 2016]. Early work showed that semiconductor NWs could be assembled into functional electronic devices, including crossed NW p-n diodes [Lysov, 2011], crossed NW- field-effect transistors (FETs) [Chen, 2011a], nanoscale logic gates and computation circuits [Kim, 2010], as well as optoelectronic devices such as nanoscale light-emitting diodes (LEDs) and lasers [Könenkamp, 2004]. Silicon nanowires (SiNWs) have attracted great interest because of the element abundance, stability, and nontoxicity, and they are usable for different electronic, sensing, optoelectronic and photovoltaic applications [Cui, 2001b, Puglisi, 2019].

The publication of Treuting and Arnold of 1957 [Treuting, 1957] represents the first publication on Si wire growth to the best of our knowledge. Therein, the authors report on the successful synthesis of silicon whiskers (actually filamentary crystals of diameters larger than about hundred nanometers.) with <111> orientation. In the 1960s, Wagner and Ellis published the pioneering work [Wagner, 1964], in which they claimed their famous vapor–liquid–solid (VLS) mechanism of single-crystal growth. This method set the basis for a new research field and, until today, represents the most common way to synthesize SiNWs. In the mid-1990s, when advances in microelectronics triggered a renewed interest in SiNW research, Morales and Lieber managed to synthesize nanowires of truly nanoscopic dimensions [Morales, 1998].

Aiming at future electronics applications, SiNW research activities have started by nanowire synthesis. We thus propose a short summary of the various silicon-wire synthesis methods established so far. Following thereupon, we introduce the VLS mechanism, because it is really at the heart of SiNW research. Concerning the electronics applications, the choice of the catalyst material is essential. As, moreover, the present thesis is focused on the use of original catalysts, the current status of research regarding the various possible catalyst materials is discussed at length. After this, the focus is shifted to small diameter nanowires (below 10 nm), which change material properties at the smallest scale and have become the target due to predicted quantum effects [Hu, 1999].

1.2. **Methods of silicon nanowire fabrication**

There are many different approaches for fabricating SiNWs, which can be classified under two main categories: (a) the bottom-up approaches, and (b) the top-down approaches.

a) Bottom-up fabrication methods

All bottom-up methods are based on the vapor-liquid-solid (VLS) process mentioned above or on one of its parent mechanisms (VSS: vapor-solid-solid; SLS: solution–liquid–solid...). The VLS method is the focus of next sub-chapter.

b) Top-down fabrication methods

There are several attractive top-down approaches for the fabrication of single crystalline SiNWs. Due to the processing-related differences, one should distinguish between the fabrication of horizontal NWs and vertical NWs. Horizontal SiNWs are mostly fabricated from either silicon-on-insulator (SOI) wafers [Tezuka, 2007] or bulk silicon wafers [Ming, 2009] using a sequence of lithography and etching steps, often employing electron-beam lithography and reactive ion etching. In most cases, horizontal NW processing is finalized by an oxidation step, which also serves to reduce the SiNW diameter. In this way, diameters well below 10 nm have been achieved [Singh, 2008, Sung Dae, 2008]. Reactive-ion etching is often used to etch vertical SiNWs out of a silicon wafer. The diameter of the NWs is defined by a lithography step. A variety of different nano structuring methods, such as electron-beam lithography [Chen, 1993], nanosphere lithography [Hsu, 2008], nanoimprint lithography [Morton, 2008], or block-copolymers [Zschech, 2007] have been employed for this purpose. As an alternative to reactive-ion etching, metal-assisted etching of silicon has attracted some attention recently. In this approach Si is wet-chemically etched, with the Si dissolution reaction being catalyzed by the presence of a noble metal that is added as a salt to the etching solution [Peng, 2002].

To summarize this sub-chapter on fabrication techniques, so far none of the bottom-up synthetic methods of SiNWs can compete with the in-place fabrication methods in terms of controllability, reliability, and size variability [Schmidt, 2009]. However, they are limited to the laboratory scale due to their high cost and low throughput. The one that comes closest is presumably CVD, as it allows for an epitaxial growth on silicon substrates at specific positions and additionally offers great versatility concerning process conditions, NW dimensions, and properties. MBE, although combining epitaxial growth with a good controllability of composition, lacks the variability of CVD concerning NW diameters and aspect ratios. The non-substrate-bound NWs fabrication techniques laser ablation combines a good controllability and variability of the NW composition with excellent NW quality and reasonable yield and solution-based growth techniques offer a high NW yield, which makes this approach especially attractive for large-scale nanowire production.

1.3. **The vapor-liquid-solid (VLS) growth technique**

1.3.1. **Vapor–Liquid–Solid (VLS) Mechanism**

The name VLS mechanism refers to the fact that atoms from the vapor pass through a liquid droplet and finally end up in a solid phase. As mentioned above, the VLS mechanism, first proposed by Wagner and Ellis [Wagner, 1964], is the key mechanism for SiNW growth. Their proposed VLS mechanism is based on two observations: that the addition of certain metal impurities is an essential prerequisite for the growth of silicon wires in experiments, and that small globules of the impurity are located at the tip of the wire during the growth. From this, Wagner and Ellis deduced that the globule at the wire tip must be involved in the growth of the silicon wires by acting ‘‘as a preferred sink for the arriving Si atoms or, perhaps more likely, as a catalyst for the chemical process involved’’.

For example, when Au catalyst is deposited on a silicon substrate, and this substrate is then heated to temperatures above about 363 °C, small liquid eutectic Au–Si alloy droplets will form on the substrate surface. Exposing such a substrate to a gaseous silicon precursor, such as silicon tetrachloride ($SiCl_4$), or silane (SiH_4), precursor molecules will crack on the surface of the Au–Si alloy droplets, whereupon Si is incorporated into the droplet. The silicon supply from the gas phase causes the droplet to become supersaturated with Si until silicon freezes out at the silicon/droplet interface. The continuation of this process then leads to the growth of a NW with the alloy droplet riding atop the growing wire (see Figure 1.1). It is often noted that in VLS wire growth the radius R of the catalyst droplet exceeds the radius r of the nanowire. One can easily derive that, in equilibrium, $R = r\sqrt{1/(1-(\sigma_{ls}/\sigma_l)^2)}$ [Nebol'sin, 2003],with σ_{ls} and σ_l being the surface tension of the liquid catalyst and the interface tension of the liquid/solid interface, respectively. The VLS mechanism works well from wires several hundreds of micrometers thick down to NW of just a few nanometers in diameter.

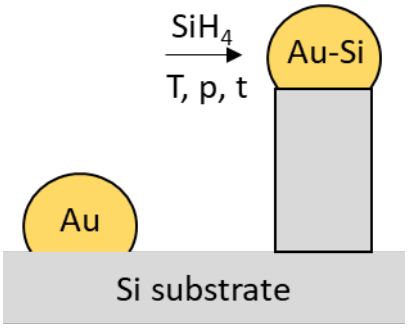

Figure 1.1. Schematic of the VLS growth mechanism.

Analogously to the VLS mechanism, also other growth mechanisms were proposed and accordingly named, such as the vapor–solid–solid (VSS) mechanism, which comes into play when the nanowire growth is catalyzed by a solid catalyst particle instead of a liquid catalyst droplet. Whether wire growth proceeds via the VLS or VSS mechanism depends on catalyst material and temperature. For example, Cu is often used as catalyst for SiNW growth via VSS mechanism [Kalache, 2006, Arbiol, 2007, Yao, 2007, Arbiol, 2008].

1.3.2. **Means to bring matter for the growth**

Chemical Vapor Deposition (CVD)

The most common approach to synthesize SiNWs is based on the use of a CVD system with the assistance of metal catalysts, via vapor-liquid-solid (VLS) or vapor-solid-solid (VSS) mechanism as introduced above. The silicon precursors are transported to the catalyst surface where they react at elevated temperatures, and are cracked into their constituents as depicted in Figure 1.2a. When Si atoms become supersaturated in the catalyst particle, they overcome the nucleation barrier and precipitate at the catalyst-substrate interface and lead to SiNW growth. A large range of lengths (a few hundreds of nanometers to 100 μm) and diameters (a few nanometers to several micrometers) of SiNW configurations can be fabricated [Misra, 2014]. CVD also offers the opportunity of a controlled doping by intentionally offering additional doping precursors. By switching the doping precursor, doping profiles in axial direction can be created [Pan, 2005, Wang, 2005, Mouchet, 2008, Schmid, 2008]. One of the major problems of SiNW

grown by CVD is that they exhibit a certain variation of the growth direction, especially for diameters smaller than about 50 nm [Schmidt, 2005a].

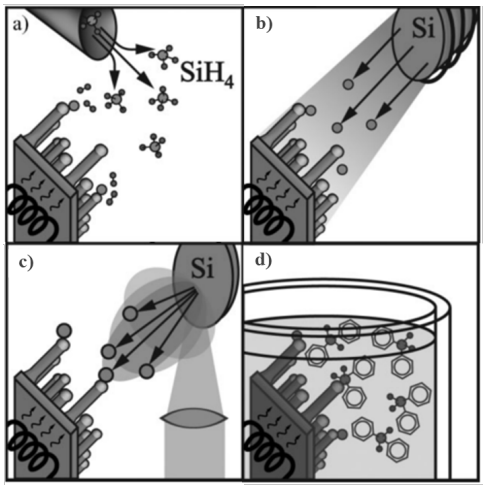

Figure 1.2. Schematics of experimental setups for silicon nanowire growth. a) CVD, b) MBE, c) laser ablation, and d) solution-based growth [Schmidt, 2009].

The relatively high process temperature used in the CVD method limits the use of low-cost substrates. In cases where the thermal load is critical or where a high supersaturation of the droplet is necessary, nanowire growth can be enhanced using plasma-enhanced CVD (PECVD). By modifying the precursor before reacting with the sample surface, the temperature budget of the substrate can be lowered. Moreover, the presence of plasma also broadens the range of metals that can be used for SiNW growth [Misra, 2014].

Molecular Beam Epitaxy (MBE)

In MBE, a solid high-purity silicon source is heated until Si starts to evaporate. Figure 1.2b schematically depicts an MBE setup. A directional gaseous beam of silicon atoms is aimed at the substrate, on which the atoms adsorb and crystallize. Similar to CVD, MBE also uses metal catalyst to cause SiNW growth. Differing from CVD, no precursor gas is cracked at the surface of the liquid metal–silicon alloy. The nanowires produced by MBE (usually grown on Si (111) substrates) are epitaxial and <111> oriented.

MBE offers excellent controllability in terms of the incoming flux, such that doped wires [Das Kanungo, 2008] or heterostructures [Zakharov, 2006] can be grown by switching between evaporation sources. One disadvantage of MBE is that the method is limited with respect to the minimally possible Si-nanowire diameter. Werner mentions that only nanowires with diameters greater than about 40 nm can be obtained [Werner, 2006]. Another disadvantage of MBE is the low nanowire growth velocity of a just a few nanometers per minute [Schubert, 2004].

Laser ablation

Laser ablation is schematically displayed in Figure 1.2c: a high-power pulsed laser ablates material from a mixed Si–catalyst target, which is placed in a tube furnace held at high temperatures and purged with an inert gas. The silicon material ablated from the target cools by colliding with inert-gas molecules, and the atoms condense to liquid nanodroplets with the same composition as the target [Morales, 1998]. Thus, these nanoparticles contain both Si and the catalyst material. SiNWs start to grow once the catalyst gets supersaturated with silicon and proceeds as long as the catalyst nanoparticles remain liquid. The advantages of laser-ablated NW production are manifold. First, there is no need for a substrate. Second, the composition of the resulting NWs can be varied by changing the composition of the laser target. One can easily obtain large quantities of ultrathin nanowires with high aspect ratios [Zhang, 1998, Zhou, 1998]. Due to the high growth temperatures, catalyst metals such as Fe, possessing a high eutectic temperature, can be used. The resulting NW growth velocities are typically of the order of micrometers per minute [Morales, 1998].

Solution-Based Techniques

Solution-based growth techniques are the methods of choice for high-yield SiNW production. One method utilizes highly pressurized supercritical organic fluids enriched with a liquid silicon precursor, such as diphenylsilane, and metal catalyst particles, as indicated in Figure 1.2d. At reaction temperatures above the metal–silicon eutectic, the silicon precursor decomposes and silicon forms an alloy with gold.

Analogously to the VLS mechanism, the alloy droplet in this supercritical–fluid–liquid–solid (SFLS) method starts to precipitate a NW once the alloy gets supersaturated with silicon [Holmes, 2000, Hanrath, 2003, Lu, 2003]. Crystalline nanowires with diameters as low as 5 nm and several micrometers in length have been fabricated using this approach. Another high-yield silicon-nanowire production method is the so-called solution–liquid–solid (SLS) method. Here, the growth environment is an organic solvent at atmospheric pressure. The SLS method probably represents the most-cost-effective nanowire-production method, as it can be realized without high-priced equipment.

1.4. **Catalyst materials for silicon nanowires**

This thesis work being centered on the use of new types of catalysts, let us review the literature on those materials in detail.

1.4.1. **Elemental metals**

The advantages that render Au a favorable catalyst material are that Au is nontoxic, chemically inert, and easily available, that it possesses a eutectic point at a low temperature but high Si solubility, that Au has a low vapor pressure at elevated temperatures, and that the Au–Si liquid alloy has a high-enough surface tension. Unfortunately, this bundle of advantages is balanced by one serious drawback. This is that Au, which is a known impurity in nanowires [Allen, 2008], is considered incompatible with industrial electronic production standards.

In recent years, numerous research efforts have focused on identifying an alternative, *i.e.*, non-Au, catalyst material for SiNW growth. Figure 1.3 shows the impurity levels of various potential catalyst materials as a function of the corresponding minimum temperature required for a VLS growth [Sze, 2006]. The closer the impurity level is to the band-gap middle, the more efficient it is as a recombination center. Therefore, the incorporation of impurities with levels close to band-gap middle (the so-called deep levels), is avoided as far as possible. The metals with impurity levels close to the valence or conduction bands, would cause a doping of Si: p-doping for In, Ga, Al; n-doping for Bi, Li, Sb, Te. Depending on whether a

doping of the Si wires is intended or not, these materials could be attractive candidates for SiNW growth. Beside Au, other impurities have levels close to the band-gap middle, such as Zn, Cu, Fe, Cr, Pb, or Co. If both high doping and active charge-carrier recombination are to be avoided, isoelectronic impurities like Sn, or intermediate-level impurities like Tl, Ag, Pt, Pd, Ni could possibly be attractive catalyst materials.

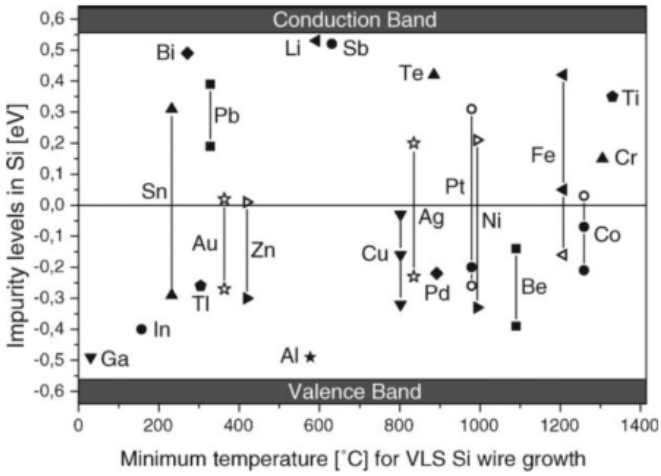

Figure 1.3. Ionization energies of various impurities in Si (after Sze [Sze, 2006]) given with respect to the middle of the bandgap (assuming a bandgap of Si of 1.12 eV) as a function of the minimum temperature necessary for VLS growth. In case an impurity possesses two or more levels, these are shown connected by a line. Levels above the bandgap middle that are marked with solid symbols are donor levels, whereas open symbols indicate acceptor levels. Analogously, full symbols below the bandgap middle are acceptor levels, whereas open symbols are donor levels.

In order to discuss the differences and similarities between the various catalysts in a concise manner, it is helpful to classify them with respect to the characteristics of the corresponding metal–Si binary phase diagram. We adopt the following classification scheme, shown in Figure 1.4. Type A catalysts have a simple eutectic phase diagram, which means that the phase diagram is dominated by a single eutectic point. This eutectic point is located at a Si concentration greater than 10 at.%. Furthermore, type A catalysts are characterized by the absence of any metal–silicide phases. Type B catalysts are also characterized by a dominant eutectic point and the absence of silicide phases. In contrast to type A catalysts, the eutectic point

is located at very low Si concentrations, smaller than 1 at.%. Type C catalysts are characterized by the presence of one or more silicide phases. In addition, their eutectic points can all be found at temperatures >800 °C.

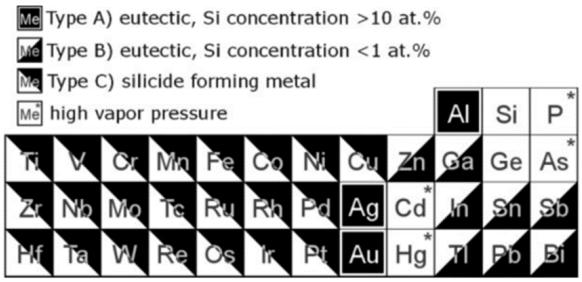

Figure 1.4. Periodic table with potential catalyst metals classified according to their phase diagrams [Cahn, 1991]. Type A) phase diagram dominated by a eutectic point at a Si concentration >10%; Type B) phase diagram dominated by a eutectic point at a Si concentration <1%; Type C) phase diagram shows the existence of one or more metal– silicide phase. Elements marked with a star * have a vapor pressure of more than 0.01 mbar at 300 °C.

The examples of the phase diagrams corresponding to the three types are shown in Figure 1.5.

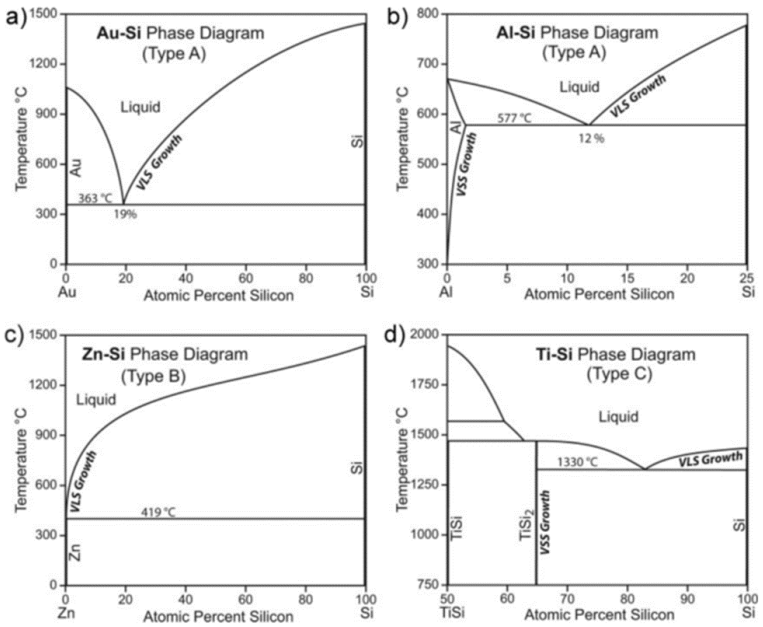

Figure 1.5. Schematics of various metal–Si phase diagrams or parts of the metal–Si phase diagrams: a) Au–Si, b) Al–Si, c) Zn–Si, d) Ti–Si after [Cahn, 1991]. The types refer to the classification shown in Figure 1.4.

a) Type A Catalysts

Al is a type A catalyst. The eutectic point of the Al–Si system is located at higher temperatures (577 °C) and slightly lower Si concentrations (12 at.%) compared to Au, but otherwise the two phase diagrams are very similar (see Figure 1.5a and b). It is therefore not astonishing that VLS growth using Al indeed works. Osada *et al*. demonstrated Al-catalyzed VLS growth of well-crystalline SiNWs by means of a CVD process using silane and temperatures between 580 and 700 °C [Osada, 2019]. Wang *et al*. demonstrated the synthesis of single-crystalline SiNWs grown epitaxially on Si (111) substrates at a growth temperature between 430 and 490 °C, well below the Al–Si eutectic point, via the VSS mechanism [Wang, 2006]. Compared to the VLS growth of SiNWs, synthesis via solid Al particles brings the advantage that the solubility of Si in the catalyst particle is about one order of magnitude smaller. This low solubility might turn out to be a useful feature if one aims at the fabrication of axial Si/Ge heterostructures. Due to the low Si solubility in solid Al, sharp transitions between Si and Ge should be achievable [Schmidt, 2009].

The other non-gold type A catalyst is silver. The Ag–Si system possesses a single eutectic point at 11 at.% Si and 835 °C. Consequently, rather high temperatures are required for a VLS growth of SiNWs. Analogously to VSS Si-nanowire growth with Al, VSS growth via solid Ag particle seems to be promising, in particular as the impurity levels of Ag (see Figure 1.3) are neither very close to the band-gap center nor to the band-gap edges.

b) Type B Catalysts

The characteristic feature of type B catalysts is a eutectic point at very low Si concentrations. Let us first consider the transition metal Zn. The Zn–Si binary phase diagram, schematically reproduced Figure 1.5c, is dominated by a eutectic point at 420 °C and a 0.02 at.% Si. Chung *et al*. [Chung, 2000] and Yu *et al*. [Yu, 2000] demonstrated VLS SiNW growth by means of a CVD process using silane at a partial pressure of 6.7 mbar and a temperature between 440 and 500 °C. Concerning the electronic properties (see Figure 1.3), one must conclude that the impurity levels of Zn in Si are as unfortunate as those of Au. Overall, it seems there is little to gain by switching from Au to Zn, except that a Zn contamination could possibly be more easily removed (by annealing) than Au contamination.

Much more interesting from an electronics point of view is the use of Ga or In as catalyst, because In and Ga would cause a strong p-type doping of the wires (see Figure 1.3). Also in terms of vapor pressure, In and Ga are much more favorable than Zn. At 500 °C, the vapor pressure of In is below 10^{-7} mbar and the vapor pressure of Ga below 10^{-10} mbar. SiNW growth using In and Ga catalysts has been demonstrated possible via both CVD [Givargizov, 1971] and PECVD [Iacopi, 2007, Iacopi, 2008] methods. Concerning the other type B catalysts, Sn [Yu, 2008, Yu, 2010, Misra, 2013a, Misra, 2015, Tang, 2017b, Hyvl, 2020]and Bi [Yu, 2012, Yu, 2015] are frequently used for SiNW growth by PECVD method despite their low surface tensions. Considering the electronic properties in Si, the use Bi and Sn as catalyst seems attractive.

c) Type C Catalysts

This is the group of catalyst metals that may form one or more silicide phases. Due to the presence of the silicide phases, the type C catalyst offer the opportunity of VSS wire growth via the solid silicide particle in addition to growth via the VLS mechanism. This can be understood by considering the growth of Si nanowires with the help of Ti. Figure 1.5d shows the Si-rich half of the Ti–Si phase diagram depicted. As indicated therein, Ti–Si possesses a eutectic point at 1330 °C neighboring the pure Si side. If growth temperatures below 1330 °C are applied, growth should proceed via the phase that is neighboring the pure Si side-$TiSi_2$. SiNW growth via the VSS mechanism catalyzed by a $TiSi_2$ particle has first been observed by Kamins *et al*. at 640–670 °C by means of CVD process [Kamins, 2000]. However, the crystallographic quality of Si nanowires grown via $TiSi_2$ catalyst particles seems to be poor compared to what can be obtained by using Au as catalyst. Similarly to Ti, the use of Fe as catalyzing impurity in CVD processes at temperatures around 600 °C leads to the growth of SiNWs with a high density of crystallographic defects [Schmidt, 2005b].

The noble metals Pd and Pt have similar physical and chemical properties. According to their phase diagrams with Si, both noble metals require high temperatures for VLS growth (892 °C for Pd and 979 °C for Pt). Applying such high temperatures, similar results as with Au as catalyst have been obtained. In his work, Weyher used $SiCl_4$ CVD processes to synthesize Pt-catalyzed SiNWs via the VLS mechanism at temperatures around 1000 °C [Weyher, 1978]. In the case of Pd, the reported growth temperature is almost 100 K below the minimum temperature required for VLS growth [Bootsma, 1971]. Circumstantial evidence for VSS SiNW growth via a Pd–silicide particle (presumably Pd_2Si) has been given by Hofmann *et al*. They used in situ transmission electron microscopy (TEM) to study the growth of SiNWs at temperatures around 892 °C, and found that SiNW growth works via lateral ledge flow at the silicide–silicon interface [Hofmann, 2008]. Baron *et al*. demonstrated VSS SiNWs growth using PtSi catalyst particles at temperatures as low as 500 °C [Baron, 2006].

Cu and Ni as well are very interesting catalyst materials from an electronics point of view: Cu, like Au, is a very efficient recombination center in Si, and is interesting because Cu is already used for

interconnects in integrated circuits (ICs), so that Cu cannot be considered CMOS incompatible; Ni, because its impurity levels in Si (Figure 1.3) are not too close to the band-gap middle and because Ni–silicide electrical contacts are well-known standard contacts in IC technology. The minimum temperature required for VLS SiNW growth using Ni is 993 °C, about 200 K higher than that of Cu (802 °C). At high temperatures both Cu and Ni are known to produce SiNW growth results comparable to those obtained with Au. Kayes *et al*. managed to synthesize large arrays of perfectly aligned <111> oriented SiNWs with both Au and Cu as catalyst in a $SiCl_4$ CVD process at temperatures of 850–1100 °C [Kayes, 2007]. Yao and Fanclaim to have grown <111> SiNWs at 500 °C via the VSS growth mode using a SiH_4 CVD process [Yao, 2007]. In consistence with the Cu–Si phase diagram, they found a Cu_3Si silicide particle at the tip of the NWs. Unfortunately, the obtained SiNWs show of a significant number of crystallographic defects. Similar results were obtained by Arbiol *et al*. [Arbiol, 2008].

To conclude, the type C catalysts work well but only in the VLS mode and at high temperatures. At temperatures below the eutectic, problems with the crystalline quality of the wires arise. The type B catalysts In, Ga and Sn work but only under harsh experimental conditions (high temperature or plasma assisted). Growth using Zn seems to be easier compared to In or Ga, but there is no real advantage of Zn compare to Au. Thus, for low-temperature CVD, everything boils down to the use of the three type A catalysts, Au, Al, and Ag.

1.4.2. **Alloy catalysts**

Pure metal nanoparticles are widely used to catalyze SiNW growth, but alloy catalysts have been seldomly explored in this context. The choice of catalysts should not only be limited to pure metals. Using alloy catalysts can bring extra benefits compared with using pure metal catalyst in the adjustment of SiNW morphology, distribution and doping. The exploration of alloy catalyst for SiNW growth and Si/Ge heterojunctions mostly focuses on gold-based double-element alloys. Lugstein *et al.* used a Ga-Au alloy catalyst for SiNW growth via CVD method [Lugstein, 2007]: in comparison to the pure gold catalyst, they obtained a much higher proportion of NWs growing perpendicular to the Si (111) substrate and the NWs

showed almost no kinks; their average diameter was smaller, and the diameter and length distributions were narrowly dispersed. Ga-Au alloys have also been used for the growth of Ge–Si heterojunctions. Gamalski [Gamalski, 2013] *et al*. used the environmental transmission electron microscope to observe the Ge–Si heterojunction growth and found that the morphology of the Ge–Si heterojunction depended on the alloy composition. In particular, the extent of a local, asymmetric increase in nanowire diameter, depended on the Ga composition of the catalyst.

Maksimova *et al.* [Maksimova, 2018] used a two-component Au/Cu alloy catalyst (Au/Cu ≈ 60:1) for pulsed laser deposition growth of silicon NWs, with gold as the main catalytic metal and copper as the doping element, where Cu is used to control the geometrical form without contaminating the NW structure. The length of NW is defined by the total amount of copper in the catalyst alloy droplet. Connell [Connell, 2010] *et al.* used Au-Cu alloy nanoparticles with the Au-Cu_2O core-shell structure to catalyze Ge NWs in a low-pressure chemical vapor deposition environment. The NW growth rate for Au-Cu nanoparticles was intermediate between those of Cu (slowest) and Au (fastest) nanoparticles under identical conditions, suggesting a VSS growth process.

Behroudj [Behroudj, 2019] *et al.* presented an approach that relies on Al/Au alloy catalysts for gas-phase SiNW synthesis, allowing intrinsically an *in situ* removal of a native silicon-oxide layer during the initial growth stages, which yields reliable and superior epitaxial growth of SiNWs on single-crystalline silicon substrates.

Meanwhile, the adoption of an alloy catalyst has also recently proven beneficial in an Ag-Au system, highlighting a unique role of alloy-catalyst as a different dimension of growth control in SiNW morphology tailoring. Chou[Chou, 2012] *et al.* demonstrated the use of a new AgAu alloy catalyst for the formation of NWs and Si/Ge/Si heterojunctions with compositionally abrupt interfaces by *in-situ* TEM. Compared to other alloy catalysts sensitive to oxidation, it showed a higher oxidation resistance and more consistent crystal shapes and catalyst/NW orientation relationships during growth. AgAu catalysts were also stable against exodiffusion during growth, making them capable of forming long nanowires with uniform

diameters. By control of the catalyst state, it was possible to switch individual NWs between VSS and VLS growth modes to optimize growth rates.

In addition to gold-based alloy catalysts, Yu [Yu, 2015] *et al.* demonstrated a Bi-Sn alloy catalyzed VLS growth of straight SiNWs with little tapering via PECVD method at 320 and 400 °C, which combines both a sufficient catalyst-doping effect and an optimized SiNW morphology control.

To summarize, compared with elemental metals, using alloy catalysts has a great potential in controlling the NW morphology, distribution, size, growth speed, and orientation, giving new insights into precise doping, which opens a new way to the controlled growth of SiNWs and the heterostructures.

1.5. **Small diameter silicon nanowires**

Small-diameter SiNWs have attracted lots of attention due to their unique one-dimensional geometry with properties suitable for different optoelectric applications [Cui, 2001b]. Early nanowire research focused on the control of the length, diameters and densities, while using different top-down and bottom-up approaches [Misra, 2014]. More recently, small diameter nanowires (below 10 nm) have become the target due to predicted quantum size effects, which change material properties at the smallest scale [Hu, 1999]. The electrical and optical properties of SiNWs are strongly size dependent. In addition, it has been demonstrated recently that small diameter nanowires made of silicon can have a hexagonal diamond crystalline structure, in contrast to the typical diamond cubic one found in bulk, which radically changes opto-electronic properties of such nanowires [Tang, 2017b]. In particular, very small diameter nanowires can have a direct bandgap, which can be tuned by the diameter size [Amato, 2016]. In the following section, we review the fabrication methods that can produce small diameter SiNWs.

1.5.1. **Fabrication of small diameter silicon quantum wires**

Tan [Tan, 2015] *et al*. used Au-Ag nanoparticles as catalyst in metal assisted chemical etching for fabricating vertical SiNW arrays with average diameter of 9.3 nm. The Au-Ag alloy nanoparticles underneath the surface of Si wafer were realized by Au film pre-deposition and Ag ion implantation. Huang

[Huang, 2008] *et al*. fabricated large-area high density (10^{10} wires/cm^2) SiNW arrays by metal-assisted chemical etching of silicon, utilizing anodic aluminum oxide (AAO) as a patterning mask of a thin metallic film on a Si (100) substrate. The SiNWs had diameters ranging from 8 to 20 nm and were vertically aligned to the (100) substrate.

Chen [Chen, 1993] *et al*. reported the fabrication of high aspect ratio, sub-10 nm size, silicon nanopillars without involving any wet chemical etching on large areas (150 μm)^2. A 5 nm thick AuPd film was deposited by ionized beam evaporation and a metal pattern was obtained by liftoff. The AuPd pattern was then used as a mask on the Si substrate which was etched with reactive ion etching. Silicon nanocolumns with diameters ranging from 5 to 7 nm and an aspect ratio of height to diameter of about 7:l were obtained.

Choi [Choi, 2003] *et al*. described a photolithography-based method which was capable of size reduction to produce sub-10-nm SiNW arrays on a wafer scale. By conformally depositing a material (silicon oxide or silicon) that had a different etching property over a lithographically defined sacrificial sidewall and selectively removing the sacrificial material, the sidewall material was preserved and can serve as nanopattern mask for further processing. The resolution of this method was not limited by photolithography but by the thickness of the material deposited.

Moreover, synthetic methods that do not rely on conventional lithographic techniques have been developed to form SiNWs with diameters below 10 nm. These methods rely on metal particles to induce nanowire growth above the semiconductor/metal solution eutectic temperature and can be used to grow large quantities efficiently in either the gas or solution phase. Nanowires grown using these methods are receiving attention for application in technologies ranging from integrated circuit interconnects to functional electronic and optical devices, for example, field effect transistors, photodetectors and biochemical sensors, light-emitting diodes, and complementary logic devices [Morales, 1998, Duan, 2000].

Y. Cui [Cui, 2001a] *et al*. demonstrated the synthesis of SiNWs with an average diameter of 6.4 ± 1.2 nm by using well-defined Au nanocluster catalysts with diameters around 5 nm and silane (SiH_4) as the vapor-phase reactant. High-resolution transmission electron microscopy (HRTEM) demonstrated that the NWs have single-crystal silicon cores sheathed with 1–3 nm of amorphous oxide and that the cores remain highly crystalline for diameters as small as 2 nm. Holmes [Holmes, 2000] *et al*. reported the synthesis of 4–5 nm diameter SiNWs with a narrow distribution using alkanethiol-coated gold nanocrystals (2.5 nm in diameter). The nanowires were grown to a length of several micrometers in supercritical hexane, however undesirable impurities such as gold and carbon were detected. Puglisi [Puglisi, 2019] *et al*. reported the formation of SiNWs as small as 2.8 nm grown by VLS in an inductively coupled plasma-CVD reactor. Au nanoparticles with an average radius of 1.6 nm were sputtered on Si wafer substrates as the catalyst material. However, the SiNWs obtained had a broad diameter distribution up to 50 nm.

Lu [Lu, 2003] *et al.* used molecularly tethered Au nanocrystals with average diameter of 7 nm to grow single-crystal SiNWs on a substrate through a supercritical fluid−liquid−solid (sc-FLS) mechanism. SiNWs with 5 to 30 nm in diameter and several micrometers long were synthesized in supercritical cyclohexane solution. Similarly, Hanrath [Hanrath, 2003] *et al.* produced SiNWs ranging from 4 to 30 nm in diameter and micrometers in length in high temperature supercritical fluids by thermally degrading organosilane precursors in the presence of organic-monolayer protected gold nanocrystals.

To explore the effects of quantum confinement on electrical and optical properties, high quality SiNWs with well-defined and monodisperse diameters are necessary. Small diameter silicon quantum wires have been produced in the past either in negligible quantities (e.g., only small fraction of nanowires had sufficiently small diameters) or using relatively complex approaches, often preventing the production of high densities of SiNWs [Holmes, 2000, Cui, 2001a]. Gold is often used as the catalyst to synthesize small diameter SiNWs, which brings undesirable impurities. In order to consider using large area quantum wire devices, inexpensive fabrication methods with gold-free catalysts adaptable to large areas are needed.

1.5.2. **Small diameter silicon nanowires with hexagonal phase**

J. Tang [Tang, 2017b] *et al*. demonstrated thin SiNW growth via PECVD method using Sn catalyst rather than gold. They prepared the catalyst by thermal evaporation and grew SiNWs directly on a Cu TEM grid. They obtained single crystalline SiNWs with diameters smaller than 4 nm (crystalline core). More interestingly, some of the SiNWs showed a metastable diamond hexagonal phase (see Figure 1.6), which is not present in the phase diagram [Weill, 1989].

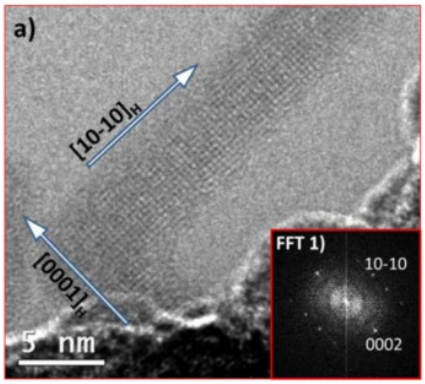

Figure 1.6. HRTEM image of the bottom part of a pure phase 2H SiNWwith a FFT of this image shown in the inset [Tang, 2017b].

In standard (pressure, temperature) conditions, silicon has a diamond cubic (dc, Fd-3m) crystalline structure, as shown in Figure 1.7a. The diamond cubic arrangement is a face-centred cubic (fcc) structure with a two-atom motif. It is one close-packed stacking arrangement, called polytype 3C. The diamond cubic silicon has an indirect bandgap. The crystalline structure of the diamond hexagonal silicon is shown in Figure 1.7b. Names for the diamond hexagonal phase include 2H, dh, hd and lonsdaleite; the term "wurtzite", which is often inaccurately used in the literature, is actually valid for cases where the two atoms of the motif are different.

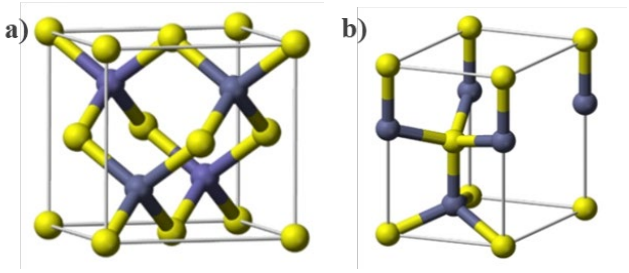

Figure 1.7. Atomic structures of (a) diamond cubic Si and (b) diamond hexagonal Si [Tang, 2017a] (both grey and yellow atoms are Si).

According to the predictions of *ab initio* calculations using the Density Functional Theory (DFT) by Amato *et al*. [Amato, 2016], the bandgap of cubic and hexagonal Si can be tuned with the SiNW diameter, for diameters smaller than 4 nm (see Figure 1.8). In addition, the bandgap of the diamond hexagonal 2H polytype of Si should become direct in nanowires, as indicated by the red arrows. Interestingly, 2H Si should provide a higher absorption of the solar spectrum [Rödl, 2015, Amato, 2016].

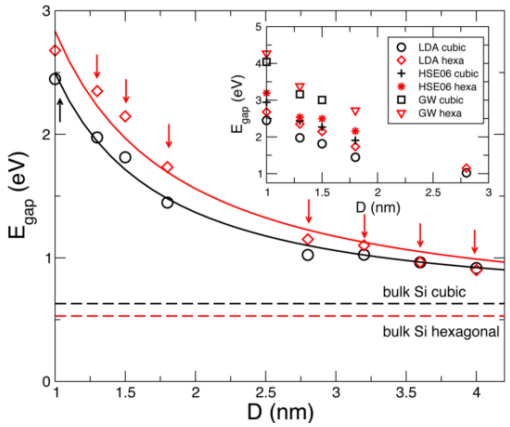

Figure 1.8. Bandgap of cubic (black dots) and hexagonal (red diamonds) Si NWs as a function of the diameter calculated with DFT-LDA [Amato, 2016].

The first report of the 2H polytype in Si was in 1963 by Wentorf [Wentorf, 1963] *et al*. They obtained the 2H phase by applying a series of high pressure (~15 to 16 GPa) and high temperature (200 °C to 1000 °C) treatments to the bulk cubic Si. Later Eremenko [Eremenko, 1972] *et al*. applied Vickers indentation above 400 °C on bulk Si, and found ribbons of 2H Si by Transmission Electron Microscopy

(TEM) observation. Pirouz [Dahmen, 1990, Pirouz, 1990a, Pirouz, 1990b] *et al*. made a crystallographic analysis and proposed that the cubic to hexagonal phase transformation was martensitic, which did not involve diffusion process. The presence of 2H Si was because the intersection of twin planes created shear stress and then relaxed through the formation of diamond hexagonal Si ribbons.

Vincent [Vincent, 2018] *et al*. realized the phase transformation from diamond structure toward the hexagonal 2H-allotrope in SiNWs by plastic deformation based on applied radial compressive stresses inside a surrounding matrix. They ingrained the SiNWs in a hydrogenated silesquioxane (HSQ) resist, then transferred the sample into an oven and increased the temperature to brought to 500 °C. The densification of the HSQ mold, followed by its transformation into SiO_2, and the subsequent cooling create a high amount of shear stress between the SiNWs and the mod. This stress is then relaxed by formation of ribbons of hexagonal phase in the SiNWs. The observations were consistent with a martensitic phase transformation. However, shear-driven transformations have the disadvantage of lacking precise control on the size of 2H domains.

PECVD method provides an easy and inexpensive way to fabricate high-quality single crystal SiNWs with well-defined small diameters, which does not necessarily bring undesirable gold impurities. It brings substantial opportunities for the exploration of the quantum effects on electrical and optical properties of one-dimensional silicon structures, and for large area quantum devices for optoelectronic applications. What makes it more interesting is that hexagonal SiNWs, which are predicted to have a direct bandgap that can be tuned by the control of diameter, can be grown spontaneously in a PECVD reactor. The predicted band structure of hexagonal SiNW makes it a better absorber than the standard diamond cubic SiNWs.

1.6. **Outline of the thesis**

In this thesis, we focus on PECVD growth of silicon quantum wires with cubic and hexagonal diamond structure and their photovoltaic applications. The work will be presented in the following sequence:

Chapter 2 will introduce the techniques and setups for catalyst preparation, Plasma-enhanced chemical vapor deposition, and SEM and TEM characterizations for SiNWs. After that, we will present fabrication of radial junction solar cells and their characterization.

In chapter 3, we will firstly analyze the SiNWs that were grown at LPICM before the present work with Sn catalyst on Cu TEM grids [Tang, 2017b]. We will look for a possible contamination of Sn by the Cu from the substrate; then we will study the influence of PECVD conditions on nanowire growth with Sn catalyst on Cu TEM grids; finally, we will report the problems with repeatability of SiNW growth on Cu TEM grids.

In chapter 4, we will choose the amounts of Cu and Sn in mixed Cu-Sn catalysts. We will start with the crystalline structure of SiNWs fabricated with pure Sn catalyst. Next, we will use nanoparticles of SnCu mixed catalysts and observe the changes compared to Sn. We will study the evolution of the catalyst crystalline structure by TEM at each step of the SiNW growth. In the last part we will introduce a special phenomenon of catalyst separation in SiNWs with diameters smaller than 25 nm.

We will use SnCu mixed catalysts to grow SiNWs in chapter 5. Firstly, we will introduce the structure of nanowires with diameters above 10 nm. Next, we will focus on making small diameter SiNWs by optimizing the co-catalyst composition and amount. Finally, we will show the presence of hexagonal SiNWs and the influence of the PECVD conditions on SiNW polytype.

In chapter 6, we will introduce SiNW growth with two other Cu-based mixed catalysts: InCu catalyst and AuCu catalyst. We will study the influence of the mixed catalyst compositions on SiNW growth and characterize the crystalline structures of the NWs.

In the last chapter, we will introduce the fabrication of radial junction solar cells based on high density thin silicon nanowire arrays, which are catalyzed by SnCu mixed catalyst and InCu mixed catalyst.

References

Allen, J.E., E.R. Hemesath, D.E. Perea, J.L. Lensch-Falk, Z.Y. Li, F. Yin, M.H. Gass, P. Wang, A.L. Bleloch, R.E. Palmer, and L.J. Lauhon, *High-resolution detection of Au catalyst atoms in Si nanowires.* Nat Nanotechnol, 2008. **3**(3): p. 168-73. https://doi.org/10.1038/nnano.2008.5

Amato, M., T. Kaewmaraya, A. Zobelli, M. Palummo, and R. Rurali, *Crystal Phase Effects in Si Nanowire Polytypes and Their Homojunctions.* Nano Lett, 2016. **16**(9): p. 5694-700. https://doi.org/10.1021/acs.nanolett.6b02362

Arbiol, J., A. Fontcuberta i Morral, S. Estradé, F. Peiró, B. Kalache, P. Roca i Cabarrocas, and J.R. Morante, *Influence of the (111) twinning on the formation of diamond cubic/diamond hexagonal heterostructures in Cu-catalyzed Si nanowires.* Journal of Applied Physics, 2008. **104**(6): p. 064312. https://doi.org/10.1063/1.2976338

Arbiol, J., B. Kalache, P.R.i. Cabarrocas, J.R. Morante, and A.F.i. Morral, *Influence of Cu as a catalyst on the properties of silicon nanowires synthesized by the vapour–solid–solid mechanism.* Nanotechnology, 2007. **18**(30): p. 305606. https://doi.org/10.1088/0957-4484/18/30/305606

Baron, T., M. Gordon, F. Dhalluin, C. Ternon, P. Ferret, and P. Gentile, *Si nanowire growth and characterization using a microelectronics-compatible catalyst: PtSi.* Applied Physics Letters, 2006. **89**(23): p. 233111. https://doi.org/10.1063/1.2402118

Behroudj, A., D. Geiger, and S. Strehle, *Epitaxial Bottom-up Growth of Silicon Nanowires on Oxidized Silicon by Alloy-Catalyzed Gas-Phase Synthesis.* Nano Lett, 2019. **19**(11): p. 7895-7900. https://doi.org/10.1021/acs.nanolett.9b02950

Bootsma, G.A. and H.J. Gassen, *A quantitative study on the growth of silicon whiskers from silane and germanium whiskers from germane.* Journal of Crystal Growth, 1971. **10**(3): p. 223-234. https://doi.org/10.1016/0022-0248(71)90188-6

Cahn, R.W., *Binary Alloy Phase Diagrams-Second edition. T. B. Massalski, Editor-in-Chief; H. Okamoto, P. R. Subramanian, L. Kacprzak, Editors. ASM International, Materials Park, Ohio, USA. December 1990. xxii, 3589 pp., 3 vol., hard- back. $995.00 the set.* Advanced Materials, 1991. **3**(12): p. 628-629. https://doi.org/10.1002/adma.19910031215

Chen, K.-I., B.-R. Li, and Y.-T. Chen, *Silicon nanowire field-effect transistor-based biosensors for biomedical diagnosis and cellular recording investigation.* Nano Today, 2011a. **6**(2): p. 131-154. https://doi.org/10.1016/j.nantod.2011.02.001

Chen, W. and H. Ahmed, *Fabrication of high aspect ratio silicon pillars of <10 nm diameter.* Applied Physics Letters, 1993. **63**(8): p. 1116-1118. https://doi.org/10.1063/1.109798

Choi, Y.-K., J. Zhu, J. Grunes, J. Bokor, and G.A. Somorjai, *Fabrication of Sub-10-nm Silicon Nanowire Arrays by Size Reduction Lithography.* The Journal of Physical Chemistry B, 2003. **107**(15): p. 3340-3343. https://doi.org/10.1021/jp0222649

Chou, Y.C., C.Y. Wen, M.C. Reuter, D. Su, E.A. Stach, and F.M. Ross, *Controlling the growth of Si/Ge nanowires and heterojunctions using silver-gold alloy catalysts.* ACS Nano, 2012. **6**(7): p. 6407-15. https://doi.org/10.1021/nn301978x

Chung, S.-W., J.-Y. Yu, and J.R. Heath, *Silicon nanowire devices.* Applied Physics Letters, 2000. **76**(15): p. 2068-2070. https://doi.org/10.1063/1.126257

Connell, J.G., Z.Y. Al Balushi, K. Sohn, J. Huang, and L.J. Lauhon, *Growth of Ge Nanowires from Au−Cu Alloy Nanoparticle Catalysts Synthesized from Aqueous Solution.* The Journal of Physical Chemistry Letters, 2010. **1**(23): p. 3360-3365. https://doi.org/10.1021/jz101436a

Cui, Y., L.J. Lauhon, M.S. Gudiksen, J. Wang, and C.M. Lieber, *Diameter-controlled synthesis of single-crystal silicon nanowires.* Applied Physics Letters, 2001a. **78**(15): p. 2214-2216. https://doi.org/10.1063/1.1363692

Cui, Y. and C.M. Lieber, *Functional nanoscale electronic devices assembled using silicon nanowire building blocks.* Science, 2001b. **291**(5505): p. 851-3. https://doi.org/10.1126/science.291.5505.851

Dahmen, U., K.H. Westmacott, P. Pirouz, and R. Chaim, *The martensitic transformation in silicon—II. crystallographic analysis.* Acta Metallurgica et Materialia, 1990. **38**(2): p. 323-328. https://doi.org/10.1016/0956-7151(90)90062-l

Das Kanungo, P., N. Zakharov, J. Bauer, O. Breitenstein, P. Werner, and U. Goesele, *Controlled in situ boron doping of short silicon nanowires grown by molecular beam epitaxy.* Applied Physics Letters, 2008. **92**(26): p. 263107. https://doi.org/10.1063/1.2953702

Duan, X. and C.M. Lieber, *General Synthesis of Compound Semiconductor Nanowires.* Advanced Materials, 2000. **12**(4): p. 298-302. https://doi.org/10.1002/(sici)1521-4095(200002)12:4<298::Aid-adma298>3.0.Co;2-y

Eremenko, V.G. and V.I. Nikitenko, *Electron microscope investigation of the microplastic deformation mechanisms of silicon by indentation.* Physica Status Solidi (a), 1972. **14**(1): p. 317-330. https://doi.org/10.1002/pssa.2210140139

Gamalski, A.D., D.E. Perea, J. Yoo, N. Li, M.J. Olszta, R. Colby, D.K. Schreiber, C. Ducati, S.T. Picraux, and S. Hofmann, *Catalyst composition and impurity-dependent kinetics of nanowire heteroepitaxy.* ACS Nano, 2013. **7**(9): p. 7689-97. https://doi.org/10.1021/nn402208p

Givargizov, E.I. and N.N. Sheftal, *Morphology of silicon whiskers grown by the VLS-technique.* Journal of Crystal Growth, 1971. **9**: p. 326-329. https://doi.org/10.1016/0022-0248(71)90250-8

Hanrath, T. and B.A. Korgel, *Supercritical Fluid–Liquid–Solid (SFLS) Synthesis of Si and Ge Nanowires Seeded by Colloidal Metal Nanocrystals.* Advanced Materials, 2003. **15**(5): p. 437-440. https://doi.org/10.1002/adma.200390101

Hofmann, S., R. Sharma, C.T. Wirth, F. Cervantes-Sodi, C. Ducati, T. Kasama, R.E. Dunin-Borkowski, J. Drucker, P. Bennett, and J. Robertson, *Ledge-flow-controlled catalyst interface dynamics during Si nanowire growth.* Nat Mater, 2008. **7**(5): p. 372-5. https://doi.org/10.1038/nmat2140

Holmes, J.D., K.P. Johnston, R.C. Doty, and B.A. Korgel, *Control of thickness and orientation of solution-grown silicon nanowires.* Science, 2000. **287**(5457): p. 1471-3. https://doi.org/10.1126/science.287.5457.1471

Hsu, C.-M., S.T. Connor, M.X. Tang, and Y. Cui, *Wafer-scale silicon nanopillars and nanocones by Langmuir–Blodgett assembly and etching.* Applied Physics Letters, 2008. **93**(13): p. 133109. https://doi.org/10.1063/1.2988893

Hu, J., T.W. Odom, and C.M. Lieber, *Chemistry and Physics in One Dimension: Synthesis and Properties of Nanowires and Nanotubes.* Accounts of Chemical Research, 1999. **32**(5): p. 435-445. https://doi.org/10.1021/ar9700365

Huang, Z., X. Zhang, M. Reiche, L. Liu, W. Lee, T. Shimizu, S. Senz, and U. Gosele, *Extended arrays of vertically aligned sub-10 nm diameter [100] Si nanowires by metal-assisted chemical etching.* Nano Lett, 2008. **8**(9): p. 3046-51. https://doi.org/10.1021/nl802324y

Hyvl, M., M. Muller, T.H. Stuchlikova, J. Stuchlik, M. Silhavik, J. Kocka, A. Fejfar, and J. Cervenka, *Nucleation and growth of metal-catalyzed silicon nanowires under plasma.* Nanotechnology, 2020. **31**(22): p. 225601. https://doi.org/10.1088/1361-6528/ab76ef

Iacopi, F., O. Richard, Y. Eichhammer, H. Bender, P.M. Vereecken, S. De Gendt, and M. Heyns, *Size-Dependent Characteristics of Indium-Seeded Si Nanowire Growth.* Electrochemical and Solid-State Letters, 2008. **11**(9): p. K98. https://doi.org/10.1149/1.2945800

Iacopi, F., P.M. Vereecken, M. Schaekers, M. Caymax, N. Moelans, B. Blanpain, O. Richard, C. Detavernier, and H. Griffiths, *Plasma-enhanced chemical vapour deposition growth of Si nanowires with low melting point metal catalysts: an effective alternative to Au-mediated growth.* Nanotechnology, 2007. **18**(50): p. 505307. https://doi.org/10.1088/0957-4484/18/50/505307

Kalache, B., P.R.i. Cabarrocas, and A.F.i. Morral, *Observation of Incubation Times in the Nucleation of Silicon Nanowires Obtained by the Vapor-Liquid-Solid Method.* Japanese Journal of Applied Physics, 2006. **45**(No. 7): p. L190-L193. https://doi.org/10.1143/jjap.45.L190

Kamins, T.I., R.S. Williams, Y. Chen, Y.L. Chang, and Y.A. Chang, *Chemical vapor deposition of Si nanowires nucleated by TiSi2 islands on Si.* Applied Physics Letters, 2000. **76**(5): p. 562-564. https://doi.org/10.1063/1.125852

Kayes, B.M., M.A. Filler, M.C. Putnam, M.D. Kelzenberg, N.S. Lewis, and H.A. Atwater, *Growth of vertically aligned Si wire arrays over large areas (>1cm2) with Au and Cu catalysts.* Applied Physics Letters, 2007. **91**(10): p. 103110. https://doi.org/10.1063/1.2779236

Kim, D.R., C.H. Lee, and X. Zheng, *Direct growth of nanowire logic gates and photovoltaic devices.* Nano Lett, 2010. **10**(3): p. 1050-4. https://doi.org/10.1021/nl100011z

Könenkamp, R., R.C. Word, and C. Schlegel, *Vertical nanowire light-emitting diode.* Applied Physics Letters, 2004. **85**(24): p. 6004-6006. https://doi.org/10.1063/1.1836873

Lieber, C.M. and Z.L. Wang, *Functional Nanowires.* MRS Bulletin, 2011. **32**(2): p. 99-108. https://doi.org/10.1557/mrs2007.41

Lu, X., T. Hanrath, K.P. Johnston, and B.A. Korgel, *Growth of Single Crystal Silicon Nanowires in Supercritical Solution from Tethered Gold Particles on a Silicon Substrate.* Nano Letters, 2003. **3**(1): p. 93-99. https://doi.org/10.1021/nl0202307

Lugstein, A., M. Steinmair, Y.J. Hyun, E. Bertagnolli, and P. Pongratz, *Ga ⁄ Au alloy catalyst for single crystal silicon-nanowire epitaxy.* Applied Physics Letters, 2007. **90**(2): p. 023109. https://doi.org/10.1063/1.2431468

Lysov, A., S. Vinaji, M. Offer, C. Gutsche, I. Regolin, W. Mertin, M. Geller, W. Prost, G. Bacher, and F.-J. Tegude, *Spatially resolved photoelectric performance of axial GaAs nanowire pn-diodes.* Nano Research, 2011. **4**(10): p. 987-995. https://doi.org/10.1007/s12274-011-0155-4

Maksimova, K.Y., A.A. Kozlov, P.V. Shvets, U.Y. Koneva, O.V. Yurkevich, O.I. Lebedev, O.F. Vyvenko, V.Y. Mikhailovskii, and A.Y. Goikhman, *Copper-Stabilized Si/Au Nanowhiskers for Advanced Nanoelectronic Applications.* ACS Omega, 2018. **3**(2): p. 1684-1688. https://doi.org/10.1021/acsomega.7b01640

Ming, L., K.H. Yeo, S.D. Suk, Y.Y. Yeoh, D. Kim, T.Y. Chung, K.S. Oh, and W. Lee. *Sub-10 nm gate-all-around CMOS nanowire transistors on bulk Si substrate*. in *2009 Symposium on VLSI Technology*. 2009.

Misra, S., *Single and tandem radial junction silicon thin film solar cells based on PECVD grown crystalline silicon nanowire arrays*. 2015, Ecole polytechnique: France.

Misra, S., L. Yu, W. Chen, M. Foldyna, and P.R.i. Cabarrocas, *A review on plasma-assisted VLS synthesis of silicon nanowires and radial junction solar cells.* Journal of Physics D: Applied Physics, 2014. **47**(39): p. 393001. https://doi.org/10.1088/0022-3727/47/39/393001

Misra, S., L. Yu, W. Chen, and P. Roca i Cabarrocas, *Wetting Layer: The Key Player in Plasma-Assisted Silicon Nanowire Growth Mediated by Tin.* The Journal of Physical Chemistry C, 2013a. **117**(34): p. 17786-17790. https://doi.org/10.1021/jp403063d

Morales, A.M. and C.M. Lieber, *A laser ablation method for the synthesis of crystalline semiconductor nanowires.* Science, 1998. **279**(5348): p. 208-11. https://doi.org/10.1126/science.279.5348.208

Morton, K.J., G. Nieberg, S. Bai, and S.Y. Chou, *Wafer-scale patterning of sub-40 nm diameter and high aspect ratio (>50:1) silicon pillar arrays by nanoimprint and etching.* Nanotechnology, 2008. **19**(34): p. 345301. https://doi.org/10.1088/0957-4484/19/34/345301

Mouchet, C., L. Latu-Romain, C. Cayron, E. Rouviere, C. Celle, and J.P. Simonato, *Growth of one-dimensional Si/SiGe heterostructures by thermal CVD.* Nanotechnology, 2008. **19**(33): p. 335603. https://doi.org/10.1088/0957-4484/19/33/335603

Nebol'sin, V.A. and A.A. Shchetinin, *Role of Surface Energy in the Vapor–Liquid–Solid Growth of Silicon.* Inorganic Materials, 2003. **39**(9): p. 899-903. https://doi.org/10.1023/a:1025588601262

Osada, Y., H. Nakayama, M. Shindo, T. Odaka, and Y. Ogata, *Growth and Structure of Silicon Fibers.* Journal of The Electrochemical Society, 2019. **126**(1): p. 31-36. https://doi.org/10.1149/1.2128983

Pan, L., K.-K. Lew, J.M. Redwing, and E.C. Dickey, *Effect of diborane on the microstructure of boron-doped silicon nanowires.* Journal of Crystal Growth, 2005. **277**(1-4): p. 428-436. https://doi.org/10.1016/j.jcrysgro.2005.01.091

Peng, K.Q., Y.J. Yan, S.P. Gao, and J. Zhu, *Synthesis of Large-Area Silicon Nanowire Arrays via Self-Assembling Nanoelectrochemistry.* Advanced Materials, 2002. **14**(16): p. 1164-1167. https://doi.org/10.1002/1521-4095(20020816)14:16<1164::Aid-adma1164>3.0.Co;2-e

Pirouz, P., R. Chaim, U. Dahmen, and K.H. Westmacott, *The martensitic transformation in silicon—I experimental observations.* Acta Metallurgica et Materialia, 1990a. **38**(2): p. 313-322. https://doi.org/10.1016/0956-7151(90)90061-k

Pirouz, P., U. Dahmen, K.H. Westmacott, and R. Chaim, *The martensitic transformation in silicon—III. comparison with other work.* Acta Metallurgica et Materialia, 1990b. **38**(2): p. 329-336. https://doi.org/10.1016/0956-7151(90)90063-m

Puglisi, R.A., C. Bongiorno, S. Caccamo, E. Fazio, G. Mannino, F. Neri, S. Scalese, D. Spucches, and A. La Magna, *Chemical Vapor Deposition Growth of Silicon Nanowires with Diameter Smaller Than 5 nm.* ACS Omega, 2019. **4**(19): p. 17967-17971. https://doi.org/10.1021/acsomega.9b01488

Rödl, C., T. Sander, F. Bechstedt, J. Vidal, P. Olsson, S. Laribi, and J.F. Guillemoles, *Wurtzite silicon as a potential absorber in photovoltaics: Tailoring the optical absorption by applying strain.* Physical Review B, 2015. **92**(4): p. 045207. https://doi.org/10.1103/PhysRevB.92.045207

Schmid, H., M.T. Björk, J. Knoch, H. Riel, W. Riess, P. Rice, and T. Topuria, *Patterned epitaxial vapor-liquid-solid growth of silicon nanowires on Si(111) using silane.* Journal of Applied Physics, 2008. **103**(2): p. 024304. https://doi.org/10.1063/1.2832760

Schmidt, V., S. Senz, and U. Gosele, *Diameter-dependent growth direction of epitaxial silicon nanowires.* Nano Lett, 2005a. **5**(5): p. 931-5. https://doi.org/10.1021/nl050462g

Schmidt, V., S. Senz, and U. Gösele, *UHV chemical vapour deposition of silicon nanowires.* Zeitschrift für Metallkunde, 2005b. **96**(5): p. 427-428. https://doi.org/10.3139/146.018129

Schmidt, V., J.V. Wittemann, S. Senz, and U. Gösele, *Silicon Nanowires: A Review on Aspects of their Growth and their Electrical Properties.* Advanced Materials, 2009. **21**(25-26): p. 2681-2702. https://doi.org/10.1002/adma.200803754

Schubert, L., P. Werner, N.D. Zakharov, G. Gerth, F.M. Kolb, L. Long, U. Gösele, and T.Y. Tan, *Silicon nanowhiskers grown on 〈111〉 Si substrates by molecular-beam epitaxy.* Applied Physics Letters, 2004. **84**(24): p. 4968-4970. https://doi.org/10.1063/1.1762701

Singh, N., K.D. Buddharaju, S.K. Manhas, A. Agarwal, S.C. Rustagi, G.Q. Lo, N. Balasubramanian, and D.-L. Kwong, *Si, SiGe Nanowire Devices by Top–Down Technology and Their Applications.* IEEE Transactions on Electron Devices, 2008. **55**(11): p. 3107-3118. https://doi.org/10.1109/ted.2008.2005154

Sung Dae, S., Y. Kyoung Hwan, C. Keun Hwi, L. Ming, Y. Yun Young, L. Sung-Young, K. Sung Min, Y. Eun Jung, K. Min Sang, O. Chang Woo, K. Sung Hwan, K. Dong-Won, and P. Donggun, *High-Performance Twin Silicon Nanowire MOSFET (TSNWFET) on Bulk Si Wafer.* IEEE Transactions on Nanotechnology, 2008. **7**(2): p. 181-184. https://doi.org/10.1109/tnano.2008.917843

Sze, S.M. and K.K. Ng, *Physics of semiconductor devices*. 2006: John wiley & sons.

Tan, Z., W. Shi, C. Guo, Q. Zhang, L. Yang, X. Wu, G.A. Cheng, and R. Zheng, *Fabrication of ultra-thin silicon nanowire arrays using ion beam assisted chemical etching.* Nanoscale, 2015. **7**(41): p. 17268-73. https://doi.org/10.1039/c5nr02876k

Tang, J., *From Silicon to Germanium Nanowires : growth processes and solar cell structures*. 2017a, Université Paris Saclay (COmUE).

Tang, J., J.L. Maurice, F. Fossard, I. Florea, W. Chen, E.V. Johnson, M. Foldyna, L. Yu, and I.C.P. Roca, *Natural occurrence of the diamond hexagonal structure in silicon nanowires grown by a plasma-assisted vapour-liquid-solid method.* Nanoscale, 2017b. **9**(24): p. 8113-8118. https://doi.org/10.1039/c7nr01299c

Tezuka, T., E. Toyoda, S. Nakaharai, T. Irisawa, N. Hirashita, Y. Moriyama, N. Sugiyama, N. Taoka, Y. Yamashita, O. Kiso, M. Harada, T. Yamamoto, and S. Takagi. *Observation of Mobility Enhancement in Strained Si and SiGe Tri-Gate MOSFETs with Multi-Nanowire Channels Trimmed by Hydrogen Thermal Etching*. in *2007 IEEE International Electron Devices Meeting*. 2007. https://doi.org/10.1109/IEDM.2007.4419092

Treuting, R.G. and S.M. Arnold, *Orientation habits of metal whiskers.* Acta Metallurgica, 1957. **5**(10): p. 598. https://doi.org/10.1016/0001-6160(57)90128-1

Vincent, L., D. Djomani, M. Fakfakh, C. Renard, B. Belier, D. Bouchier, and G. Patriarche, *Shear-driven phase transformation in silicon nanowires.* Nanotechnology, 2018. **29**(12): p. 125601. https://doi.org/10.1088/1361-6528/aaa738

Wagner, R.S. and W.C. Ellis, *Vapor-Liquid-Solid Mechanism of Single Crystal Growth.* Applied Physics Letters, 1964. **4**(5): p. 89-90. https://doi.org/10.1063/1.1753975

Wang, Y., K.K. Lew, T.T. Ho, L. Pan, S.W. Novak, E.C. Dickey, J.M. Redwing, and T.S. Mayer, *Use of phosphine as an n-type dopant source for vapor-liquid-solid growth of silicon nanowires.* Nano Lett, 2005. **5**(11): p. 2139-43. https://doi.org/10.1021/nl051442h

Wang, Y., V. Schmidt, S. Senz, and U. Gosele, *Epitaxial growth of silicon nanowires using an aluminium catalyst.* Nat Nanotechnol, 2006. **1**(3): p. 186-9. https://doi.org/10.1038/nnano.2006.133

Weill, G., J.L. Mansot, G. Sagon, C. Carlone, and J.M. Besson, *Characterisation of Si III and Si IV, metastable forms of silicon at ambient pressure.* Semiconductor Science and Technology, 1989. **4**(4): p. 280-282. https://doi.org/10.1088/0268-1242/4/4/029

Wentorf, R.H. and J.S. Kasper, *Two New Forms of Silicon.* Science, 1963. **139**(3552): p. 338-339. https://doi.org/10.1126/science.139.3552.338-a

Werner, P., N.D. Zakharov, G. Gerth, L. Schubert, and U. Gösele, *On the formation of Si nanowires by molecular beam epitaxy.* International Journal of Materials Research, 2006. **97**(7): p. 1008-1015. https://doi.org/10.3139/146.101332

Weyher, J., *Some notes on the growth kinetics and morphology of VLS silicon crystals grown with platinum and gold as liquid-forming agents.* Journal of Crystal Growth, 1978. **43**(2): p. 235-244. https://doi.org/10.1016/0022-0248(78)90173-2

Yao, Y. and S. Fan, *Si nanowires synthesized with Cu catalyst.* Materials Letters, 2007. **61**(1): p. 177-181. https://doi.org/10.1016/j.matlet.2006.04.045

Yu, J.-Y., S.-W. Chung, and J.R. Heath, *Silicon Nanowires: Preparation, Device Fabrication, and Transport Properties.* The Journal of Physical Chemistry B, 2000. **104**(50): p. 11864-11870. https://doi.org/10.1021/jp002595q

Yu, L., P.J. Alet, G. Picardi, I. Maurin, and P.R. Cabarrocas, *Synthesis, morphology and compositional evolution of silicon nanowires directly grown on SnO(2) substrates.* Nanotechnology, 2008. **19**(48): p. 485605. https://doi.org/10.1088/0957-4484/19/48/485605

Yu, L., F. Fortuna, B. O'Donnell, T. Jeon, M. Foldyna, G. Picardi, and P. Roca i Cabarrocas, *Bismuth-catalyzed and doped silicon nanowires for one-pump-down fabrication of radial junction solar cells.* Nano Lett, 2012. **12**(8): p. 4153-8. https://doi.org/10.1021/nl3017187

Yu, L., B. O'Donnell, J.-L. Maurice, and P. Roca i Cabarrocas, *Core-shell structure and unique faceting of Sn-catalyzed silicon nanowires.* Applied Physics Letters, 2010. **97**(2): p. 023107. https://doi.org/10.1063/1.3464557

Yu, Z., J. Lu, S. Qian, S. Misra, L. Yu, J. Xu, L. Xu, J. Wang, Y. Shi, K. Chen, and P. Roca i Cabarrocas, *Bi-Sn alloy catalyst for simultaneous morphology and doping control of silicon nanowires in radial junction solar cells.* Applied Physics Letters, 2015. **107**(16): p. 163105. https://doi.org/10.1063/1.4933274

Zakharov, N.D., P. Werner, G. Gerth, L. Schubert, L. Sokolov, and U. Gösele, *Growth phenomena of Si and Si/Ge nanowires on Si (111) by molecular beam epitaxy.* Journal of Crystal Growth, 2006. **290**(1): p. 6-10. https://doi.org/10.1016/j.jcrysgro.2005.12.096

Zhang, A., G. Zheng, and C.M. Lieber, *Emergence of Nanowires*, in *Nanowires: Building Blocks for Nanoscience and Nanotechnology*, A. Zhang, G. Zheng, and C. M. Lieber, Editors. 2016, Springer International Publishing: Cham. p. 1-13. https://doi.org/10.1007/978-3-319-41981-7_1

Zhang, Y.F., Y.H. Tang, N. Wang, D.P. Yu, C.S. Lee, I. Bello, and S.T. Lee, *Silicon nanowires prepared by laser ablation at high temperature.* Applied Physics Letters, 1998. **72**(15): p. 1835-1837. https://doi.org/10.1063/1.121199

Zhou, G.W., Z. Zhang, Z.G. Bai, S.Q. Feng, and D.P. Yu, *Transmission electron microscopy study of Si nanowires.* Applied Physics Letters, 1998. **73**(5): p. 677-679. https://doi.org/10.1063/1.121945

Zschech, D., D.H. Kim, A.P. Milenin, R. Scholz, R. Hillebrand, C.J. Hawker, T.P. Russell, M. Steinhart, and U. Gosele, *Ordered arrays of <100>-oriented silicon nanorods by CMOS-compatible block copolymer lithography.* Nano Lett, 2007. **7**(6): p. 1516-20. https://doi.org/10.1021/nl070275d

Chapter 2. Fabrication and characterization setups and techniques

The goal of this thesis is to fabricate thin SiNWs with hexagonal phase. We choose PECVD method to grow SiNWs as it has been reported that hexagonal SiNWs with crystalline diameters smaller than 4 nm can be grown directly by PECVD [Tang, 2017b]. To synthesize SiNWs, the first step is to prepare the catalyst by thermal evaporation, as metal nanoparticles (NPs) are required to provide nucleation sites to promote crystalline SiNW growth. Catalyst preparation will be introduced in detail in section 2.1. Then the substrates with evaporated catalysts are loaded into a PECVD reactor for SiNW growth. The PECVD technique will be presented in detail in section 2.1. After SiNW growth, the NWs will be characterized by Scanning electron microscopy (SEM) for morphology, size and distribution observation at first and then Transmission electron microscopy (TEM) for crystalline structure observation. These two characterization methods will be introduced in section 2.3.

After finishing SiNW growth and characterization, we focus on applications of SiNW based devices. Based on the experience with solar cells of LPICM for years, we decide to fabricate radial junction solar cells for the initial exploration of SiNW applications. To make solar cells, we first deposit a bottom contact using a sputtering machine on the substrates, and we evaporate catalysts on it subsequently. Then we fabricate radial junctions in a PECVD reactor. Finally, we deposit top contacts on the radial junctions to complete the solar cell fabrication. This part will be presented in section 2.4. Last of all, we present photovoltaic device characterization in section 2.5, including J-V, Electron Beam Induced Current (EBIC) and External quantum efficiency (EQE) measurements.

2.1. **Catalyst preparation**

2.1.1. **Thermal evaporation**

First let us learn about thermal evaporation. The catalyst is prepared using a Boc Edwards Auto 306 Evaporator FL 400. Figure 2.1 shows a photo of that evaporator and its internal components. The first step of thermal evaporation is to fix the substrates to the substrate holder and load the catalyst metal into the tungsten crucible. We have used a substrate holder with multiple places for different substrates such as

Corning glass, c-Si wafer or TEM grids. The nominal thickness of the evaporated catalyst is measured by a quartz crystal microbalance (QCM) *in situ* during evaporation. The density of the metal is input on the control panel on the right and the values are chosen for each evaporated metal accordingly (Figure 2.1a). The system works in a vacuum with the pressure below 5×10^{-6} mbar. The current in the crucible is then increased enough to heat and evaporate the catalyst metal, but not too much to lead to a too fast evaporation speed. The principle of the QCM is that a frequency shift is introduced when evaporated materials are deposited on the crystal. It follows equation [Latif, 2013]:

$$dm = -c(1/f_0^2)/df^2 \qquad 2.1$$

where dm is the mass of the deposited materials, f_0 is the intrinsic frequency of the quartz crystal, df is the frequency variation, and c is a constant of the quartz crystal. With the density of the material ρ, the change of the thickness dh of the evaporated material on the quartz can be calculated as follows:

$$dh = dm/\rho s \qquad 2.2$$

where S is the quartz surface. When the change of the thickness reaches a desired value, the evaporation is stopped by moving the shutter followed by turning the current down to zero value. Given the poor wetting of the metals on those substrates, nanoparticles were naturally formed by atom aggregation upon thermal evaporation.

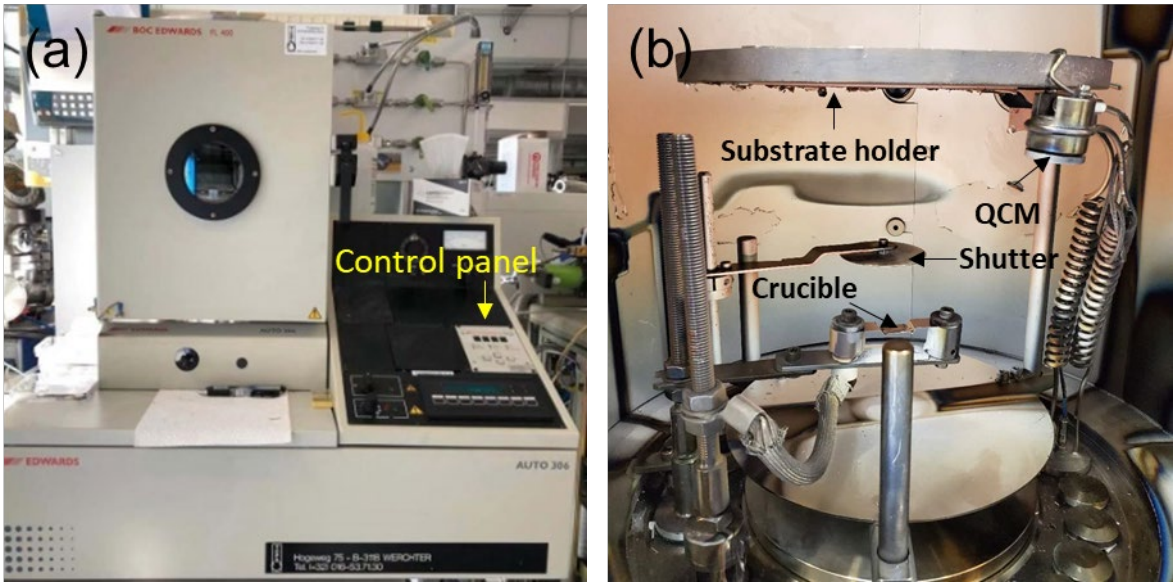

Figure 2.1. (a) Boc Edwards Auto 306 Evaporator FL 400 and (b) and its interior structures.

In order to obtain small NP diameters and reduced density, we evaporate as little amount of catalyst as possible on the substrates. The lowest nominal thickness that can be given by this evaporator is 1 Å (0.1 nm) due to its limited indicated precision. Two methods are applied to realize the deposition of catalyst with nominal thickness thinner than 0.1 nm. One method is to modify the material density ρ of the catalyst metal given as input in the microbalance. To deposit less than 0.1 nm catalyst metal, instead of using the exact value of the metal density ρ_0, we input a smaller value $\rho_1 = \rho_0/n$ on the control panel. This effectively enlarges the usable range of the QCM shown on the display. When the control panel displays 0.1 nm nominal thickness of deposited material, the actual deposited thickness equals to $0.1/n$ nm. In this way we can explore nominal thickness of the evaporated catalyst below 0.1 nm, given that the evaporation rate is sufficiently slow.

The other method to obtain catalyst evaporation less than 0.1 nm nominal thickness is to tilt the substrate. If the substrate is tilted by an angle θ to the substrate holder (see Figure 2.2), when the control panel displays 0.1 nm nominal thickness, the effective thickness of the evaporated catalyst should be $0.1\cos\theta$ nm. Both methods have been proven effective for evaporating catalyst with nominal thicknesses below 0.1 nm.

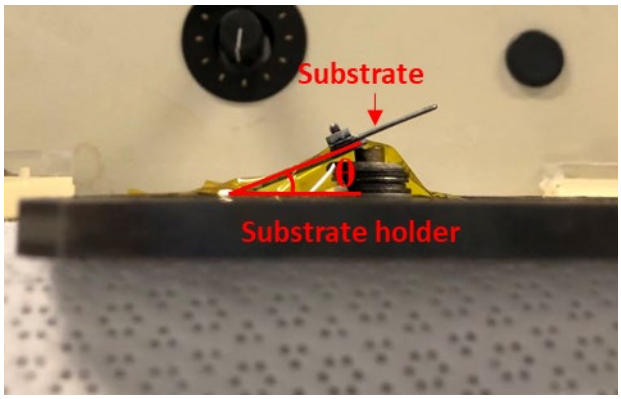

Figure 2.2. Substrate tilted by θ degree to the substrate holder of the thermal evaporator.

2.1.2. **Thermal evaporation of mixed-catalyst**

In this thesis, we use mixed metals rather than pure metal as the catalyst, for example, mixtures of Cu and Sn. To prepare the co-catalyst of Cu and Sn, these metals are subsequently evaporated. After Cu has been evaporated on the substrates, we open the chamber and exchange the crucible with another for the second metal Sn. Afterwards, Sn is deposited on top of Cu. The advantage of the two-step catalyst preparation is its flexibility, as we can choose the co-catalyst materials and compositions independently.

We have also fused Cu and Sn together in a same crucible in order to prepare the mixed-catalyst in the Boc Edwards Auto 306 Evaporator in one run. We put weighted amount of Cu and Sn ingots on the tungsten crucible in the evaporator and melted both metals using a current of 5 A (sufficient to melt both metals individually). The fusion process is observed through the window of the evaporator and we can see that the ingots were totally melted. After the fusion, a new piece of CuSn co-catalyst is obtained.

Using a fused CuSn co-catalyst simplifies the evaporation process, having the advantage of reduced risk of catalyst oxidation. Nevertheless, the use of co-catalysts with different compositions requires creation of a good mixing of both metals or an alloy. Besides, it is rather complicated to evaporate less than 0.1 nm nominal thickness with the fused co-catalyst. We always used as low as possible current in order to well control even the thinnest (sub-nanometer) material evaporation. For example, we usually apply about 2.6 A to deposit 0.1 nm Sn, which takes only a few seconds. During this process, only a small part of the metal

in the crucible is evaporated. The current we use to deposit 0.1 nm Cu is around 2.2 A and the evaporation speed is very sensitive to the current. To deposit the fused co-catalyst, a current which can ensure the evaporation of both catalysts has to be used. For instance, when we apply current of 3 A to evaporate Sn, the evaporation rate will be a few times faster and we will obtain as much as nearly 1 nm Sn immediately after we open the shutter. Considering the fast evaporation speed of the fused co-catalyst, this method it is not suitable to evaporate a small amount of material such as 0.1 nm.

2.2. **Plasma-enhanced chemical vapor deposition**

In this thesis, we use the same method - PECVD as in [Tang, 2017b] to synthesize SiNWs. PECVD takes advantage of the high energy electrons present in glow discharges to dissociate and ionize gaseous molecules to form chemically reactive species (radicals and ions) to deposit thin films [Droes, 1997]. Because thermal energy is not needed to break chemical bonds, reactions can be promoted at lower temperatures compared with the conventional CVD method thereby avoiding substrate damage. In addition, PECVD technique allows the use of a wide range of precursors, both organic and inorganic due to the improved reactivity of the precursors [Anderson, 2009, Vasudev, 2014].

In this thesis, SiNWs are grown in a home-made PECVD reactor named Plasfil at LPICM. Plasfil is a capacitively-couple radio frequency (RF) reactor operating at RF electrode frequency of 13.56 MHz, and its front view is shown in Figure 2.3a. The reactor consists of a chamber linked with a pumping system and a precursor gas inlet. The available gases include H_2, N_2, Ar, SiH_4, GeH_4, $(CH_3)_3B$ (known as TMB and used for p-type doping), PH_3 (for n-type doping) and NF_3. The reactor is also equipped with an ellipsometer to monitor the deposition process *in situ*. The interior structure of the reactor chamber is shown in **Error! Reference source not found.**b. There are two horizontal electrodes that are heated up by two regulated heaters. The top RF electrode is connected to the power injection system, and the bottom electrode works as the substrate holder. The reactor is operated after reaching vacuum with pressure below 5×10^{-5} mbar and the working pressure is of the order of 10 to 200 Pa (0.1 to 2 mbar). During NW growth, the precursor gases are injected into the chamber. When the RF power is switched on, electrons are accelerated by the

oscillating electric field between the two electrodes and collide with the molecules of the precursor gas. After having received sufficient energy, the gas molecules are dissociated, thus the plasma is ignited. The atoms diffuse into the catalyst NPs, providing atoms for NW growth.

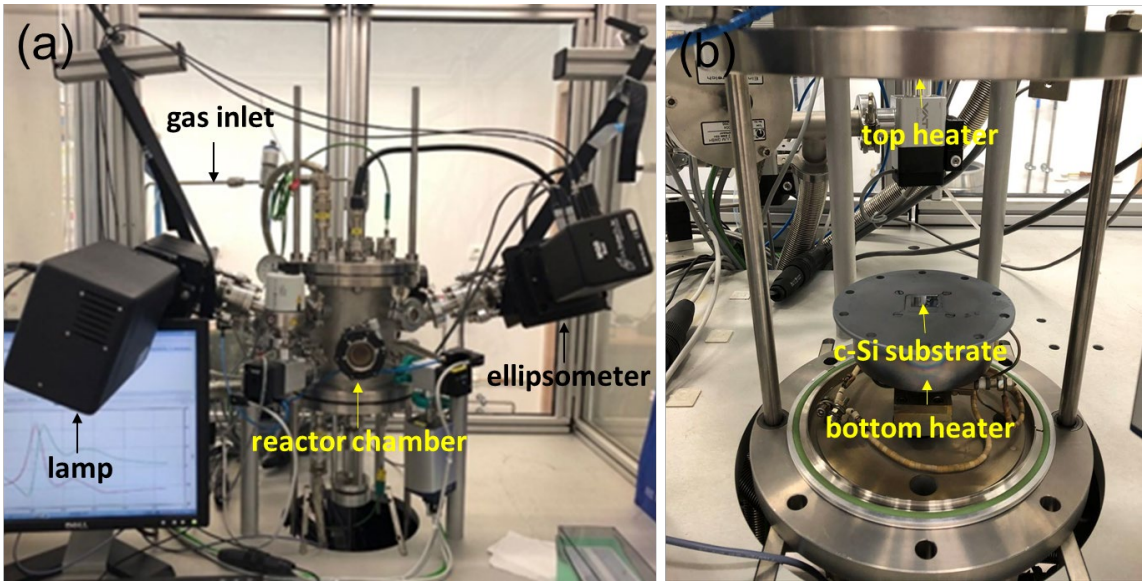

Figure 2.3. (a) Photograph of the PECVD reactor Plasfil and (b) the interior structure of the reactor chamber.

It is notable that there is a discrepancy between the displayed nominal temperature of the heaters and the real temperature of the substrate holder. This is because the temperature measurement is made by thermocouples connected to the heaters below the electrodes, not to the electrodes. The temperature of the substrate holder has been calibrated using a standard Pt 100 probe. Figure 2.4 shows the calibrated temperature as a function of the nominal temperature set on the heater connected to the substrate holder. In the thesis, we will use the calibrated temperature every time when substrate temperature is being discussed. The maximum temperature of the bottom substrate is 450 °C.

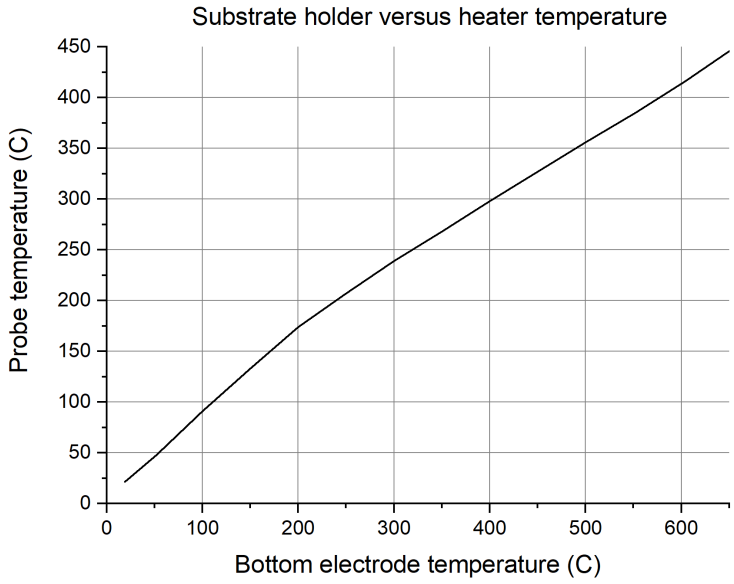

Figure 2.4. The calibrated temperature of the substrate holder as a function of the nominal temperature.

The most typical PECVD process in Plasfil to synthesize SiNWs with Sn catalyst has been developed during previous studies [Yu, 2009, Yu, 2010, Misra, 2013a, Chen, 2014, Tang, 2017b, Al-Ghzaiwat, 2019]; it is shown in the following schematic diagram inFigure 2.5: firstly the substrates with evaporated catalyst are loaded into the reactor. After the vacuum reaches 5×10^{-5} mbar, the temperature of the substrate holder is increased to 200 °C and hydrogen is introduced for a hydrogen plasma to reduce the oxide layer on the catalyst. We often use 100 sccm (standard cubic centimeters per minute) H_2 at a pressure of 0.8 mbar for 2 minutes for the treatment. The plasma treatment dewets the catalyst and metal droplets form. The size and distribution of the droplets depend on the substrate temperature and plasma conditions. Then the temperature is increased to 416 °C for SiNW growth. The specific conditions are: 100 sccm H_2 and 5 sccm SiH_4, 1.42 mbar for gas pressure, 1.5 W for RF power, and 2 minutes for growth time. After NW growth, the substrates are usually cooled down under 100 sccm H_2 at around 0.9 mbar. When the temperature of the bottom electrode is below 160 °C, we open the chamber to take out the samples for characterizations. In this work, unless the growth parameters are the objects of study, SiNWs are synthesized with the typical PECVD recipe above.

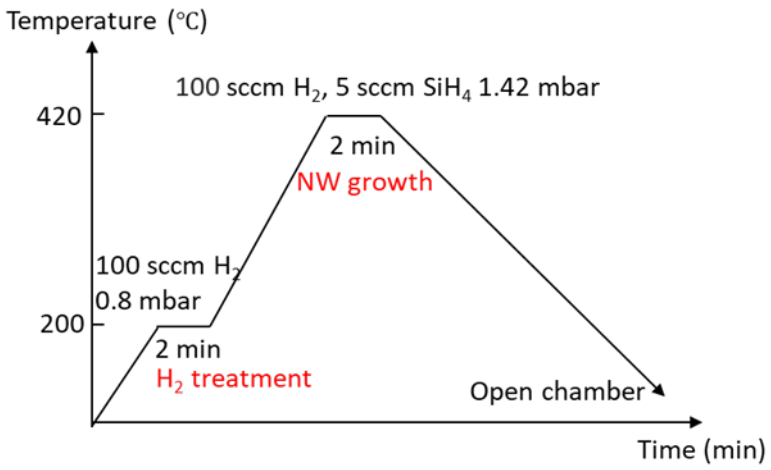

Figure 2.5. Schematic diagram of a typical SiNW PECVD growth experiment using Sn catalyst in Plasfil.

2.3. **Silicon nanowire characterization**

2.3.1. **Scanning Electron Microscopy**

After evaporation and PECVD growth, the size, morphology, distribution, and density of nanoparticles (NPs) and SiNWs are observed by scanning electron microscopy (SEM) using a Hitachi S-4800. The Hitachi S-4800 is a field emission SEM (FE-SEM). Under optimal working conditions, it can magnify images up to 800 000 times and resolve features down to 1-2 nanometer (in theory). It provides both: nanoscale topographic contrast secondary electron (SE) imaging and atomic number contrast backscattered electron (BSE) imaging. The available accelerating voltage range of the electron microscope ranges from 0.5 to 30 kV. Practically, the value of 10 kV is always used for the study of NWs on the crystalline Si wafer and Cu TEM grid substrates. For SiNWs on poor conductor substrates such as glass, we have used a lower acceleration voltage to avoid the severe charging effects that forbid imaging. SiNWs are observed either in top view or side view, on a substrate tilted by 90 °. Although the nominal resolution of this Hitachi S-4800 SEM is around 1-2 nm, its actual resolution does depend on the material of the observed objects and their sizes. In fact, according to our experience, when NW diameters are below 10 nm, it is difficult to obtain sharp images and the edges of SiNWs are always blurred. Under these circumstances, it is recommended to confirm SEM data by TEM microscopy images for the purpose of

precise determination of the diameter sizes. The diameter and length of SiNWs are measured by the ImageJ software. The NW diameter distributions and other results are plotted in the software Origin.

2.3.2. **Transmission Electron Microscopy**

Transmission electron microscopy (TEM) is a technique in which a beam of electrons is transmitted through a specimen to form an image. The specimen is most often an ultrathin section less than 100 nm thick, or a suspension on a grid. An image is formed from the interaction of the electrons with the sample as the beam is transmitted through the specimen. The image is then magnified and focused onto an imaging device, such as a fluorescent screen. TEM is capable of imaging at a significantly higher resolution than SEM, owing to the smaller de Broglie wavelength of electrons. This enables the instrument to capture fine details - as small as a single column of atoms. TEM is a major analytical method in the physical, chemical and biological sciences.

A schematic of the layout of the optical components in a basic TEM is shown in Figure 2.6. From the top down, the gun includes a source that emits electrons either by thermionic or field electron emission into the vacuum, and an electrostatic accelerator. The source (cathode) is maintained at the high voltage while the anode is connected to the earth. The beam then enters the condenser lens system. These upper lenses focus the electron beam to the desired size and location on the sample [Rose, 2008]. The other stages of lensing included in a TEM are: the objective lenses, intermediate lenses and projector lenses. The objective lenses focus the beam that comes through the sample itself, while the projector lenses are used to expand the beam onto the phosphor screen or other imaging devices. The magnification of the TEM is adjusted by changing the current in the intermediate lenses. Equally important to the lenses are the apertures. Some apertures are used to determine the beam current reaching the sample and also to improve the ability to focus the beam. Variable apertures after the sample position further allow the selection of the range of spatial positions or electron scattering angles that are used in the formation of an image or a diffraction pattern. The electron-optical system also includes deflectors and stigmators. The deflectors allow the position and angle of the beam at the sample position to be independently controlled and ensure the beams

remain near the low-aberration centers in the lens stacks. The stigmators provide an auxiliary fine focusing, compensating astigmatism. Imaging systems in a TEM consist of a phosphor screen for direct observation by the operator, and an image recording system [Faruqi, 2007, Henderson, 2007, Williams, 2009].

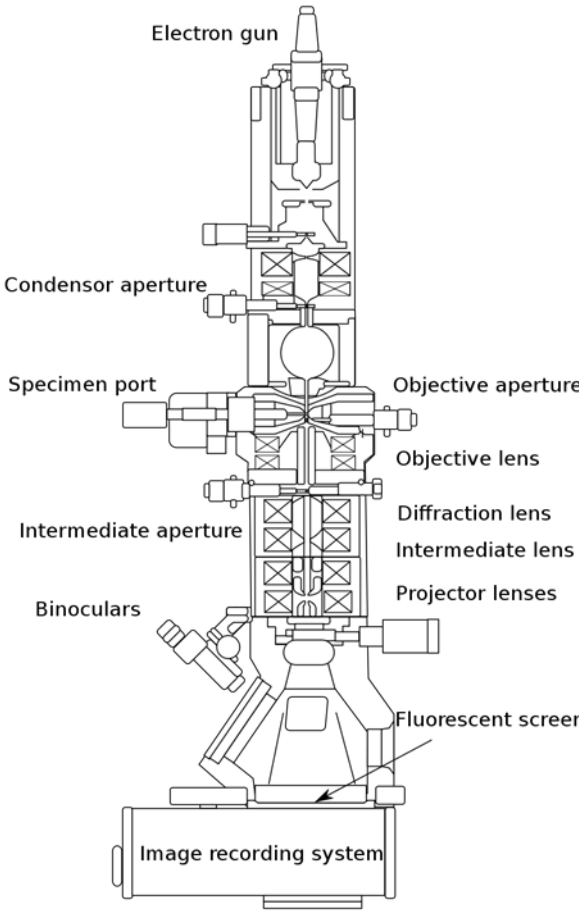

Figure 2.6. Layout of optical components in a basic TEM. (Adopted from [Wikipedia, 2020b])

Energy Dispersive X-Ray Analysis (EDX) gives the elemental composition of materials by using the energies of the X-rays emitted by the sample to identify elements by their typical K, L or M peaks. EDX systems are attachments to SEM or TEM instruments where the imaging capability of the microscope identifies the specimen of interest. The data generated by EDX analysis consist of spectra showing the characteristic peaks corresponding to the elements making up the composition of the sample being analyzed.

Transmission electron microscopes use the same acronym TEM. The SiNWs are characterized using three TEMs: a Jeol 2010F and two Thermo Fisher Titan 80-300 systems named NanoMAX and Nan'eau, for high resolution imaging and EDX analysis in this thesis. The JEOL 2010F is a Schottky field emission medium-resolution transmission electron microscope. It has an accelerating voltage of 200 kV and a point-to-point resolution of 0.23 nm. Both Titan field emission systems allow for imaging of materials with atomic resolution in both the TEM and the Scanning TEM (STEM) modes. Both equipments can work at the 80-300 kV range. The accelerating voltage used in this work is 300 kV for the Titan TEM. The resolutions for STEM and TEM mode are 0.16 nm and 0.19 nm in Nan'eau, and respectively 0.16 nm and 0.08 nm in NanoMAX, thanks to an aberration corrector. Compositional analysis is available using EDX in these two TEMs. The elemental sensitivity is < 1 wt.% with spatial resolution in the nanometer range.

NanoMAX is a very unique aberration-corrected environmental TEM in which *in-situ* experiments can be carried out. It is equipped with two different types of matter sources: CVD sources and Molecular Beam Epitaxy (MBE) sources. Recently, it has been also equipped with an Electron Cyclotron Resonance (ECR) ion source which is used to generate plasma by bombarding gas molecules with electrons excited into ECR. Thus, PECVD growth can be realized in NanoMAX.

SiNWs are either observed directly on the TEM grids or transferred from the crystalline Si substrates to the TEM grids. To transfer the SiNWs, firstly we use a diamond pen to gently scratch the NWs from the Si wafer substrates to get as many scattered individual SiNWs as possible. Then we drop one droplet of isopropanol solvent on the scratched area of the substrate. There are two methods to transfer the SiNWs to a TEM grid. The first approach is to recollect the isopropanol droplet with a pipette, drop it on the TEM grid and repeat this process a few times. The second way is to hold a TEM grid with self-handling tweezers, and then swipe the wet surface of the substrate with the TEM grid and repeat a few times. Both ways have been proved sufficient to transfer some NWs from c-Si wafers to TEM grids. For EDX analysis on the CuSn co-catalyst and the NWs, SiNWs are transferred from the c-Si substrates to Au TEM grids instead of the commonly used Cu TEM grids, to avoid the interference of signal background from Cu parts of the grids.

To determine the polymorph of crystalline Si, TEM characterizations are presented in a specific zone axis in this work: $[110]_{3C}$ / $[1\text{-}210]_{2H}$. This particular choice allows to unambiguously distinguish the cases of cubic multiple twinning from diamond hexagonal stacking. Any other zone axis will give ambiguous results [Tang, 2017b]. 0 displays a segment of a SiNW with 2H phase in the right zone axis, giving an unambiguous proof of the presence of diamond hexagonal structure.

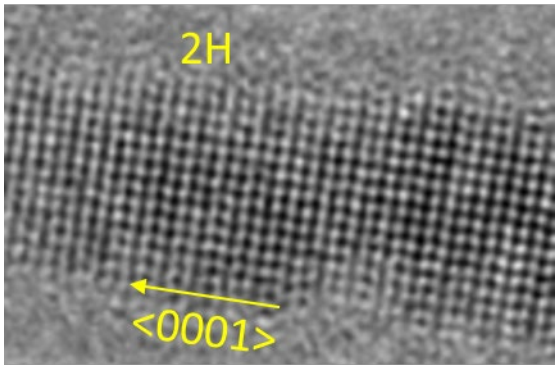

Figure 2.7. TEM image of a SiNW with 2H phase in the [1-210] zone axis.

2.4. **Solar cell fabrication**

2.4.1. **Process of solar cell fabrication**

In this thesis, we fabricate solar cell devices based on SiNWs. The steps of solar cell fabrication are shown in Figure 2.8. Firstly, ZnO:Ag layers are sputtered using an Alliance Concept DP 650 RF magnetron sputtering machine - on "1 inch × 1 inch" corning glass (Cg) substrates as the bottom contact. Then the substrates are loaded into a thermal evaporator for catalyst deposition. Catalyst NPs are formed after this step. Next, PIN junctions are fabricated in the PECVD reactor Plasfil based on p-type SiNWs which are grown using a (SiH_4+H_2+TMB) plasma; then an amorphous intrinsic layer is deposited on the SiNWs with SiH_4 plasma at a lower temperature; finally, a n-type a-Si:H layer is deposited from the dissociation of a SiH_4+H_2+PH_3 gas mixture. The PECVD parameters of the radial junction fabrication will be presented in detail in Chapter 7. In the end, the samples are transferred to a sputtering machine and a thin film of Indium tin oxide (ITO) is sputtered as top contact of the solar cells. Indium tin oxide is a ternary

composition of indium, tin and oxygen in varying proportions. ITO is one of the most widely used transparent conducting oxides because of its electrical conductivity and optical transparency, as well as the ease with which it can be deposited as a thin film. A compromise must be made between conductivity and transparency, since increasing the thickness and increasing the concentration of charge carriers increases the material's conductivity, but decreases its transparency. According to our experience, we usually sputter an ITO layer with a nominal thickness of 240 nm for radial junction solar cells. After the sputtering, the solar cells are annealed at 240 °C for 20 minutes in an oven for strain relaxation and improvement of the interfaces between ITO and Si and thus improving the performance of the PIN junctions.

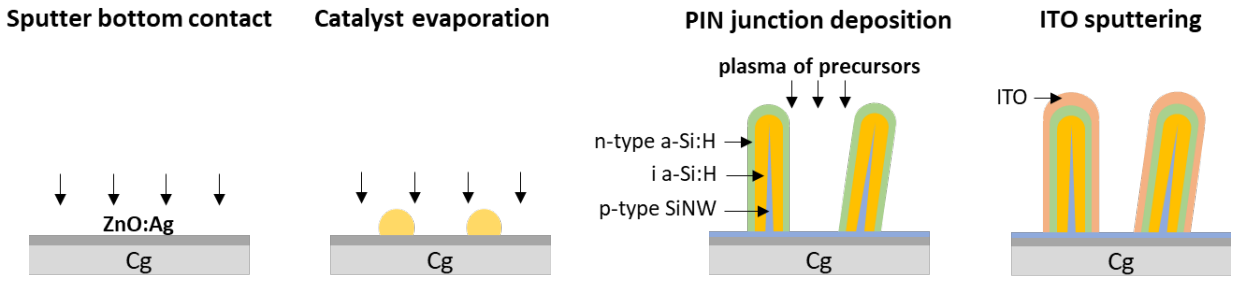

Figure 2.8. Schematic of the process of a solar cell fabrication.

Since we have already introduced the techniques and setups for catalyst evaporation (thermal evaporator) and PIN radial junctions (PECVD reactor) in section 2.1 and section 2.2, we no longer repeat here. We introduce the sputtering machine in the following, which is used for the deposition of bottom and top contacts for radial junction solar cells.

2.4.2. **Sputtering of contacts**

In this thesis we use an Alliance Concept DP 650 RF magnetron sputtering machine to prepare the contacts of solar cells. Sputtering is a physical vapor deposition technique, in which atoms from a solid material are ejected from its surface, after the material is itself bombarded by energetic ions generated in the plasma [Behrisch, 2007]. It is used to deposit thin film layers in the manufacture of optical coatings, semiconductor devices and nanotechnology products. Depositing thin films by sputtering involves eroding

material from a "target" source onto a substrate. Sputtered atoms are ejected into the gas phase but are not in their thermodynamic equilibrium state, and tend to deposit on all surfaces in the vacuum chamber. A substrate placed in the chamber will be coated with a thin film. Sputtering deposition usually uses an argon plasma because argon is a noble gas, and will not react with the target material.

To sputter the bottom contact of the solar cells on the corning glass, Ag is firstly deposited with 41 sccm Ar and with a RF power of 50 W for 3 minutes at room temperature. The estimated thickness of Ag layer is 100 nm. The ZnO layer is then sputtered on top of Ag immediately. We do not open the chamber during the process; we just rotate the substrate holder and change the position of the substrate to the next target. The parameters for sputtering ZnO in our experiments are: 30 sccm Ar, 250 W for RF power and 3 minutes for deposition time. This process is done at room temperature and the estimated thickness of the ZnO layer is 100 nm.

A shadow mask with circular holes is used for sputtering the separated ITO top contacts which determine the area of the solar cells. The ITO layer is sputtered with a gas mixture of 43 sccm Ar and 3 sccm O_2 and the substrate temperature was set at 180°C. The deposition of ITO lasts 7 minutes for a nominal thickness of about 240 nm. A photograph of complete solar cells is shown in 0. Normally, we have 6 big solar cells with 4 mm diameter and 15 small solar cells with 2 mm diameter on a “1 inch × 1 inch” substrate. To ensure a good electrical contact with the probes during J-V measurements, we also put some tiny silver paste dots on the solar cells.

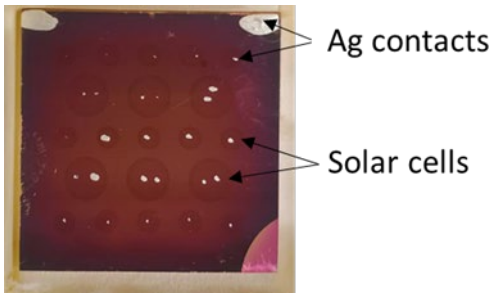

Figure 2.9. Photograph of solar cells with a circular shape.

2.5. **Photovoltaic device characterization**

2.5.1. **J-V characterization**

After solar cell fabrication, we characterize the performance of the solar cells. The J-V curve of a solar cell under one sun illumination (AM 1.5G, 100 mW/cm^2) can be used to evaluate the power conversion efficiency. In this thesis, we use a solar simulator Newport Oriel Sol3A to measure the J–V characteristics of the radial junction solar cells under standard AM1.5G illumination conditions. During measurement, the light is shined on the solar cell and a sweeping voltage is applied, while the current flowing through the solar cell is measured. An example of measured J-V curve is shown in Figure 2.10. V_{oc} and J_{sc} represent the open-circuit voltage and short-circuit current density, respectively. When the applied voltage is zero, the current at this condition is called J_{sc}; when the output current is zero, the voltage at this condition is called as V_{oc}. The fill factor (FF) is defined as the maximum output power divided by the product of J_{sc} and V_{oc}. And the power conversion efficiency of the solar cell is the maximum output power divided by the power of the incident light.

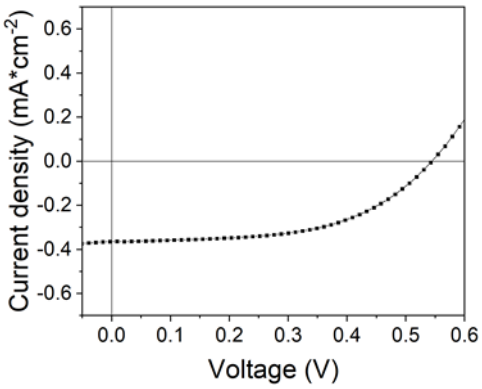

Figure 2.10. J-V curve of a radial junction solar cell under standard AM1.5G illumination conditions.

2.5.2. **Electron beam induced current**

Electron-beam-induced current (EBIC) is a semiconductor analysis technique performed in a SEM or scanning TEM (STEM). It is used to identify buried junctions or defects in semiconductors, or to examine minority carrier properties. In EBIC, energetic electrons take the role of the photons in solar cells, causing the EBIC current to flow. However, because the electron beam of an SEM or STEM is very small, it is scanned across the sample and variations in the induced EBIC are used to map the electronic activity of the sample. By using the signal from the picoammeter as the imaging signal, an EBIC image is formed on the screen of the SEM or STEM.

EBIC mapping was carried out on RJ solar cell samples in a Hitachi SU8000 SEM system in this thesis. The RJ solar cell was fixed on a sample holder, with two probes connected to the bottom contact and the Ag dot on ITO, respectively. The measurement was performed under an acceleration voltage of 25 kV, the beam current of 5 μA and a zero bias.

2.5.3. **External quantum efficiency**

External quantum efficiency (EQE) is the ratio of the number of carriers collected by the solar cell (electrical current) to the number of photons of a given energy incident on the solar cell, and thus including the optical and electrical losses. During the EQE measurement, the solar cell is illuminated with a single wavelength, and the amplified photo-generated current is measured. By repeating this process over a broad

spectrum of wavelengths, we can acquire the wavelength dependent EQE graph as shown in Figure 2.11, which summarizes the ideal and the typical experimental EQE response measured for a radial junction solar cell.

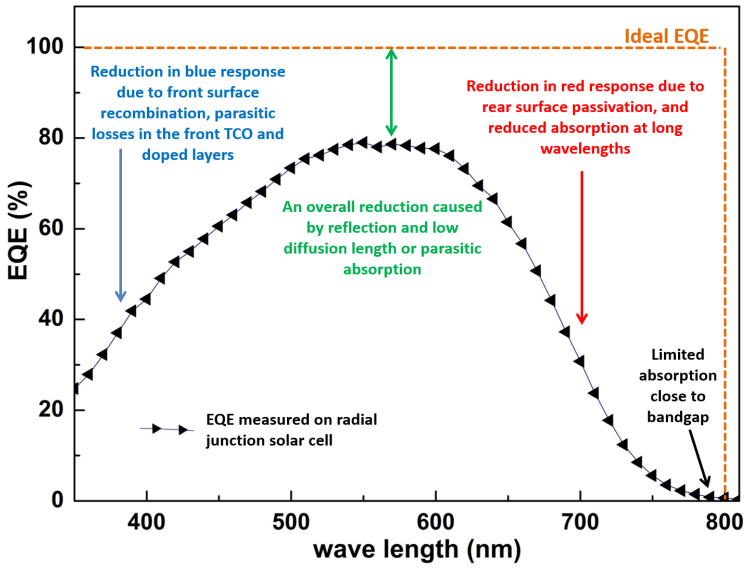

Figure 2.11. Typical EQE curve of a radial junction solar cell (black curve), and the ideal EQE curve is indicated in orange dashed curve. Possible reasons of the reduced EQE response at different wavelength regions are indicated [Al ghzaiwat, 2018].

The measurements of several RJ SiNW solar cells were conducted using Newport system (Oriel Instruments QEPVSI-b) which consists of light source (Xenon light) with a mechanical chopper to create a pulsed source of light and a monochromator to select the wavelength of the incident light. The calibration of the measurement setup was carried out using a certified photo-diode. The EQE response was recorded with an interval of 10 nm within the range of 350-850 nm.

References

Al-Ghzaiwat, M., A. Foti, A. Nuesslein, L. Halagacka, J. Meot, A. Labouret, R. Ossikovski, P. Roca i Cabarrocas, and M. Foldyna, *Toward Efficient Radial Junction Silicon Nanowire-Based Solar Mini-Modules.* physica status solidi (RRL) - Rapid Research Letters, 2019. **13**(2): p. 1800402. https://doi.org/10.1002/pssr.201800402

Al ghzaiwat, M., *Fabrication and study of solar cell modules based on silicon nanowire based radial junction solar cells*. 2018, Université Paris Saclay (COmUE).

Anderson, K.D., J.M. Slocik, M.E. McConney, J.O. Enlow, R. Jakubiak, T.J. Bunning, R.R. Naik, and V.V. Tsukruk, *Facile plasma-enhanced deposition of ultrathin crosslinked amino acid films for conformal biometallization.* Small, 2009. **5**(6): p. 741-9. https://doi.org/10.1002/smll.200801843

Behrisch, R. and W. Eckstein, *Sputtering by particle bombardment: experiments and computer calculations from threshold to MeV energies*. Vol. 110. 2007: Springer Science & Business Media.

Chen, W., L. Yu, S. Misra, Z. Fan, P. Pareige, G. Patriarche, S. Bouchoule, and P. Roca i Cabarrocas, *Incorporation and redistribution of impurities into silicon nanowires during metal-particle-assisted growth.* Nat Commun, 2014. **5**(1): p. 4134. https://doi.org/10.1038/ncomms5134

Droes, S.R., T.T. Kodas, and M.J. Hampden-Smith, *Plasma-Enhanced Chemical Vapor Deposition (PECVD)*, in *Carbide, Nitride and Boride Materials Synthesis and Processing*, A.W. Weimer, Editor. 1997, Springer Netherlands: Dordrecht. p. 579-603. https://doi.org/10.1007/978-94-009-0071-4_23

Faruqi, A.R. and R. Henderson, *Electronic detectors for electron microscopy.* Curr Opin Struct Biol, 2007. **17**(5): p. 549-55. https://doi.org/10.1016/j.sbi.2007.08.014

Henderson, R., D. Cattermole, G. McMullan, S. Scotcher, M. Fordham, W.B. Amos, and A.R. Faruqi, *Digitisation of electron microscope films: six useful tests applied to three film scanners.* Ultramicroscopy, 2007. **107**(2-3): p. 73-80. https://doi.org/10.1016/j.ultramic.2006.05.003

Latif, U., S. Can, O. Hayden, P. Grillberger, and F.L. Dickert, *Sauerbrey and anti-Sauerbrey behavioral studies in QCM sensors—Detection of bioanalytes.* Sensors and Actuators B: Chemical, 2013. **176**: p. 825-830. https://doi.org/10.1016/j.snb.2012.09.064

Misra, S., L. Yu, W. Chen, and P. Roca i Cabarrocas, *Wetting Layer: The Key Player in Plasma-Assisted Silicon Nanowire Growth Mediated by Tin.* The Journal of Physical Chemistry C, 2013a. **117**(34): p. 17786-17790. https://doi.org/10.1021/jp403063d

Rose, H.H., *Optics of high-performance electron microscopes.* Sci Technol Adv Mater, 2008. **9**(1): p. 014107. https://doi.org/10.1088/1468-6996/9/1/014107

Tang, J., J.L. Maurice, F. Fossard, I. Florea, W. Chen, E.V. Johnson, M. Foldyna, L. Yu, and I.C.P. Roca, *Natural occurrence of the diamond hexagonal structure in silicon nanowires grown by a plasma-assisted vapour-liquid-solid method.* Nanoscale, 2017b. **9**(24): p. 8113-8118. https://doi.org/10.1039/c7nr01299c

Vasudev, M.C., H. Koerner, K.M. Singh, B.P. Partlow, D.L. Kaplan, E. Gazit, T.J. Bunning, and R.R. Naik, *Vertically aligned peptide nanostructures using plasma-enhanced chemical vapor deposition.* Biomacromolecules, 2014. **15**(2): p. 533-40. https://doi.org/10.1021/bm401491k

Wikipedia. *Layout of optical components in a basic TEM*. 2020b 20 October 2020; Available from: https://en.wikipedia.org/wiki/Transmission_electron_microscopy#/media/File:Scheme_TEM_en.svg.

Williams, D.B. and C.B. Carter, *The Transmission Electron Microscope*, in *Transmission Electron Microscopy*, D.B. Williams and C.B. Carter, Editors. 2009, Springer US: Boston, MA. p. 3-22. https://doi.org/10.1007/978-0-387-76501-3_1

Yu, L., B. O'Donnell, P.J. Alet, S. Conesa-Boj, F. Peiro, J. Arbiol, and P.R. Cabarrocas, *Plasma-enhanced low temperature growth of silicon nanowires and hierarchical structures by using tin and indium catalysts.* Nanotechnology, 2009. **20**(22): p. 225604. https://doi.org/10.1088/0957-4484/20/22/225604

Yu, L., B. O'Donnell, J.-L. Maurice, and P. Roca i Cabarrocas, *Core-shell structure and unique faceting of Sn-catalyzed silicon nanowires.* Applied Physics Letters, 2010. **97**(2): p. 023107. https://doi.org/10.1063/1.3464557

Chapter 3. Silicon nanowire growth with Sn catalyst on Cu TEM grids

In this chapter, we study the SiNW growth with Sn catalyst using Cu TEM grid substrates. In the publication Tang *et al.*, SiNWs with the diamond hexagonal structure were grown spontaneously by PECVD method [Tang, 2017b] directly on sidewall of Cu TEM grid as shown in Figure 3.1. The diameters of SiNW crystalline cores were smaller than 4 nm with amorphous shell thickness around 1-2 nm. The presence of Cu in the catalyst could not be excluded under the circumstances.

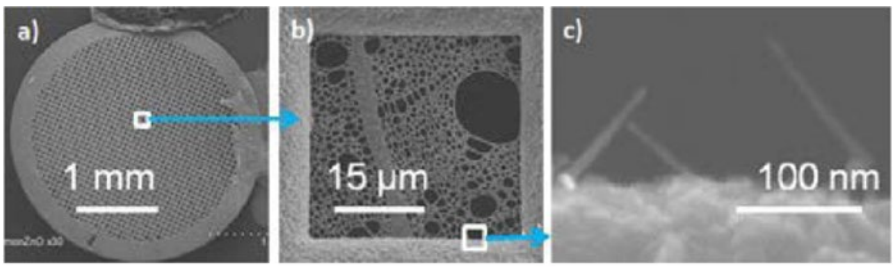

Figure 3.1. SEM image of a Cu TEM grid and its detail (b); (c) SiNWs grown on the sidewall of the Cu TEM grid [Tang, 2017b].

Since Cu have been used as catalyst for SiNW growth in the literature [Kalache, 2006, Yao, 2007, Arbiol, 2008], and Cu can form many intermetallic compounds with Sn [Furtauer, 2013], it is of great importance to understand whether Cu has played a role in the growth of the thin SiNWs with hexagonal phase. In this chapter, we first look for evidence for the presence of Cu in the SiNWs of the sample in Figure 3.1. Next, we will study the influence of PECVD conditions on SiNW growth on Cu TEM grids using Sn catalyst. Finally, we characterize the crystalline structures of the SiNWs by TEM.

3.1. **Analyzing silicon nanowires grown at LPICM before the present work**

Firstly, we have investigated the TEM images of the sample in Figure 3.1 to look for the presence of Cu in the SiNWs. At first, we looked through all the TEM images of the SiNWs to find the crystalline structures of the catalyst NPs. A TEM image of a crystalline SiNW is shown in Figure 3.2a. A High-resolution TEM (HRTEM) image with a higher magnification is shown in the inset and its Fast Fourier Transform (FFT) image is shown in Figure 3.2b. The FFT pattern indicates that the bottom of the SiNW has hexagonal structure and the [0001] growth direction. The top part of the SiNW has multiple catalyst

nanoparticles (NPs). However, none of the NPs are in the zone axis and we are not able to observe the crystalline structure. In the selected area diffraction pattern (SADP) of the SiNW top part (Figure 3.2c), the three brightest spots correspond to an interplanar distance of 0.31 nm and 0.19 nm respectively. None of these two values correspond to the interplanar distance of Cu. We did not obtain useful information about crystalline structures of the SiNW catalyst NPs from these images.

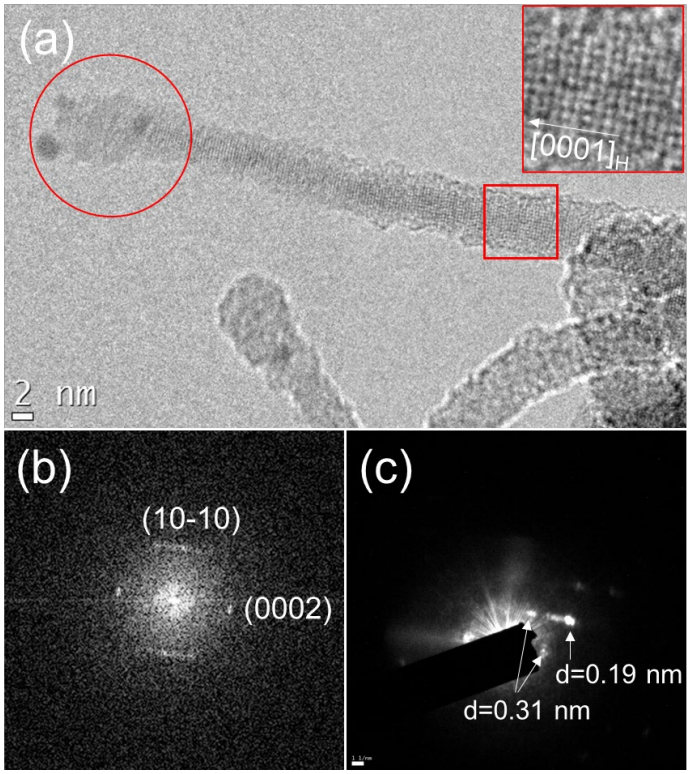

Figure 3.2. (a) A SiNW with the diamond hexagonal structure at the bottom. A HRTEM image with a higher magnification of the bottom structure is shown in the inset of (a); (b) the FFT image of the SiNW bottom from (a); (c) SADP of the SiNW top part as indicated in (a).

Next, we have taken the TEM images of the SiNWs after annealing at 700 °C to investigate the crystalline structures of the catalyst NPs. Two SiNWs after annealing are shown in Figure 3.3a and b. Both SiNWs have become shorter and thicker upon annealing, while no crystallographic planes of Si are observed. A crystalline NP is found in both SiNWs, which is likely to be the remnants of a catalyst NP. In Figure 3.3a, the NP has a hexagonal shape. The FFT image of the NP in the inset indicates that it contains

crystalline planes with a quasi-hexagonal symmetry, which have an interplanar spacing of about 0.21 nm. In Figure 3.3b, the FFT image of the NP displays one group of planes with a spacing around 0.2 nm and another group at 90° (weaker spots) with a spacing of about 0.15 nm. These values and structures cannot belong to either alpha or beta Sn [Weiqiang, 2005, Haq, 2019]. These particles thus include other elements, probably also O, Si and Cu.

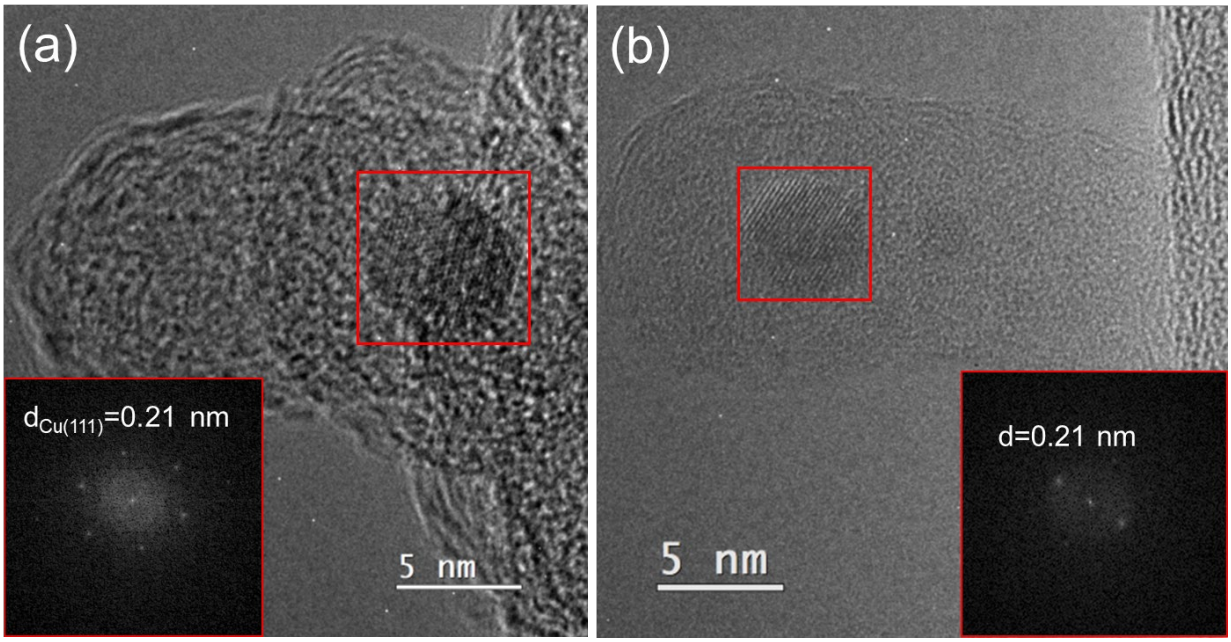

Figure 3.3. SiNWs with crystalline NPs inside after annealing at 700 °C. The FFT images of the NPs are shown in the insets.

In the next experiments, we focus on exploring the key conditions for the hexagonal SiNWs. We start by using Sn as catalyst and Cu TEM grids as substrates for SiNW growth. We firstly reproduce the SiNW growth experiment in the paper of Tang *et al.*, then we study the influence of PECVD conditions on SiNW growth. The crystalline structures of SiNWs are characterized by TEM.

3.2. **Influence of PECVD conditions on nanowire growth with Sn catalyst on Cu TEM grids**

The PECVD experiment conditions similar to those in the paper [Tang, 2017b] are listed in Table 3.1. In the following paragraphs in this thesis, we call them “typical conditions”. Firstly, Sn catalyst with a

nominal thickness of 1 nm is evaporated on a Cu TEM grid substrate in a thermal evaporator. The nominal thickness of the deposited catalyst is provided by the micro quartz balance. Dense catalyst NPs with diameters around 10 nm are observed on Cu surface after thermal evaporation Figure 3.4a. In fact, these NPs in the SEM image are from area 1 Figure 3.4b, however, we can only observe SiNWs grown at the sidewall of Cu grid, i.e. area 2, by TEM. Because the sidewall of Cu grid receives the evaporated metal at a glancing angle, there is much less catalyst deposited on it.

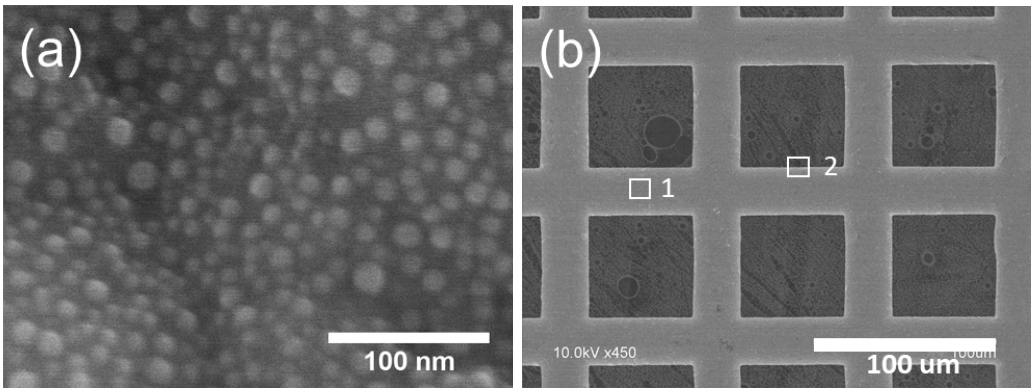

Figure 3.4. Sn catalyst with 1 nm nominal thickness evaporated on a Cu grid from area 1 in figure (b); (b) a Cu TEM grid under SEM.

Next, the substrate is loaded into the PECVD reactor Plasfil for SiNW growth experiment following the typical conditions in Table 3.1. The experiment begins when the chamber pressure is below 5×10^{-5} mbar. We firstly increase the substrate temperature to 200 °C to carry out a hydrogen plasma treatment with 100 sccm H_2. Then the substrate temperature is increased to 416 °C for SiNW growth. Afterwards, the sample is cooled down with H_2 and then taken out for SEM and TEM observation.

Table 3.1. The conditions of the typical PECVD process

	Substrate temperature (°C)	Flux of H_2/SiH_4 (sccm)	Gas pressure (mbar)	RF power (W)	Time duration (min)
H_2 plasma treatment	200	100/0	0.8	5	2

SiNW growth	416	100/5	1.42	1.5	3

A SEM image of SiNWs grown directly on the sidewall of the Cu TEM grid under the typical PECVD condition in Table 3.1 is shown in Figure 3.5. SEM image of SiNWs grown directly on the sidewall of a Cu TEM grid using the typical PECVD experiment conditions in Table 3.1. It can be seen that the surface of the Cu TEM grid is not flat. The SiNWs are randomly oriented and most of them are straight. The SiNWs have lengths around 100 nm and have an average diameter of 8.7 nm. However, due to the limited SEM resolution and the fact that some of the NWs are not at the focal plane, the SiNW diameters can be overestimated. In order to obtain a higher resolution and to study the crystalline structure of the SiNWs, we have observed some SiNWs using TEM.

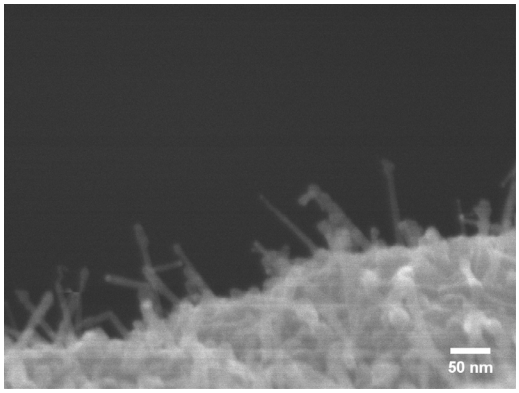

Figure 3.5. SEM image of SiNWs grown directly on the sidewall of a Cu TEM grid using the typical PECVD experiment conditions in Table 3.1.

A SiNW with the diamond cubic structure is shown in Figure 3.6. The SiNW has a total diameter of 7.9 nm, while the diameter of the NW crystalline core is 6.0 nm. The SiNW has a single crystal structure. The area in the red square is selected for a FFT analysis, and the FFT result is shown in the inset of the figure. The spots in the FFT image correspond to the (111) planes of Si, which have an interplanar spacing of 0.31 nm.

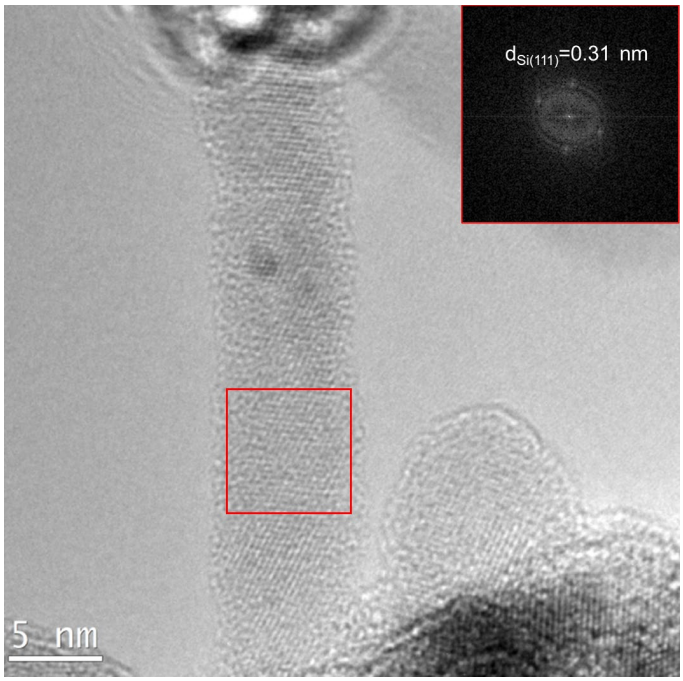

Figure 3.6. A single crystalline SiNW with diamond cubic structure on the Cu TEM grid.

We observed more than 100 SiNWs, but only 17 SiNWs were in the <110> zone axis. All the observed SiNWs have total diameters smaller than 10 nm. Sixteen of the SiNWs have a cubic structure, and one SiNW shows hexagonal structure (see Figure 3.7). An HRTEM image with a higher magnification of the selected area in Figure 3.7a is shown in Figure 3.7b, and its FFT image is shown in Figure 3.7c. The FFT image indicates the existence of hexagonal 2H phase in (b), with $d_{(0002)} = 0.311\ nm$, $d_{(10-10)} = 0.333\ nm$. In Figure 3.7b, there are alternating 2H and 3C (diamond cubic) phase. At the bottom, it is 3C phase; then it switches to 2H phase; and then it switches back to 3C phase again. There is no abrupt change in NW diameter or shape at the place of the phase transition. The SiNW has a total diameter of 8 nm, with a crystalline core diameter of 6 nm. The SiNW with hexagonal phase has a similar diameter with the cubic SiNWs in Figure 3.6, and the diameter of the 2H phase and of the 3C also have similar diameter, which means that NW diameter is not the determining factor for 2H Si phase.

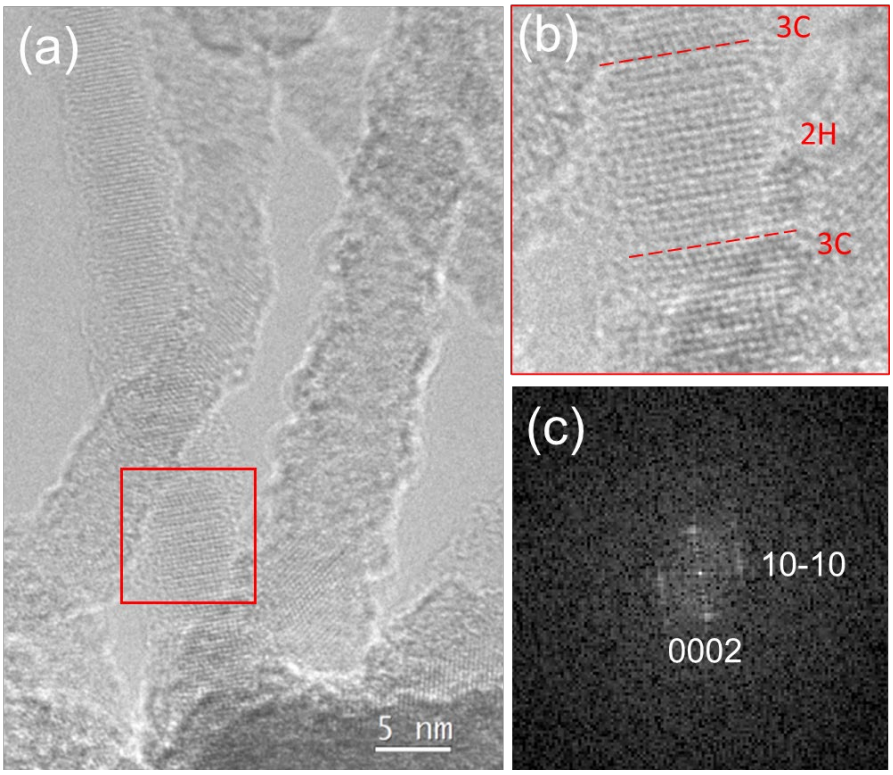

Figure 3.7. A SiNW with 2H phase at the bottom; (b) HRTEM image with a higher magnification of the selected area in (a) and (c) its FFT image.

This statistical occurrence of 2H phase in SiNWs is much smaller than that observed by in [Tang, 2017b] (one in seventeen versus 5 in seven). It is due to the exact growth conditions in 2015 (time when experiments were done for [Tang, 2017b]) have been different from the present ones, notably since the Plasfil reactor has been upgraded and all pumps, mass-flow controllers and power generator have been exchanged since then. Therefore, we have explored the experimental parameter space in the vicinity of the conditions given in Table 3.1. We start by applying relatively small changes to temperature and gas pressure. We still use Sn as the evaporated catalyst and Cu TEM grid as the substrates. Figure 3.8a shows SiNWs grown at 385 °C, while other parameters remain the same as the typical conditions in Table 3.1; Figure 3.8b and c show the SiNWs synthesized at the pressure of 2 mbar and 1 mbar respectively, other parameters remaining the same as in Table 3.1. Compared with the SiNWs synthesized at the typical conditions (see Figure 3.5), the SiNWs synthesized at a lower temperature in Figure 3.8a have similar lengths and diameters.

When the SiNWs are synthesized at a higher pressure Figure 3.8b), the lengths of the NWs are about 200 nm longer than the SiNWs fabricated at the typical conditions (around 100 nm at 1.42 mbar) and the SiNW arrays become denser. When the SiNWs are synthesized at a lower pressure Figure 3.8c), they are less dense and have similar lengths and diameters with the SiNWs fabricated in the typical conditions.

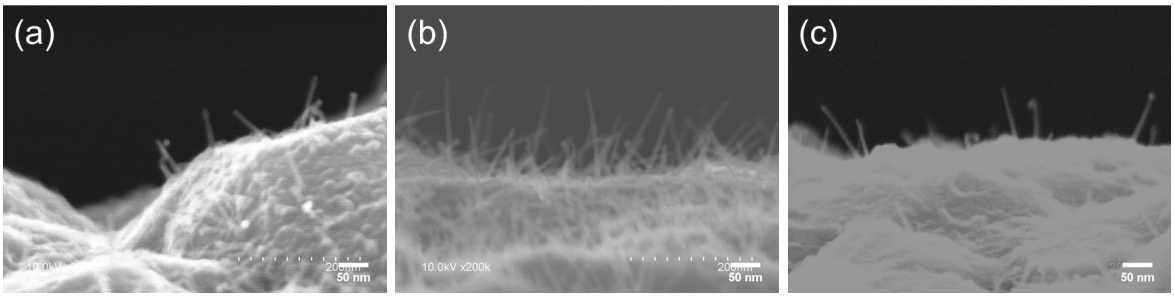

Figure 3.8. SEM images of SiNWs synthesized (a) at 385 °C; (b) at 2 mbar; (c) at 1 mbar on the sidewall of the Cu TEM grid while other parameters remain the same as in Table 3.1.

The crystalline structures of the SiNWs of samples in Figure 3.8 were observed under TEM. We observed more than 100 SiNWs of each sample, however, less than 20% of them were in the <110> zone axis. In the sample of Figure 3.8a, we found 1 SiNW with hexagonal phase and 16 SiNWs with cubic phase. In the other two samples, we only found cubic SiNWs. The SiNW with hexagonal structure is shown in Figure 3.9a. The SiNW has a total diameter around 6 nm and the diameter of the crystalline core is about 4 nm. The length of the NW is about 40 nm and there is no catalyst NP remaining on top. A HRTEM image with a higher magnification of the bottom part of the SiNW is shown in Figure 3.9b and its FFT image is shown in Figure 3.9c. Like the SiNW in Figure 3.7, there are alternating 3C and 2H phases. Nanowire has 3C phase at the beginning, then it switches to 2H phase, and finally it becomes 3C phase again. The FFT image confirms the existence of 2H phase in (b).

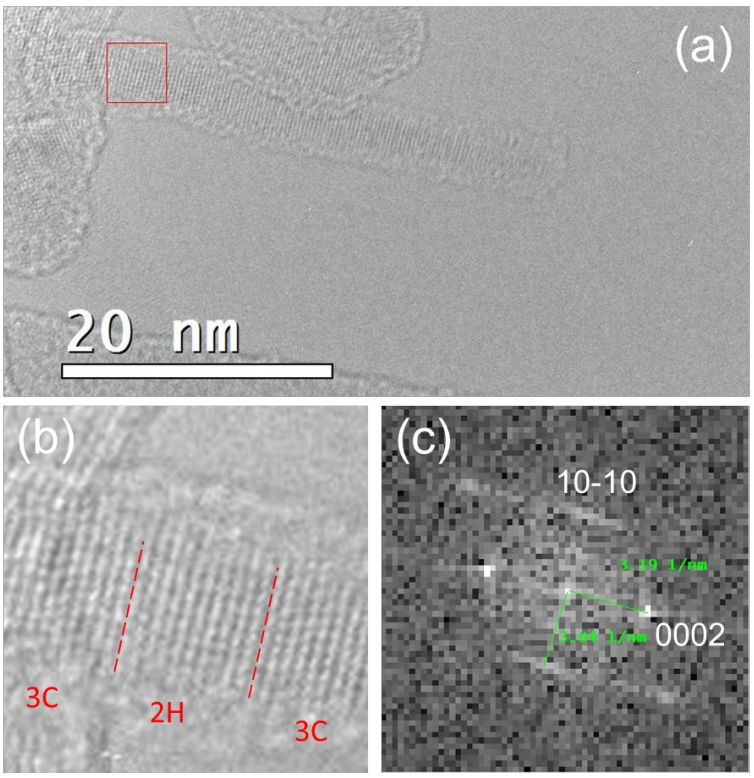

Figure 3.9. A SiNW with 2H phase at the bottom; (b) a HRTEM image with a higher magnification of the selected in (a) and (c) its FFT image.

3.3. **Repeatability of SiNW growth on Cu TEM grids**

In the previous sub-section, we grew SiNWs directly on Cu TEM grids with Sn catalyst, using the typical PECVD conditions from [Tang, 2017b]. However, we did not find as many hexagonal SiNWs as in the paper. Firstly, the SiNWs were a little bit larger in diameter compared with the SiNWs reported in the paper. The SiNWs with hexagonal phase we found had crystalline core diameters of 4 nm and 6 nm respectively; while the hexagonal SiNWs reported in [1] had crystalline core diameters of 2-4 nm. In addition, we did not find as much SiNWs in the <110> zone axis. Although we observed many SiNWs, less than 20% of them were in the right zone axis which allows us to unambiguously distinguish their crystalline structures. Most SiNWs still had cubic structure. We changed NW growth temperature and gas pressure, nevertheless, the yield of hexagonal SiNWs did not increase.

In addition to the difficulties of finding hexagonal SiNWs, we also find that there are many problems with the repeatability of SiNW growth on Cu TEM grids. Each time we evaporated Sn catalyst with 1 nm nominal thickness on different Cu TEM grid substrates, however, we did not always get the same SiNW distributions (see Figure 3.10). Sometimes we obtained SiNWs with a high density (Figure 3.10a); sometimes we obtained less dense SiNWs (Figure 3.10b); sometimes SiNWs can barely grow at all (Figure 3.10c). Even at different places of the sample Cu TEM grid, the SiNW distributions can be quite different. This should be related to the rough surfaces of Cu TEM grids without guaranteed vertical wall angles. As a consequence, the amount of Sn catalyst evaporated on sidewalls is uncontrollable and changes from sample to sample. In addition, we do not know how much Cu exactly has been involved in SiNW growth. This leads to uncontrollable SiNW density, diameter, length and orientation.

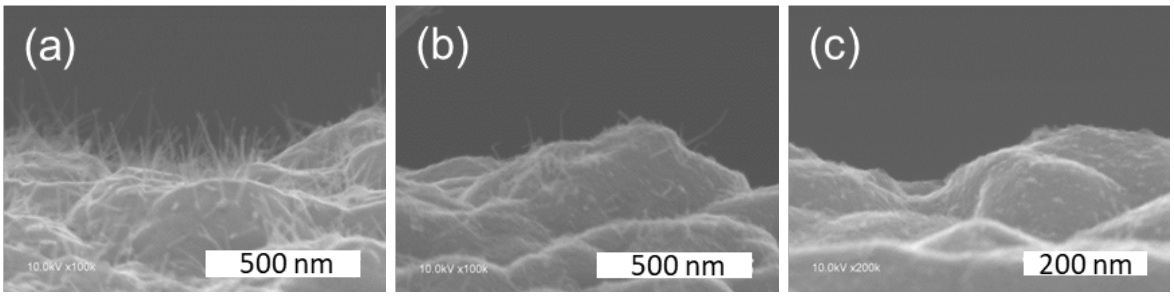

Figure 3.10. Sn catalyst with 1 nm nominal thickness was evaporated on different Cu TEM grids, while different SiNW distributions were obtained.

All these reasons make Cu TEM grids less than ideal substrates for SiNW growth. Therefore, for the reliable and quantitative study of catalysts and SiNW growth we have changed the substrates to crystalline Si wafers. Since not only Sn but also Cu may play a role in growth of hexagonal SiNWs, we propose to use a combined catalyst of Sn and Cu to catalyze SiNW growth. The catalyst evaporation and NW growth on crystalline Si substrates shows high level of repeatability as compared to Cu TEM grids. Instead of evaporating Sn catalyst on Cu TEM grids, we firstly evaporate Cu catalyst followed by the Sn catalyst directly on crystalline Si substrates. The thermal evaporator chamber is opened between those two processes and the catalyst crucible is changed. In this way, we can realize accurate control of catalyst

compositions and a good experimental repeatibility. In the following chapters, we will firstly investigate the structures of co-catalysts of Sn and Cu (Chapter 4) and then (Chapter 5) study the influence of co-catalyst composition and PECVD conditions on the SiNW growth.

3.4. **Chapter conclusions**

In this chapter, we have investigated the TEM images of SiNWs with hexagonal phase grown at LPICM using the same experimental conditions as it was done in the past. We found that pure Sn cannot be the only catalyst element involved in SiNW growth according to the TEM analysis of catalyst NPs on the top of SiNWs after the annealing. We repeated the growth conditions reported in [1], using Sn as catalyst and Cu TEM grid as substrates. However, we did not obtain as many hexagonal SiNWs as reported in [1]. We changed growth temperature and gas pressure, but the yield of hexagonal SiNWs did not increase, even though the length and density of SiNWs changed substantially. One possible reason is that SiNWs we obtained have larger diamaters than SiNWs in [1]. That might be due to the problem with repeatability of SiNW growth on Cu TEM grids. Because of the rough surface of Cu grids and uncontrolled side wall angles, the amount of Sn catalyst evaporated on them was uncontrollable, which lead to inhomogeneous SiNW distributions even within the same grid.

References

Arbiol, J., A. Fontcuberta i Morral, S. Estradé, F. Peiró, B. Kalache, P. Roca i Cabarrocas, and J.R. Morante, *Influence of the (111) twinning on the formation of diamond cubic/diamond hexagonal heterostructures in Cu-catalyzed Si nanowires.* Journal of Applied Physics, 2008. **104**(6): p. 064312. https://doi.org/10.1063/1.2976338

Furtauer, S., D. Li, D. Cupid, and H. Flandorfer, *The Cu-Sn phase diagram, Part I: New experimental results.* Intermetallics (Barking), 2013. **34**: p. 142-147. https://doi.org/10.1016/j.intermet.2012.10.004

Haq, A.U., S. Askari, A. McLister, S. Rawlinson, J. Davis, S. Chakrabarti, V. Svrcek, P. Maguire, P. Papakonstantinou, and D. Mariotti, *Size-dependent stability of ultra-small alpha-/beta-phase tin nanocrystals synthesized by microplasma.* Nat Commun, 2019. **10**(1): p. 817. https://doi.org/10.1038/s41467-019-08661-9

Kalache, B., P.R.i. Cabarrocas, and A.F.i. Morral, *Observation of Incubation Times in the Nucleation of Silicon Nanowires Obtained by the Vapor-Liquid-Solid Method.* Japanese Journal of Applied Physics, 2006. **45**(No. 7): p. L190-L193. https://doi.org/10.1143/jjap.45.L190

Tang, J., J.L. Maurice, F. Fossard, I. Florea, W. Chen, E.V. Johnson, M. Foldyna, L. Yu, and I.C.P. Roca, *Natural occurrence of the diamond hexagonal structure in silicon nanowires grown by a plasma-assisted vapour-liquid-solid method.* Nanoscale, 2017b. **9**(24): p. 8113-8118. https://doi.org/10.1039/c7nr01299c

Weiqiang, W., D. Ying, and W. Chunqing. *Molecular dynamics (MD) simulation of uniaxial tension of /spl beta/-Sn single crystals with nanocracks*. in *2005 6th International Conference on Electronic Packaging Technology*. 2005. https://doi.org/10.1109/ICEPT.2005.1564654

Yao, Y. and S. Fan, *Si nanowires synthesized with Cu catalyst.* Materials Letters, 2007. **61**(1): p. 177-181. https://doi.org/10.1016/j.matlet.2006.04.045

Chapter 4. Exploring catalyst composition

In the previous chapter, we presented the experiments where we tried to repeat SiNW growth by PECVD method using the conditions reported in the published work on 2H SiNWs by Tang *et al*., with Sn catalyst and Cu TEM grid substrates. However, we did not obtain as much hexagonal SiNWs as reported in the paper. One possible reason is that Cu TEM grids are not ideal substrates for SiNW growth *i*) due to the fact that Cu may enter the catalyst and have an uncontrollable effect and *ii*) due to their rough surfaces, which make it impossible to control the distribution and the amount of catalyst deposited. To solve these problems, we have decided to use crystalline Si wafers as substrates instead for higher repeatability, and measured amounts of Cu in addition to Sn in catalyst particles. In this chapter, we firstly study SiNWs synthesized with pure Sn catalyst (Chapter 4.1), to serve as a reference, then investigate the effects of Cu on the catalyst shape and distribution, by studying the properties of CnSn mixed catalysts for SiNWs (Chapter 4.2 and 4.3).

4.1. **Crystalline structures of SiNWs fabricated with pure Sn catalyst**

In this sub-section, we study the crystalline structures of SiNWs fabricated with pure Sn catalyst of 1 nm nominal thickness, which is the amount of Sn catalyst used in the publication of Tang *et al*. [Tang, 2017b]. Pure Sn catalyst was evaporated on (100) Si wafer substrates, then loaded into PECVD reactor for SiNW growth with the typical conditions (see Table 3.1). A SEM image of the SiNWs is shown in Figure 4.1. The SiNWs are mostly straight and have lengths around 150 nm. The SiNWs have an average diameter of 14.9 nm with a standard deviation of 3.4 nm. We found that these SiNWs are thicker than the SiNWs grown on Cu TEM grids using the same amount of Sn catalyst. Next, the SiNWs were transferred to TEM grids for more detailed observation of the crystalline structures.

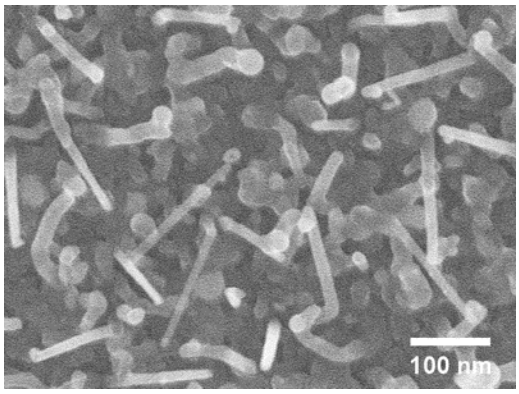

Figure 4.1. SiNWs synthesized with pure Sn catalyst of 1 nm nominal thickness on (100) Si wafer.

For the SiNWs synthesized with pure Sn catalyst with the typical PECVD conditions, we observed more than 50 NWs by TEM, and found 10 of them close to a <110> zone axis; all of them had diamond cubic structures. A HRTEM image of a SiNW is shown in Figure 4.2. The FFT image in the inset indicates that it has a cubic structure. The NW changed orientation during growth. There is no catalyst NP on top of the NW.

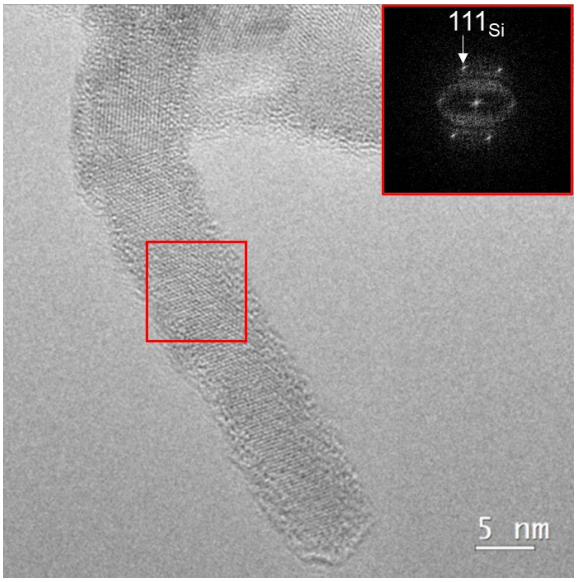

Figure 4.2. A SiNW with diamond cubic structure fabricated with Sn catalyst.

In fact, we found many SiNWs without capped catalyst NPs on top. The SiNW shown in Figure 4.3 is another example. We found some dark nano objects on the NW, which can be Sn falling down from

the top due to its low surface tension and finally settling on the surface of the NW either during or after NW growth.

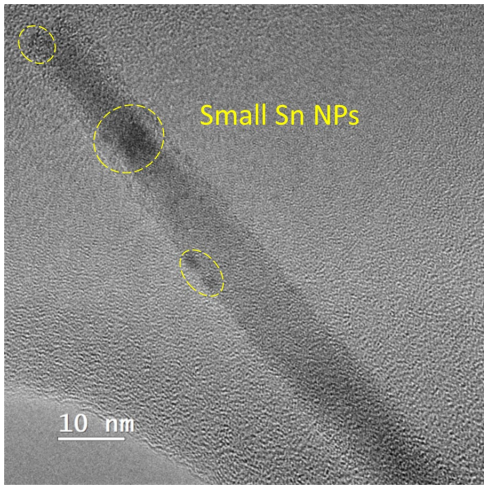

Figure 4.3. A SiNW with Sn catalyst NPs on its body.

HRTEM images of two SiNWs are shown in Figure 4.4. The two SiNWs have crystalline structures. The SiNW above has a diamond cubic structure, while the NW below only shows one group of atomic planes and it is not possible to decide the structure. The FFT images of the selected areas of what could be catalyst NPs are shown in the insets in this figure. According to the indexing results, the crystallographic planes in both FFT images correspond to Si (111) planes, which have an interplanar distance of 0.31 nm. We thus think that both NWs are kinked and that those dark contrasts mainly come from NW parts that are at right angle with the parts on the left and which are seen end-on.

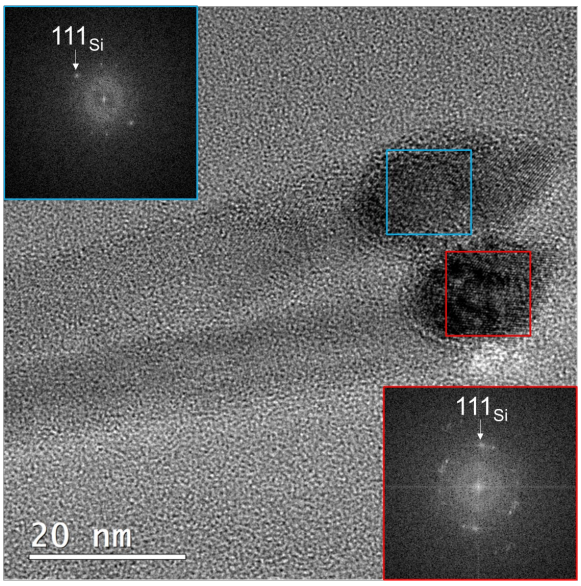

Figure 4.4. Two crystalline SiNWs fabricated with pure Sn catalyst. FFTs correspond to areas with the same frame color.

According to TEM characterizations on SiNWs grown with pure Sn catalyst on crystalline Si substrates, we found that pure Sn catalyst with 1 nm nominal thickness did not lead to hexagonal SiNWs under the current experiment conditions. Unlike the SiNWs grown on Cu grid substrates, where it is common that catalyst particles are on top (see Figure 4.5), the SiNWs catalyzed by pure Sn are always capless. Another notable difference between the SiNWs fabricated on the two substrates is that SiNWs on Si wafer substrates are thicker than their counterparts on Cu grids.

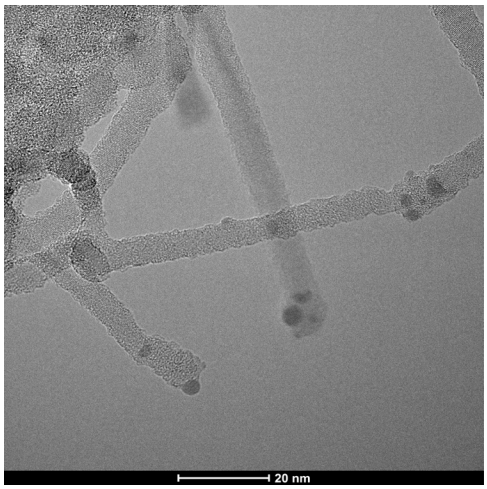

Figure 4.5. SiNWs grown directly on Cu TEM grids using Sn catalyst.

Based on the discussion above, we assume that Cu has played a significant role in fabrication of hexagonal SiNWs. In the following sub-chapters, we will prepare NPs of CuSn mixed catalyst and study the evolution of NP crystalline structures during different steps of SiNWs growth.

4.2. **Making nanoparticles of CuSn mixed catalyst**

The catalyst nanoparticles (NPs) play an important role in NW growth: they influence the NW size, morphology, density, structure, orientation and thus, the performance of the devices based on NWs. However, unlike pure metal catalysts which have been widely investigated, Cu-Sn mixtures have not been used as catalysts for SiNW growth and the properties of novel CuSn mixed-catalysts are to be explored. Although Cu-Sn mixtures are new to catalyze SiNW growth, bronze - the most famous Cu-Sn alloy, has been used by mankind since prehistoric times. In the recent decades, Cu-Sn alloys have become a widespread lead-free soldering material because of its low melting temperature, low cost, and non-toxic nature [Dariavach, 2006, Chen, 2011b]. The Cu-Sn bulk phase diagram is shown in Figure 4.6 [Furtauer, 2013, Sanabria, 2018]. Cu and Sn can form a eutectic alloy with a composition of 98.7 at% Sn at the temperature of 227 °C, which is lower than the melting point of pure Sn at 232 °C. There are two intermetallic compounds of Cu and Sn in the phase diagram at lower temperatures: Cu_6Sn_5 (η phase and η' phase) and Cu_3Sn (ε phase). These two compounds form sequentially during a soldering reaction followed

by a solid-state process between Sn and Cu [Tu, 2007b]: typically, when a small drop of molten Sn touches the Cu surface, it spreads and forms a cap on the Cu surface. In the wetting reaction, liquid Sn reacts with Cu to first form Cu_6Sn_5. The initial formation of Cu_3Sn comes from the reaction between Cu_6Sn_5 and Cu afterwards [Tu, 2007b, Shang, 2008].

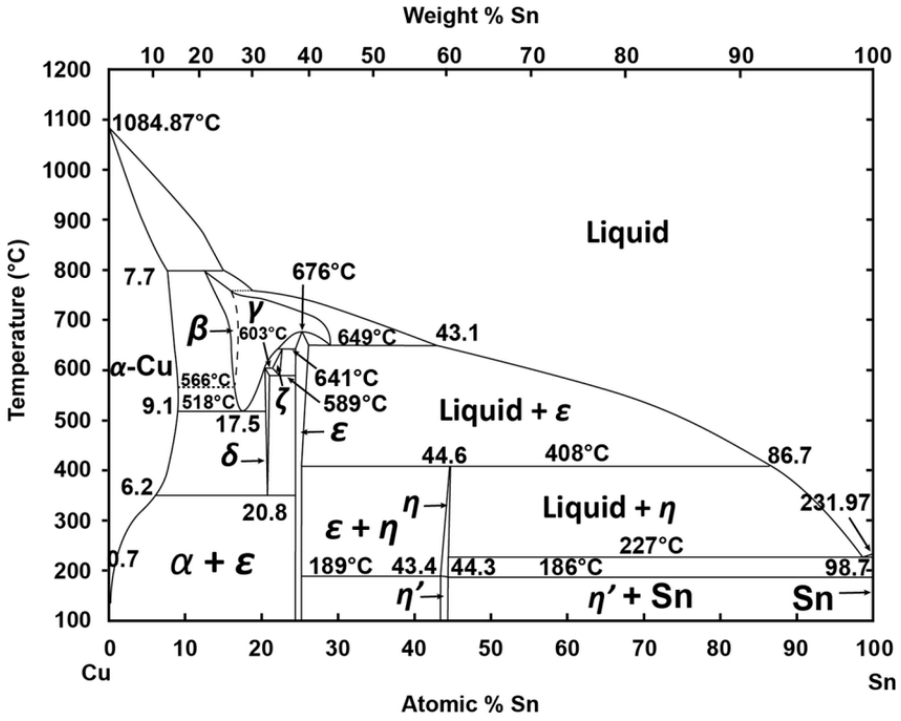

Figure 4.6. The Cu-Sn phase diagram [Furtauer, 2013, Sanabria, 2018].

Cu-Sn nano solders have been researched extensively for electronic device interconnections and for flexible display materials, since Cu-Sn eutectic alloy has a lower melting temperature than pure metals, and a melting point depression occurs when the size of a particle reaches the nanoscale [Jeong, 2008b, Cui, 2009]. According to a study by Yun Hwan Jo *et al.*, the eutectic composition shifts from 1.3 at% Cu in the bulk phase diagram to 11.3 at% Cu when using nano solders with diameters of 14 nm. Moreover, a significant melting temperature reduction of up to 30.3 °C is achieved as shown in Figure 4.7a [Jo, 2011]. The size-dependent melting properties of small Sn particles was studied by S. L. Lai *et al.* [Lai, 1996] (Figure 4.7b). The curve in Figure 4.7b is the calculated result and the discrete points with error bars are experimental results, which are consistent with the calculated curve. The melting point of the Sn NPs with

a diameter of 14 nm is at 218 °C, higher than the melting temperature (205.2 °C) of the NPs with the same diameter and eutectic composition mentioned above[Jo, 2011]. With the diameter decreasing, the difference in the melting points between the two kinds of NPs increases as we can see from Figure 4.7a and b [Jo, 2011] [Lai, 1996].

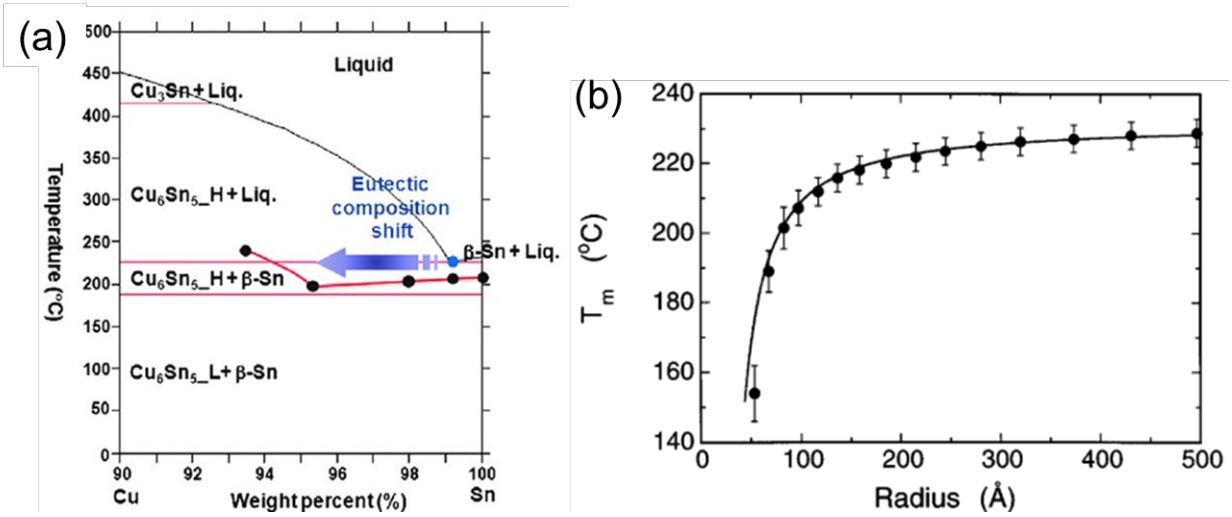

Figure 4.7. Sn rich side of Cu–Sn binary phase diagram. The Eutectic composition shifts from Sn–0.7 weight% Cu (1.3 at% Cu) in the bulk phase diagram to Sn–5.3 weight% Cu (11.2 at% Cu) in a 14 nm nanoscale phase diagram [Jo, 2011]; (b) Size dependence of the melting points of Sn NPs [Lai, 1996].

With the previous knowledge of the Cu-Sn phase diagrams and the solder reactions in the Cu-Sn system, we decided to fabricate SiNWs with CuSn mixed catalyst for the first try. We grew SiNWs using a co-catalyst of 1 nm Sn/0.8 nm Cu on (100) Si substrates under the typical PECVD conditions. Cu was firstly evaporated on the substrates in a thermal evaporator, and then Sn was deposited on top of Cu to prepare the mixed catalysts. We also used pure Sn and pure Cu with 1 nm nominal thickness catalysts respectively for SiNW growth as control groups. SEM images of the as-deposited catalyst NPs are shown in Figure 4.8a - c. As-deposited Sn catalyst NPs have diameters from 10-20 nm (Figure 4.8a). We do not see a lot of NPs in as-deposited Cu catalyst, instead we find island-like structures (Figure 4.8b). Meanwhile, as-deposited co-catalyst NPs of 1 nm Sn/0.8 nm Cu have the smallest diameters (Figure 4.8c), which can be attributed to the combination of Sn and Cu since neither of the individual metal have such small sizes (around 10 nm).

SiNWs grown with pure Sn catalyst have an average diameter around 15 nm (Figure 4.8d). Most of the SiNWs are within the diameter range of 10 to 20 nm. It is interesting to find that pure Cu catalyst did not lead to NW growth under the current experimental conditions. Homogeneous Cu-based NPs have formed after the PECVD experiment as displayed in Figure 4.8e.When using a CuSn mixed catalyst, the SiNWs have a bi-modal diameter distribution (Figure 4.8f): both thin NWs (around ⌀ 10 nm) and thick NWs (≥ ⌀ 35 nm) exist at the same time, which has never been observed in the case of SiNWs synthesized with pure Sn catalyst. Adding Cu into Sn to make a co-catalyst does have an influence on SiNW diameter distributions. What makes it more interesting is the presence of thin SiNWs, which is a good direction for exploration of conditions of hexagonal Si phase.

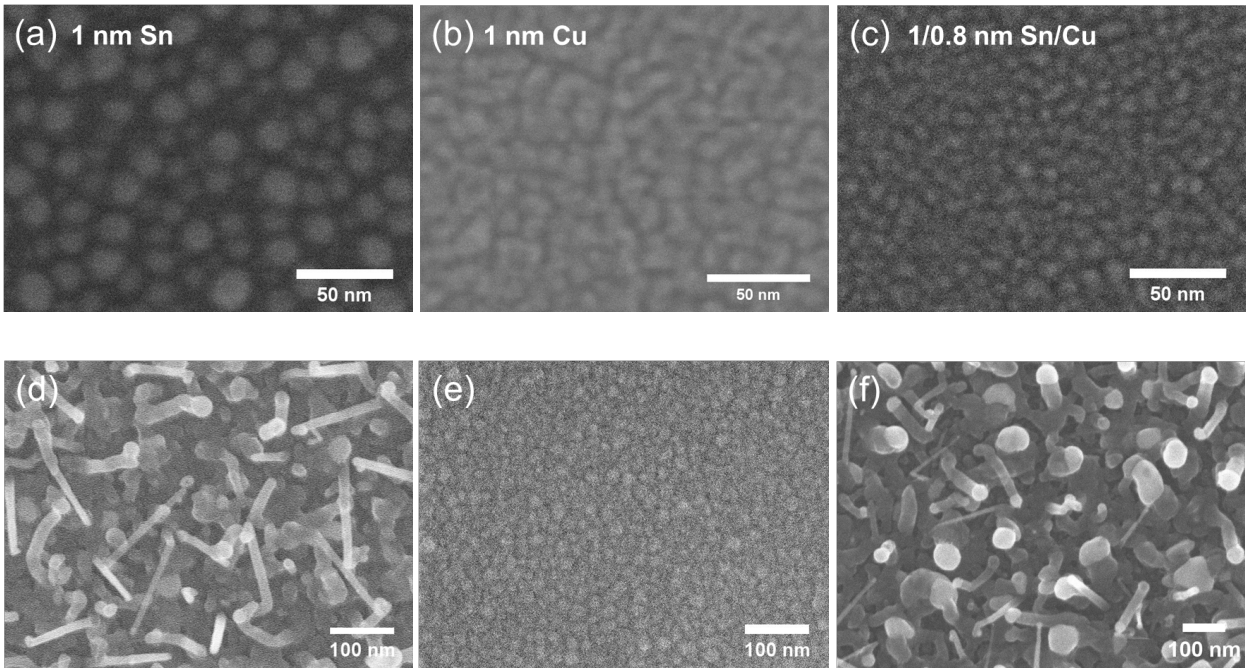

Figure 4.8. As-deposited Sn (a) and Cu (b) with 1 nm nominal thickness; (c) as-deposited mixed catalyst NPs of 1 nm Sn/0.8 nm Cu; (d) SiNWs grown with Sn catalyst; (e) Cu NPs after PECVD experiment; (f) SiNWs grown with a CuSn mixed catalyst.

In the following sub-sections, we will study the evolution of the CuSn co-catalyst NPs during the different stages of the PECVD experiments. The size and distribution of the CuSn co-catalyst NPs will be

characterized by SEM, while the structure and elemental composition of the NPs will be studied by TEM and EDX.

4.2.1. **As-deposited CuSn co-catalyst nanoparticles**

At first, we have studied the as-deposited CuSn co-catalysts NPs with compositions of 1 nm Sn/0.8 nm Cu (65 at% Cu), 0.6 nm Sn/0.6 nm Cu (70 at %Cu), 0.1 nm Sn/0.1 nm Cu (70 at% Cu), respectively. The evaporated thicknesses of Cu and Sn above are nominal thicknesses given by the microquartz balance of the evaporator. In the published work on 2H SiNWs by Tang *et al*. [11], 1 nm Sn (nominal thickness) was evaporated on the Cu TEM grid as the catalyst. We still used 1 nm Sn as in the paper, even though it was evaporated on the walls of TEM grid in [11] and a small nominal thickness of Cu as the initial co-catalyst composition for the investigation. We also chose compositions with smaller total nominal thicknesses, which would be closer to the actual thickness on the grid walls, to study the influence of amount of co-catalyst on NP size. At first, we evaporated was evaporated at first on (100) Si substrates, then we opened the chamber, switched the source material, and evaporated Sn on top of Cu. Images of the as-deposited co-catalyst NPs taken by SEM are shown in Figure 4.9. The SEM image in Figure 4.9a shows that the as-deposited co-catalyst NPs of 1 nm Sn/0.8 nm Cu on the Si substrate have diameters mostly around 15-25 nm. Meanwhile, the NPs are close-packed with a distance of only a few nm between each other. It was difficult to get clear SEM images of the as-deposited NPs of 0.6 nm Sn/0.6 nm Cu and 0.1 nm Sn/0.1 nm Cu by Hitachi S-4800 because of its resolution limitation. Therefore, we have decided to use TEM to characterize the small NPs. The co-catalysts were evaporated directly on the carbon membrane of the gold TEM grids for the convenience of TEM observation. The TEM images of the as deposited co-catalysts of 0.6 nm Sn/0.6 nm Cu and 0.1 nm Sn/0.1 nm Cu are shown in b and c. We can see that there are NPs formed on the substrates after thermal evaporation. The as-deposited NPs of 0.6 nm Sn/0.6 nm Cu co-catalyst have diameters about 3-6 nm. The as-deposited NPs of 0.1 nm Sn/0.1 nm Cu co-catalyst have diameters about 2-3 nm, which are more interesting to us as we aim for small diameter SiNWs. We can see

that with the total nominal thickness of co-catalyst reducing, the as-deposited NP diameters decreases, while the distances between the adjacent NPs are found between 2 and 5 nm.

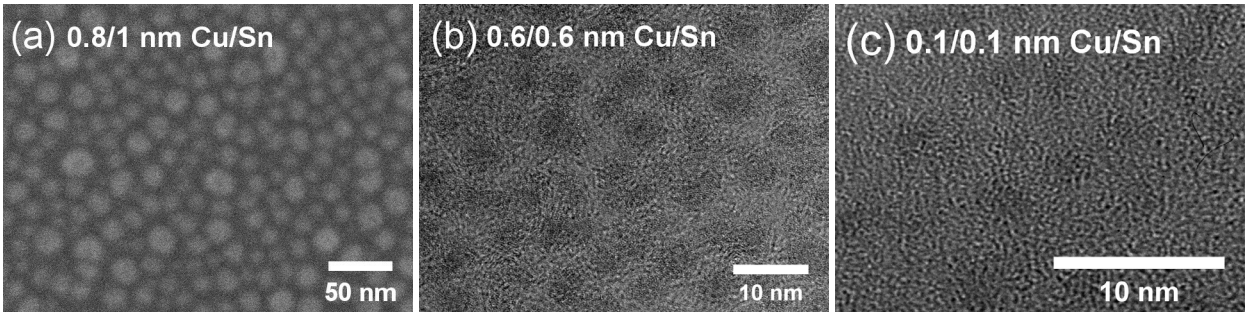

Figure 4.9. (a) SEM image of the as-deposited co-catalyst NPs of 1 nm Sn/0.8 nm Cu on (100) Si substrate; (b,c) TEM images of the as-deposited co-catalyst NPs of 0.6 nm Sn/0.6 nm Cu and 0.1 nm Sn/0.1 nm Cu on carbon membrane of Au TEM grids.

We carried out EDX analysis on the as-deposited co-catalyst NPs of 0.6 nm Sn/0.6 nm Cu and 0.1 nm Sn/0.1 nm Cu on gold TEM grids, over surfaces averaging particles and void areas. The EDX results show the presence of five elements in both samples: Cu, Sn, O, Au and C. The signals of Au and C come from the TEM grids. The presence O in the samples might be caused by the oxidation of the co-catalyst NPs after thermal evaporation. The elemental compositions of Cu and Sn in the two samples are shown in Table 4.1. Quite interestingly, the detected atomic ratios of Cu and Sn in the two samples are close to their nominal atomic ratio of 69.6%:30.4%. This means both that little matter exits the sample after evaporation, on the one hand, and that our handling of the evaporator (one closes the shutter by hand upon reading the quartz balance display) is reasonably accurate, on the other hand.

Table 4.1. EDX measurements of the elemental compositions of Cu and Sn in the as-deposited co-catalyst NPs with the thicknesses indicated. The nominal atomic ratio for equal thicknesses is 69.6% Cu/30.4% Sn.

Nominal deposited thickness	0.6 nm Sn/0.6 nm Cu	0.1 nm Sn/0.1 nm Cu

Element	Cu K	Sn K	Cu K	Sn K
EDX atomic%	65.0 ± 0. 8	35.0 ± 0.3	73.3 ± 12.5	26.7 ± 6.7

Next, we have investigated the atomic structure of the as-deposited co-catalyst NPs in more detail. A high-magnification TEM image of the as-deposited NPs of 0.6 nm Sn/0.6 nm Cu co-catalyst is shown in Figure 4.10a. The as-deposited NPs of 0.6 nm Sn/0.6 nm Cu are amorphous like and we do not observe clear atomic planes inside the particles. However, after two-minute exposure to the TEM electron beam at 300 kV, the irradiated NPs have changed their structures and atomic planes appear as shown in Figure 4.10b. The FFT image of the irradiated NPs is shown in the upper right corner. There are two groups of spots in the FFT image: the smaller ring, $1/d = 4.68$ nm^{-1}, corresponds to an interplanar spacing of 0.21 nm; the spots outside the inner ring as indicated by the arrow, $1/d = 5.44$ nm^{-1} corresponds to an interplanar spacing of 0.18 nm. Cu has a face-centered cubic (fcc) structure with a lattice constant of 0.3613 nm [Suh, 1988], with interplanar distances of: $d_{\mathrm{Cu}\{111\}} = 0.21$ nm, $d_{\mathrm{Cu}\{200\}} = 0.18$ nm. Therefore, the irradiated nanocrystals correspond to Cu crystals formed after the irradiation by the TEM electron beam.

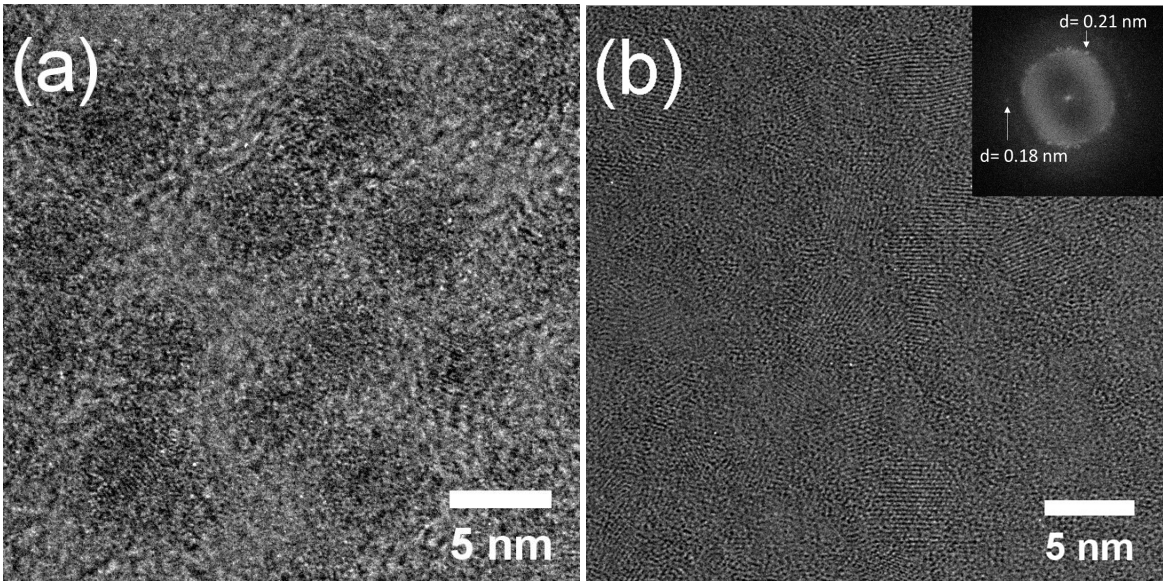

Figure 4.10. Amorphous as-deposited co-catalyst NPs of 0.6 nm Sn/0.6 nm Cu and (b) the NPs after two-minute irradiation under the electron beam of 300 kV in TEM Nan'eau. Top right corner is the corresponding FFT image.

In order to verify that the irradiated nanocrystals are pure Cu and not another compound, we have compared the situation with literature. Selected area diffraction patterns (SADP) of other potential phases - Cu_2O, CuO, β-Sn, SnO, Cu_6Sn_5, Cu_3Sn - are shown in Figure 4.11a - f. Since O was detected in the previous EDX experiments, there was a chance for Cu to be oxidized. The diffraction patterns of two copper oxides Cu_2O and CuO are shown in Figure 4.11a and b [Shang, 2008, Zhang, 2008, Svintsitskiy, 2013]. Neither of the copper oxide diffraction patterns have diffraction spot arrangements or ring diameters compatible with the FFT in Figure 4.10b, indicating that the irradiated nanocrystals are not Cu oxides. As the EDX experiments also confirmed the existence of Sn in the co-catalyst NPs, hence we also compare our FFT image with a selected area diffraction pattern image of Sn. The tetragonal phase (β-Sn) in the bulk form is known to be stable at room temperature and it transforms to a diamond cubic phase (α-Sn) only below ~13 °C [Busch, 1960]. A SADP image of β-Sn is shown in Figure 4.11c [Lee, 2016]. Although one set of β-Sn planes have an interplanar distance ($d_{\mathrm{Sn}\{211\}} = 0.202$ nm) close to $d_{\mathrm{Cu}\{111\}}$, other reflections of β-Sn, more intense and representing larger interplanar spacings, are absent from the FFT image in Figure

4.10b. Therefore, the nanocrystals are not β-Sn. Next, we have checked the possibility of SnO_2. A selected area diffraction pattern image of SnO_2 is shown in Figure 4.11d [Lee, 2016]. Although $d_{SnO_2\{211\}} = 0.177$ nm is close to the interplanar spacing of 0.18 nm in the FFT image, again, the largest interplanar spacings of SnO_2 do not match our result at all. Therefore, the nanocrystals are not likely to be SnO_2.

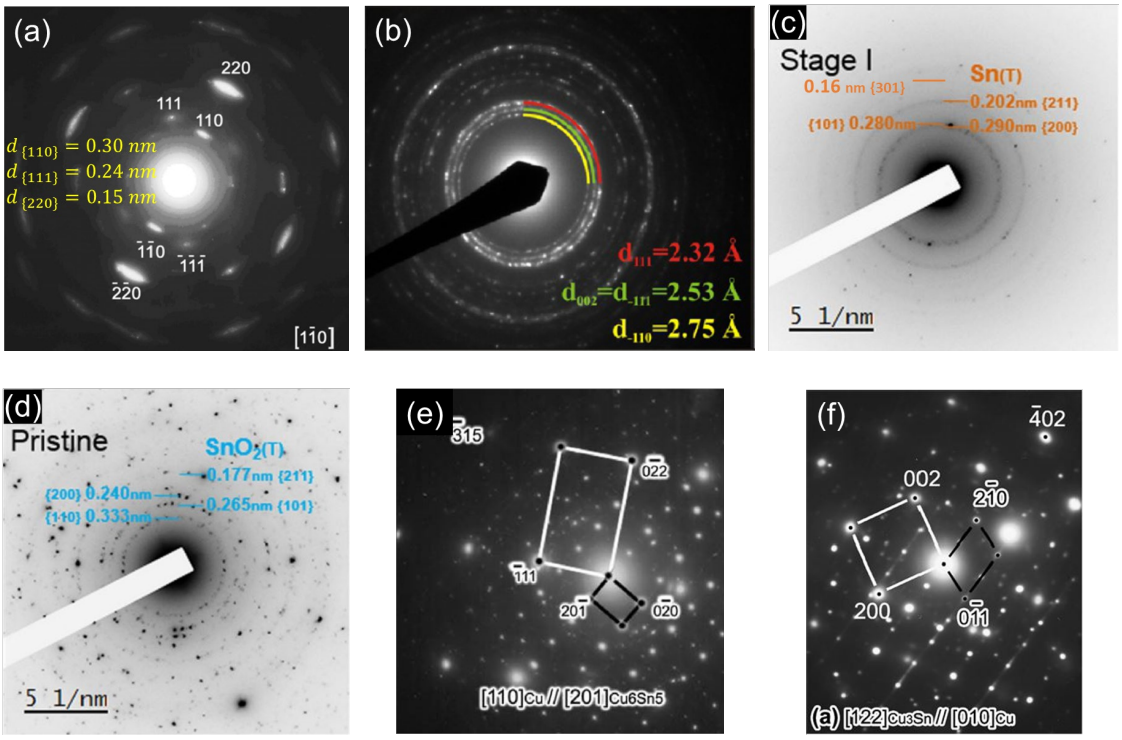

Figure 4.11. SADPs of the other potential phases: (a) Cu_2O, (b) CuO, (c) β-Sn, (d) SnO_2, (e) Cu_6Sn_5, and (f) Cu_3Sn from literature [Shang, 2008, Zhang, 2008, Svintsitskiy, 2013] [Busch, 1960] [Lee, 2016] [Shang, 2009].

It is also necessary to distinguish the crystalline structures of Cu and the Cu-Sn intermetallic compounds. At 25 °C, the diffusivity of Cu along the a- and c-axes of β-Sn is about 5×10^{-9} and 2×10^{-6} cm^2/sec, respectively. This indicates that the mobility of Cu in Sn is high enough so that the growth of Cu-Sn Intermetallic compounds can occur at room temperature [Tu, 2007c]. Two polymorphs Cu_6Sn_5 are shown in the Cu-Sn phase diagram in Figure 4.6: η and η'. A polymorphic transformation from hexagonal η (with cell parameters of a = 0.4190 nm and c = 0.5086 nm) to monoclinic η' (with cell parameters of a = 1.1022 nm, b = 0.7282 nm, c = 0.9827 nm, β = 98.84˚) occurs as the temperature falls below 186 °C [Larsson,

1994b, Peplinski, 1996]. A SADP image of Cu/Cu_6Sn_5 soldering interface is shown in Figure 4.11e [Shang, 2009]. The diffraction spots from the Cu substrate are marked and indexed in white, while those from Cu_6Sn_5 are in black, having an orientation relationship of $[201]_{Cu6Sn5}$ //$[110]_{Cu}$. In the FFT image in Figure 4.10b, we did not observe the spots of Cu_6Sn_5, indicating there were no Cu_6Sn_5 crystals in the co-catalyst NPs. The basic unit of Cu_3Sn is orthorhombic with lattice dimensions of a = 0.5514 nm, b = 0.4765 nm and c = 0.4329 nm [Brooks, 1970]; it may be disordered or ordered, or have a long-period superlattice [Watanabe, 1983]. A selected area diffraction pattern image of Cu/Cu_3Sn interface from ref [Shang, 2008] is shown in Figure 4.11f. The diffraction spots from Cu are marked and indexed in white, while those from Cu_3Sn are in black. There is no superlattice structure like in Figure 4.11f in our FFT image of the nanocrystals. Therefore, we have not detected Cu_3Sn crystals in the co-catalyst NPs.

In addition, we did not observe atomic planes either on the as-deposited NPs of 0.1 nm Sn/0.1 nm Cu in Figure 4.9c, even at a higher magnification. However, because the small NPs had a lower contrast compared with the larger NPs of 0.6 nm Sn/0.6 nm Cu, it was difficult to decide on the structures of the small NPs.

4.2.2. **Influence of the substrate temperature during hydrogen plasma treatment on CuSn co-catalyst nanoparticle size**

After TEM observation on the as-deposited CuSn co-catalyst NPs, the substrates were loaded into the Plasfil reactor chamber for PECVD experiments. Process started when pressure reached 5×10^{-5} mbar. In the typical PECVD process using the Sn catalyst, a hydrogen plasma treatment has been applied to reduce the superficial oxide of the Sn NPs to guarantee the SiNW growth. As we use a co-catalyst containing Sn, we also need to carry out hydrogen plasma treatment using the same parameters as in the conditions for the applied PECVD process (see Table 3.1 in Chapter 3).

The hydrogen plasma treatment process can also change the size, the distribution and the structure of as-deposited catalyst NPs depending on the annealing temperature and time. Therefore, in this sub-

section, we focus on the influence of hydrogen plasma treatment on the as-deposited CuSn co-catalyst NPs. Firstly, we study the influence of the substrate temperature during the plasma treatment on the co-catalyst NP size and distribution. Then, we characterize by TEM and EDX the structure and composition of the co-catalyst NPs after the hydrogen plasma treatment, similarly to the previous section. Since the as-deposited NPs of 0.1 nm Sn/0.1 nm Cu co-catalyst had the smallest size according to the last experiment in Chapter 4.2.1, which is advantageous for the growth of small diameter SiNWs, therefore we focus on as-deposited NPs of 0.1 nm Sn/0.1 nm Cu in this sub-section.

A co-catalyst deposit with composition of 0.1 nm Sn/0.1 nm Cu was evaporated on (100) c-Si substrates in the first step. Then, we transferred the samples to Plasfil and carried out hydrogen plasma treatments at a substrate temperature of 170, 200 and 416 °C, respectively, for 2 minutes. The other parameters remained the same as for the standard hydrogen plasma process in Table 3.1 (100 sccm for H_2 flux, 5 W for plasma power and 0.8 mbar for gas pressure). Next, we opened the reactor chamber after it cooled down and took out the samples for SEM observation (Figure 4.12). As we can see from Figure 4.12 a and b, small, homogeneous and dense NPs were obtained after the plasma treatment at 170 °C and 200 °C. The NPs of the two samples have similar diameters. Co-catalyst NPs after the plasma treatment at 170 °C have an average diameter of 4.4 nm, with a standard deviation of 1.4 nm; while for the sample annealed at 200 °C, the average diameter is 4.5 nm, with a standard deviation of 1.2 nm (see the histogram in Figure 4.12d). Compared with the average diameter of the as-deposited NPs of 0.1 nm Sn/0.1 nm Cu on the carbon membrane of TEM grids (without irradiation effect by TEM electron beam), the NP diameter increased by about 3 nm after the hydrogen plasma treatment at 170 °C and 200 °C. When the plasma treatment is done at a higher temperature of 416 °C, most of the NPs grow larger, while at the same time the density is reduced. It is notable that some abnormally large NPs have appeared, caused by the coalescence of a few smaller NPs or due to the Ostwald ripening effect. Based on these results, in order to obtain small co-catalyst NPs, it is important to carry out hydrogen plasma treatment at a lower temperature such as 170 or 200 °C. It is enough to help removing the oxide and change the catalyst distribution.

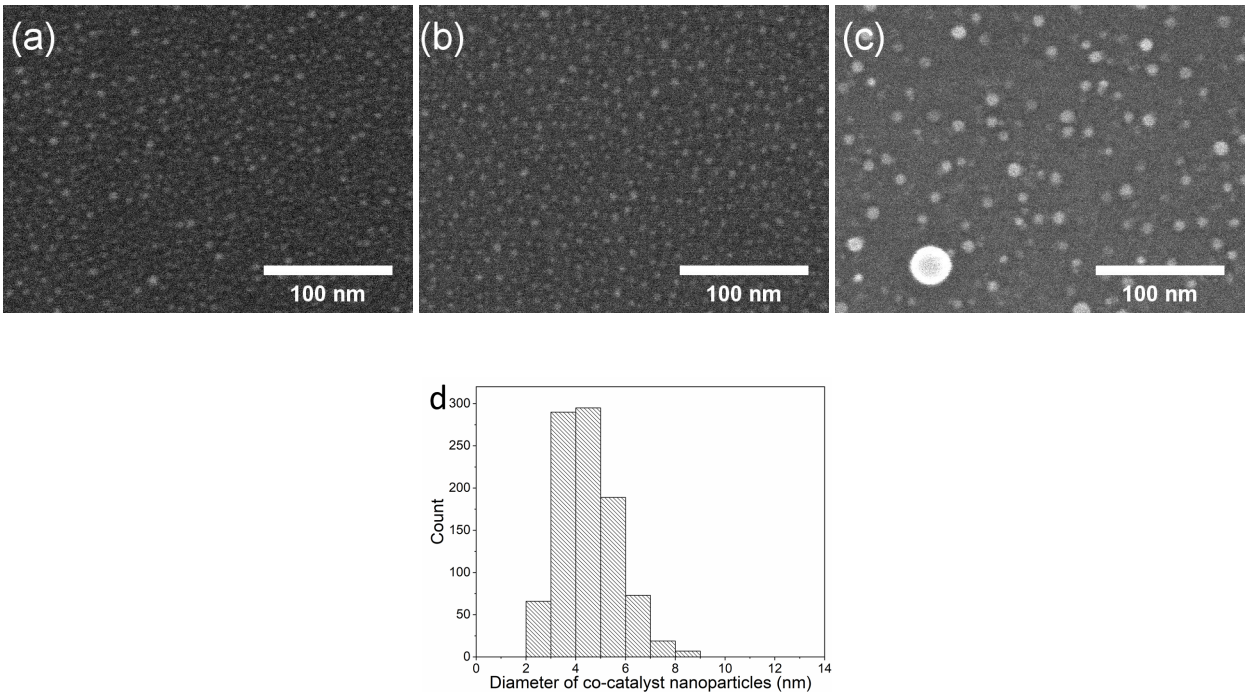

Figure 4.12. Nanoparticles from 0.1 nm Sn/0.1 nm Cu co-catalyst after being submitted to the same hydrogen plasma treatment at (a) 170 °C, (b) 200 °C and (c) 416 °C. Histogram of diameters of NPs in (b) is shown in (d).

4.2.3. **Structures of CuSn co-catalyst nanoparticles after hydrogen plasma treatment at 200 °C**

To characterize the structures of co-catalyst NPs after hydrogen plasma treatment by TEM, we have evaporated 0.1 nm Sn/0.1 nm Cu on carbon-coated TEM gold grids directly. The substrates were then loaded in the PECVD reactor for a hydrogen plasma treatment following the typical conditions in Table 3.1. After the experiment, the sample was examined in TEM NanoMAX (Figure 4.13). The NPs in the figure have diameters around 3 nm. Compared with the as-deposited NPs in Figure 4.9c, the NPs after the treatment grew larger and had a higher contrast. However, due to the small size, it was still difficult to observe the NP structure unambiguously. Therefore, we now investigate the structures of the larger co-catalyst NPs of 0.6 nm Sn/0.6 nm Cu after the treatment.

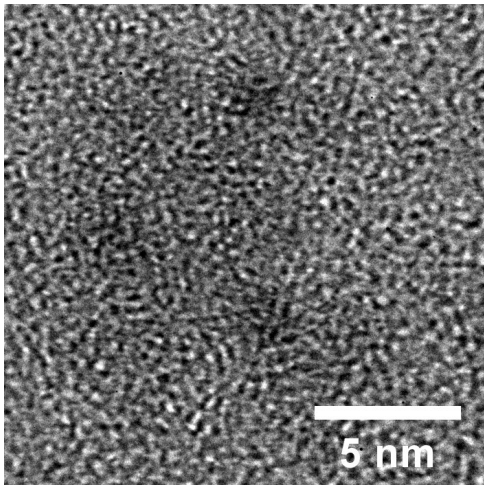

Figure 4.13. TEM image of NPs of 0.1 nm Sn/0.1 nm Cu co-catalyst on the carbon membrane of TEM grid after hydrogen plasma treatment at 200 °C.

A co-catalyst of 0.6 nm Sn/0.6 nm Cu was evaporated on carbon-coated TEM gold grids, then the substrates were loaded into the PECVD reactor for a hydrogen plasma treatment following the same procedures as above. The same co-catalyst has also been loaded into PECVD reactor and annealed at 200 °C in vacuum for 2 minutes without hydrogen plasma treatment as control group. A TEM image of the co-catalyst NPs of 0.6 nm Sn/0.6 nm Cu after hydrogen plasma treatment is shown in Figure 4.14a with diameters around 3-10 nm. Compared with the as-deposited NPs in Figure 4.9b, the NPs became larger after the hydrogen plasma treatment. We can see the atomic planes in some NPs, which means that the NPs crystallized during the plasma treatment. To confirm the crystalline structures of more NPs, we made a select area diffraction pattern on a larger selected area (Ø = 150 nm) of the TEM sample (see Figure 4.15). The three diffraction rings correspond to the {111}, {200} and {220} planes of Cu. That is, the nanocrystals in Figure 4.14a are clearly Cu crystals. Co-catalyst NPs after annealing at the same temperatures are mostly amorphous-like, only one NP shows crystallographic planes as indicated in Figure 4.14b, which can be reflected in the FFT image of the whole area. By comparison, we find that hydrogen plasma treatment at 200 °C can make Cu in co-catalyst NPs crystallize, whereas the crystallization efficiency of co-catalyst NPs annealed at 200 °C is much lower. Although at room temperature the driving force for crystallization, in

terms of supercooling, is large, the diffusion of atoms at room temperature is more difficult. Therefore, crystallization of Cu atoms does not happen immediately at room temperature after the thermal evaporation. The hydrogen plasma treatment at 200 °C can assist Cu atoms to overcome the activation energy of diffusion and realize crystallization. The irradiation by TEM electron beam has a similar effect on the as-deposited co-catalyst NPs as the hydrogen plasma treatment to make amorphous NPs crystalize (Figure 4.10b). However, annealing at 200 °C for 2 minutes only is not sufficient enough to lead to crystallization of Cu NPs. We assume a higher temperature and/or a longer time would be needed for this situation.

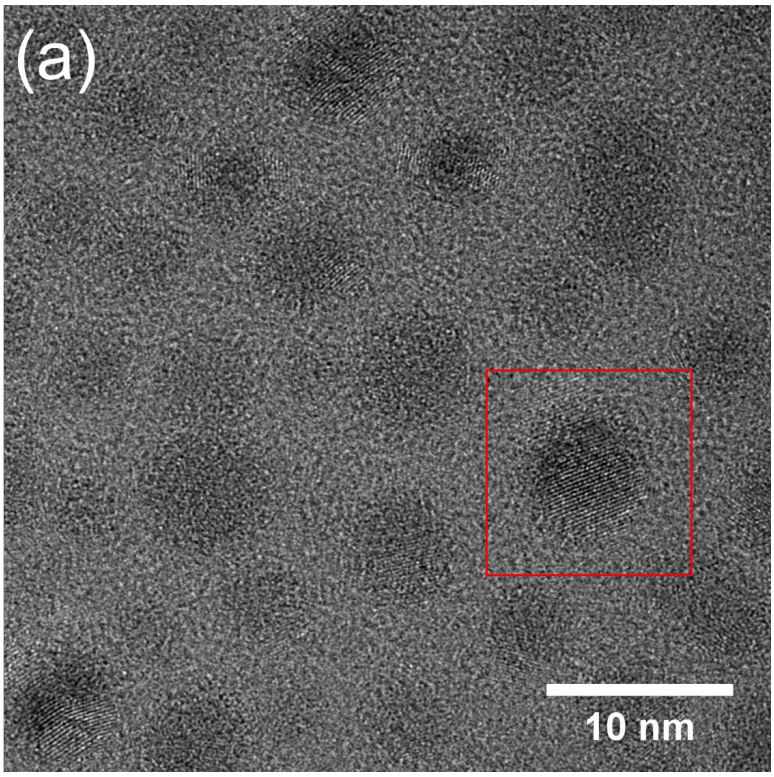

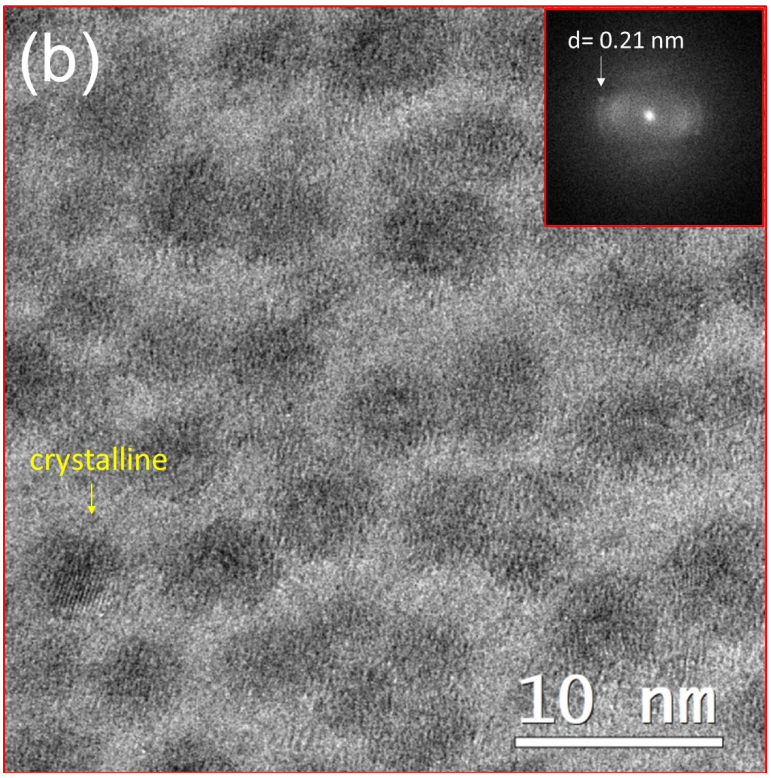

Figure 4.14. Co-catalyst NPs of 0.6 nm Sn/0.6 nm Cu on the carbon membrane of gold grids (a) after the hydrogen plasma treatment at 200 °C; (b) after annealing at 200 °C for 2 minutes without hydrogen plasma. FFT images of corresponding areas is shown in the inset.

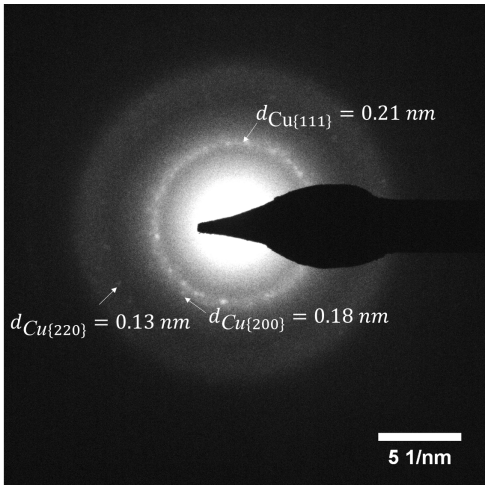

Figure 4.15. Selected area diffraction pattern of the co-catalyst NPs of 0.6 nm Sn/0.6 nm Cu on the carbon membrane after the hydrogen plasma treatment.

To learn about the elemental distribution of Cu and Sn in the co-catalyst NPs after annealing, we carried out elemental analysis on this sample. First, we recorded the bright field (BF) image and the MBE (HAADF) image of the NPs in the scanning transmission electron microscope (STEM) mode, as shown in Figure 4.16a and b. There are different contrasts between the central part and the peripheral part of the co-catalyst NPs in both images, especially for the larger NPs, implying there might be a phase segregation. In the HAADF image (see Figure 4.16b), the central part is brighter than the peripheral part of the NPs. Usually for elements with a higher Z, more electrons are scattered at higher angles due to greater electrostatic interactions between the nucleus and electron beam, causing them to appear brighter in the HAADF image [Nellist, 2000]. However, in our experiment, although Sn has a higher Z number (50) than Cu (29), its density (7.31 g/cm^3) is lower than the density of Cu (8.96 g/cm^3). As a result, we cannot distinguish the distribution of Cu and Sn by the contrast of the NPs in the HAADF image.

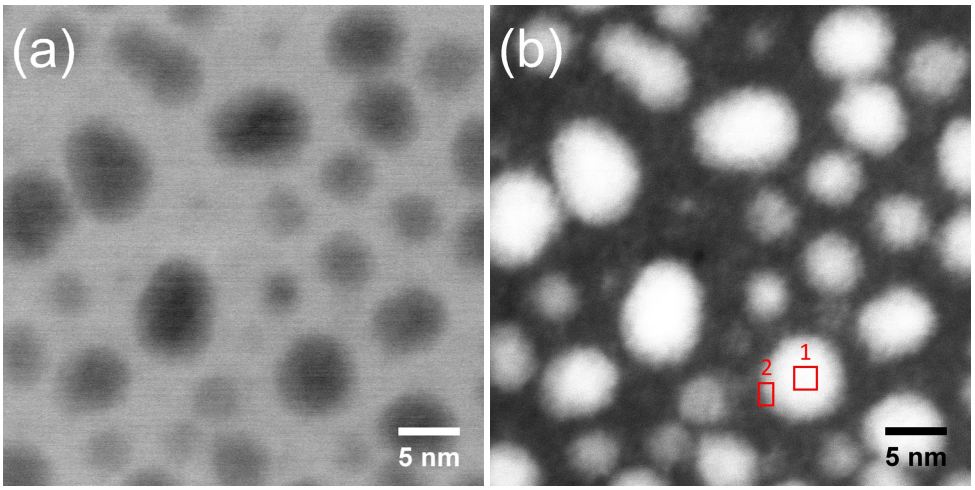

Figure 4.16. BF image and (b) HAADF image in STEM mode of the co-catalyst NPs of 0.6 nm Sn/0.6 nm Cu after the hydrogen plasma treatment.

In order to identify the composition of the elements in the co-catalyst NPs with different contrasts, we performed an EDX analysis in the selected areas 1 and 2 respectively, located in the center and at the periphery of the NP in Figure 4.16b. The obtained EDX spectra are shown in Figure 4.17. In the center (Spectrum 1), Cu, Sn and O are detected and the intensity of Cu is higher than that of the other elements.

At the periphery (Spectrum 2), the intensity of Cu and Sn has decreased compared with the intensity in the center. However, the peak of O has become higher, which means that the peripheral part of the NP is more oxidized. The elemental compositions are shown in detail in Table 4.2. We find that the values of O at both areas, the values of Cu signals at the peripheral part have higher errors than the detected results. That is probably caused by the very short detection time to protect the small NP from being totally destroyed by the electron beam. But as we can see the peaks of O and Cu in the spectrums, these elements do exist in the NP.

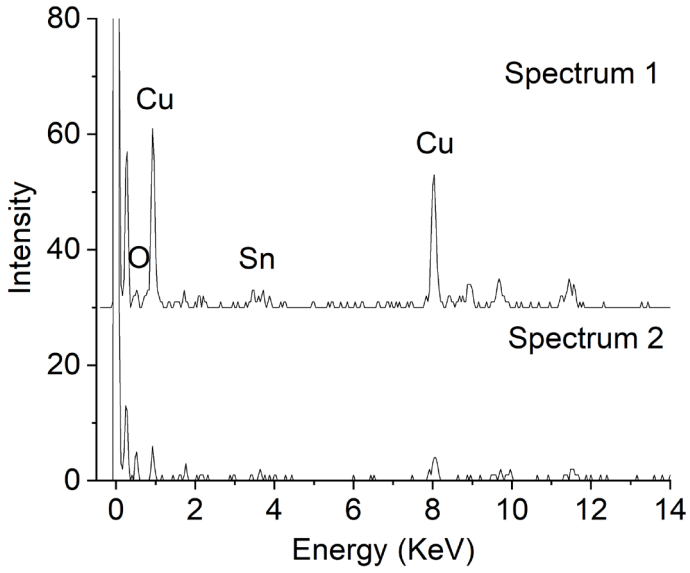

Figure 4.17. EDX spectrums of areas 1 and 2 of the co-catalyst NPs in Figure 3.10 (b), obtained by TEM Nan'eau.

Table 4.2. Elemental compositions in the center and at the periphery of the particle shown in 0 (b), deduced from the EDX spectra 1 and 2 in 0, respectively.

	Center			Periphery		
Element	O K	Cu K	Sn K	O K	Cu K	Sn K
Atomic%	5.8 ± 10	52.1 ± 25	42.1 ± 14	43.4 ± 63	22.5 ± 31	34.1 ± 24

We also made an EDX line scan on co-catalyst NPs of the 0.6 nm Sn/0.6 nm Cu deposit after the hydrogen plasma treatment (Figure 4.18). The EDX line goes through the center of a NP with diameter around 7 nm. The EDX spectra show that the Cu signal (red line) has a much higher intensity than Sn (yellow line) in the central brighter part. The Sn/Cu atomic ratio (blue line) shows that Cu dominates in the center of the NP, while Sn dominates at the periphery. By combining the TEM results and EDX analysis of NPs after the hydrogen plasma treatment, we can conclude that the NPs are formed from Cu nanocrystal cores covered by amorphous shells of Cu and Sn. The line scan results are consistent with the EDX spectra in Figure 4.17 and the quantified results in Table 4.2.

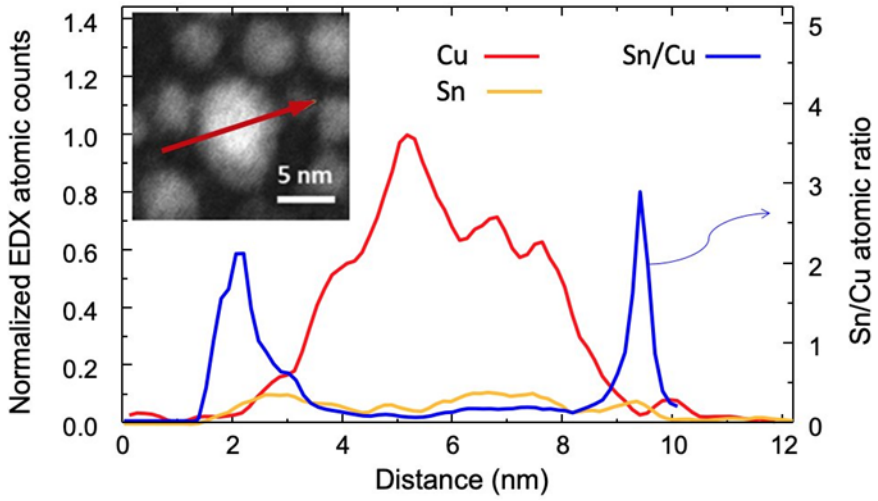

Figure 4.18. EDX line scan of a NP of mixed catalyst NP of 0.6 nm Sn/0.6 nm Cu after the hydrogen plasma treatment at 200 °C. HAADF STEM image in inset. Normalized atomic counts along the red arrow for Cu (red) and Sn (yellow) (left scale), and Sn/Cu atomic ratio (blue line, right).

By combining the TEM results and EDX analysis, we propose the following model for the co-catalyst 0.6 nm Sn/0.6 nm Cu NPs formation after the hydrogen plasma treatment at 200 °C: a Cu nanocrystal covered by an amorphous shell of Cu and Sn (see Figure 4.19). During thermal evaporation, Cu was firstly evaporated on the substrates and then Sn was evaporated on top of Cu. Amorphous as-deposited co-catalyst NPs formed at this step. Then the substrates were loaded into the PECVD reactor for a hydrogen plasma treatment at 200 °C. At both 200°C and room temperature, Cu has a high mobility and

is the dominant diffusing species in the interdiffusion of Cu-Sn system [Tu, 2007c]. When the temperature was increased to the melting temperature of the Cu-Sn eutectic alloy, the Cu-Sn alloy would melt, like in the wetting process of the Cu-Sn solders during the soldering. Because of the size-reduction effect on the melting temperatures at nanoscale [Jeong, 2008b, Cui, 2009], the Cu-Sn eutectic alloy with sizes of a few nm is likely to be melted below 200 °C. The eutectic composition may also shift from 1.3 at% Cu in a bulk state phase diagram to a composition with a little more Cu in a nanoscale phase diagram (see Figure 4.7a) [Jo, 2011]. However, in our NPs with a Sn/Cu atomic ratio of 70 at% of Cu, the pure Cu core remains solid during this process since bulk Cu has a high melting point of 1084.87 °C. According to the well-studied solder reactions in the Cu-Sn system, the molten Sn reacts with Cu to first form Cu_6Sn_5 [Tu, 2007b, Shang, 2008]. We assume that this reaction can also happen in our experiment when increasing the temperature, because the EDX results showed that the composition of Cu at the peripheral part of the NP was not as low as the eutectic composition in the Cu-Sn systems. After the hydrogen plasma treatment at 200 °C, the solid Cu crystallized and formed small Cu nanocrystals. However, no nanocrystals of Cu_6Sn_5 or Sn were detected by diffraction pattern. That is probably because, after the plasma treatment, the plasma switching off would correspond to the stop of a strong heating source, provoking the sharp fall of the substrate temperature which would additionally be speeded up by the use of H_2 gas. This would cause the quenching of the NPs in liquid-like (amorphous) structure.

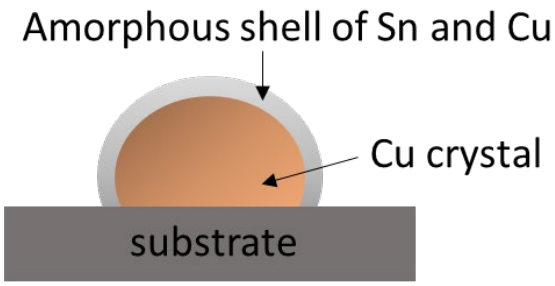

Figure 4.19. Schematic diagram of CuSn co-catalyst NP structure after hydrogen plasma treatment at 200 °C. It is composed of a Cu crystalline core and an amorphous shell of Sn and Cu.

To summarize this sub-section, after the hydrogen plasma treatment at 200 °C, the NPs of 0.6 nm Sn/0.6 nm Cu and 0.1 nm Sn/0.1 nm Cu co-catalysts grew larger. The amorphous as-deposited NPs of 0.6 nm Sn/0.6 nm Cu crystallized during the process and subsequent cooling. The typical structure of NPs at the end of the process is a Cu nanocrystal core covered by an amorphous shell of Cu-Sn alloy (Figure 4.19). In the next step, we study the co-catalyst NPs after a short hydrogen plasma treatment at SiNW growth temperature 416 °C to see its influence on the NP size and distribution.

4.2.4. **Co-catalyst NPs after a second hydrogen plasma treatment at SiNW growth temperature**

Firstly, co-catalyst NPs of 0.1 nm Sn/0.1 nm Cu were evaporated on (100) Si substrates following the typical process. Next, the substrates were loaded into the PECVD reactor for a first hydrogen plasma treatment at 200 °C using the conditions in Table 3.1, then we increased the temperature to 416 °C, the SiNW growth temperature, immediately after the initial treatment, and carried out a second plasma treatment for 30s. The conditions were the same with the NW growth conditions in Table 3.1 (100 sccm for H_2 flux, 1.42 mbar for gas pressure and 1.5 W for plasma power), except that no SiH_4 was used. The purpose was to study the evolution of the co-catalyst NPs at the growth temperature under the influence of the hydrogen plasma without the SiNW growth. Then we cooled down the chamber and took out the samples for SEM observations (Figure 4.20a). We also used pure Sn catalysts with nominal thickness of 0.1 nm for comparison (Figure 4.20b).

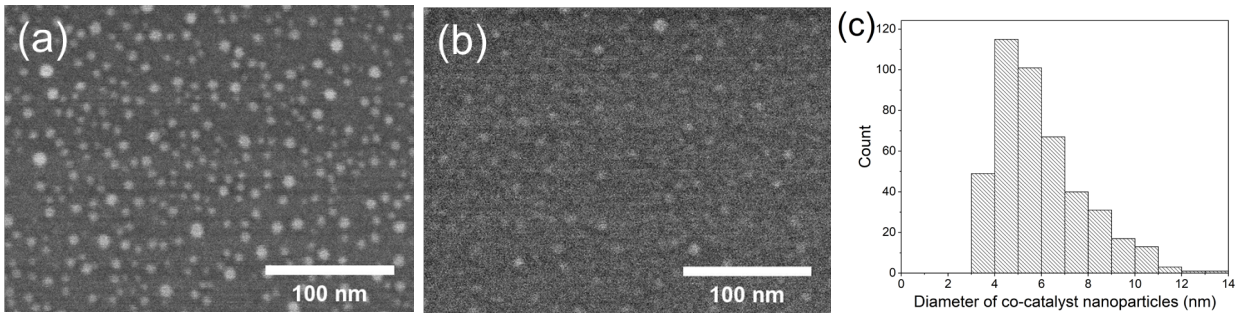

Figure 4.20. SEM images of co-catalyst NPs after a second plasma treatment of (a) 0.1 nm Sn/0.1 nm Cu, and (b) 0.1 nm Sn; The diameter histogram of co-catalyst NPs in (a) is shown in (c).

After a second hydrogen plasma treatments at 416 °C for 30 s, the co-catalyst NPs grew much larger due to the ripening effect compared with the co-catalyst NPs after the first plasma treatment at 200 °C (4.5 ± 1.2 nm) (Figure 4.12b) and the diameter distribution became wider. The diameters of the NPs of 0.1 nm Sn/0.1 nm Cu in Figure 4.20a had a distribution range of 3-14 nm with an average diameter of 6 nm and a standard deviation of 1.9 nm (see the histogram in Figure 4.20c). The NPs of 0.1 nm Sn catalyst have been observed by SEM after the second plasma treatment with image shown in Figure 4.20b. The pure Sn catalyst NPs had similar sizes with the co-catalyst NPs in Figure 4.20a, but they were less dense.

After the study on the influence of a first hydrogen plasma treatment at 200 °C and a second hydrogen plasma treatment at growth temperature, in the next sub-chapter, we continue our investigation of the evolution of CuSn co-catalysts by now watching it during SiNW growth.

4.3. **Evolution of CuSn co-catalyst during NW growth**

with co-catalysts of 1 nm Sn/0.8 nm Cu (Cu-rich) and 1 nm Sn/0.2 nm Cu (Sn-rich) are shown in Figure 4.21a and b. Thin and thick SiNWs have been found in both samples. SiNWs of the two samples both have average diameters around 20 nm (calculated from 100 NW statistics), while the SiNWs synthesized with the Cu rich catalyst have a higher standard deviation of 8.3 nm compared with 5.4 nm for the SiNWs synthesized with the Sn rich catalyst. In addition, the Cu rich sample has both a higher fraction of SiNWs with an average diameter smaller than 10 nm (8 %, compared with 6% for the Sn-rich sample)

and a higher fraction of SiNWs with an average diameter larger than 30 nm. The SiNWs of all the samples were transferred from the Si substrates to gold grids for TEM and EDX characterizations.

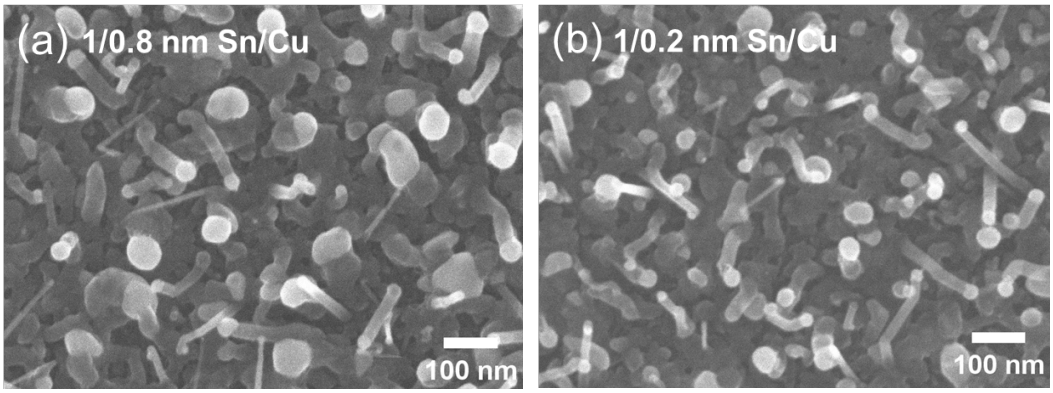

Figure 4.21. SEM images of the SiNWs grown with the co-catalysts of (a) 1 nm Sn/0.8 nm Cu (65 at% of Cu) and (b) 1 nm Sn/0.2 nm Cu (31 at% of Cu).

4.3.1. **CuSn co-catalyst with a dominant amount of Cu**

Figure 4.22 shows a HRTEM image of a SiNW fabricated with co-catalyst of 1 nm Sn/0.8 nm Cu. It has a total diameter of 26 nm including an amorphous layer with thickness around 1-2 nm It is notable that the catalyst NP of the SiNW has a special shape: there is a planar boundary separating the top of the NP (which often has a darker contrast) from its bottom. In fact, most observed NWs in this sample have similar catalyst NPs like this (see Figure 4.23).

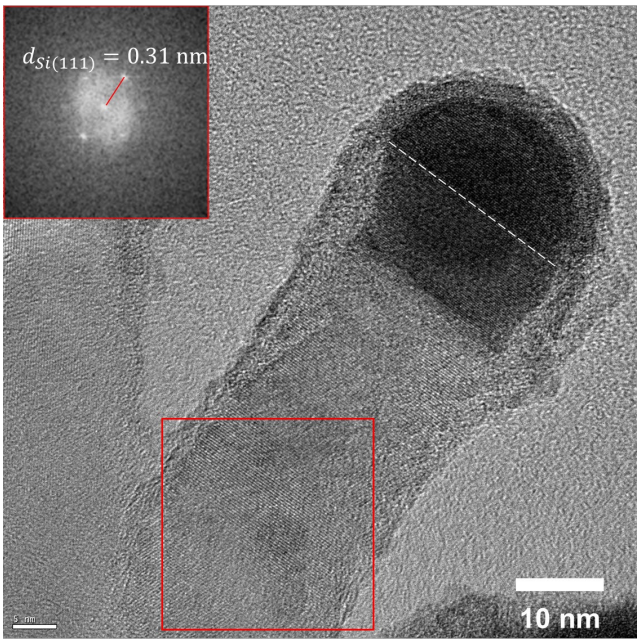

Figure 4.22. HRTEM image of a typical SiNW synthesized with 1 nm Sn/0.8 nm Cu co-catalyst.

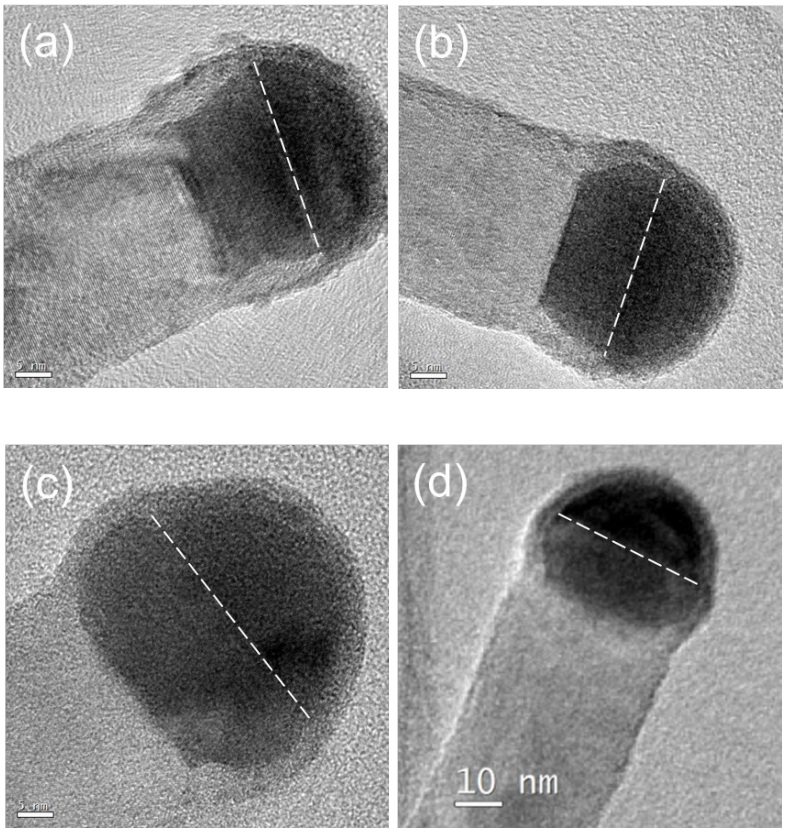

Figure 4.23. Cu-rich co-catalyst NPs of SiNWs with a planar boundary separating the top from its bottom. The top of the NPs often has a darker contrast.

A HRTEM image of the catalyst NP in Figure 4.22 with a higher magnification is shown in Figure 4.24a. The top part of the NP has a hemispherical shape, including a dark amorphous-like contrast at the surface, while the bottom part exhibits crystalline facets, also covered by an amorphous-like matter, although with lighter contrast. In other words, the catalyst NP is mostly crystalline but the crystalline structure vanishes at the top of the particle, where we are tempted to attribute the amorphous layer to the Sn that must have been liquid at the growth temperature. In contrast, the lighter amorphous structure around the base of the catalyst could come from an oxide.

When performing FFTs of the HRTEM image in Figure 4.24a (squared areas), we find well-defined zone-axis patterns, very similar in either part of the catalyst (Figure 4.24b and c). Fitting the two patterns with JEMS software, we find a good correspondence with the hexagonal CuSn structure [Bernal, 1928], – an approximant of η-Cu_6Sn_5 - in the [11-20] zone axis for the top part (Figure 4.24b) and with rhombohedral η Cu_3Si, also in the [11-20] zone axis in hexagonal coordinates,[Wen, 2007] for the bottom part.

We thus conclude that the catalyst NP is essentially made, from top to bottom, of hexagonal Cu_6Sn_5 with, possibly, an *a*-Sn shell, and at the bottom, feeding the SiNW growth, of a modified hexagonal cell of η-Cu_3Si. Quite remarkably, the three crystalline parts: 1) Cu_6Sn_5, 2) Cu_3Si, 3) SiNW are epitaxially related: the two formers have their hexagonal base in common, the Si NW has developed its (111) planes parallel to these bases, with <112> axes parallel to the hexagonal <1-100> axes of the catalyst. Considering the actual deformation of the present Cu_3Si cell, the in-plane mismatch between that cell and the cubic Si cell is of the order of 10%; it appears to be fully relaxed.

According to the Sn-Cu binary phase diagram [Furtauer, 2013], solid Cu_6Sn_5 is stable below 408 °C. Therefore, Cu_6Sn_5 is unlikely to present at SiNW growth temperature and we assume that it has formed during the cooling down process.

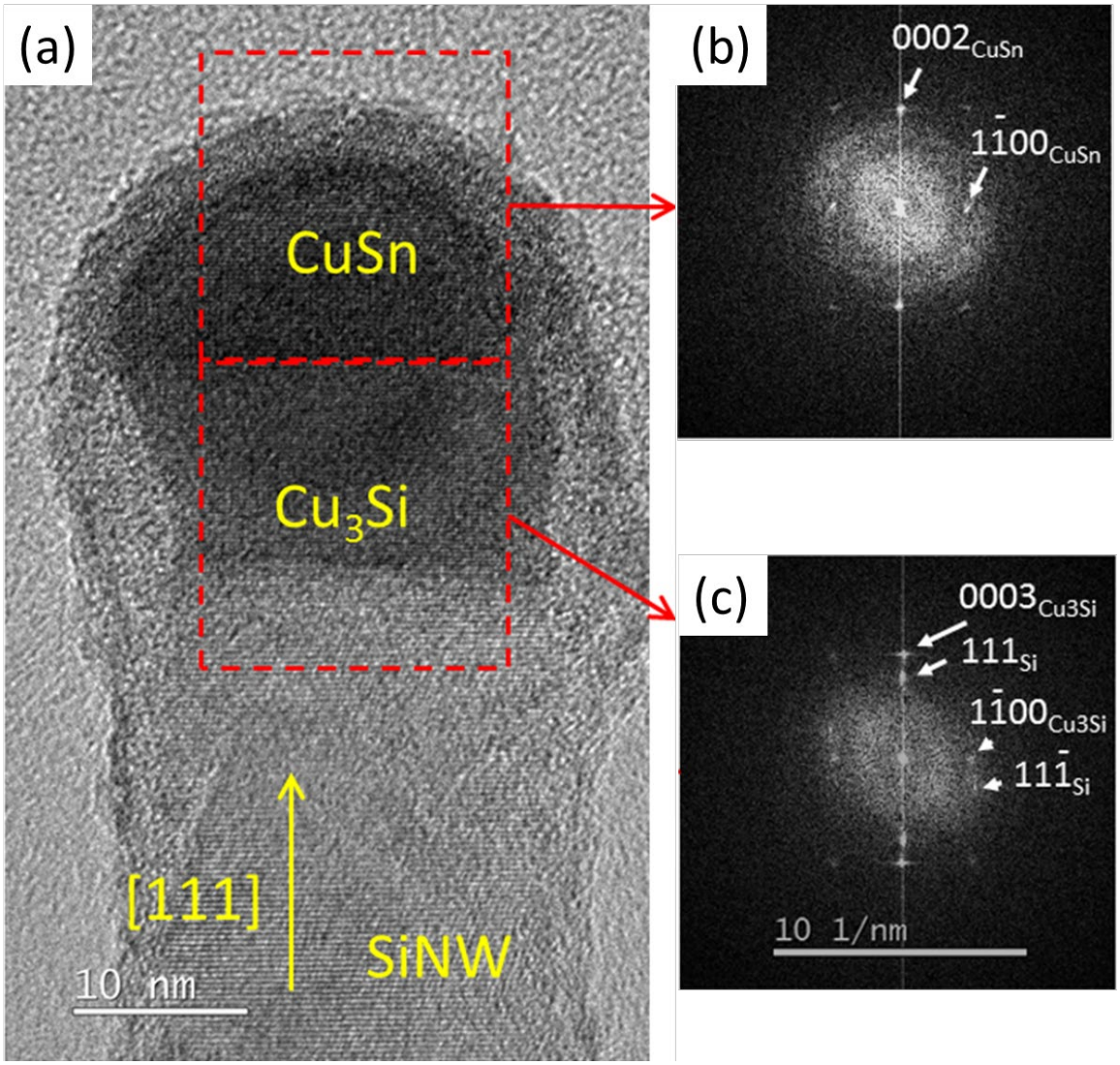

Figure 4.24. (a) High-magnification HRTEM image of the catalyst NP in Figure 4.22; (b) and (c) are the FFTs of the square areas in (a).

Detailed EDX mapping was performed on another similar SiNW and the results are shown in Figure 4.25. Four detected elements are shown: Si, O, Cu and Sn. Silicon is distributed mainly in the NW body, but extends to the catalyst NP. Oxygen is present in the whole NW, with a higher count in the catalyst NP, implying that the NW surface is oxidized and formed a thin layer in the air after the PECVD experiment. Most interestingly, Cu and Sn have different distributions in the catalyst NP. Cu appears in most parts of

the NP, whereas Sn is mostly detected on the top half part of the particle. Moreover, residual Sn is also found in the NW, indicating that there are Sn atoms distributed in the volume or at the surface of SiNW. Whereas the signal of Cu in the NW is weaker than that of Sn (basically on the background level), which is due to Cu mainly distributed as a part of Cu_3Si crystal in the catalyst. This result confirms our assumption based on the previous HRTEM observation: the co-catalyst particle is mostly crystalline Cu_3Si, and the darker top of the NP (amorphous structure) is a Sn-rich shell.

In order to confirm the position of Sn in catalyst NPs of the majority Cu deposit, presented in Figure 4.24, we performed EDX mapping on a similar SiNW from the same deposit (Figure 4.25). Cu appears in most parts of the NP, whereas Sn is mostly detected in its top half part. We quantified the elemental composition of the whole nanoparticle area in the EDX map and obtained Cu and Sn with atomic fractions of 63.8 % and 36.2 %, respectively. It is very close to the nominal atomic ratio of the thermally evaporated materials (65 at.% Cu and 35 at.% Sn). This result shows that *i*) the deposits remain uniform at the particle level – at least for this size of particle – and *ii*) there is no catalyst leak during the NW growth. Considering the position of Sn in the particle and its very low amount in the bottom part, together with the presence of Si and Cu in the bottom part, it indeed supports the existence of a Cu-silicide. Moreover, the fact that the Sn curve (brown-yellow, Figure 4.25b) has a higher intensity than either Cu or Si at the very top of the catalyst indicates that the amorphous structure at the top of the NP in Figure 4.24a is indeed Sn-rich. The oxygen appearing in the catalyst (O-K image in Figure 4.25a) would come from a Si-oxide that develops in the air after the NW growth. We finally conclude that, after NW growth, the catalyst NPs obtained with 65 at% of Cu in the deposit are essentially made of crystalline Cu_6Sn_5 and Cu_3Si, which would be solid at the growth temperature [Song, 2015] [Olesinski, 1986], with a Sn-rich part, most probably liquid at the growth temperature (eutectic temperature of the Sn-Si system is 227 °C) [Olesinski, 1984].

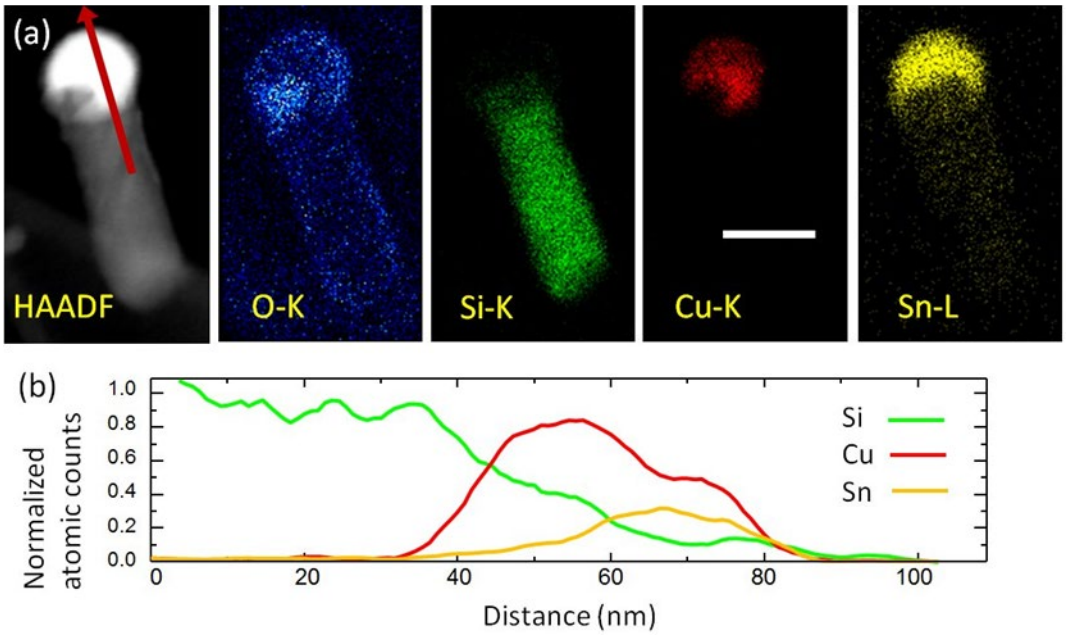

Figure 4.25. EDX mapping analysis of a SiNW synthesized with 1 nm Sn/0.8 nm Cu bimetallic catalyst (65 at. % Cu). (a) HAADF image and maps of the elements, scale bar 50 nm; the contrasts of O-K and Sn-L images have been enhanced, compared to Si-K and Cu-K, for the sake of visibility. b) Normalized atomic profiles of Si, Cu and Sn along the red arrow in (a). Note the segregation between Sn and Cu in the catalyst.

The quantified element composition of the mapped area in Figure 4.25 gives Cu and Sn with atomic fractions of 63.8% and 36.2% respectively, very close to the calculated nominal atomic ratio of the thermal evaporated 1 nm Sn/0.8 nm Cu (65% Cu and 35% Sn).

In the following analysis, we have selected four different areas of the SiNW as shown in Figure 4.26, to acquire the element compositions of the selected areas using software Inca. The atomic fractions of the detected elements in the selected areas are shown in Table 4.3. In area 1 at the top part of the catalyst particle, where Sn is most abundant compared with other areas, the atomic ratios of Sn and Cu were 16.2% and 28.7 %, respectively. In area 2, the bottom part of the particle, there is nine times more Cu than Sn. Area 3 is mainly an oxide considering the detected dominant atomic fraction of O. In Area 4, although there

is very small content of Cu and Sn detected, according to the EDX spectrum of this area there are both peaks of Cu and Sn (see Figure 4.27), which come from the slow catalyst consumption during the growth.

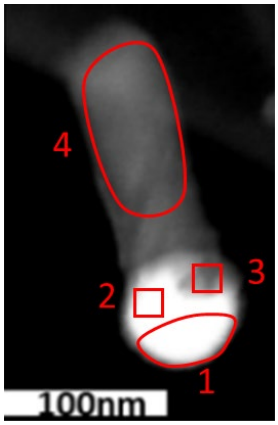

Figure 4.26. Four selected areas of the SiNW in Figure 4.25 for further element analysis.

Table 4.3. Element compositions of selected areas of the SiNW in Figure 4.26.

Atomic%	1	2	3	4
O K	32.4	22.5	62.9	19.0
Si K	22.7	41.2	21.9	79.6
Cu K	28.7	32.7	7.9	0.41
Sn L	16.2	3.6	7.4	1.03

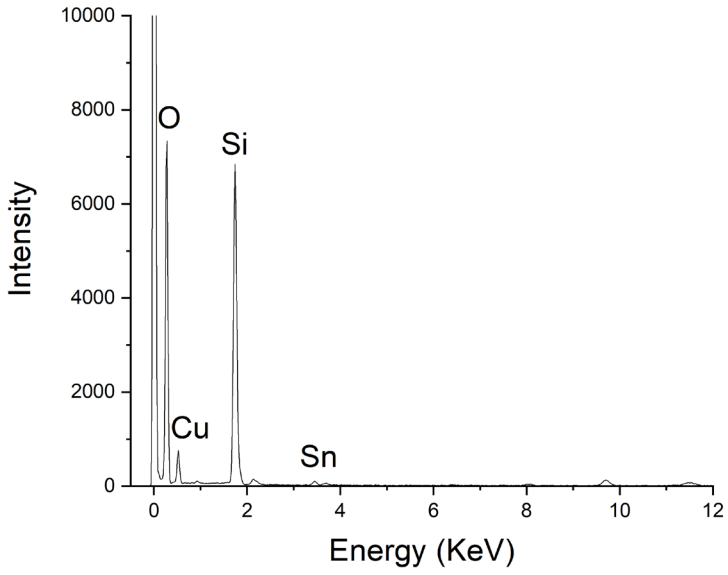

Figure 4.27. Spectrum of area 4 in Figure 4.26.

To summarize, SiNWs were grown on (100) Si substrates using a co-catalyst of 1 nm Sn/0.8 nm Cu following the typical PECVD conditions used in this thesis. The SiNWs were transferred to gold grids for TEM and EDX characterization. The observed SiNWs had diameters from 10 nm to 36 nm. Most of the co-catalyst NPs of the SiNWs were composed of a crystalline core of mostly Cu_3Si, with a small Cu-Sn shell located on the top part of the crystalline core of the NP.

4.3.2. **CuSn co-catalyst with a dominant amount of Sn**

In this sub-section, we study the crystalline structures of Sn-rich co-catalyst NPs after SiNW growth. The SiNWs synthesized with a co-catalyst of 1 nm Sn/0.2 nm Cu on the Si substrate were transferred to a gold grid and were observed using TEM Jeol 2010F. The observed SiNWs had diameters from 15 nm to 36 nm. A HRTEM image of a SiNW synthesized with the Sn-rich catalyst is shown in Figure 4.28. It has a diameter of 20 nm. The co-catalyst NP has a near-spherical shape and we did not observe any crystal facets. Most of the NP body has a dark contrast. There is no such feature as a planar boundary separating the co-catalyst NP into two parts with different shapes and contrasts like in Cu-rich co-catalyst NPs in Figure

4.24a. In that figure, the FFT image of a selected area in the SiNW, indicates that the latter has a diamond cubic structure.

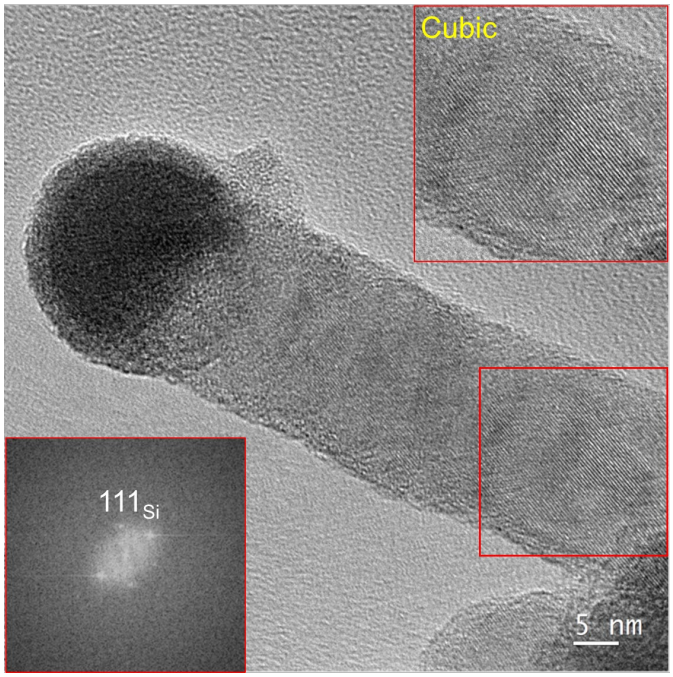

Figure 4.28. A SiNW with the cubic structure synthesized with the co-catalyst of 1 nm Sn/0.2 nm Cu.

Since the co-catalyst NP in Figure 4.28 above is not in the zone axis, we are not be able to know its crystalline structure. In another example of the co-catalyst NP in Figure 4.29a we are able to observe three groups of crystallographic planes. The NP has a spherical shape and there are some fringes on it. We have performed an FFT on the NP and the result is shown in Figure 4.29b. We find $d_1 = 0.24$ nm, and $d_2 = 0.21$ nm, which are commonly found in the Cu-rich co-catalyst in the previous sub-section 4.3.1. Most intense spot d_1 might be β-Sn (as a 220 spot), Cu_3Si (as a 009 spot); spot d_2 might be Cu (as a 111 spot); spot $d_3 = 0.29$ nm, could also signal the presence of β-Sn (as a 200 spot). Sn has a tetragonal phase at room temperature, i.e. β-Sn, and the lattice constants are a=b=0.58197 nm, c=0.31750 nm [Jeong, 2008b]. Figure 4.29a shows a HRTEM image of a SiNW synthesized with the majority-Sn catalyst. In this case, the catalyst NP has a near-spherical shape and there is also, although less visible, a planar boundary separating the catalyst NP into two regions. However, we find no fit with a silicide in this case, the top and bottom

parts having zone axes corresponding to Cu_6Sn_5 phases: the top part having the [5-78] zone axis of the monoclinic form of that compound (at equilibrium at room temperature) [Larsson, 1994a] and the bottom one that of the [1-100] zone axis of the same CuSn cell as above. Given the 69 at.% Sn and the Sn-Cu phase diagram [Song, 2015], some of Sn must have remained outside the crystalline compounds during the growth, thus liquid at that time. The thick amorphous layer around the crystalline catalyst is thus the remains of that liquid part. According to the analysis above, the NP of the Sn-rich catalyst consist essentially of crystalline Cu-Sn compounds and an amorphous shell.

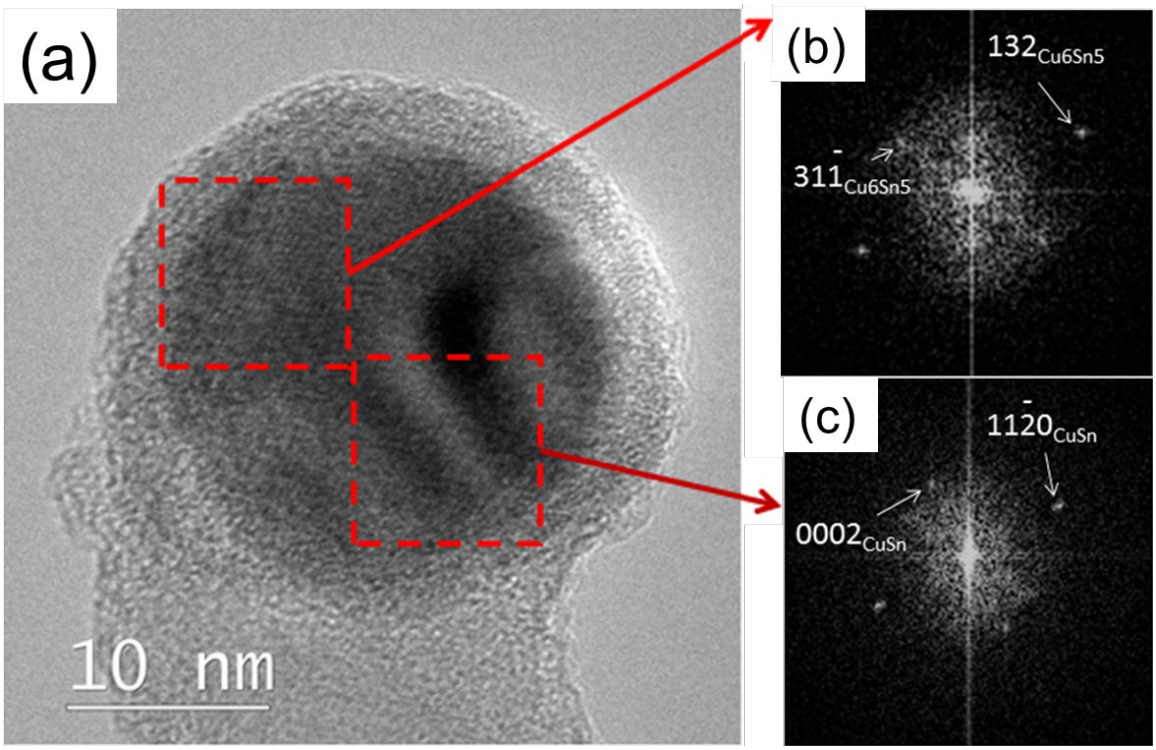

Figure 4.29. (a) Crystalline structure of a co-catalyst NP of 1 nm Sn/0.2 nm Cu; (b) and (c) are its FFT images.

4.3.3. **Summary of the observations, model of catalyst evolution**

We can now propose a mechanism for the catalyst formation and the catalyst evolution during the hydrogen plasma treatment and the NW growth (Figure 4.30). Let us recall that Cu and Sn are evaporated sequentially, so that Sn covers Cu at the beginning. With the temperature increasing in the PECVD reactor,

Cu would diffuse into Sn, rather than the opposite, as Cu has a high mobility and is the dominant diffusing species in the Cu-Sn system.[Tu, 2007a] However, its solubility in Sn being low (0.018% at eutectic temperature[Snugovsky, 2004]), it would not reach the concentration necessary for creating a new compound. After that, melting will occur when the substrate temperature reaches the melting temperature of the Cu-Sn eutectic (227 °C in the bulk probably below 200°C in the present small nanoparticles[Jeong, 2008a, Cui, 2009]). The rest of Cu would remain solid since bulk Cu has a high melting point of 1084.87 °C. After the hydrogen plasma treatment at 200 °C, Cu would crystallize and the Cu-Sn mixed catalyst NPs would consist of a Cu crystalline core and a Sn-rich, probably liquid, shell. When the temperature is increased to 416 °C for the NW growth, Cu-based compounds would form. When Si radicals from the plasma start introducing Si in the catalyst NPs, Cu_3Si would develop, rather than a Si-Sn compound, as the Si solubility in liquid Sn remains very low (< 0.25% [Olesinski, 1984]). The balance between Cu_6Sn_5 and Cu_3Si probably evolves upon cooling.[Ngo, 2021] Regarding the Cu_3Si, the epitaxy of Si and the presence of Sn would stabilize a modified unit cell with a *c*-axis having 1/3 of the normal *c*-axis of the (hexagonal) unit cell of rhombohedral η-Cu_3Si. The part of the catalyst NP where SiNW would develop would thus consist mostly of Cu_3Si. In the Sn-rich co-catalyst NPs, the Sn-rich shell would cover the crystalline core almost completely. Thus, we suggest that SiNW growth using a Cu-Sn bimetallic catalyst would actually be a liquid-assisted vapour-solid-solid (LAVSS) process. During the cooling process, after the NW growth, the molten Sn-rich alloy would solidify but keep the spherical shape. Tin finally appears as amorphous at room temperature.

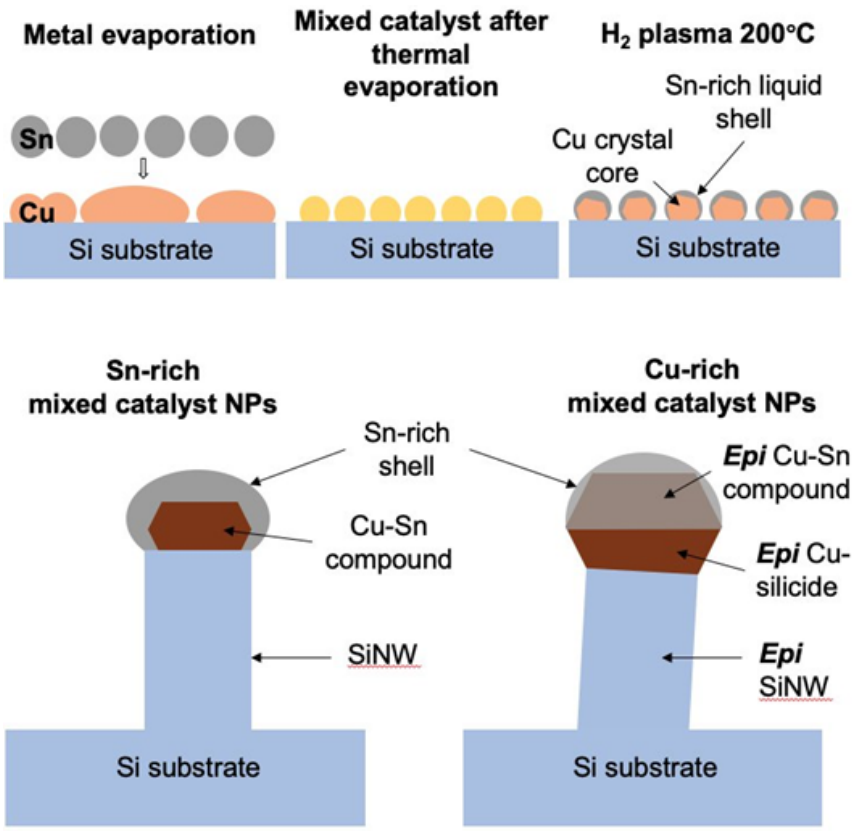

Figure 4.30. Schematic diagram of bimetallic Cu-Sn catalyst evolution at various stages of the SiNW growth process The two figures at the bottom highligth the case of a NW growth lead by a Sn-rich mixed catalyst NP (left) and a Cu-rich mixed catalyst NP (rigth).

With the data on mixed CuSn catalysts presented in this chapter, we may now discuss the effects of mixing Sn and Cu in catalysts, compared to the pure Sn and Cu cases. Let us first discuss the absence of NW growth with pure Cu (Chapter 4.2 and Figure 4.8). Cu has a high melting point (1084.87 °C for bulk Cu) and it can form a liquid eutectic alloy with Si only above 802 °C, which is high compared to our experimental conditions. It has been reported in the literature that the activation energy was 0.98 eV for SiNW growth with Cu catalyst in a CVD process, which is high compared with 0.68 eV in the case of using Au catalyst [Kalache, 2006]. The temperatures used in the literature for SiNW growth by the CVD method were in the range of 500-750 °C [Kalache, 2006, Arbiol, 2007, Yao, 2007, Arbiol, 2008]. At 500 °C, the SiNW nucleation times with Cu catalyst were around 2 minutes. In our PECVD experiment, when the

growth temperature is 416 °C, the incubation time for the pure Cu catalyst would be much longer. Even with the assistance of plasma, the diffusion of Si into solid Cu and formation of Cu_3Si was still difficult at such a low temperature. As a result, we did not obtain SiNWs under those conditions with pure Cu catalyst. Increasing the growth time to 6 minutes at the same temperature did not lead to SiNW growth either.

Let us now introduce the CuSn co-catalyst. When we use the CuSn mix instead of a pure Cu catalyst, the Cu crystal is surrounded by a liquid Sn-rich shell at 416 °C; the diffusion of Si atoms becomes a two-step process: the Si atoms firstly diffuse into the liquid shell and then into Cu crystal and form Cu_3Si with Cu. The NW growth thus follows a combined VLS-VSS mechanism. The existence of the liquid Cu-Sn eutectic shell allows SiNW growth after a very short incubation time. SiNWs with lengths around 30-40 nm were obtained after a 30-second growth at 416 °C (see Figure 4.31).

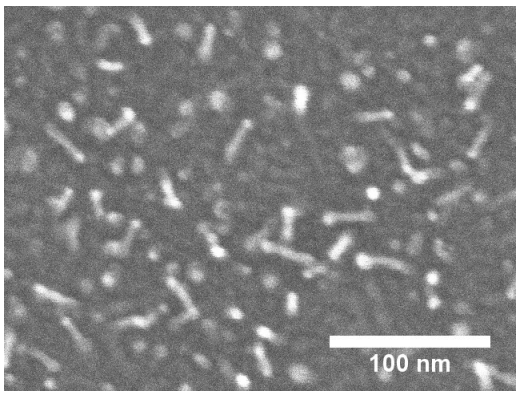

Figure 4.31. SiNWs synthesized with 0.1 nm Sn/0.1 nm Cu co-catalyst at 416 °C for 30 seconds.

Furthermore, compared to NW growth catalyzed by pure Sn, we have found that using a CuSn mix decreased the minimum growth temperature for SiNWs. When we used pure Sn catalyst, SiNWs could barely grow at 356 °C (the other parameters being those of the typical conditions), whereas we obtained dense and thin SiNWs using Cu-Sn co-catalyst at the same growth temperature (Figure 4.32a and b). At 327 °C, SiNWs did not grow using pure Sn catalyst under the circumstances; while Cu-Sn co-catalyst could still lead to SiNW growth, just with alower density and growth rate (Figure 4.32c). In brief, the effect of

the Cu-Sn co-catalyst NPs with the core-shell structures is decreasing the activation energy for SiNW growth, to reduce the incubation time, and to make it possible for NW growth at a lower temperature.

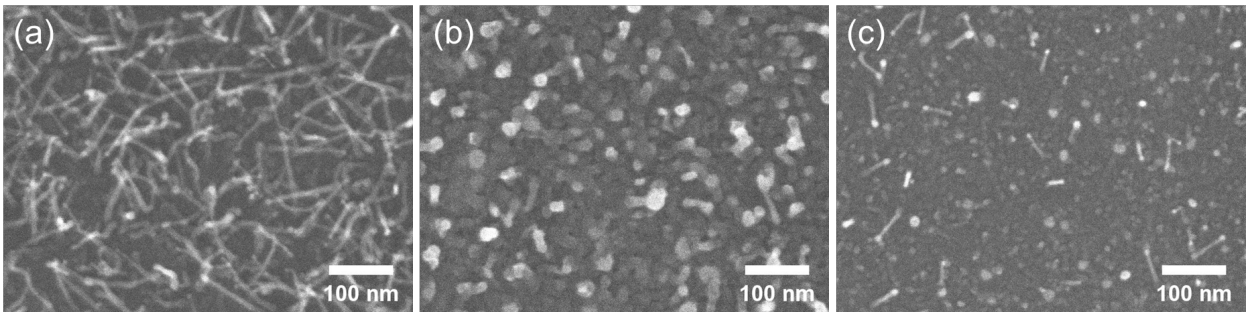

Figure 4.32. SEM images of SiNWs grown with (a) 0.1 nm Sn/0.1 nm Cu at 356 °C, (b) 1 nm Sn at 356 °C and (c) 0.1 nm Sn/0.1 nm Cu at 327 °C.

The discussion above provides new ideas when choosing the catalyst for NW growth. The choice of catalysts should not be only limited to pure metals. By using alloy catalysts, we can realize SiNW growth at a lower temperature, and adjust NW morphology and distribution. By alloying two certain metals, we can obtain a eutectic alloy which has a melting point lower than that of both two pure metals, which can break through the limitation on SiNW growth due to the melting temperatures of the metal-Si alloys, and bring new opportunities to decrease NW growth temperatures. Taking Sn alloy solders for example, although the decrease of melting temperature compared to Sn (232 °C) is small in the case of Sn-Cu (227 °C), it gets significant in the cases of Sn-Zn (198 °C) or Sn-Bi (139 °C) [Mei, 1992, Tu, 2001, Date, 2004, Dariavach, 2006], which is promising for SiNW growth at a lower temperature in comparison to the growth temperature when pure Sn catalyst is used. Moreover, using co-catalysts can modify the NW morphology in a way that cannot be achieved using pure metal catalysts. In our experiments, the SiNWs fabricated with Cu-Sn co-catalysts are much denser and thinner compared with the SiNWs catalyzed by pure Sn. In other respects, Lugstein *et al.* used a Ga-Au alloy catalyst for SiNW growth via CVD method [Lugstein, 2007]: in comparison to the pure gold catalyst, they obtained a much higher proportion of NWs growing perpendicular to the Si (111) substrate and the NWs showed almost no kinks; their average diameter was smaller, and the diameter and length distributions were narrowly dispersed. In brief, using

alloy co-catalyst for NW growth can bring extra benefits: decrease the growth temperature, improve the NW morphology and distribution, etc.

4.3.4. **Catalyst separation during SiNW growth**

In sub-section 4.3.1 and 4.3.2, we have discussed about structures of CuSn co-catalyst NPs during SiNW growth: a crystalline core with mostly Cu_3Si and a liquid Sn-rich shell, while the size of the Sn-rich shell depends on the proportion of Sn in the co-catalyst. However, we found that these catalyst structures have only been observed in large NPs ($\geq \varnothing$ 25 nm). In smaller co-catalyst NPs, we cannot observe the crystalline structure; more often we can find separated NPs, as shown in Figure 4.32. It is notable that the catalyst particle connected to the crystalline NW core is not at the end of the NW, there is an amorphous part above the crystalline core, on top of which lies another one or more catalyst particles. The length of the amorphous part can range from a few nanometers to tens of nanometers. In order to figure out the compositions of the separated catalyst NPs, it is necessary to make an EDX analysis.

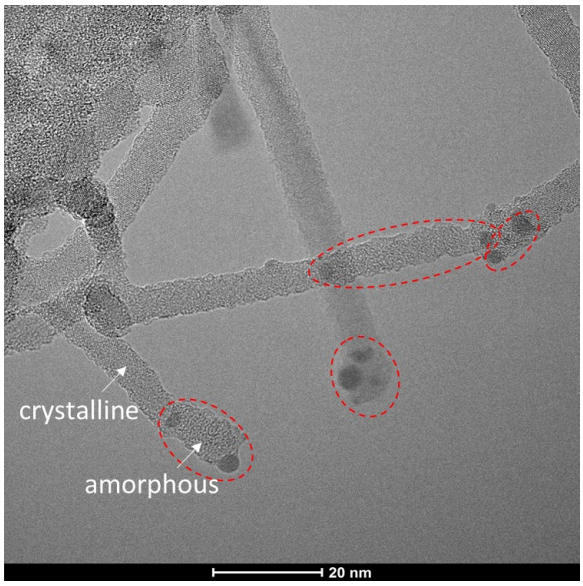

Figure 4.33. Catalyst separation phenomenon in thin SiNWs synthesized with 0.1 nm Sn/0.1 nm Cu under the typical PECVD conditions on carbon-coated Cu TEM grids.

We carried out EDX analysis on two separated catalyst NPs and the amorphous part between them, in the case of a thin SiNW grown with 0.1 nm Sn/0.1 nm Cu co-catalyst (Figure 4.34). In area 1, the catalyst NP in contact with the crystalline NW, O, Si and Cu are found. Cu has a strong signal. No trace of Sn is found in this catalyst NP. In area 2, the amorphous part, O and Si are mainly detected. The atomic ratio of O and Si is 9:4, close to the ratio in SiO_2. Therefore, it is reasonable to speculate that the part between the two catalyst NPs is SiO_2. The signals of Cu and Sn in this area are relatively low, just above the background noise. On the top particle of the NW in area 3, the presence of O, Si, Cu and Sn are confirmed. Putting aside the signals from Si and O, that are influenced by the proximity of the SiO_2, the atomic fraction of Cu and Sn in this area are 20 % and 80 % respectively. Thus, compared with area 1, Sn is present and the amount of Cu has drastically decreased.

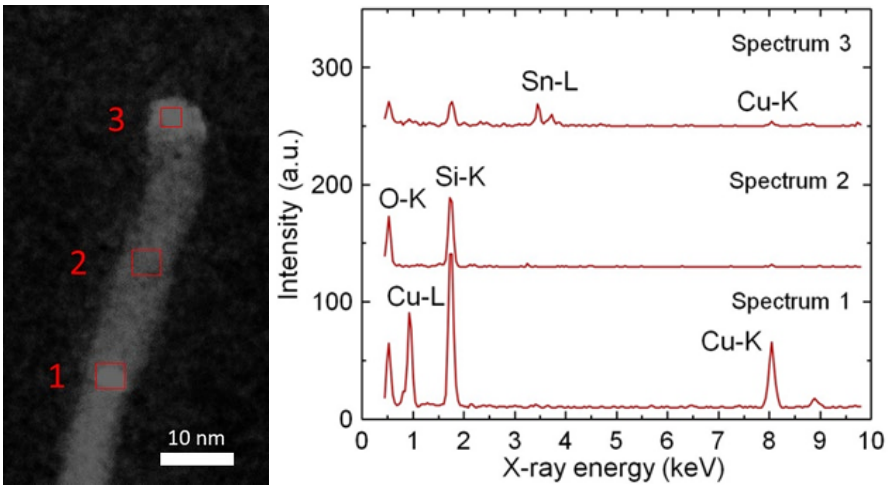

Figure 4.34. EDX analysis on a silica NW and a split catalyst. (a) STEM-HAADF image; (b) EDX spectra. Area and spectrum 1 correspond to the catalyst part that is connected to the SiNW, area and spectrum 2 to the amorphous part between the two catalyst NPs, and area and spectrum 3 to the top catalyst NP. The SiNW is synthesized with 0.1 nm Sn/0.1 nm Cu co-catalyst at the typical conditions.

To analyze the structure of the split parts of catalyst, we synthesized SiNWs with a larger amount of mixed catalyst (1 nm Sn/0.8 nm Cu – 65 at. % Cu); this allowed us to observe the structure of the crystalline particles in detail. The NW analyzed in Figure 4.35a has a diameter of 18 nm. The HRTEM image has been recorded in an orientation close to the [110] zone axis of Si. There are two catalyst NPs with darker contrasts on the top part of the NW. One catalyst NP is connected to the crystalline SiNW (green square in Figure 4.35a); the other catalyst NP is separated from the first one by about 5 nm of lighter-contrast matter (red square in Figure 4.35a). Figure 4.35b and c show the power spectra of the FFTs of the two selected areas. In both areas, we find 0.21-nm spots that are Cu 111 reflections (blue arrows).

In addition, in Figure 4.35b, a well-defined zone axis pattern also shows up. An examination of this pattern indicates that its orientation is parallel to the [1-12] SiNW axis, indicating an epitaxial relationship with the Si NW crystal and, thus, the fact that this particle was in contact with the Si crystal during growth. When fitting the whole zone pattern with JEMS, we find an equivalent excellent correspondence with either the [10-10] zone of the hexagonal compound Cu_6Sn_5, which has the NiAs structure [Zemann, 1965], or the

[102] zone of the monoclinic phase of that compound, stable below 188 °C [Bernal, 1928, Larsson, 1994b, Song, 2015], phases which we had also found in bigger wires with no silica NW on top [6]. We finally indexed the pattern in terms of the [102] zone of the latter. When looking closely, the spots at the corners of the pattern appear to include two components, the less intense ones, with slightly larger interplanar distances, belong to the zone axis above mentioned; the stronger ones, with an interplanar spacing a little shorter, are the 111_{Cu} spots mentioned in the first paragraph (in blue in the Figure); they belong to a [110] zone axis pattern of pure Cu. As we have shown elsewhere, the Cu_6Sn_5 compound actually develops, upon cooling after growth, in epitaxy with the Cu_3Si that is present during growth, the latter Cu is thus the remains (still in epitaxy) of the original Cu-silicide that has lost its Si to the benefit of the new SiO_2 NW.

In the NP connected to the crystalline SiNW (Figure 4.35c), the FFT indicates the presence of spots that do not belong to Cu. One characteristic spot, elongated due to the small extension of the crystal it comes from is the 0003 spot of a disordered variant of η-Cu_3Si. No crystalline structures of Sn or Sn-compounds have been observed in this part of the catalyst.

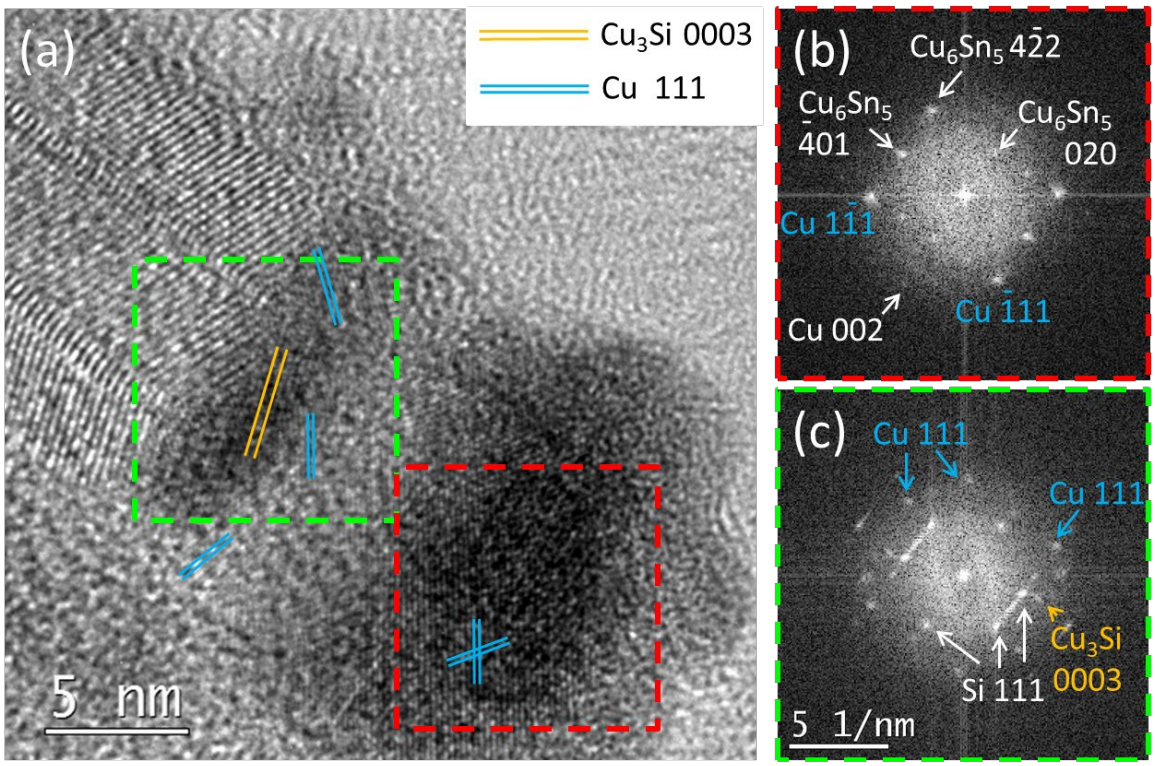

Figure 4.35. (a) HRTEM image of the top part of a SiNW and its FFT images (b) and (c).

Catalyst separation has also been observed in SiNWs with diameters as large as 24 nm (see Figure 4.36). The NW in Figure 4.35 was synthesized with the typical conditions using a co-catalyst of 1 nm Sn/0.8 nm Cu on Si substrates. The top catalyst NP is mostly composed of Cu_3Si, like many other Cu-rich co-catalyst NPs. In addition to Cu_3Si, some nanocrystals are also found in the catalyst NP. We make FFT of the selected areas, and found that those nanocrystals have an interplanar distance of 0.33 nm (Figure 4.36b and c). Since there only displays one crystallographic plane group, we cannot obtain more information about its structure. This distance can correspond to the planes of SiO_2 011 [Persson, 2014b], or SnO_2 110 [Busch, 1960]. It cannot be β-Sn or copper oxides, because the distance doesn't match with any planes of the two materials. If there is the possibility of Cu_6Sn_5 202 and 310, Cu_3Sn 011, or $Cu_{15}Si_4$ 022, because these interplanar distances are within 0.33±0.1 nm [Watanabe, 1983, Larsson, 1994b, Persson, 2014a], we tend to think that the most likely solution is that of an oxide. As Sn has disappeared in its metallic form,

and as the silicon native oxide generally occurs in amorphous form, the present oxide would thus be that of tin.

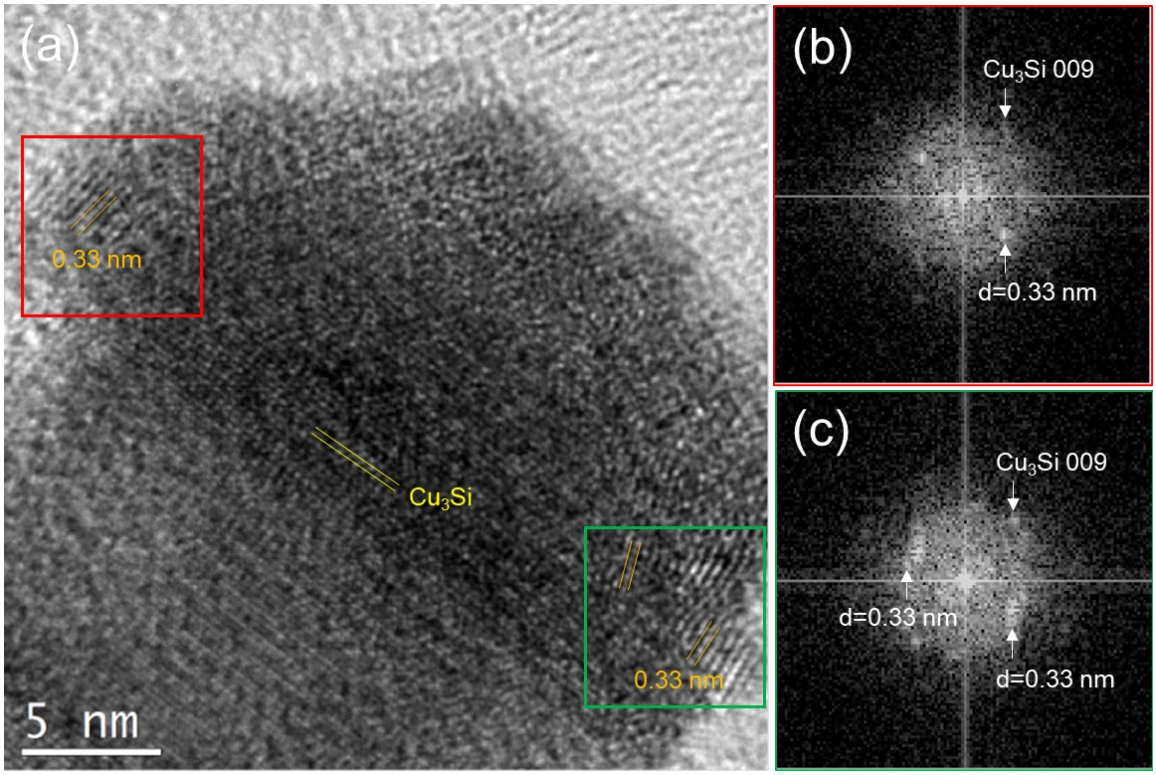

Figure 4.36. (a) HRTEM image of the top catalyst NP of a SiNW. (b) and (c) FFT images show presences of Cu_3Si 009 and nanocrystals with an interplanar distance of 0.33 nm, as indicated by yellow and orange lines in Figure (a).

Since such catalyst separation together with an amorphous part have never been observed in *in-situ* SiNW growth experiments in TEM using the same CuSn co-catalyst, or in an *in-situ* cooling down process, therefore, we assume that this happens after SiNW growth in the atmosphere. In order to confirm our assumption, after SiNW growth (with 0.1/0.1 nm Sn/Cu under the typical conditions), we deposited a thin layer of amorphous Si on SiNWs to "freeze" the original NW structure and protect the crystalline SiNWs and catalyst NPs from exposure to the air when the chamber was opened. Immediately after NW growth finished, we decreased the substrate temperature to 185 °C and deposited an amorphous silicon layer on the SiNWs for 30 seconds. The PECVD parameter we used in this process was: 10 sccm for SiH_4 flux, 0.17

mbar for gas pressure, and 1 W for RF power. Then we continued to cool down the substrate. When the temperature was below 160 °C, we opened the chamber. The SiNWs has been transferred from (100) Si substrate to a Cu grid for TEM observation.

We have observed the structures of 30 SiNWs, while none of them had separated catalyst NPs. A TEM image of one example of one SiNW with amorphous silicon layer is shown in Figure 4.37. The SiNW has a total diameter of 10 nm and the shell outside the NP has a thickness around 2 nm. In this NW, we only find one catalyst NP on top of it. We have observed the structures of 30 SiNWs, and none of them had separated catalyst NPs. Therefore, we can conclude that catalyst separation and the growth of the silica NW happen after SiNW growth in the ambient air.

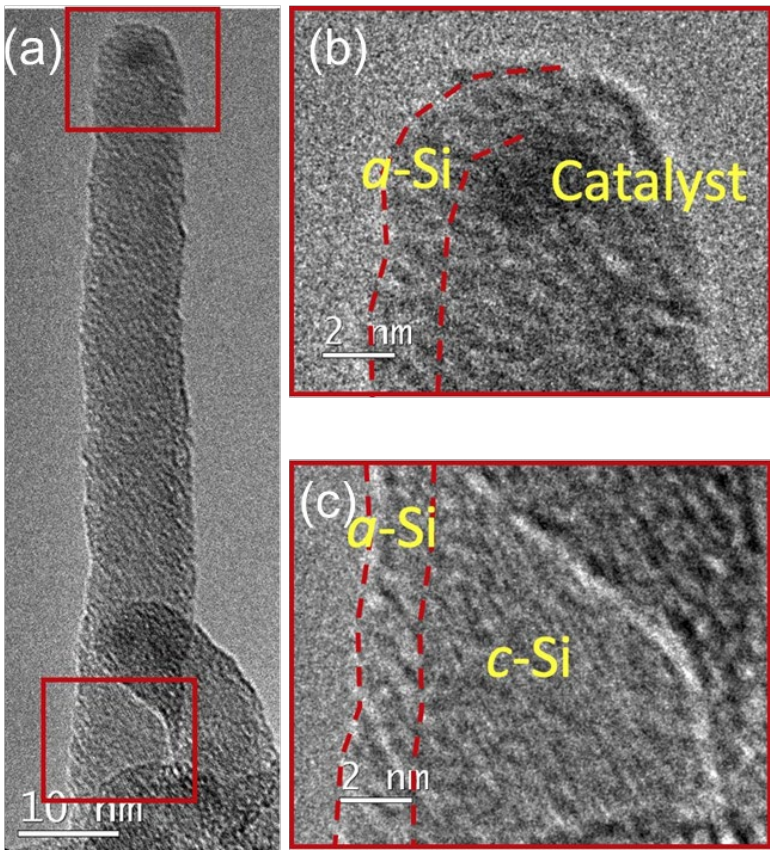

Figure 4.37. (a) TEM image of a SiNW with a thin layer of amorphous Si deposited immediately after NW growth. (b, c) Enlargements of the squared areas in (a) showing the *a*-Si layer around the catalyst (b) and the NW body (c) (the Si crystal planes in the NW, visible in (c), were not visible elsewhere).

Next, we discuss the possible formation of separated catalyst NPs in SiNWs with the help of data from the literature. As mentioned above, the catalyst separation and oxidation most likely happens after NW growth in the atmosphere. It has been demonstrated by several authors [Harper, 1990, Stolt, 1991, Lampe-Önnerud, 1992, Li, 1994, Huang, 2000] that Cu_3Si catalyzes the oxidation of (100) silicon at room temperature. It produces a layer of SiO_2 underneath the copper-rich surface layer [Harper, 1990, Stolt, 1991, Lampe-Önnerud, 1992, Li, 1994, Huang, 2000]. Harper *et al.* [Harper, 1990] have deposited thin films of Cu (100 nm) onto (100) Si (cleaned in HF) by sputtering, and heated the wafer above 200 °C to form Cu_3Si. A thick layer of SiO_2 formed under the copper-rich surface layer after exposure to air at room temperature for a few weeks. A schematic diagram of the overall oxidation process is shown in Figure 4.38 [Harper, 1990]. Oxygen reacts with Cu_3Si to form SiO_2 and Cu according to: $Cu_3Si + O_2 \rightarrow SiO_2 + 3Cu$. Then the Cu atoms released by oxidation of Cu_3Si diffuses through the silica layer steadily to the Si substrate and gives rise to the second reaction: $3Cu + Si \rightarrow Cu_3Si$. A TEM image (see Figure 4.39) shows particles of Cu_3Si epitaxially oriented relative to the substrate Si, which is a proof of the reactions above. As long as oxygen is supplied to the Cu_3Si nanoparticles at the SiO_2/Si interface, Cu_3Si can react with oxygen again to form SiO_2 and Cu, then Cu atoms diffuse through silica to react with Si. In this way this sequence may continue catalytically to form a thick SiO_2 layer. It has not been determined how oxygen is supplied to the buried interface for the continued formation of SiO_2. There may be channels or filamentary paths in the SiO_2 layer connecting the upper Cu-rich layer to the buried interface.

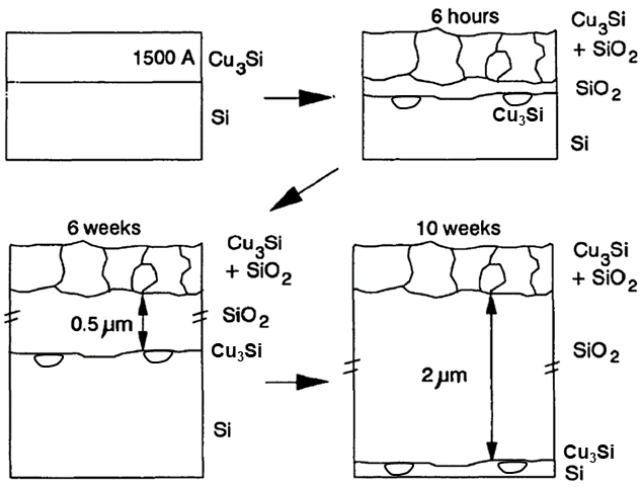

Figure 4.38. Schematic diagram of the catalytic oxidation of (100) silicon by Cu_3Si at room temperature [Harper, 1990].

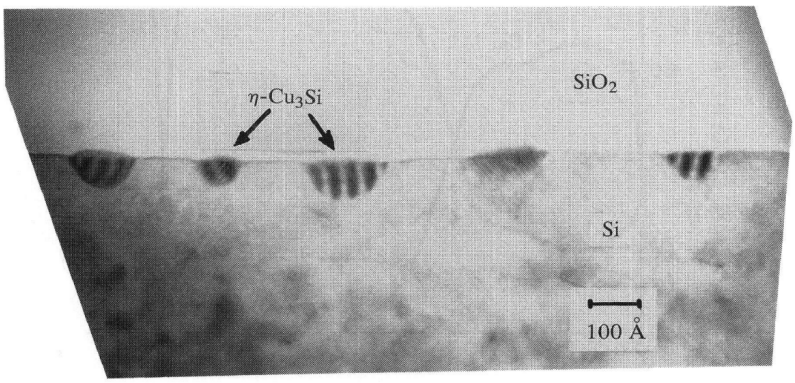

Figure 4.39. High-resolution cross-sectional TEM of interface between SiO_2 layer and substrate Si, viewed along <110> zone axis, showing Cu_3Si particles at the interface [Harper, 1990].

Figure 4.40 shows a schematic of the reactions that occurred in air after SiNW growth and of the formation of separated catalyst NPs. The entire process would be: Cu_3Si first reacts with oxygen to form SiO_2 and Cu. Then the Cu atoms released by oxidation of Cu_3Si would move towards the SiNW through SiO_2 and react with Si to form new Cu_3Si. Figure 4.40 summarizes the reactions that occur in the SiNWs in the air after PECVD growth. We have shown that, during SiNW growth, the mixed Sn-Cu catalyst NPs consist of a crystalline core of Cu_3Si and a Sn-rich shell. The SiNWs grown with the current PECVD conditions mostly have single crystalline structure (Figure 4.40a). When the reactor chamber is open and

the NWs are exposed to the air, Cu_3Si in the catalyst first reacts with oxygen to form SiO_2 and Cu: $Cu_3Si + O_2 \rightarrow SiO_2 + 3\ Cu$. It produces a layer of SiO_2 between the catalyst NP and the crystalline SiNW (Figure 4.40b). Then the Cu atoms released by oxidation of Cu_3Si diffuse through the SiO_2 to the SiNW (Figure 4.40c) and give rise to the second reaction: $3\ Cu + Si \rightarrow Cu_3Si$ (Figure 4.40d). The Cu and Cu-silicide crystals found at the interface with the Si NW have different orientations (see Figure 4.35), and the Cu_6Sn_5 planes of the top NP are always found perpendicular to the growth direction of the SiNWs (Figure 4.35); this shows that the latter are the remnants of the original catalyst, active during growth, while the former have developed afterwards. In addition, no Sn has ever been found in these parts at the interface with the SiNW. Therefore, we think that the Cu silicide nanocrystals connected to the crystalline NW core have formed due to the reaction of Cu and Si after the growth.

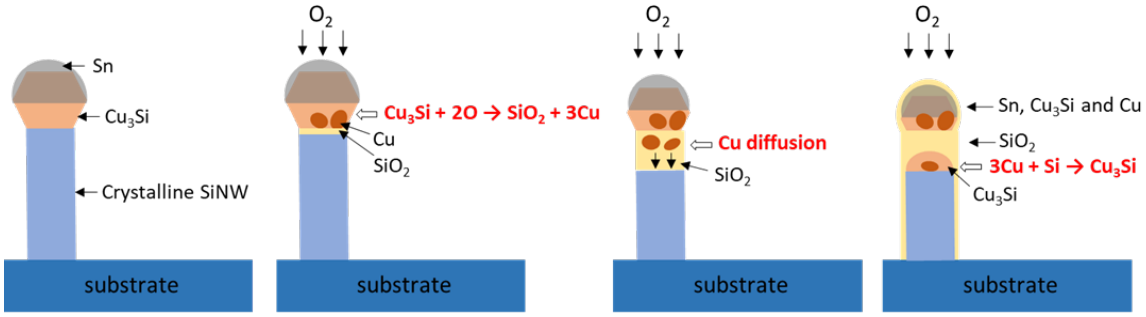

Figure 4.40. Schematic diagram of formation of separated catalyst NPs in thin SiNWs.

However, this reaction sequence does not continue catalytically until the whole SiNW is consumed and has become a NW of SiO_2. One may assume that it stops when the Cu_3Si particles become small and buried in SiO_2. In other respect, this reaction does not seem to occur in thick nanowires; the explanation could be related to the fact that, to feed the production of SiO_2, oxygen from the air must diffuse through the interface between Cu_3Si and the existing SiO_2, down to the middle of the wire, over a distance worth a wire radius. That distance of would just become too large in thick wires.

4.4. **Chapter conclusions**

In this chapter, firstly, we have studied the crystalline structure of SiNWs fabricated with pure Sn catalyst on (100) Si wafers. The SiNWs had larger averaged diameters than the SiNWs with hexagonal phase grown on Cu grids reported in the publication of J. Tang *et.al*. We only found cubic phase SiNWs by TEM observation. As a result, we decided to use a mixed catalyst of Cu and Sn instead of pure Sn for SiNW growth. By evaporating firstly Cu on crystalline Si substrates then Sn on top of Cu, we obtained smaller catalyst NPs than pure with Sn and pure Cu. SiNWs synthesized with CuSn mixed catalyst had a bi-modal distribution in diameters: both thin NWs (in which we are interested for the exploration of hexagonal Si phase) and thick NWs existed at the same time. As a contrast, pure Cu did not lead to SiNW growth under the current PECVD conditions.

Next, we made CuSn mixed catalyst NPs and studied the evolution of the NPs, during each step of PECVD experiment, by SEM and TEM characterizations. As-deposited CuSn catalyst NPs were amorphous. As Cu has a high mobility and is the dominant diffusing species in the Cu-Sn system, Cu firstly diffused into Sn during the hydrogen plasma treatment at 200°C prior to the PECVD experiment. After that treatment, the NPs had a core-shell structure, which consisted of a Cu crystal core and a Sn-rich shell. We checked that annealing at 200 °C without hydrogen plasma could barely make Cu crystallize. With substrate temperature increasing during hydrogen plasma treatment, the Cu-Sn eutectic alloy probably melted and co-catalyst NPs became larger and less dense. A second hydrogen plasma treatment at growth temperature led to even larger co-catalyst NPs. During SiNW growth, the co-catalyst NPs were composed of a crystalline core with mostly Cu_3Si and a liquid Sn-rich shell. The size of the liquid shell depended on the composition in the co-catalyst, if Cu was dominant, the liquid shell would only cover a small area on top of Cu_3Si crystal; if Sn was dominant, the liquid shell can cover almost the entire Cu_3Si crystal. The NW growth followed a combined VLS-VSS mechanism. The liquid Cu-Sn eutectic with a low melting temperature seem to play a preeminent role in this process, allowing SiNW growth after a very short incubation time.

We also found that the co-catalyst NPs appeared to be physically more stable than the pure Sn catalysts and always stayed on top of the SiNWs. We explain this by the presence of Cu in the catalyst: the Cu core remains solid during NW growth, thus it is stable on the NW. As Sn has an affinity with Cu; it can wet the Cu catalyst NP. As a result, Sn is preserved as a shell around the Cu core. In the case of pure Sn catalyst droplets, due to their low surface tension and higher mobility compared with solid catalysts, they easily fall down and form small droplets on the sidewalls of the SiNWs.

In the case SiNWs with diameter smaller than 24 nm, of particular interest in this work, we observed a separation phenomenon: the catalyst particle that should be connected to the crystalline NW core is not at the end of the NW, an amorphous silicon oxide has developed above the crystalline core, on top of which lies another one or more catalyst particles. This is most probably caused by the oxidation of Cu_3Si at room temperature in the air after growth.

Using a CuSn co-catalyst for SiNW growth is interesting to us for the purpose of exploring conditions for hexagonal SiNWs since it can bring about growth of thin SiNWs. Using alloy catalysts brings new opportunities for SiNW growth to decrease the growth temperature, to improve the NW morphology and distribution, etc.

References

Arbiol, J., A. Fontcuberta i Morral, S. Estradé, F. Peiró, B. Kalache, P. Roca i Cabarrocas, and J.R. Morante, *Influence of the (111) twinning on the formation of diamond cubic/diamond hexagonal heterostructures in Cu-catalyzed Si nanowires.* Journal of Applied Physics, 2008. **104**(6): p. 064312. https://doi.org/10.1063/1.2976338

Arbiol, J., B. Kalache, P.R.i. Cabarrocas, J.R. Morante, and A.F.i. Morral, *Influence of Cu as a catalyst on the properties of silicon nanowires synthesized by the vapour–solid–solid mechanism.* Nanotechnology, 2007. **18**(30): p. 305606. https://doi.org/10.1088/0957-4484/18/30/305606

Bernal, J.D., *The Complex Structure of the Copper–Tin Intermetallic Compounds.* Nature, 1928. **122**(3063): p. 54-54. https://doi.org/10.1038/122054a0

Brooks, P.L. and E. Gillam, *The ϵ-phase in the Cu Sn system.* Acta Metallurgica, 1970. **18**(11): p. 1181-1185. https://doi.org/10.1016/0001-6160(70)90108-2

Busch, G.A. and R. Kebn, *Semiconducting Properties of Gray Tin*, in *Solid State Physics*, F. Seitz and D. Turnbull, Editors. 1960, Academic Press. p. 1-40. https://doi.org/10.1016/s0081-1947(08)60166-6

Chen, W.T., C.E. Ho, and C.R. Kao, *Effect of Cu concentration on the interfacial reactions between Ni and Sn–Cu solders.* Journal of Materials Research, 2011b. **17**(2): p. 263-266. https://doi.org/10.1557/jmr.2002.0036

Cui, Q., F. Gao, S. Mukherjee, and Z. Gu, *Joining and interconnect formation of nanowires and carbon nanotubes for nanoelectronics and nanosystems.* Small, 2009. **5**(11): p. 1246-57. https://doi.org/10.1002/smll.200801551

Dariavach, N., P. Callahan, J. Liang, and R. Fournelle, *Intermetallic growth kinetics for Sn-Ag, Sn-Cu, and Sn-Ag-Cu lead-free solders on Cu, Ni, and Fe-42Ni substrates.* Journal of Electronic Materials, 2006. **35**(7): p. 1581-1592. https://doi.org/10.1007/s11664-006-0152-7

Date, M., T. Shoji, M. Fujiyoshi, K. Sato, and K.N. Tu, *Ductile-to-brittle transition in Sn–Zn solder joints measured by impact test.* Scripta Materialia, 2004. **51**(7): p. 641-645. https://doi.org/10.1016/j.scriptamat.2004.06.027

Furtauer, S., D. Li, D. Cupid, and H. Flandorfer, *The Cu-Sn phase diagram, Part I: New experimental results.* Intermetallics (Barking), 2013. **34**: p. 142-147. https://doi.org/10.1016/j.intermet.2012.10.004

Harper, J.M.E., A. Charai, L. Stolt, F.M. d'Heurle, and P.M. Fryer, *Room-temperature oxidation of silicon catalyzed by Cu3Si.* Applied Physics Letters, 1990. **56**(25): p. 2519-2521. https://doi.org/10.1063/1.103260

Huang, H.Y. and L.J. Chen, *Growth kinetics of SiO2 on (001) Si catalyzed by Cu3Si at elevated temperatures.* Journal of Applied Physics, 2000. **88**(3): p. 1412-1417. https://doi.org/10.1063/1.373832

Jeong, S., K. Woo, D. Kim, S. Lim, J.S. Kim, H. Shin, Y. Xia, and J. Moon, *Controlling the Thickness of the Surface Oxide Layer on Cu Nanoparticles for the Fabrication of Conductive Structures by Ink-Jet Printing.* Advanced Functional Materials, 2008a. **18**(5): p. 679-686. https://doi.org/https://doi.org/10.1002/adfm.200700902

Jeong, S., K. Woo, D. Kim, S. Lim, J.S. Kim, H. Shin, Y. Xia, and J. Moon, *Cover Picture: Controlling the Thickness of the Surface Oxide Layer on Cu Nanoparticles for the Fabrication of Conductive Structures by Ink-Jet Printing (Adv. Funct. Mater. 5/2008).* Advanced Functional Materials, 2008b. **18**(5): p. NA-NA. https://doi.org/10.1002/adfm.200890021

Jo, Y.H., J.C. Park, J.U. Bang, H. Song, and H.M. Lee, *New synthesis approach for low temperature bimetallic nanoparticles: size and composition controlled Sn-Cu nanoparticles.* J Nanosci Nanotechnol, 2011. **11**(2): p. 1037-41. https://doi.org/10.1166/jnn.2011.3052

Kalache, B., P.R.i. Cabarrocas, and A.F.i. Morral, *Observation of Incubation Times in the Nucleation of Silicon Nanowires Obtained by the Vapor-Liquid-Solid Method.* Japanese Journal of Applied Physics, 2006. **45**(No. 7): p. L190-L193. https://doi.org/10.1143/jjap.45.L190

Lai, S.L., J.Y. Guo, V.V. Petrova, G. Ramanath, and L.H. Allen, *Size-Dependent Melting Properties of Small Tin Particles: Nanocalorimetric Measurements.* Phys Rev Lett, 1996. **77**(1): p. 99-102. https://doi.org/10.1103/PhysRevLett.77.99

Lampe-Önnerud, C., U. Jansson, A. Hårsta, and J.-O. Carlsson, *Chemical vapour deposition of copper on Si(111) and SiO2 substrates.* Journal of Crystal Growth, 1992. **121**(1-2): p. 223-234. https://doi.org/10.1016/0022-0248(92)90191-k

Larsson, A.-K., L. Stenberg, and S. Lidin, *The superstructure of domain-twinned [eta]'-Cu6Sn5.* Acta Crystallographica Section B, 1994a. **50**(6): p. 636-643. https://doi.org/doi:10.1107/S0108768194004052

Larsson, A.K., L. Stenberg, and S. Lidin, *The superstructure of domain-twinned η'-Cu6Sn5.* Acta Crystallographica Section B Structural Science, 1994b. **50**(6): p. 636-643. https://doi.org/10.1107/s0108768194004052

Lee, S.-Y., K.-Y. Park, W.-S. Kim, S. Yoon, S.-H. Hong, K. Kang, and M. Kim, *Unveiling origin of additional capacity of SnO2 anode in lithium-ion batteries by realistic ex situ TEM analysis.* Nano Energy, 2016. **19**: p. 234-245. https://doi.org/10.1016/j.nanoen.2015.10.026

Li, J., D. Adams, S.W. Russell, T.L. Alford, and J.W. Mayer, *Room temperature oxidation of silicon in the Cu3Si/Si structure*, in *Control of Semiconductor Interfaces*, I. Ohdomari, M. Oshima, and A. Hiraki, Editors. 1994, Elsevier: Amsterdam. p. 217-220. https://doi.org/10.1016/b978-0-444-81889-8.50041-9

Lugstein, A., M. Steinmair, Y.J. Hyun, E. Bertagnolli, and P. Pongratz, *Ga ⁄ Au alloy catalyst for single crystal silicon-nanowire epitaxy.* Applied Physics Letters, 2007. **90**(2): p. 023109. https://doi.org/10.1063/1.2431468

Mei, Z. and J.W. Morris, *Characterization of eutectic Sn-Bi solder joints.* Journal of Electronic Materials, 1992. **21**(6): p. 599-607. https://doi.org/10.1007/bf02655427

Nellist, P.D. and S.J. Pennycook, *The principles and interpretation of annular dark-field Z-contrast imaging*, in *Advances in Imaging and Electron Physics*, P.W. Hawkes, Editor. 2000, Elsevier. p. 147-203. https://doi.org/10.1016/s1076-5670(00)80013-0

Ngo, É., W. Wang, P. Bulkin, I. Florea, M. Foldyna, P. Roca i Cabarrocas, and J.-L. Maurice, *New silicon nanowire growth mode revealed by in situ TEM when using Cu-Sn bimetallic catalysts.* To be published, 2021.

Olesinski, R.W. and G.J. Abbaschian, *The Si−Sn (Silicon−Tin) system.* Bulletin of Alloy Phase Diagrams, 1984. **5**(3): p. 273-276. https://doi.org/10.1007/bf02868552

Olesinski, R.W. and G.J. Abbaschian, *The Cu−Si (Copper-Silicon) system.* Bulletin of Alloy Phase Diagrams, 1986. **7**(2): p. 170-178. https://doi.org/10.1007/BF02881559

Peplinski, B., G. Schulz, D. Schultze, and E. Schierhorn, *Improved X-Ray Powder Diffraction Data for the Disordered η-Cu₆Sn₅ Alloy Phase.* Materials Science Forum, 1996. **228-231**: p. 577-582. https://doi.org/10.4028/www.scientific.net/MSF.228-231.577

Persson, K., *Materials Data on Si4Cu15 (SG:220) by Materials Project*. 2014a: United States. https://doi.org/10.17188/1190588

Persson, K., *Materials Data on SiO2 (SG:154) by Materials Project*. 2014b: United States. https://doi.org/10.17188/1272701

Sanabria, C., M. Field, P.J. Lee, H. Miao, J. Parrell, and D.C. Larbalestier, *Controlling Cu–Sn mixing so as to enable higher critical current densities in RRP®Nb3Sn wires.* Superconductor Science and Technology, 2018. **31**(6): p. 064001. https://doi.org/10.1088/1361-6668/aab8dd

Shang, P., Z. Liu, D. Li, and J. Shang, *Directional growth of Cu3Sn at the reactive interface between eutectic SnBi solder and (100) single crystal Cu.* Scripta Materialia, 2008. **59**(3): p. 317-320. https://doi.org/10.1016/j.scriptamat.2008.03.031

Shang, P.J., Z.Q. Liu, D.X. Li, and J.K. Shang, *TEM Observations of the Growth of Intermetallic Compounds at the SnBi/Cu Interface.* Journal of Electronic Materials, 2009. **38**(12): p. 2579-2584. https://doi.org/10.1007/s11664-009-0894-0

Snugovsky, L., C. Cermignani, D.D. Perovic, and J.W. Rutter, *The solid solubility of Ag and Cu in the Sn phase of eutectic and near-eutectic Sn-Ag-Cu solder alloys.* Journal of Electronic Materials, 2004. **33**(11): p. 1313-1315. https://doi.org/10.1007/s11664-004-0159-x

Song, Y., X. Su, Y. Liu, H. Peng, C. Wu, and J. Wang, *Phase Equilibria of the Cu-Si-Sn System at 700 and 500 °C.* Journal of Phase Equilibria and Diffusion, 2015. **36**(5): p. 493-502. https://doi.org/10.1007/s11669-015-0405-3

Stolt, L., A. Charai, F.M. D'Heurle, P.M. Fryer, and J.M.E. Harper, *Formation of Cu3Si and its catalytic effect on silicon oxidation at room temperature.* Journal of Vacuum Science & Technology A: Vacuum, Surfaces, and Films, 1991. **9**(3): p. 1501-1505. https://doi.org/10.1116/1.577653

Suh, I.-K., H. Ohta, and Y. Waseda, *High-temperature thermal expansion of six metallic elements measured by dilatation method and X-ray diffraction.* Journal of Materials Science, 1988. **23**(2): p. 757-760. https://doi.org/10.1007/bf01174717

Svintsitskiy, D.A., T.Y. Kardash, O.A. Stonkus, E.M. Slavinskaya, A.I. Stadnichenko, S.V. Koscheev, A.P. Chupakhin, and A.I. Boronin, *In Situ XRD, XPS, TEM, and TPR Study of Highly Active in CO Oxidation CuO Nanopowders.* The Journal of Physical Chemistry C, 2013. **117**(28): p. 14588-14599. https://doi.org/10.1021/jp403339r

Tang, J., J.L. Maurice, F. Fossard, I. Florea, W. Chen, E.V. Johnson, M. Foldyna, L. Yu, and I.C.P. Roca, *Natural occurrence of the diamond hexagonal structure in silicon nanowires grown by a plasma-assisted vapour-liquid-solid method.* Nanoscale, 2017b. **9**(24): p. 8113-8118. https://doi.org/10.1039/c7nr01299c

Tu, K.-N., *Copper–Tin Reactions in Bulk Samples*, in *Solder Joint Technology: Materials, Properties, and Reliability*. 2007a, Springer New York: New York, NY. p. 37-71. https://doi.org/10.1007/978-0-387-38892-2_2

Tu, K.-N., *Copper–Tin Reactions in Bulk Samples*, in *Solder Joint Technology*, K.-N. Tu, Editor. 2007b, Springer New York: New York, NY. p. 37-71. https://doi.org/10.1007/978-0-387-38892-2_2

Tu, K.-N., *Copper–Tin Reactions in Thin-Film Samples*, in *Solder Joint Technology*, K.-N. Tu, Editor. 2007c, Springer New York: New York, NY. p. 73-109. https://doi.org/10.1007/978-0-387-38892-2_3

Tu, K.N. and K. Zeng, *Tin–lead (SnPb) solder reaction in flip chip technology.* Materials Science and Engineering: R: Reports, 2001. **34**(1): p. 1-58. https://doi.org/10.1016/s0927-796x(01)00029-8

Watanabe, Y., Y. Fujinaga, and H. Iwasaki, *Lattice modulation in the long-period superstructure of Cu3Sn.* Acta Crystallographica Section B Structural Science, 1983. **39**(3): p. 306-311. https://doi.org/10.1107/s0108768183002451

Wen, C.Y. and F. Spaepen, *In situ electron microscopy of the phases of Cu3Si.* Philosophical Magazine, 2007. **87**(35): p. 5581-5599. https://doi.org/10.1080/14786430701675829

Yao, Y. and S. Fan, *Si nanowires synthesized with Cu catalyst.* Materials Letters, 2007. **61**(1): p. 177-181. https://doi.org/10.1016/j.matlet.2006.04.045

Zemann, J., *Crystal structures, 2nd edition. Vol. 1 by R. W. G. Wyckoff.* Acta Crystallographica, 1965. **18**(1): p. 139-139. https://doi.org/https://doi.org/10.1107/S0365110X65000361

Zhang, H., D. Zhang, L. Guo, R. Zhang, P. Yin, and R. Wang, *One-pot assembly of Cu2O chain-like hollow structures.* J Nanosci Nanotechnol, 2008. **8**(12): p. 6332-7. https://doi.org/10.1166/jnn.2008.18389

Chapter 5. Making silicon nanowires with CuSn mixed-catalyst

In the previous chapter, we have studied the evolution of CuSn co-catalyst NPs at different stages of PECVD experiment for fabrication of SiNWs. Based on the previous knowledge and experiences, in this chapter, we make SiNWs using CuSn co-catalysts. Firstly, we study crystalline structures of the SiNWs that have been reported in Chapter 4.3.1 and 4.3.2 respectively. In the previous sub-sections, we focused on characterization of structures of catalyst NPs of the SiNWs. In sub-chapter 5.1, we study crystalline structures of the SiNWs by TEM. In sub-chapter 5.2, we devote to exploring conditions for small-diameter SiNWs catalyzed by CuSn co-catalysts, since hexagonal Si phase have been fabricated in SiNWs with crystalline diameters no larger than 6 nm using Sn catalyst on Cu TEM grids (see 3.1). Then in sub-chapter 5.3, we investigate the influence of PECVD parameters on the crystalline structures in order to obtain hexagonal SiNWs.

5.1. **Structure of nanowires with diameters above 10 nm**

In this sub-chapter, we study crystalline structures of SiNWs fabricated with CuSn co-catalyst with a dominant amount of Cu and Sn respectively, which have been used to study the structures of catalyst NPs in Chapter 4.3.1 and 4.3.2. Although the SiNWs synthesized with the CuSn co-catalysts have bi-modal distributions, however, we only observed SiNWs with diameters larger than 10 nm. Compared with the hexagonal SiNWs we have reported in Chapter 3, they are larger. Thus, we focus on structures of larger SiNWs at first.

5.1.1. **Crystalline structure of SiNWs fabricated with CuSn co-catalyst with a dominant amount of Cu**

Firstly, we characterized the crystalline structures of SiNWs fabricated with co-catalyst of 1 nm Sn/0.8 nm Cu on (100) Si substrates (from Figure 4.21a) using TEM Jeol 2010F. More than 50 SiNWs were observed, with diameters ranging from 10 nm to 36 nm, in agreement with the SEM measurements. Most of the SiNWs were straight and had crystalline structure. Figure 5.1 shows a HRTEM image of a SiNW. It has a total diameter of 32 nm including an amorphous layer with thickness around 1-2 nm. The FFT image

in the upper right corner indicates that the NW has a diamond cubic structure. Among the observed SiNWs, only 9 NWs were in the $[110]_C/[1\text{-}210]_H$ zone axis, which is the only unambiguous zone axis to distinguish the cubic and the hexagonal phase of Si with absolute certainty [Tang, 2017b]. All these SiNWs had the diamond cubic structure.

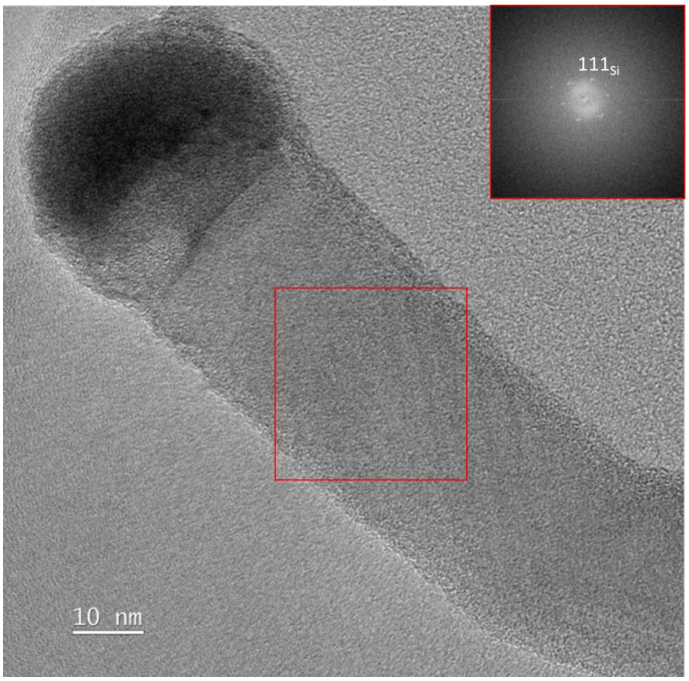

Figure 5.1.HRTEM image of a typical SiNW synthesized with 1 nm Sn/0.8 nm Cu co-catalyst.

5.1.2. **Crystalline structures of SiNWs fabricated with CuSn co-catalyst with dominant amount of Sn**

In this sub-section, we observe the SiNWs synthesized with the co-catalyst of 1 nm Sn/0.2 nm Cu on (100) Si substrates (from Figure 4.21b) by TEM. In the 49 observed SiNWs in this sample, there were 10 SiNWs close to the zone axis, and they all had cubic structures. A HRTEM image of a SiNW synthesized with the Sn-rich catalyst is shown in Figure 5.2. It has a diameter of 19 nm. The FFT image is shown in the inset of the figure, indicating that the SiNW has a diamond cubic structure.

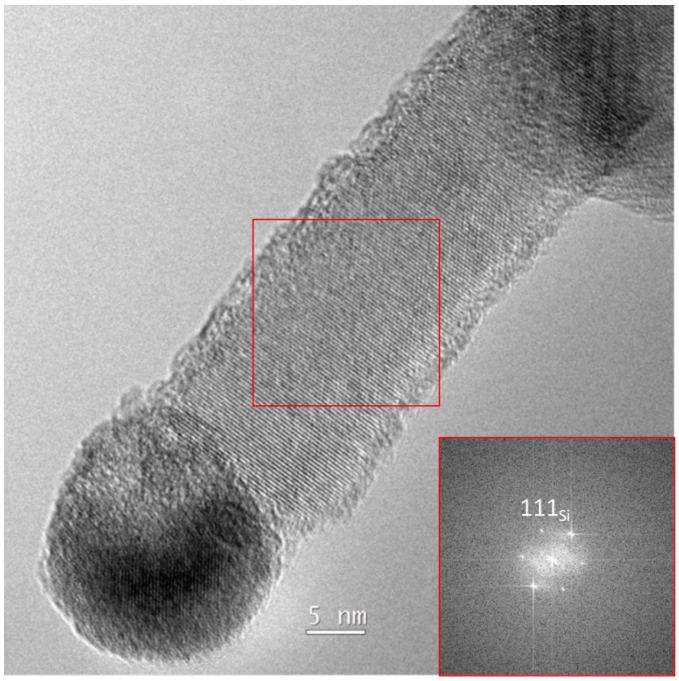

Figure 5.2. A SiNW with the cubic structure synthesized with the co-catalyst of 1 nm Sn/0.2 nm Cu.

In summary, we have studied the crystalline structures of SiNWs synthesized with a Cu-rich co-catalyst (1 nm Sn/0.8 nm Cu), and a Sn-rich co-catalyst (1 nm Sn/0.2 nm Cu). Both two co-catalyst NPs of SiNWs have core-shell structures. All the observed SiNWs had diamond cubic structures. No hexagonal structures in SiNWs have been found, as all observed SiNWs had diameters larger than 10 nm, whereas the spontaneous growth of hexagonal phase has only been found in SiNWs with crystalline cores no larger than 6 nm on Cu TEM grids (see Chapter 3). Therefore, in the next chapter 5.2, we will study the crystalline structures of SiNWs with smaller diameters to explore the presence of hexagonal phase of Si.

5.2. **Making small-diameter silicon nanowires**

Since we are interested in small diameter SiNWs, using CuSn co-catalysts brings potentialities for thin SiNW fabrication. In this sub-chapter, we aim to obtain small-diameter SiNWs synthesized with CuSn co-catalysts from two aspects: firstly, we systematically study the influence of Cu-Sn composition in co-catalysts on SiNW diameter distribution; secondly, we study the influence of co-catalyst amount on SiNW diameter and optimize the ingredients of co-catalysts.

5.2.1. **Influence of co-catalyst composition on SiNW diameter distribution**

In this sub-section, we investigate the influence of CuSn co-catalyst composition of on SiNW growth. We fix the total nominal thickness of CuSn co-catalyst, and then vary the composition of Cu and Sn. In the following, all the catalyst thickness and composition mean nominal thickness and nominal composition. Two groups of experiments are carried out using two different total nominal thicknesses of co-catalyst: 2 nm and 1.2 nm respectively.

Firstly, we explore the influence of co-catalyst composition on the NW growth with a total nominal thickness of 2 nm. We evaporated 1.7 nm Sn/0.3 nm Cu (28.8 at% Cu), 1.4 nm Sn/0.6 nm Cu (49.5 at% Cu), 1.1 nm Sn/0.9 nm Cu (65.2 at% Cu), 0.8 nm Sn/1.2 nm Cu (77.5 at% Cu), 0.5 nm Sn/1.5 nm Cu (87.3 at% Cu), 0.2 nm Sn/1.8 nm Cu (95.3 at% Cu) on polished (100) c-Si wafer substrates. Cu was firstly deposited on the substrates in a thermal evaporator (see Chapter 2.1.2), and then Sn was deposited on top of Cu to prepare the co-catalysts. Choosing a total nominal thickness of 2 nm allows us to have several combinations of Cu and Sn co-catalyst compositions. The purpose of using 0.3 nm as a thickness increment of the catalyst is to reduce the influence caused by the actual error value of the evaporated material as much as possible. According to our experience, when we vary the evaporated amount of metal catalyst only by 0.1 nm every time, we cannot guarantee that the co-catalyst composition has really changed accordingly. Therefore, we choose a relatively large thickness step of 0.3 nm to ensure the varying tendency of the co-catalyst composition. Next, the substrates are transferred into the PECVD reactor Plasfil for NW growth with a typical procedure described in Table 3.1. The SEM images of the acquired SiNWs are shown in Figure 5.3. When there is 28.8 at% Cu, the SiNW diameter looks homogeneous, with few thin NWs (Figure 5.3a). With the nominal atomic fraction of Cu increasing, the range of NW diameter becomes broader and the diameter distribution shows a bi-modal tendency: thin and thick SiNWs are found simultaneously (Figure 5.3b to f). The thin NWs are usually straight and have lengths from 150 nm to 300 nm. Whereas the thick NWs are likely to be kinked. It is especially obvious when the atomic fraction of Cu is as high as

95.3%. Almost all the thick SiNWs were kinked and often changing growth direction, as shown in Figure 5.3f.

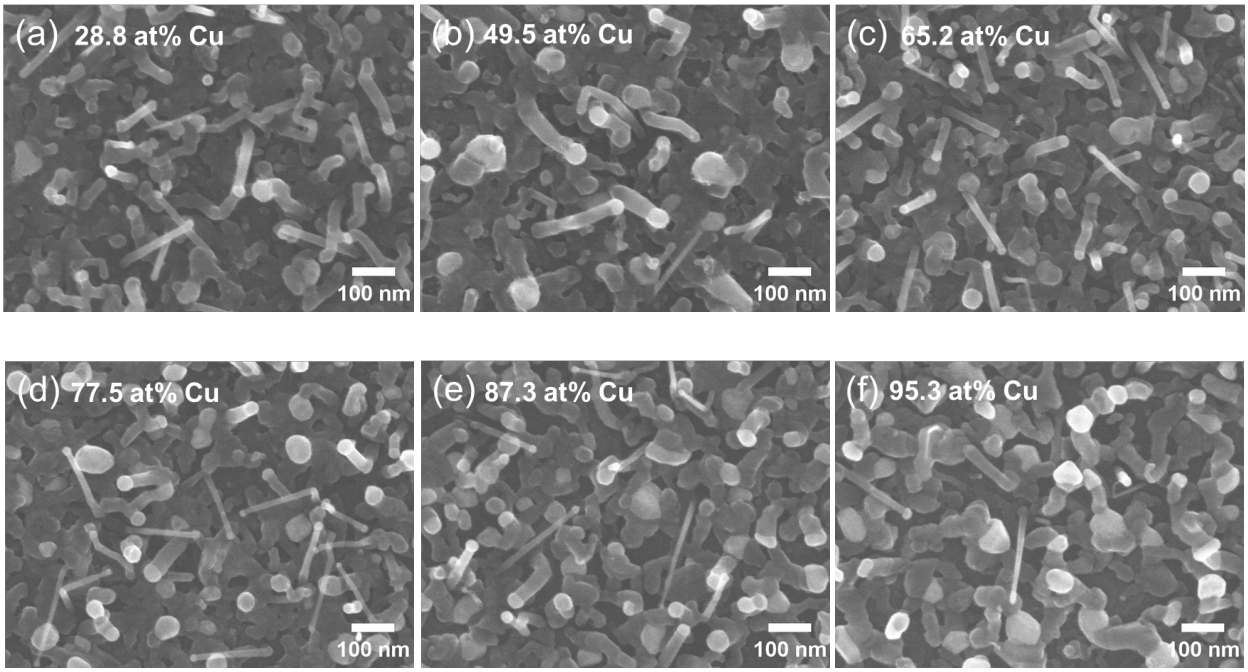

Figure 5.3. SEM images of SiNWs synthesized with nominally 2 nm thick co-catalyst consisting of: (a) 1.7 nm Sn/0.3 nm Cu (28.8 at% Cu), (b) 1.4 nm Sn/0.6 nm Cu (49.5 at% Cu), (c) 1.1 nm Sn/0.9 nm Cu (65.2 at% Cu), (d) 0.8 nm Sn/1.2 nm Cu (77.5 at% Cu), (e) 0.5 nm Sn/1.5 nm Cu (87.3 at% Cu), (f) 0.2 nm Sn/1.8 nm Cu (95.3 at% Cu).

The average diameter and the diameter distribution of SiNWs are plotted as a function of atomic fraction of Cu in Figure 5.4. The X axis represents the atomic fraction of Cu in co-catalysts and the Y axis represents SiNW diameters. The average diameters are shown with standard deviations as error bars. The median diameters are indicated as short blue lines on those bars. The histograms are based on statistics over 100 SiNWs for each sample, which are chosen from multiple SEM images without bias. The NW diameters are measured using ImageJ software within an error of 1.8 nm due to the effects of image contrast and finite pixel resolution. Each counted SiNW is displayed as a red dot in the histogram. The diameter distribution of these SiNWs can be observed directly in Figure 5.4. In this graph, the smaller the Cu content is, the

narrowest the diameter distribution; the histogram for the lowest Cu-content (28.8 at%) has only one peak with an average diameter at around 22 nm and the median diameter just about 0.5 nm smaller. For the samples with higher atomic fraction of Cu, SiNWs have broader diameter ranges: thinner and thicker SiNWs are present at the same time, creating valleys in histograms. The SiNWs grown with 95.3 at% of Cu co-catalyst have the broadest range of diameters, from 5 nm to 60 nm. It's worth noting that the highest peaks of the histograms of all these samples are shifted towards the smaller diameters in comparison with the sample of 28.8 at% of Cu in its co-catalyst. In addition, this phenomenon can also be reflected in SiNW median diameters, since they are smaller or no larger than NW average diameters for each sample. This is a thrilling tendency as we are interested in thin SiNWs. However, the most of the NWs still have diameters larger than 10 nm, which was mainly on account of the 2 nm nominal thickness of co-catalysts. Co-catalysts of 2 nm thickness are too much to synthesize smaller-diameter SiNWs. Thus, we carry out another group of experiment using a smaller nominal thickness of co-catalyst.

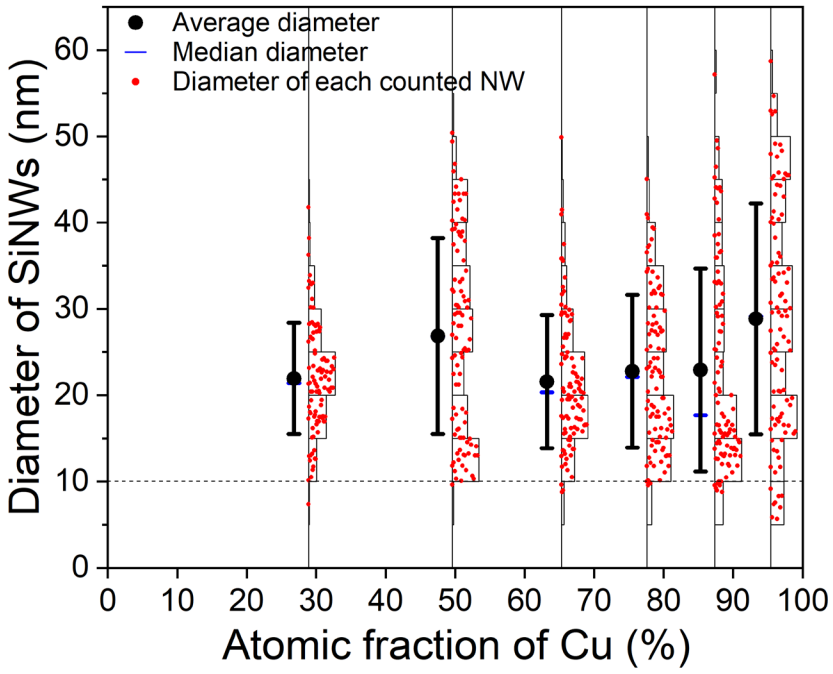

Figure 5.4. The average diameters and diameter distributions of SiNWs as a function of the atomic fraction of Cu in the co-catalyst. Small blue bars indicate median diameters. The total nominal thickness of Cu and Sn was 2 nm.

In order to figure out the impact of the total thickness on the SiNW diameter distribution, we now explore co-catalyst compositions with a total nominal thickness of 1.2 nm. We evaporate 1 nm Sn/0.2 nm Cu (31.4 at% Cu), 0.6 nm Sn/0.6 nm Cu (69.6 at% Cu), 0.2 nm Sn/1 nm Cu (92.0 at% Cu) on (100) c-Si wafer substrates. Cu is first thermally evaporated on the c-Si substrates and then Sn is deposited on top of Cu to make the co-catalysts. We also evaporate 1.2 nm pure Sn (0% Cu) and 1.2 nm pure Cu (100% Cu) on the Si substrates respectively as control groups. Then these substrates are loaded in Plasfil to fabricate SiNWs with the typical procedure. The SEM images of the samples after PECVD growth are shown in Figure 5.5. SiNWs catalyzed by pure Sn are mostly straight and the range of NW diameter is not broad (Figure 5.5a). When the catalyst contains 31.4 at% Cu, thin SiNWs begin to appear (Figure 5.5b). When we use a co-catalyst of 69.6 at% Cu, the fabricated SiNWs become much thinner and denser (Figure 5.5c). With Cu atomic fraction increased to 92.0%, NW diameters go to bi-modal distribution, and become less dense compared with the previous sample (Figure 5.5d). Finally, we have confirmed again that pure Cu

catalyst does not lead to SiNW growth under the current experimental conditions at a substrate temperature of 416 ˚C. A SEM image of Cu NPs after the PECVD experiment is shown in Figure 5.5e. There were a few larger particles among the small dense NPs.

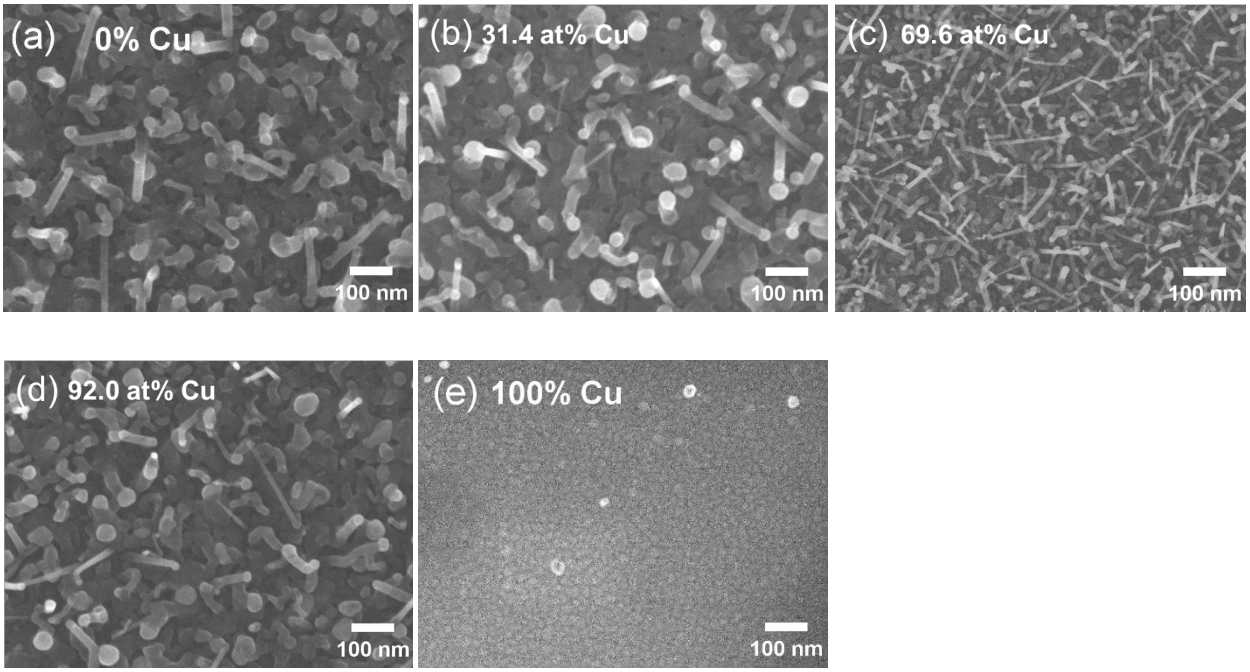

Figure 5.5. SEM images after PECVD experiment with (a) 1.2 nm Sn (0% Cu); (b) 1 nm Sn/0.2 nm Cu (31.4 at% Cu); (c) 0.6 nm Sn/0.6 nm Cu (69.6 at% Cu); (d) 0.2 nm Sn/1 nm Cu (92.0 at% Cu) and (e) 1.2 nm Cu (100% Cu).

The average diameter of SiNWs as a function of CuSn co-catalyst composition and the histograms of NW diameters are plotted in Figure 5.6. SiNWs grown with pure Sn and co-catalyst of 31.4 at% Cu seem to have similar SiNW distributions, as shown in the left two columns; in fact, SiNWs in the second column have a broader diameter distribution and thin NWs with diameters smaller than 10 nm begin to appear. When SiNWs are grown with 69.6 at% Cu co-catalyst, a narrower diameter distribution of thinner SiNWs is realized. An average diameter of 10.7 nm has been achieved, about 9 nm smaller in comparison with average diameters of the two previous samples. In that case, all SiNWs have diameters smaller than 16 nm and 39% of them are thin SiNWs (diameter < 10 nm). The small diameter of SiNWs grown with 0.6 nm Sn/0.6 nm Cu (69.6 at% Cu) is attributed to the small-size co-catalyst NPs, which has been mentioned in

Chapter 4.2. The as-deposited 0.6 nm Sn/0.6 nm Cu co-catalyst NPs have diameters around 3-6 nm (see Figure 4.10 in Chapter 4.2.1). After a hydrogen plasma treatment at 200 ˚C, the diameters of co-catalyst NPs have increased to 3-10 nm (see Figure 4.14 in Chapter 4.2.3), which is a little smaller than the SiNW diameters after PECVD growth. When the Cu content of co-catalyst is increased to 92.0 at%, the NWs have a much broader distribution from 6 nm to 39 nm, and SiNW average diameter increases to 17.7 nm. The ratio of thin SiNWs (< 10 nm) is 24% for this sample.

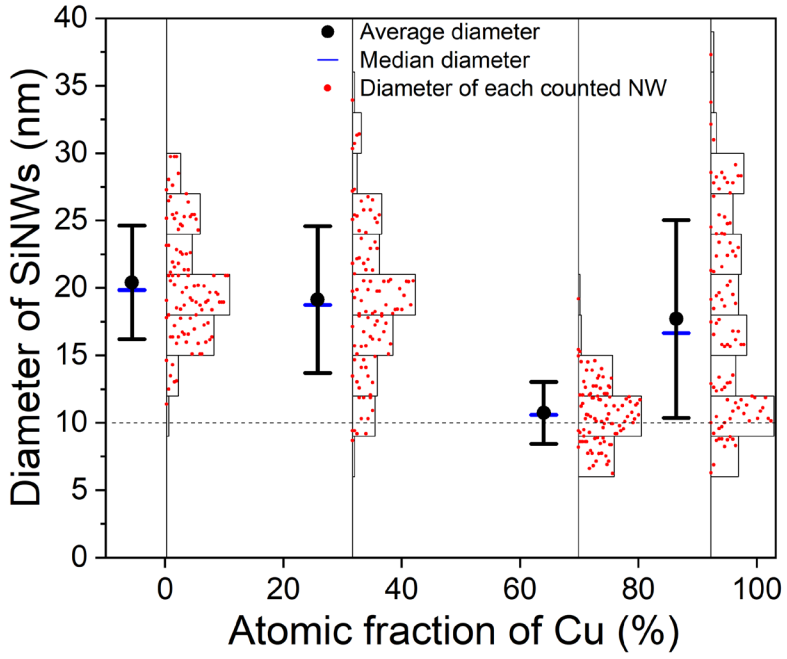

Figure 5.6. The average diameter and histograms of NW diameter distribution as a function of the atomic fraction of Cu in the co-catalyst. Small blue bars indicate median diameters. The total nominal thickness of Cu and Sn was 1.2 nm.

According to the two groups of experiments described above, the co-catalyst composition has an influence on SiNW diameter and distribution. From both experiments (total thicknesses of 2 and 1.2 nm), we can conclude that:

1) when the atomic fractions of Cu are low (28.8% and 31.4%), the diameter distribution of SiNWs peaks in the middle area (average and median diameters about equal) and has a monomodal distribution;

2) when Cu atomic fractions are 65.2% (1.1 nm Sn/0.9 nm Cu) and 69.6% (0.6 nm Sn/0.6 nm Cu), the average diameters of SiNWs are the smallest in each group. It is particularly evident in the second experimental group with 0.6 nm Sn/0.6 nm Cu co-catalyst. That is, in thickness-fixed co-catalysts, when the thickness ratio of Cu and Sn are close to 1:1, neither material has a larger amount. As a result, the obtained SiNWs are relatively thinner compared with other compositions;

3) when the atomic fractions of Cu are more than 90%, the ranges of NW diameter values are the broadest in each group: compared with samples grown with Sn-rich co-catalysts, the SiNWs grown with Cu-rich co-catalysts have higher fractions of both thin and thick SiNWs;

4) SiNWs grown with co-catalysts with 2 nm nominal thickness have larger average diameters and broader ranges of diameter distribution than SiNWs grown with 1.2 nm-thick co-catalysts.

From the studied co-catalyst compositions, a co-catalyst of 0.6 nm Sn/0.6 nm Cu is leading to the most desirable SiNW diameter distribution and density as we aim at small-diameter SiNWs. Indeed, for this composition we could obtain the SiNWs with the smallest average diameter of 10.7 nm, the highest ratio of thin SiNWs (39% with diameter below 10 nm), the narrowest diameter distribution (standard deviation of 2.3 nm), and the highest density (2.58×10^{10} /cm^2). We also observe that, independently of the distribution width, the smallest-diameter nanowires are obtained with the above 50/50 composition and in Cu-rich groups, we thus continued to optimize co-catalyst compositions towards two directions:

1) reducing the total nominal thickness of co-catalyst;

2) using a Cu-rich co-catalyst.

5.2.2. **Optimization of co-catalyst recipe for small-diameter SiNWs**

Based on previous results, we investigate the influence of decreasing co-catalyst nominal thickness on SiNW diameter and distribution. We prepare the co-catalyst on Si substrates in a thermal evaporator with the following compositions: 0.2 nm Sn/0.4 nm Cu, and 0.1 nm Sn/0.1 nm Cu. The order of evaporating

catalyst materials is the same as before: Cu is evaporated firstly on substrates and then Sn is deposited on the top of Cu. We follow the typical PECVD process to fabricate SiNWs. SiNWs are also synthesized with 0.1 nm Sn catalyst to serve as a control group. The SEM images of SiNWs are shown in Figure 5.7 associated with their diameter distribution histograms. The SiNWs grown with 0.2 nm Sn/0.4 nm Cu co-catalyst are straight, without any thick NWs (Figure 5.7a), unlike thin and thick SiNWs with bi-modal distributions when grown with 1.2 and 2 nm co-catalysts in Figure 5.3 and Figure 5.5, respectively. According to statistics, the SiNWs have a diameter distribution of 9.9 ± 1.6 nm (Figure 5.7d). When SiNWs are grown with a reduced amount of 0.1 nm Sn/0.1 nm Cu co-catalyst, we find that NW diameters decrease furthermore, having a distribution of 7.5 ± 1.5 nm, meanwhile the NW density increases significantly (Figure 5.7b and e). These diameter sizes can move grown NWs into the domain of quantum wires with properties modified by significant quantum effects as predicted in theoretical works [Read, 1992, Capasso, 1994, Band, 2013]. The density of the SiNWs is 5.72 $\times 10^{10}$ /cm^2, two orders of magnitude higher than the density of the SiNWs grown with 0.1 nm Sn in Figure 5.7c. The SiNWs grown with pure Sn have a diameter distribution of 16 ± 2.5 nm, about twice larger than SiNWs grown with 0.1 nm Sn/0.1 nm Cu co-catalyst. This control group confirms the fact that only with CuSn co-catalyst can we realize uniform thin SiNWs with ultra-high density.

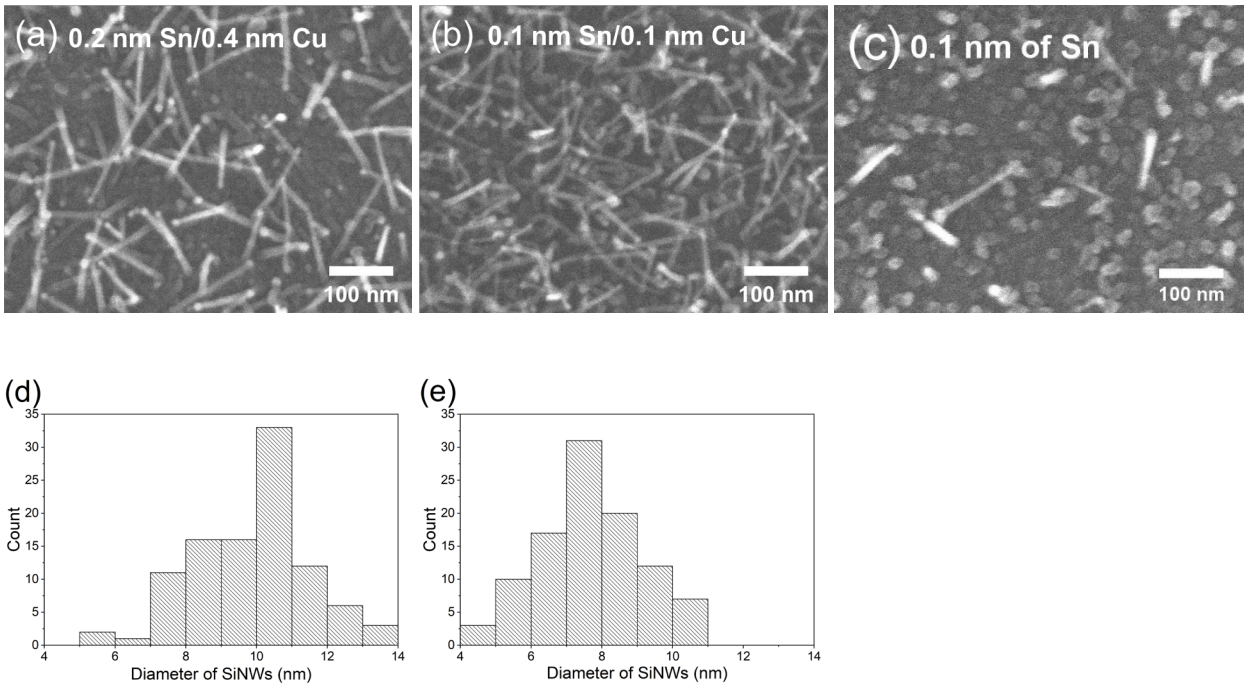

Figure 5.7. SEM images of SiNWs synthesized with thermally evaporated films of nominal thicknesses: (a) 0.2 nm Sn/0.4 nm Cu, (b) 0.1 nm Sn/0.1 nm Cu, (c) 0.1 nm of Sn; (d) and (e): histograms of diameter distribution of SiNWs in (a) and (b).

Next, we study the relationships between nanowire diameter and catalyst size. For this, we observe catalyst NPs before nanowire growth, then the nanowires obtained after a short growth time. We choose two nominal catalyst deposits: *i*) 0.1 nm Sn/0.1 nm Cu co-catalyst and *ii*) a larger co-catalyst of 0.2 nm Sn/1 nm Cu. The two co-catalysts are evaporated on Si substrates following the orders used above. The co-catalyst NPs have firstly been through a hydrogen plasma treatment at 200 °C for 2 minutes (see Figure 5.8a and c), and then SiNWs are grown only for 30 s at 416 °C with the typical PECVD conditions (see Figure 5.8b and d). SiNWs grown with 0.1 nm Sn/0.1 nm Cu are thin and relatively dispersed (Figure 5.8b). Meeting of NWs during growth provoking catalyst coalescence barely happens. As a result, most SiNWs can preserve small diameters. That is mainly on account of the small size and the relatively long distance (which can be a few times larger than the catalyst diameter) between the catalyst NPs (Figure 5.8a), which can reduce the odds that adjacent NPs merge with each other. In contrast with the small, dispersed NPs of

0.1 nm Sn/0.1 nm Cu co-catalyst, catalyst NPs of 0.2 nm Sn/1 nm Cu are bigger and more crowded due to the higher amount of materials evaporated (Figure 5.8c). The distance between neighboring NPs is only a few nanometers, therefore, some catalyst NPs have merged with each other during NW growth, as indicated by the yellow arrows (Figure 5.8d). Consequently, SiNWs grown with larger co-catalyst NPs have larger average diameters with bi-modal distribution: SiNWs grown from single catalyst NPs are thin, while SiNWs grown from coalescent NPs are thick.

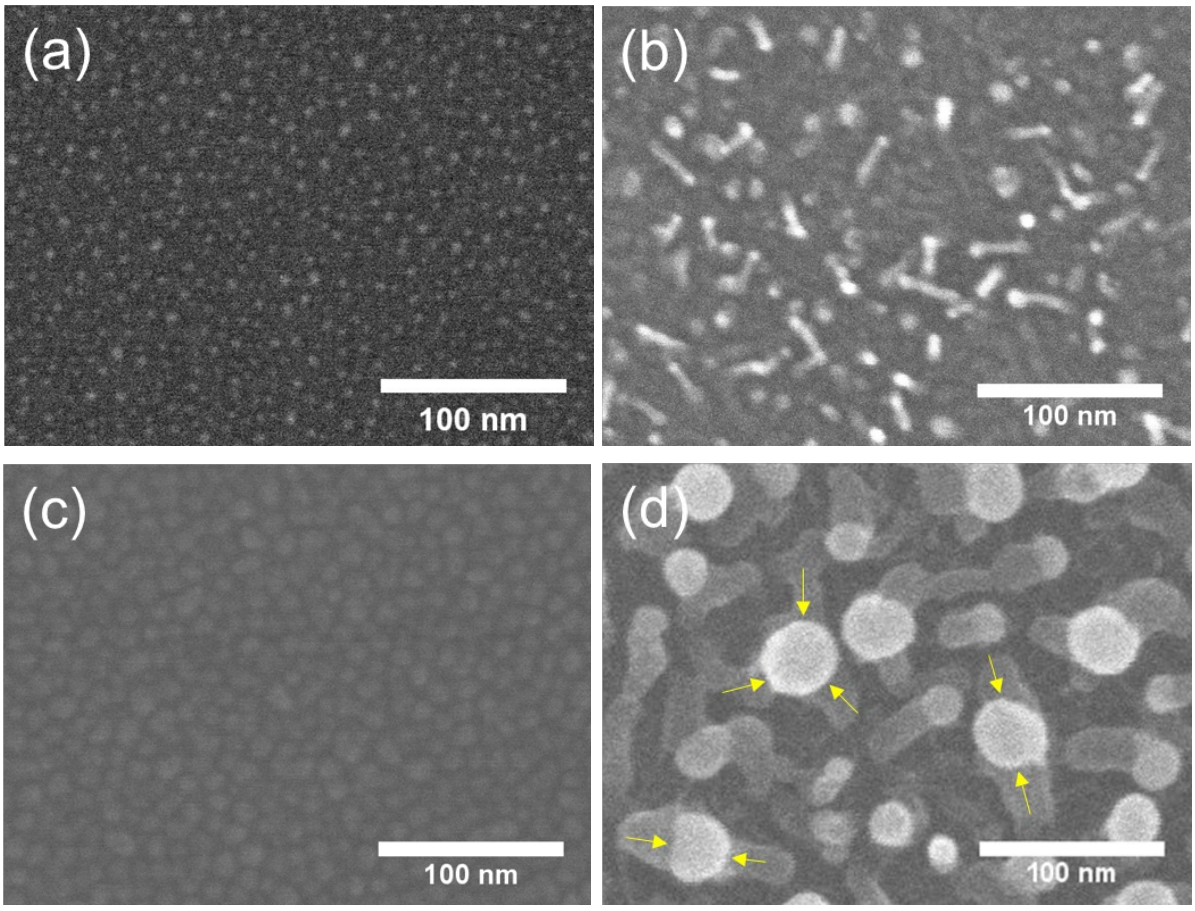

Figure 5.8. SEM images of (a) 0.1 nm Sn/0.1 nm Cu co-catalyst NPs after hydrogen plasma treatment at 200 °C for 2 minutes; (b) SiNWs after 30 s growth at 416 °C with 0.1 nm Sn/0.1 nm Cu co-catalyst at the typical conditions; (c) 0.2 nm Sn/1 nm Cu co-catalyst NPs after hydrogen plasma treatment at 200 °C for

2 minutes; and (d) SiNWs after 30 s growth at 416 °C with 0.2 nm Sn/1 nm Cu co-catalyst at the typical conditions.

Table 5.1 summarizes the diameters of the CuSn co-catalyst NPs after a hydrogen plasma treatment and the SiNWs after 30s growth from Figure 5.8 with standard deviations. For NPs of 0.1 nm Sn/0.1 nm Cu, the average diameter increases from 4.5 nm (after a hydrogen plasma treatment for 2 minutes) to 7.1 nm, which is the average diameter of SiNWs after 30s growth. Whereas for the NPs of 0.2 nm Sn/1 nm Cu after the treatment, they are more than twice larger in diameters compared with NPs of 0.1 nm Sn/0.1 nm. And after NW growth for 30s, the diameter increases 7.1 nm, which is nearly three times increment of the other group. This is mainly caused by the coalescence of the larger catalyst NPs at elevated temperatures.

Table 5.1. Diameters of CuSn co-catalyst NPs and SiNWs from 0 with standard deviations.

Catalsyt	NP diameter after hydrogen plasma treatment	NW diameter after 30s growth
0.1 nm Sn/0.1 nm Cu	4.5 ± 1.2 nm	7.1 ± 1.5 nm
0.2 nm Sn/1 nm Cu	10.6 ± 1.9 nm	17.7 ± 7.3 nm

On the basis of the results above, we find that SiNW average diameters decrease with total nominal thickness of evaporated co-catalysts. However, 0.1 nm is the smallest nominal thickness that can be distinguished by the microbalance quartz in Boc Edwards Auto 306 Evaporator used in this thesis due to its limited value indication. We have developed two methods to realize the deposition of catalyst with nominal thickness thinner than 0.1 nm (see details in Chapter 2.1.2). First, we modified the material density ρ_0 of the catalyst metal given as an input in the microbalance. Instead of using the exact value of the catalyst density ρ_0 (8.96 g/cm³ for Cu and 7.31 g/cm³ for Sn), we input half of the value $\rho_1 = \rho_0/2$. When we evaporated a displayed 0.1 nm nominal thickness of the deposited metal, the actual deposited thickness equaled to 0.1 nm/2= 0.05 nm. We thus obtained a first deposit with 0.05/0.05 nm Sn/Cu. The SEM image of the SiNWs grown with a co-catalyst of 0.05/0.05 nm Sn/Cu is shown in Figure 5.9a. These SiNWs have

similar diameter with the SiNWs grown with 0.1 nm Sn/0.1 nm Cu co-catalyst, but with a reduced density. The other method we used to obtain catalyst evaporation less than 0.1 nm nominal thickness was to tilt the substrates. The substrates were tilted by an angle of 20° with respect to the substrate holder plane in the evaporator. The calculated thicknesses on two tilted substrates are 0.09/0.09 nm for a displayed nominal thickness of 0.1 nm. Then we loaded the samples on the bottom electrode of the PECVD reactor for NW growth. SEM images of obtained SiNWs are shown in Figure 5.9b. Again, the NW density decreased compared with the untitled sample while NW diameter remained similar. By continuing reducing the nominal thickness of catalyst, we did not decrease NW diameter furthermore. Instead, we only decreased the NW density.

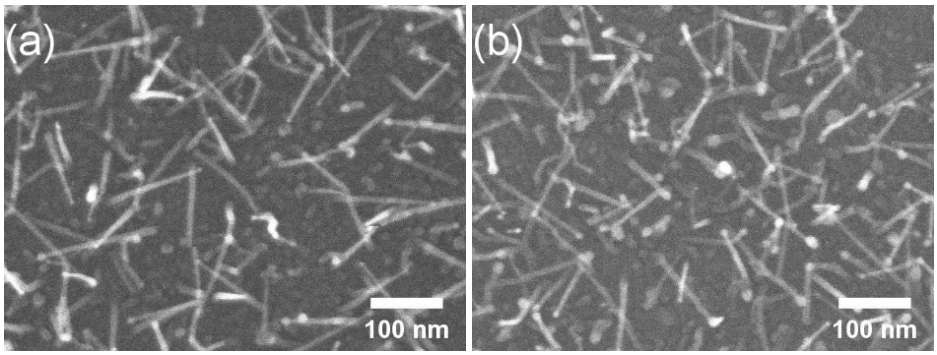

Figure 5.9. SEM images of: (a) SiNWs grown with a nominal thickness of 0.05/0.05 nm Sn/Cu; (b) SiNWs grown with a nominal thickness of 0.09/0.09 nm Sn/Cu.

Figure 5.10 summarizes the influence of Cu and Sn deposited amounts on SiNW diameters. The SiNW average diameter D_{avg} has been measured in SEM images. We can see that, not surprisingly, it globally decreases as the catalyst total nominal thickness decreases. When the total nominal thickness of the two catalysts is larger than 1.2 nm, most samples have D_{avg} around 20-30 nm. When the total nominal thickness is below 0.6 nm, most SiNW samples have D_{avg} smaller than 10 nm, except for the samples with either no Cu in them or almost no Sn (92 at% Cu). When the total nominal thickness of both catalysts is reduced to 0.2 nm (0.1 nm Sn/0.1 nm, 70 at% Cu), D_{avg} reaches the lowest limit for the used PECVD growth conditions. By further reducing the catalyst thickness to 0.1 nm (0.05 nm Sn/0.05 nm Cu, 69.6 at% Cu), we do not decrease the SiNW diameters; instead, we only decrease NW density. As mentioned above, the

diameter *distribution* also gets narrower with decreasing nominal thickness, with a lower sensitivity to the catalyst composition.

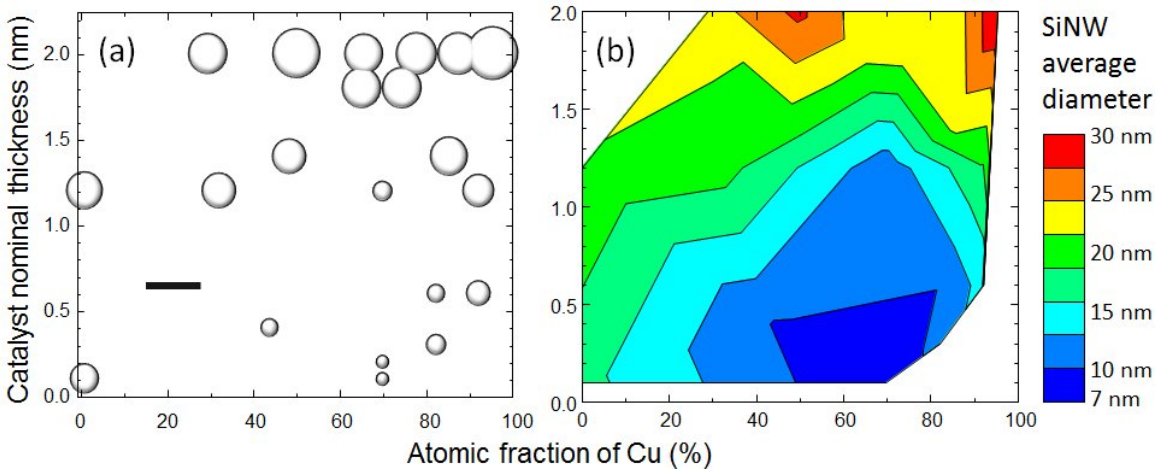

Figure 5.10. SiNW average diameter as a function of total nominal thickness (Y axis) and atomic fraction of Cu (X axis) in the multi-phase catalyst. The SiNWs are grown on *c*-Si substrates and the average diameters of SiNWs are measured by SEM. (a) Plot showing the 21 data points; the size of the disks indicates the NW average diameter, scale bar 30 nm. (b) Contour plot of the same data.

Now let us discuss about the smallest NW diameters we were able to obtain. According to our results (Figure 5.3 to Figure 5.10):

i) smallest NW diameters are obtained with 0.1 nm Sn/0.1 nm Cu;

ii) decreasing the nominal catalyst thickness below 0.1 nm Sn/0.1 nm Cu has no further effect on decreasing NW diameter.

To obtain the smallest nanowire, one has firstly to obtain the smallest catalyst particle and, secondly, to be able to nucleate a nanowire form it. Thus, the observed limitation could be due both to the existence of a surface concentration threshold for the nucleation of catalyst nanoparticles and to the existence of a particle size threshold for the nucleation of SiNWs. Forming stable metal clusters has been demonstrated for sizes as small as 0.49 nm for Cu [Zhao, 2017, Bu, 2019]. Moreover, NW growth takes

place after a catalyst particle ripening process. We thus think that the existence of that low limit in NW diameter is essentially due to Si precipitation becoming impossible in nanoparticles below a given critical radius: the well-known "Gibbs-Thomson effect" [Givargizov, 1975, Dubrovskii, 2009, Schmidt, 2009].

Let us now recall some basic ideas about precipitation. In three dimensions in a liquid or solid solution, the critical nucleus radius is the minimum particle size from which a cluster formed by atoms or molecules is thermodynamically stable. In classical nucleation theory, the critical radius r^* of a system is determined from its excess Gibbs free energy [Ashby, 1988]:

$$\Delta G = -\frac{4}{3}\pi r^3 \Delta G_V + 4\pi r^2 \gamma$$

ΔG_V denotes the Gibbs free-energy difference per unit volume between solid and liquid, and $\Delta G_V \cong \Delta H_m(T_m - T)/T_m$ [Christian, 1965]. In a nucleus of radius r, the interfacial energy γ depends on the surface curvature. The expression of this dependence can be approximated as [Báez, 1995]:

$$\gamma(r) = \frac{\gamma_\propto}{1 + \frac{2\delta}{r}}$$

where δ is a characteristic length scale for the interface, and subscript $\propto$ refers to planar interface. Critical nucleus radius r^* is obtained by making the first derivative of $\Delta G(r)$ equal to 0 (see Figure 5.11a). Below the critical radius r^*, the increase of interfacial energy $4\pi r^2\gamma$ is larger than the decrease of volume free energy $\frac{4}{3}\pi r^3 \Delta G_V$, thus, the Gibbs free energy change ΔG is positive and nucleation process is not prosperous. Above the critical radius r^*, ΔG is decreasing and the particles will form and grow as it is thermodynamically favorable. Critical radii in homogeneous nucleation and heterogeneous nucleation are the same (see Figure 5.11b), while $\Delta G^*_{het} < \Delta G^*_{hom}$ [Callister, 2014]. That is because nucleation on preferential sites can reduce interfacial energy effectively. Cluster volume can be significantly less for heterogeneous nucleation due to the wetting angle of the cluster and the nucleation site affecting the shape of the cluster.

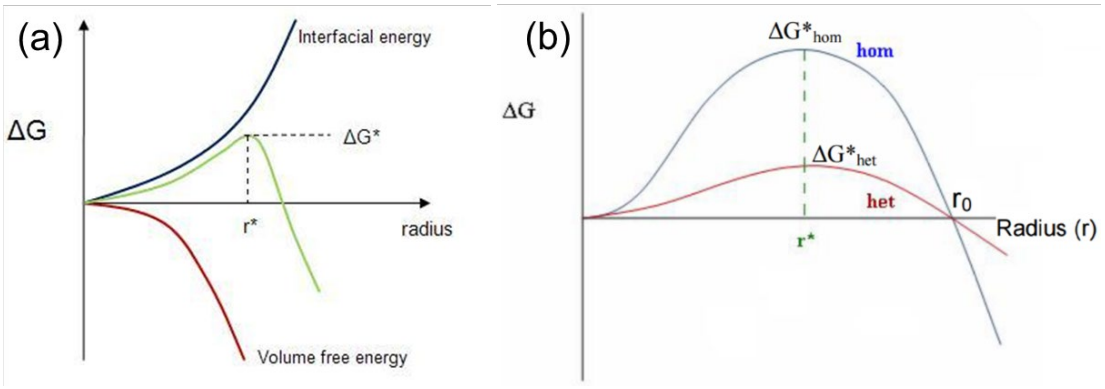

Figure 5.11. Excess Gibbs free energy change versus the nanoparticle radius. Critical radius r^* corresponds to the minimum size at which a particle can survive in solution without being redissolved; (b) comparison of critical radius r^* and excess Gibbs free energy in homogeneous and heterogeneous nucleation. Adopted from [Wikipedia, 2020a]

V. G. Dubrovskii *et al*. has described the 2D nucleus of SiNWs in (metal organic chemical vapor deposition) MOCVD growth, which is mainly promoted by the direct impingement and the sidewall diffusion, while the substrate contribution can be neglected for sufficiently tall SiNWs (500 nm) [Dubrovskii, 2009]. U. Gösele *et al*. has proposed an expression of SiNW minimum size [Tan, 2003]: it contains two contributions, one depending on the liquid droplet (Au-Si) composition and one depending on the droplet size. These expressions do not impose a limit on the minimum droplet and SiNW sizes. Thus, the SiNW can be grown to ever smaller sizes until reaching a kinetic limit that is presently not known.

In our experiments, the minimum SiNW diameter is slightly larger than the smallest co-catalyst NPs under current experiment conditions. This is because of the ripening effect of NPs at increasing temperatures. In brief, under the current conditions, the minimum SiNW diameter mainly depends on the size of as-deposited co-catalyst NPs, until this size does not allow Si nucleation anymore due to the Gibbs-Thomson effect. This is due to the increasing vapor pressure and solubility of Si as the diameter of the NWs becomes smaller [Givargizov, 1975]. We have realized minimizing SiNW diameter by controlling evaporated co-catalyst amount.

In sub-section 5.2.1 and 5.2.2, we have learned the influence of co-catalyst composition and nominal thickness on SiNW growth. Evaporating Sn on Cu can reduce NP size, compared to the sizes of as-deposited nano-objects of pure Sn and pure Cu. Bi-modal distributions of SiNW diameters have been caused by the coalescence of adjacent co-catalyst NPs during NW growth, whereas "uncoalescent" NPs lead to thin SiNWs. With co-catalyst nominal thickness decreasing, SiNW average diameter decreased until a nominal thickness of 0.1 nm Sn/0.1 nm Cu. Below that deposited thickness, no further decrease is observed, which we attribute to the Gibbs-Thomson effect. A co-catalyst composed of 0.1 nm Sn/0.1 nm Cu has led to the optimized catalyst composition for the goal of small diameter SiNWs with high density. In addition to catalysts, PECDV conditions also have a significant influence on SiNW size, distribution, morphology, and crystalline structure. In the following, we will focus our study on this important part: the influence of PECVD parameters on SiNW growth.

5.3. **Obtaining 2H-silicon nanowires**

In sub-chapter 5.1, we characterized crystalline structures of SiNWs synthesized with larger CuSn co-catalysts (1 nm Sn/0.8 nm Cu, 65 at% Cu and 1 nm Sn/0.2 nm Cu, 31 at% Cu) by TEM. The observed SiNWs had total diameters (crystalline core + amorphous shell) larger than 10 nm and only cubic structures were found. In sub-chapter 5.2, we have optimized the compositions of CnSn co-catalyst for the purpose of obtaining small diameter SiNWs and we found that 0.1 nm Sn/0.1 nm Cu has led to the smallest diameter SiNWs with high density under the current PECVD conditions. In this sub-section, firstly we investigate the crystalline structures of thin SiNWs (diameter < 10 nm) by TEM (sub-section 5.3.1); then we study the influence of PECVD conditions on NW crystalline structures (sub-section 5.3.2 to 5.3.5) to find the key parameters of hexagonal Si phase. To study the influence of PECVD conditions on SiNW growth, we use the optimized co-catalyst of 0.1 nm Sn/0.1 nm Cu and (100) Si substrate. Based on the typical PECVD process, we investigate the influence of growth temperature, partial pressure of SiH_4, plasma power, and growth time on SiNW growth.

5.3.1. **Influence of NW diameter on its crystalline structure**

In this sub-section, we study crystalline structures of SiNWs synthesized with less CuSn catalyst materials (0.2 nm Sn/0.4 nm Cu, 82 at% Cu and 0.1 nm Sn/0.1 nm Cu, 70 at% Cu) from in Chapter 5.2.2 to investigate the influence of NW diameter on crystalline structures. SiNWs were fabricated with the typical PECVD conditions on (100) Si substrates. SiNWs grown with a co-catalyst of 0.2 nm Sn/0.4 nm Cu (Figure 5.7a) have an average diameter of 9.9 nm with a standard deviation of 1.6 nm; while SiNWs grown with a co-catalyst of 0.1 nm Sn/0.1 nm Cu (Figure 5.7b) have an average diameter of 7.5 nm, with a standard deviation of 1.5 nm. The SiNWs were transferred to TEM grids for TEM observation.

More than 100 SiNWs were observed by TEM. Among these, 17 SiNWs were in the $[110]_C$/$[1\text{-}210]_H$ zone axis, which allowed there unambiguous characterization as cubic or hexagonal. Two of them were found to have hexagonal structure (Figure 5.12). In Figure 5.12a, the NW in the middle has a total diameter of 5.4 nm, with a crystalline core diameter of 4.4 nm. The FFT image of the selected area is shown in the inset, indicating the SiNW has hexagonal structure. We measured $d_{(0002)} = 0.313\ \text{nm}$, and $d_{(10-10)} = 0.336\ \text{nm}$. The ratio of $d_{(10-10)}/d_{(0002)}$ equals to 1.073. The angle of (10-10) plane and (0002) plane is 89.7°. Within the error +/- 0.005 nm, these values are those of the theoretical 2H polytype, which is calculated by Rödl et al.: a = 0.3828 nm, c = 06325 nm [Rödl, 2015]. The theoretical angle between planes of (10-10) and (0002) is 90°. In Figure 5.12b, the SiNW has a total diameter of 7.0 nm, with a crystalline core diameter of 5.3 nm. The FFT images of the selected areas are shown in the insets. Quite interestingly, at the bottom part, the NW has cubic structure, as indicated by the FFT image; this could mean that the cubic phase has become less stable than the hexagonal one at a certain point. In the middle part, the NW has hexagonal phase, with $d_{(0002)} = 0.311\ \text{nm}$, and $d_{(10-10)} = 0.332\ \text{nm}$. The ratio of $d_{(10-10)}/d_{(0002)}$ is 1.068. The angle of (10-10) plane and (0002) plane is 89.6°. Again, taking measurement error into account, these values are equal to the theoretical ones. The two SiNWs with hexagonal phase are both straight. There is no abrupt change in diameter either. They both have small diameters. The observed

SiNWs have total diameters from 4.7 nm to 12.3 nm. However, the thinnest NWs have a cubic structure. Other SiNWs that have similar diameters with the hexagonal SiNWs all have cubic structures.

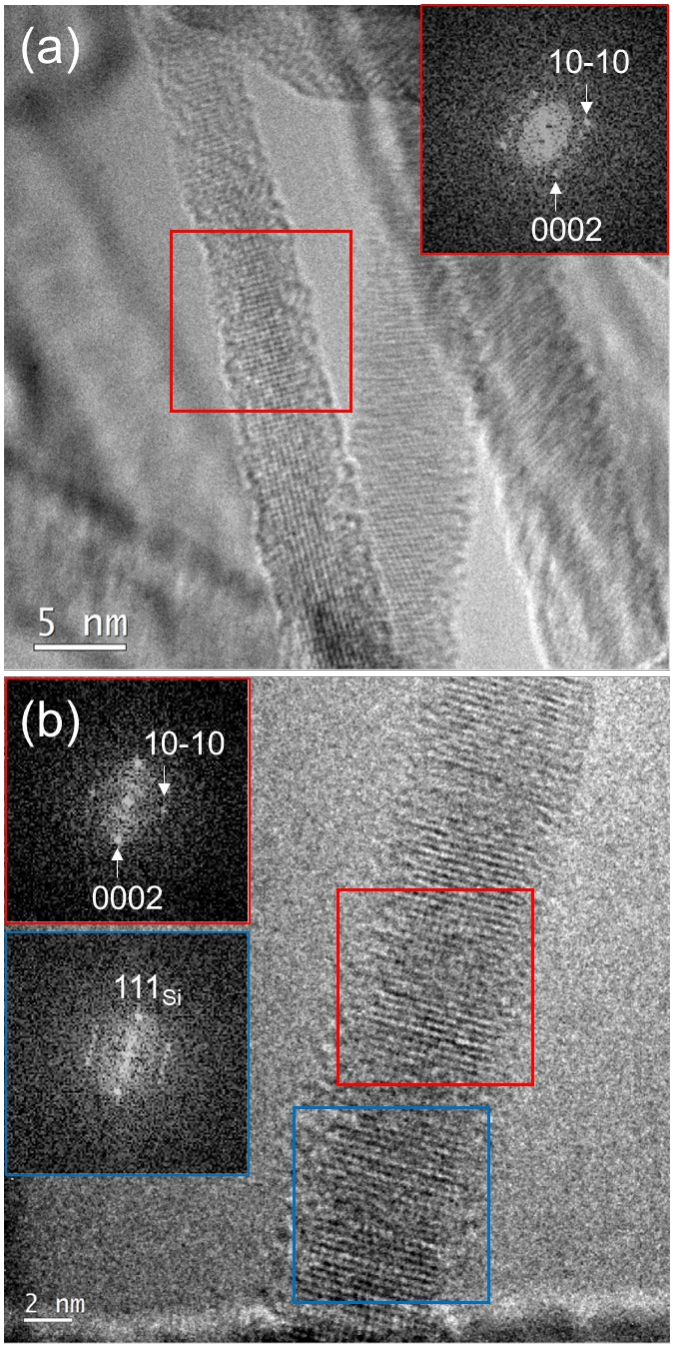

Figure 5.12. Two SiNWs grown with 0.2 nm Sn/0.4 nm Cu, 82at%Cu have partly hexagonal structures. The FFT images of the selected areas are shown in the insets.

In this sample, we thus found two SiNWs with hexagonal phase, with total diameters of 5.4 nm and 7.0 nm. In the following study, we will observe the crystalline structures of thinner SiNWs grown with 0.1

nm Sn/0.1 nm Cu, 70 at% Cu to explore whether the fraction of SiNWs with hexagonal phase will increase when the diameter decreases.

SiNWs grown using a co-catalyst of 0.1 nm Sn/0.1 nm Cu with the typical PECVD conditions (Figure 5.7b) were transferred to TEM grids for TEM characterization. More than 100 SiNWs were observed. The SiNWs have an average total diameter of 6.3 nm with a standard deviation of 0.9 nm. According to the histogram of SiNW diameter distribution (Figure 5.13), all the observed SiNWs have diameters smaller than 9 nm. Most of the NWs have diameter of 6.0-7.5 nm. Compared with the measurements made on SEM images (average diameter of 7.5 nm), the average diameter of SiNWs based on TEM image measurement is smaller. Therefore, due to the limitation of resolution, the SiNW diameter based on SEM measurement is overestimated.

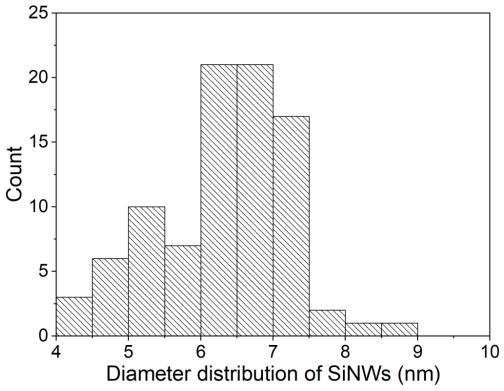

Figure 5.13. Histogram of diameter distribution of SiNWs fabricated with a co-catalyst of 0.1 nm Sn/0.1 nm Cu with the typical PECVD conditions.

In this sample, we found 20 SiNWs in the $[110]_C/[1\text{-}210]_H$ zone axis, among which there was one SiNW with hexagonal phase (Figure 5.14). That NW has a total diameter of 6.5 nm, with a crystalline core diameter of 4.2 nm. At the bottom of the NW (Figure 5.14b), it has alternating hexagonal and cubic phase, which is reflected in the FFT image (Figure 5.14c). Then it switches to hexagonal phase in its middle part (Figure 5.14d). The FFT image (Figure 5.14e) indicates that $d_{(0002)} = 0.314\ \text{nm}$, and $d_{(10-10)} = 0.335\ \text{nm}$. The ratio of $d_{(10-10)}/d_{(0002)}$ is 1.068. The angle of (10-10) plane and (0002) plane is 89.8°.

Again, these values equal those of the theoretical 2H structure within error. At the top part of the crystalline core, the phase is mostly hexagonal with some stacking faults (Figure 5.14f and g). It is notable that the catalyst separation phenomenon has appeared in this sample. The catalyst particle of the crystalline NW core is not at the end of the NW, there's still an amorphous part above the crystalline core, on top of which lies another catalyst particle. This special NW structure with an amorphous top not only exists in the hexagonal NW, but also in cubic NWs.

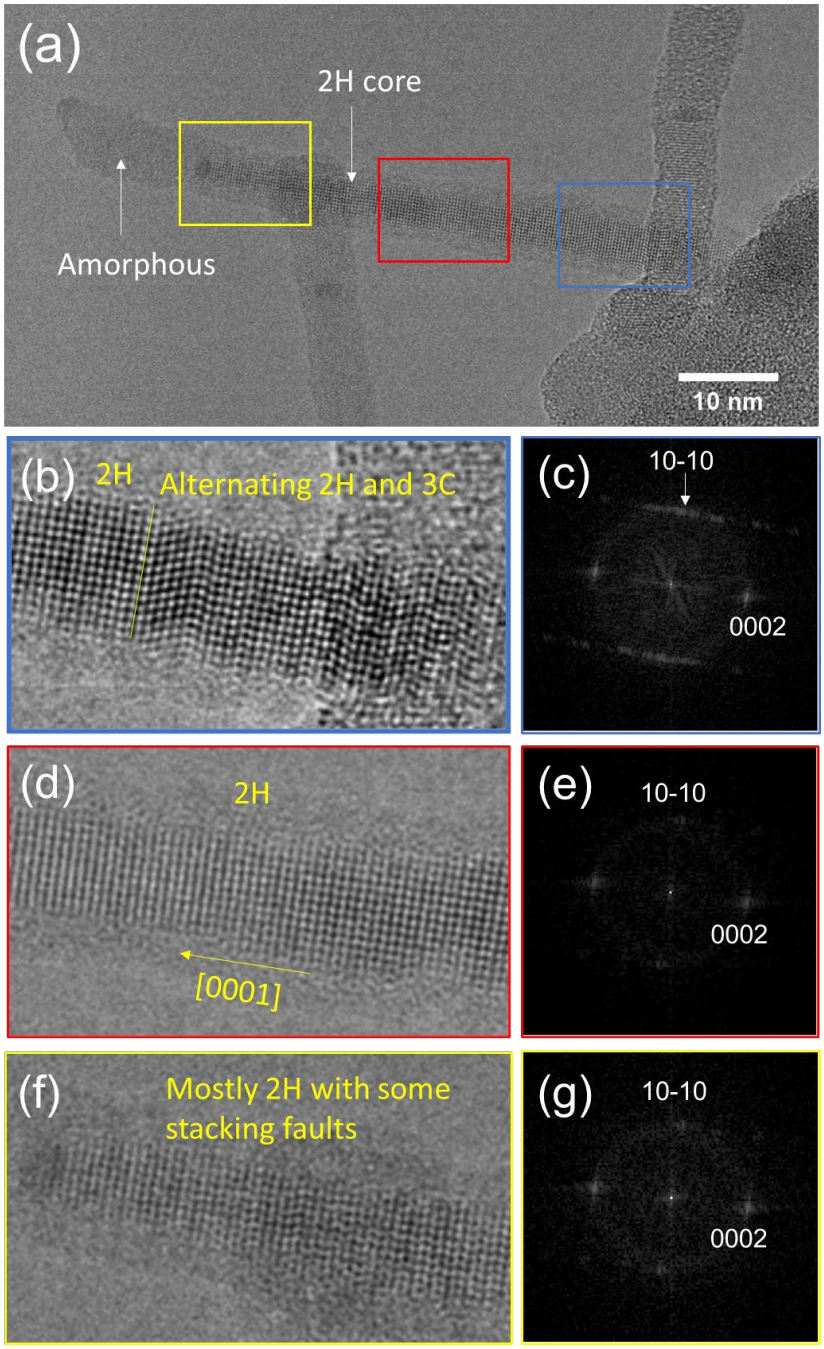

Figure 5.14. HRTEM image of a SiNW with mostly 2H phase. (b) There are alternating 2H and 3C domains at the bottom; (d) 2H phase in the middle; and (f) 2H phase with stacking faults on the top. The corresponding FFT images of (b), (d), (f) are shown in (c), (e), (g).

In this sub-section, we studied the influence of SiNW diameters on crystalline structures. NW diameters decreased with the amount of co-catalyst used. No hexagonal structures were found when NW

diameters were larger than 10 nm. Hexagonal structures were found in SiNWs with total diameters of 5.4 nm, 7.0 nm and 6.5 nm. However, most of the observed SiNWs in the two samples in this sub-section had cubic structures. The diameter of some cubic SiNWs are smaller than that of hexagonal SiNWs. The yield of SiNWs with hexagonal structures did not increase with the NW average diameters decreasing in the studied diameter ranges. In conclusion, SiNW diameter is a crucial factor for hexagonal phase since hexagonal Si is only found in thin SiNWs. However, small diameter is not the only determining factor for hexagonal Si, because most of the SiNWs with similar or smaller diameters still have cubic phase. In order to investigate the other factors for hexagonal structures, we will study the influence of PECVD parameters on SiNW crystalline structures.

5.3.2. **Influence of temperature on NW polytype**

In this sub-section, we investigate the influence of growth temperature on SiNW growth. 0.1 nm Sn/0.1 nm Cu has been used as the catalyst and (100) Si wafer has been used as the substrate. Let us recall the conditions of the typical PECVD process in Table 3.1 here. Catalyst NPs firstly have been through a hydrogen plasma treatment at 200 °C, then temperature has been increased directly to 416 °C for SiNW growth with a precursor of SiH_4.

SiNWs were grown in Plasfil at temperatures of 327, 356, 385, 416 (typical condition) and 447 °C. The other growth parameters remained the same as those of the typical PECVD process. SEM images of SiNWs grown at different temperatures are shown in Figure 5.15. Average diameters of SiNWs based on the SEM images are measured using ImageJ software and are listed from line 1 to 5 in Table 5.2 at the end of the present section together with the PECVD parameters. When compared to the previous values, this gives us a rough idea about the repeatability of the experiment from the evaporation of ultra-small amount of Cu and Sn materials to SiNW growth. We observe a variation of about 1 nm in average SiNW diameter from sample to sample, while keeping all conditions the same. This variation probably comes from: *i*) the uncertainty of evaporation of 0.1 nm films of metals, *ii*) the local variation of plasma conditions and temperature as well as *iii*) the uncertainty of the SEM analysis. We find that 327 °C is close to the minimum

temperature for SiNW growth under the current conditions. At this temperature, the NWs are shorter and much less dense (Figure 5.15a) when compared with NWs grown at higher temperatures. According to the statistics, the SiNWs have a diameter distribution of 6.6 ± 1.0 nm, a smaller average than in the other samples. When growth temperatures are between 356-447 °C, the average diameters have little change over the temperature (Figure 5.15b to e), with values between 7.5 and 7.9 nm. We also present for comparison a PECVD experiment performed at 356 °C with pure Sn catalyst of 1 nm nominal thickness, while the other conditions were the same as the typical process. The SiNWs obtained are very short and have a low density (Figure 5.15f). Using CuSn co-catalyst makes it possible to synthesize dense SiNWs at relatively low temperature around 350 °C.

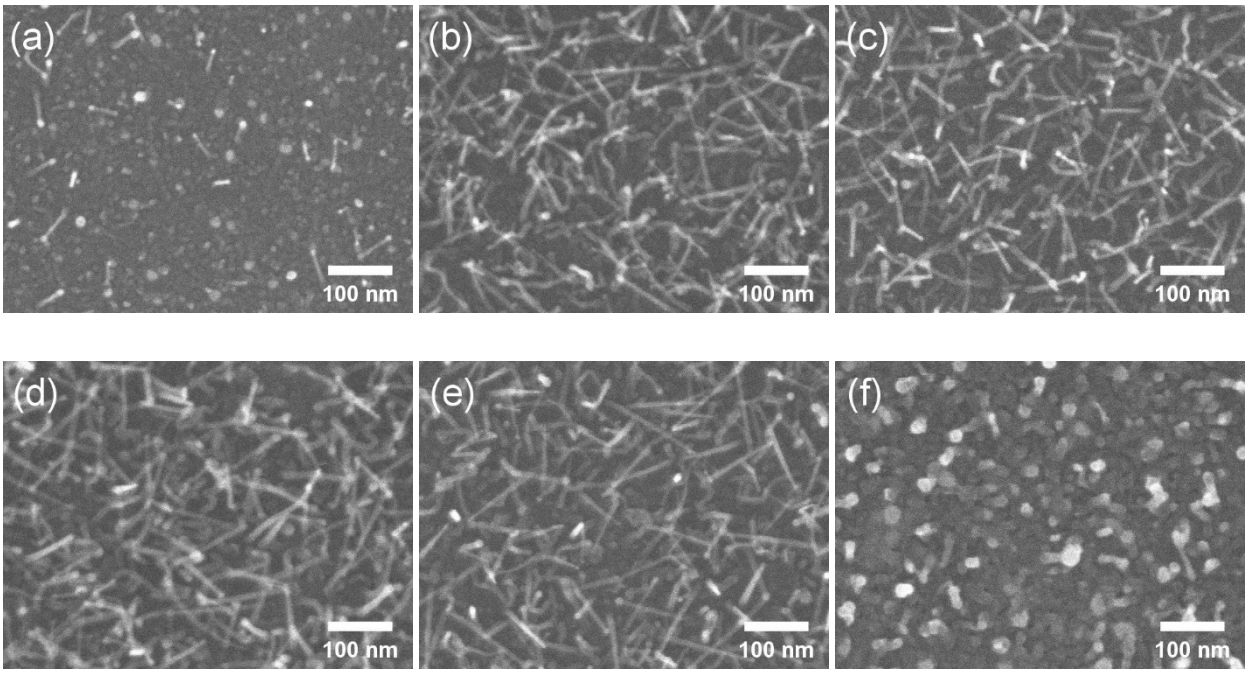

Figure 5.15. SEM images of SiNWs grown with 0.1/0.1 nm Cu/Sn co-catalyst at (a) 327 °C, (b) 356 °C, (c) 385 °C, (d) 416 °C and (e) 447 °C; (f) SiNWs grown with 1 nm Sn catalyst at 356 °C.

We also carried out a PECVD experiment performed at 327 °C with 1 nm pure Sn catalyst, while the other conditions were the same as the typical process. However, we barely obtained any SiNWs. Using a CuSn co-catalyst can lower the minimum growth temperature of SiNWs compared with using pure Sn

catalyst. We assume it is relevant to the existence of the liquid shell. With the assistance of the liquid shell, it might be easier for Si atoms diffusion in Cu and for the formation of Cu_3Si. However, the observed minimum growth temperatures of SiNWs grown with both catalysts are significantly higher than their melting temperatures under the current experimental conditions. This is probably because: 1) the solubility of Si in catalyst metals is relatively low at such temperatures. And those catalyst NPs only have diameters of a few nanometers, there are limited number of Si atoms that can be dissolved in the catalysts, which makes NW growth difficult to process; 2) diffusion rate of Si atoms are low at lower temperatures. As a result, catalyst NPs have already been buried by amorphous Si before they can incubate any SiNWs.

Now we characterize the crystalline structures of SiNWs grown at different temperatures by TEM. In Chapter 3.2 and Chapter 5.3.1, we reported that hexagonal structures were found in SiNWs grown at 385 °C and 416 °C on Cu TEM grids and (100) Si substrates respectively. Now we want to try SiNW growth at a higher temperature to see if we can obtain more NWs with hexagonal phase. Therefore, we choose the SiNWs grown at 447 °C (Figure 5.15e) for TEM observation. The SiNWs have an average diameter of 7.9 nm based on the measurement results of the SEM image.

More than 50 SiNWs were observed, while only 8 NWs were in the zone axis. We found 1 SiNW with hexagonal phase (Figure 5.16). The SiNW has a total diameter of 8.1 nm with crystalline core diameter of 7.2 nm. Like other SiNWs with hexagonal phase in the thesis, this NW is straight. The selected area diffraction pattern of the NW shows a pattern of hexagonal phase, with $d_{(0002)} = 0.313$ nm, $d_{(10-10)} = 0.334$ nm. According to the results above, we found that hexagonal SiNWs are reproducible within a certain range of temperatures (385 - 447 °C). Next, we continue our exploration by investigating the influence of partial pressures of H_2/SiH_4 on SiNW crystalline structures.

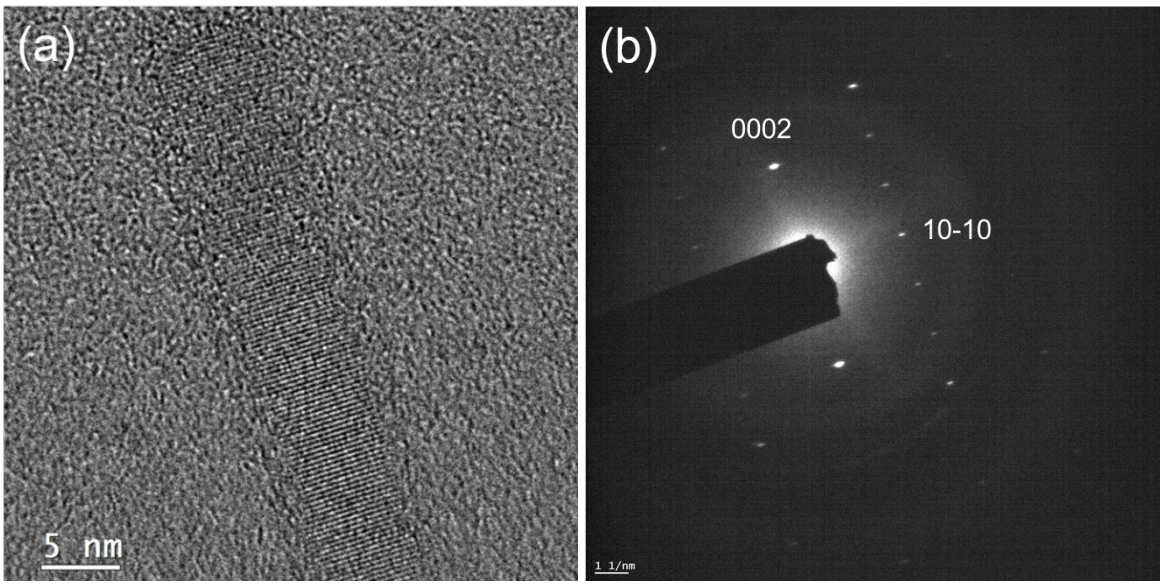

Figure 5.16. HRTEM image of a SiNW with hexagonal phase synthesized at 447 °C and (b) its selected area diffraction pattern.

5.3.3. **Influence of SiH4 partial pressure on NW polytype**

In the following, we discuss the influence of the partial pressure of SiH_4 on NW diameter. We used 0.1 nm Sn/0.1 nm Cu co-catalyst and (100) c-Si substrates. A sample fabricated with the typical process at a total pressure of 1.42 mbar is shown in Figure 5.17a (P_{SiH4} = 0.068 mbar). In Figure 5.17b, the SiNWs were synthesized with 2 sccm SiH_4 and 200 sccm H_2 and carried out growth at 2.58 mbar (P_{SiH4} = 0.026 mbar), while other parameters remained the same with the typical conditions. In Figure 5.17c, the SiNWs were synthesized with 10 sccm SiH_4 and 50 sccm H_2 at a total pressure of 1.42 mbar (P_{SiH4} = 0.237 mbar) and the while other conditions were not changed. Thus, the partial pressure P_{SiH4}/P_{H2} of the samples from (a) to (c) were: 0.068/1.352 mbar, 0.026/2.554 mbar, and 0.237/1.183 mbar. Compared with the SiNWs in figure (a), the SiNWs become thinner and shorter (50-100 nm) in figure (b) with a lower SiH_4 partial pressure; whereas the NWs in figure (c) are longer and thicker (200-300 nm) with a higher SiH_4 partial pressure The diameter distributions of the three samples were: 7.5 ± 2 nm, 6.0 ± 0.7 nm and 11.3 ± 1.0 nm based on measurement of SEM images. The SiNWs grown with a lower partial pressure of SiH_4 (P_{SiH4} = 0.026 mbar) have broken the record of the smallest SiNW total diameter in this thesis. The average

diameters of the SiNWs and the growth conditions are listed in line 4, 6, and 7 in Table 5.2. Therefore, we found that the higher the partial pressure of SiH_4, the thicker and the longer the SiNWs are.

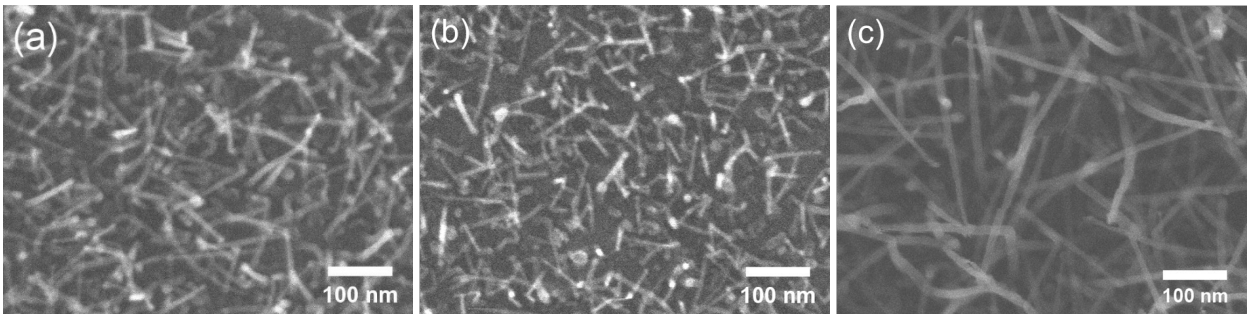

Figure 5.17. SiNWs grown with: (a) 5/100 sccm SiH_4/H_2 at a total pressure of 1.42 mbar (P_{SiH4}/P_{H2}= 0.068/1.352 mbar), (b) 2/200 sccm SiH_4/H_2 at a total pressure of 2.58 mbar (P_{SiH4}/P_{H2}= 0.026/2.554 mbar), (c) 10/50 sccm SiH_4/H_2 at a total pressure of 1.42 mbar (P_{SiH4}/P_{H2}=0.237/1.183 mbar), with respect to line 4, 6 and 7 in 0.

With the partial pressure of SiH_4 increasing, the supersaturation of Si atoms increases, therefore the driving force for SiNW axial growth rate increases [Givargizov, 1973, Givargizov, 1975]. At the meantime, the lateral deposition rate of amorphous silicon on NWs also increases with the partial pressure of SiH_4, as we can see the SiNWs in Figure 5.17c are more tapered than the other two samples in a and b. Next, the SiNWs of the samples from Figure 5.17b and c are transferred to TEM grids for crystalline structure observation. Since NW diameters are likely to be overestimated by SEM measurement, we will measure the NW diameters on TEM images.

For SiNWs grown with a lower partial pressure of SiH_4 (P_{SiH4} = 0.026 mbar), we observed more than 100 SiNWs by TEM. Among the observed SiNWs, 17 of them are in the zone axis. One SiNW has hexagonal phase (Figure 4.8). The NW has a total diameter of 6.8 nm, with a crystalline core diameter of 5.7 nm. The NW changes growth direction at the top part (Figure 5.18a). We found hexagonal structure at the bottom part of the NW (Figure 5.18b). In fact, there are alternating hexagonal and cubic phases, The FFT image of figure b is shown is Figure 5.18c. The upper part of the NW is far away from the zone axis,

as a result, we are not able to know its structure. Hexagonal structures are present, however, most SiNWs are still cubic. Next, we study the crystalline structures of SiNWs grown with nine times higher SiH_4 partial pressure (0.237 mbar).

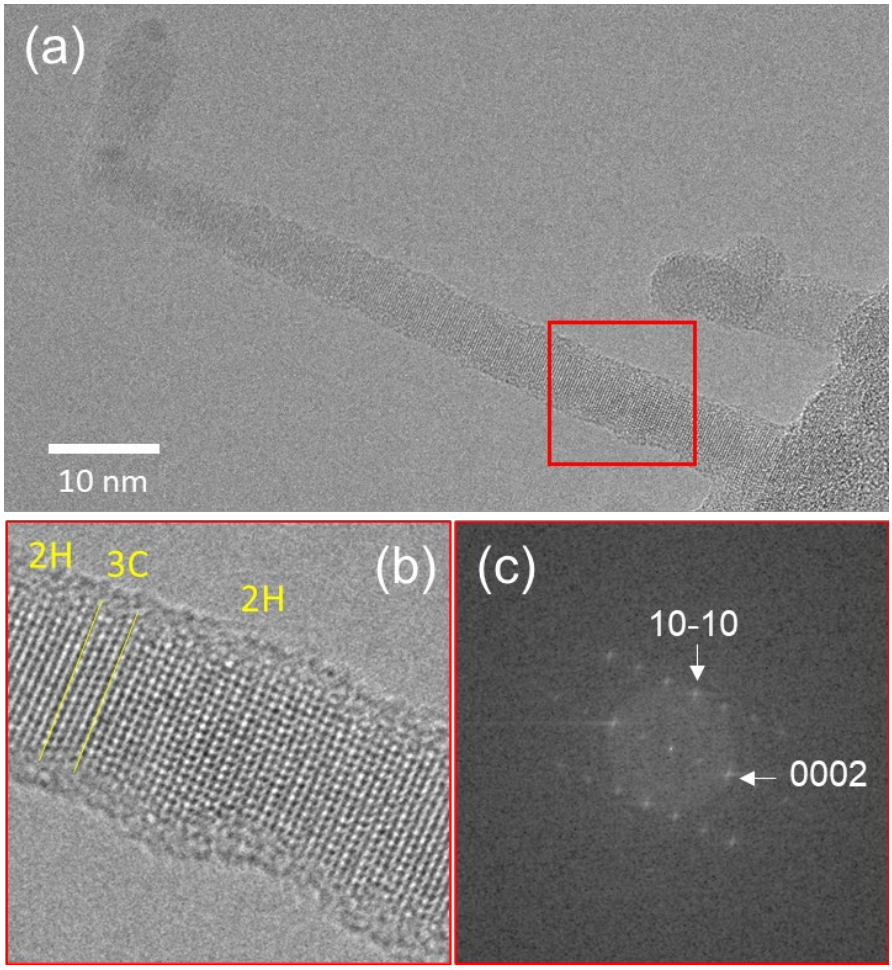

Figure 5.18. (a) SiNW with hexagonal phase synthesized with a lower partial pressure of SiH_4 (0.026 mbar) using a co-catalyst of 0.1 nm Sn/0.1 nm Cu. (b) and (c) A HRTEM image of alternating hexagonal and cubic structures and its FFT image.

According to TEM observation, SiNWs grown with a higher partial pressure of SiH_4 (0.237 mbar) have an average diameter of 11.1 nm, which is close to SEM measurement results. More than 100 SiNWs were observed, we found 20 cubic SiNWs. We did not observe any SiNWs with hexagonal phase, which can be due to their "large" diameters compared to SiNWs grown with lower SiH_4 partial pressures.

To summarize, hexagonal Si is reproducible in the SiNWs grown with SiH_4 partial pressures of 0.026 mbar and 0.068 mbar. When SiNWs are grown at a higher SiH_4 partial pressures of 0.237 mbar, the SiNWs have an average diameter over 11 nm, among which we don't find hexagonal phase.

5.3.4. **Influence of plasma power NW polytype**

Next, we studied the influence of plasma power on NW growth. SiNWs were grown with a plasma power of 0.5 W, 1.5 W (typical process) and 3 W while other parameters were the same with the typical conditions. SEM images of the SiNWs are shown in Figure 5.19 and the diameter distribution results of these SiNWs are listed in lines 8, 4 and 9 in Table 5.2. The NW diameter distributions of the three samples are: 7.6 ± 1.3 nm, 7.5 ± 2 nm and 7.6 ± 2 nm based on SEM measurement. There is no obvious influence of plasma power on SiNW diameter. While the SiNWs fabricated with the RF power of 0.5 W were shorter than the SiNWs fabricated with a higher RF power.

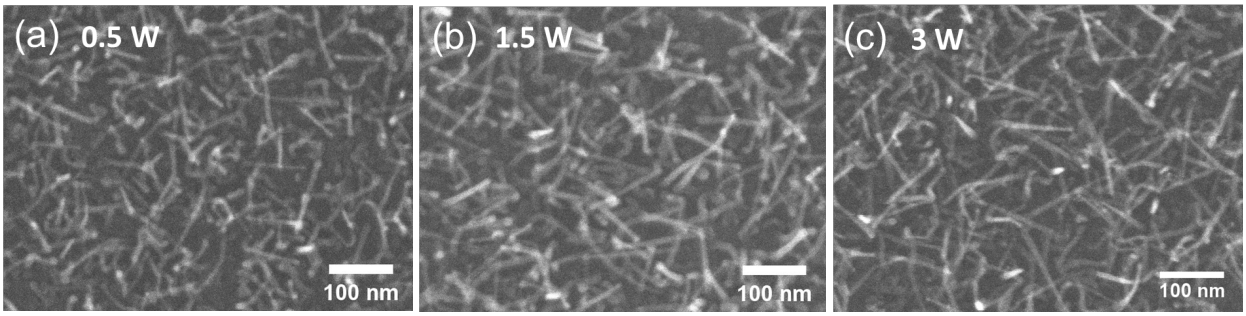

Figure 5.19. SiNWs synthesized by a plasma power of: (a) 0.5 W, (b) 1.5 W, and (c) 3 W, with respect to lines 8, 4 and 9 in Table 5.2.

The SiNWs were transferred to Cu grids for TEM observation. More than 100 SiNWs were observed; we found 16 NWs with the cubic phase and none with hexagonal phase.

5.3.5. **Influence of time duration on SiNW structure and shape**

Finally, we studied SiNW growth as a function of time duration. At the typical conditions, SiNWs were grown for 3 minutes (Figure 5.20a). The lengths of the NWs were around 100-200 nm. When the growth time was increased to 8 min, the NW morphology changed significantly (Figure 5.20b). The lengths of the SiNWs have increased to 300-500 nm. The NWs become tapered because of the a-Si deposition on the NW sidewalls: the diameters of the bottom of the NWs are around 20-25 nm, while the diameters of top of the NWs are smaller than 10 nm, with the catalyst nanoparticles remaining on top. The sidewall deposition rate of the a-Si is about 0.9 nm/min. Moreover, the NW density is lower than the density of those grown for 3 min.

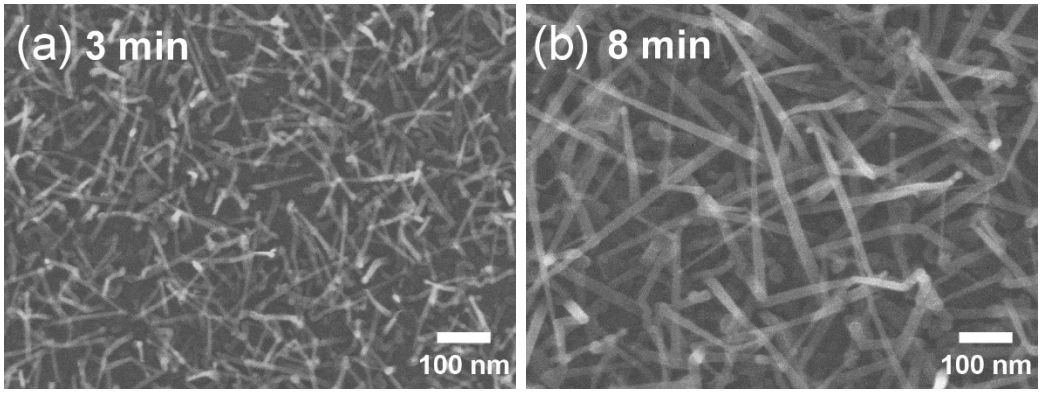

Figure 5.20. SiNWs with a growth time for (a) 3 min and (b) 8 min.

5.4. **Chapter conclusions**

In this chapter, we have firstly studied the crystalline structures of SiNWs synthesized with CuSn catalysts with diameters above 10 nm by TEM, nevertheless, we only found cubic phase in the observed NWs. Next, we have studied the influence of co-catalyst composition and nominal thickness on SiNW. With co-catalyst nominal thickness decreasing, SiNW average diameter decreased until a nominal thickness of 0.1 nm Sn/0.1 nm Cu. Below that deposited thickness, no further decrease is observed, which we attribute to the Gibbs-Thomson effect. A co-catalyst composed of 0.1 nm Sn/0.1 nm Cu has led to the optimized catalyst composition for the goal of small diameter SiNWs with high density. Then we have studied the

influence PECVD conditions on SiNW growth. Table 5.2 has summarized the influence of PECVD parameters on NW diameter distribution (based on SEM measurements). SiNWs remain thin and dense with the varying parameters of the growth temperature, gas pressure and plasma power when mixture of 0.1 nm of Cu and 0.1 nm of Sn is used as the co-catalyst. The NW diameter and density change very little with temperature (from 356 to 447 °C) and plasma power (0.5 to 3 W) in the selected range. Reducing the partial pressure of SiH_4 proved to be useful for decreasing the NW diameter. An average diameter of 6.0 nm of SiNWs with high density has been realized by using a co-catalyst of 0.1 nm Sn/0.1 nm Cu and a low ratio of SiH_4/H_2 partial pressure of 0.026/2.554 mbar. The SiNWs turned to tapered, thicker and less dense after a longer growth time of 8 min.

Table 5.2. Influence of PECVD parameters on NW diameter distribution

	Growth temperature (°C)	Gas pressure (mbar)	Flux of H_2/SiH_4 (sccm)	RF power (W)	NW diameter distribution (nm)
1	327	1.42	100/ 5	1.5	6.6 ± 1.0
2	356	1.42	100/5	1.5	7.9 ± 1.6
3	385	1.42	100/5	1.5	7.5 ± 1.2
4	416	1.42	100/5	1.5	7.5 ± 2
5	447	1.42	100/5	1.5	7.8 ± 1.5
6	416	2.58	200/2	1.5	6.0 ± 0.7
7	416	1.42	50/10	1.5	11.3 ± 1.0
8	416	1.42	100/5	0.5	7.6 ± 1.3
9	416	1.42	100/5	3	7.6 ± 1.3

Table 5.3 summarizes the geometrical properties of all the SiNWs with hexagonal phase grown at different conditions in this thesis and shows their $d_{(10\text{-}10)}$ interplanar spacings and the angles between their (0002) and (10-10) planes, as measured in FFTs and diffraction patterns. We found that hexagonal Si is reproducible from 385 to 447 °C, and within the SiH_4 partial pressure range of 0.026 to 0.068 mbar, and on both Cu TEM grid and (100) Si wafer substrates. The SiNWs with hexagonal phase have crystalline

diameters ranging from 4.0 nm to 7.2 nm, larger than the hexagonal NWs (2-4 nm) reported in [Tang, 2017b]. The total diameters of the hexagonal SiNWs are smaller than 10 nm.

TEM measurement results depend on the equipment used. Even with the same microscope, variations between different magnifications in imaging mode and between imaging and diffraction modes reached 3% on the same object, due to different calibrations and varying departures from the exact [1-210] zone axis [Tang, 2017b]. The averaged $d_{(10\text{-}10)}$ from our experiments is 0.334 nm, close to the theoretical value 0.335 nm. The theoretical bulk values for 2H Si in 0 were derived using the crystal parameters calculated by Rödl et al.: a = 0.3828 nm, c = 06325 nm [Rödl, 2015]. We estimate the relative measurement error for $d_{(10\text{-}10)}$ to be within +/- 0.2%. The averaged $d_{(10\text{-}10)}/d_{(0002)}$ ratio is 1.069 nm, close to the theoretical value 1.068. The angles between planes of (10-10) and (0002) are all close to 90°, the theoretical value. The measurement results confirm that the SiNWs discussed here have hexagonal structure.

2H appears statistically rarely, with no particular condition except the small diameter. The largest hexagonal SiNWs found in this thesis had a NW crystalline diameter of 7.2 nm. Only cubic phases were found in SiNWs with diameters larger than this value. The small size of SiNWs plays an important role for the growth of hexagonal Si, which is in consistent with the calculated results that the 2H phase would be favored in small NWs oriented in the [0002] direction [Kagimura, 2005, Akiyama, 2006]. In the crystalline diameter range of 4.0 – 7.2 nm, the yield of hexagonal SiNWs is around 5-6% most of the time in our experiments. However, small diameter is not the only decisive factor for hexagonal SiNWs with since most of the thin SiNWs still have cubic structures. According to the statistics in [Tang, 2017b], five hexagonal SiNWs (with crystalline diameters in the range of 2 – 4 nm) out of seven SiNWs have been found. Therefore, we assume that the yield of hexagonal SiNWs increases with the NW crystalline diameter decreasing. On (100) Si substrates, we can realize a smallest average diameter of 6.0 nm (whose crystalline diameters are around 4-5 nm) for the moment. To achieve NW crystalline diameters below 4 nm, it is necessary to explore SiNW growth on other substrates with CuSn co-catalysts.

Akiyama, T., K. Nakamura, and T. Ito, *Stacking sequence preference of pristine and hydrogen-terminated Si nanowires on Si(111) substrates.* Physical Review B, 2006. **74**(3): p. 033307. https://doi.org/10.1103/PhysRevB.74.033307

Ashby, M.F. and D.R.H. Jones, *Engineering materials 2: an introduction to microstructures, processing, and design*. International series on materials science and technology ;v. 39. 1988, Oxford [Oxfordshire] ; New York: Pergamon Press. x, 369 p.

Báez, L.A. and P. Clancy, *The kinetics of crystal growth and dissolution from the melt in Lennard-Jones systems.* The Journal of Chemical Physics, 1995. **102**(20): p. 8138-8148. https://doi.org/10.1063/1.469225

Band, Y.B. and Y. Avishai, *Low-Dimensional Quantum Systems*, in *Quantum Mechanics with Applications to Nanotechnology and Information Science*, Y.B. Band and Y. Avishai, Editors. 2013, Academic Press: Amsterdam. p. 749-823. https://doi.org/10.1016/b978-0-444-53786-7.00013-7

Bu, Y.F., M. Zhao, G.X. Zhang, X. Zhang, W. Gao, and Q. Jiang, *Electroreduction of CO2 on Cu Clusters: The Effects of Size, Symmetry, and Temperature.* ChemElectroChem, 2019. **6**(6): p. 1831-1837. https://doi.org/10.1002/celc.201801830

Callister, W.D. and D.G. Rethwisch, *Materials science and engineering : SI version*. 2014.

Capasso, F., F. Beltram, S. Sen, A. PalevskO, and A.Y. Cho, *Quantum Electron Devices: Physics and Applications*, in *High Speed Heterostructure Devices*, R.A. Kiehl and T.C.L.G. Sollner, Editors. 1994, Elsevier. p. 1-77. https://doi.org/10.1016/s0080-8784(08)62475-8

Christian, J.W., *The theory of transformations in metals and alloys: an advanced textbook in physical metallurgy*. International series of monographs in metal physics and physical metallurgy ;v. 7. 1965, Oxford: Pergamon Press. xvi, 973 p.

Dubrovskii, V.G., N.V. Sibirev, G.E. Cirlin, I.P. Soshnikov, W.H. Chen, R. Larde, E. Cadel, P. Pareige, T. Xu, B. Grandidier, J.P. Nys, D. Stievenard, M. Moewe, L.C. Chuang, and C. Chang-Hasnain, *Gibbs-Thomson and diffusion-induced contributions to the growth rate of Si, InP, and GaAs nanowires.* Physical Review B, 2009. **79**(20): p. 205316. https://doi.org/10.1103/PhysRevB.79.205316

Givargizov, E. and A. Chernov, *Rate of whisker growth by the vapor-liquid-crystal mechanism and the role of surface energy.* Sov. Phys. Cryst., 1973. **18**(1): p. 89-92.

Givargizov, E.I., *Fundamental aspects of VLS growth.* Journal of Crystal Growth, 1975. **31**: p. 20-30. https://doi.org/10.1016/0022-0248(75)90105-0

Kagimura, R., R.W. Nunes, and H. Chacham, *Structures of Si and Ge nanowires in the subnanometer range.* Phys Rev Lett, 2005. **95**(11): p. 115502. https://doi.org/10.1103/PhysRevLett.95.115502

Read, A.J., R.J. Needs, K.J. Nash, L.T. Canham, P.D. Calcott, and A. Qteish, *First-principles calculations of the electronic properties of silicon quantum wires.* Phys Rev Lett, 1992. **69**(8): p. 1232-1235. https://doi.org/10.1103/PhysRevLett.69.1232

Rödl, C., T. Sander, F. Bechstedt, J. Vidal, P. Olsson, S. Laribi, and J.F. Guillemoles, *Wurtzite silicon as a potential absorber in photovoltaics: Tailoring the optical absorption by applying strain.* Physical Review B, 2015. **92**(4): p. 045207. https://doi.org/10.1103/PhysRevB.92.045207

Schmidt, V., J.V. Wittemann, S. Senz, and U. Gösele, *Silicon Nanowires: A Review on Aspects of their Growth and their Electrical Properties.* Advanced Materials, 2009. **21**(25-26): p. 2681-2702. https://doi.org/10.1002/adma.200803754

Tan, T.Y., N. Li, and U. Gösele, *Is there a thermodynamic size limit of nanowires grown by the vapor-liquid-solid process?* Applied Physics Letters, 2003. **83**(6): p. 1199-1201. https://doi.org/10.1063/1.1599984

Tang, J., J.L. Maurice, F. Fossard, I. Florea, W. Chen, E.V. Johnson, M. Foldyna, L. Yu, and I.C.P. Roca, *Natural occurrence of the diamond hexagonal structure in silicon nanowires grown by a plasma-*

assisted vapour-liquid-solid method. Nanoscale, 2017b. **9**(24): p. 8113-8118. https://doi.org/10.1039/c7nr01299c

Wikipedia. *Critical radius*. 2020a 2020 Oct 19; Available from: https://en.wikipedia.org/w/index.php?title=Critical_radius&oldid=984376437.

Zhao, B., R. Zhang, Z. Huang, and B. Wang, *Effect of the size of Cu clusters on selectivity and activity of acetylene selective hydrogenation.* Applied Catalysis A: General, 2017. **546**: p. 111-121. https://doi.org/10.1016/j.apcata.2017.08.001

Table 5.3. Growth conditions and TEM measurements of 2H SiNWs compared to theoretical and experimental values from papers.

Catalyst	Substrate	T (°C)	Partial pressure of SiH_4/H_2 (mbar)	Number 2H/3C SiNWs	Crystalline diameter of 2H NWs (nm)	$d_{(10\text{-}10)}$ (nm)	$d_{(10\text{-}10)}/d_{(0002)}$ Ratio	(10-10)-(0002) Angle (°)
1nm Sn	Cu grid	416	1.352/0.068	1/17	6.0	0.333	1.071	89.3
1nm Sn	Cu grid	385	1.352/0.068	1/16	4.0	0.331	1.062	89.5
0.2/0.4 nm Sn/ Cu	c-Si	416	1.352/0.068	2/15	4.4, 5.3	0.336, 0.332	1.073, 1.068	89.7, 89.4
0.1/0.1 nm Sn/ Cu	c-Si	416	1.352/0.068	1/19	4.2	0.335	1.068	89.6
0.1/0.1 nm Sn/ Cu	c-Si	447	1.352/0.068	1/8	7.2	0.334	1.067	89.8
0.1/0.1 nm Sn/ Cu	c-Si	416	2.554/0.026	1/16	5.7	0.337	1.077	89.1
Theoretical bulk 2H Si						0.335	1.068	90
Results from J. Tang's paper					2-4	0.336-0.343	1.064-1.088	85-89.5

References

Akiyama, T., K. Nakamura, and T. Ito, *Stacking sequence preference of pristine and hydrogen-terminated Si nanowires on Si(111) substrates.* Physical Review B, 2006. **74**(3): p. 033307. https://doi.org/10.1103/PhysRevB.74.033307

Ashby, M.F. and D.R.H. Jones, *Engineering materials 2: an introduction to microstructures, processing, and design*. International series on materials science and technology ;v. 39. 1988, Oxford [Oxfordshire] ; New York: Pergamon Press. x, 369 p.

Báez, L.A. and P. Clancy, *The kinetics of crystal growth and dissolution from the melt in Lennard-Jones systems.* The Journal of Chemical Physics, 1995. **102**(20): p. 8138-8148. https://doi.org/10.1063/1.469225

Band, Y.B. and Y. Avishai, *Low-Dimensional Quantum Systems*, in *Quantum Mechanics with Applications to Nanotechnology and Information Science*, Y.B. Band and Y. Avishai, Editors. 2013, Academic Press: Amsterdam. p. 749-823. https://doi.org/10.1016/b978-0-444-53786-7.00013-7

Bu, Y.F., M. Zhao, G.X. Zhang, X. Zhang, W. Gao, and Q. Jiang, *Electroreduction of CO2 on Cu Clusters: The Effects of Size, Symmetry, and Temperature.* ChemElectroChem, 2019. **6**(6): p. 1831-1837. https://doi.org/10.1002/celc.201801830

Callister, W.D. and D.G. Rethwisch, *Materials science and engineering : SI version*. 2014.

Capasso, F., F. Beltram, S. Sen, A. PalevskO, and A.Y. Cho, *Quantum Electron Devices: Physics and Applications*, in *High Speed Heterostructure Devices*, R.A. Kiehl and T.C.L.G. Sollner, Editors. 1994, Elsevier. p. 1-77. https://doi.org/10.1016/s0080-8784(08)62475-8

Christian, J.W., *The theory of transformations in metals and alloys: an advanced textbook in physical metallurgy*. International series of monographs in metal physics and physical metallurgy ;v. 7. 1965, Oxford: Pergamon Press. xvi, 973 p.

Dubrovskii, V.G., N.V. Sibirev, G.E. Cirlin, I.P. Soshnikov, W.H. Chen, R. Larde, E. Cadel, P. Pareige, T. Xu, B. Grandidier, J.P. Nys, D. Stievenard, M. Moewe, L.C. Chuang, and C. Chang-Hasnain, *Gibbs-Thomson and diffusion-induced contributions to the growth rate of Si, InP, and GaAs nanowires.* Physical Review B, 2009. **79**(20): p. 205316. https://doi.org/10.1103/PhysRevB.79.205316

Givargizov, E. and A. Chernov, *Rate of whisker growth by the vapor-liquid-crystal mechanism and the role of surface energy.* Sov. Phys. Cryst., 1973. **18**(1): p. 89-92.

Givargizov, E.I., *Fundamental aspects of VLS growth.* Journal of Crystal Growth, 1975. **31**: p. 20-30. https://doi.org/10.1016/0022-0248(75)90105-0

Kagimura, R., R.W. Nunes, and H. Chacham, *Structures of Si and Ge nanowires in the subnanometer range.* Phys Rev Lett, 2005. **95**(11): p. 115502. https://doi.org/10.1103/PhysRevLett.95.115502

Read, A.J., R.J. Needs, K.J. Nash, L.T. Canham, P.D. Calcott, and A. Qteish, *First-principles calculations of the electronic properties of silicon quantum wires.* Phys Rev Lett, 1992. **69**(8): p. 1232-1235. https://doi.org/10.1103/PhysRevLett.69.1232

Rödl, C., T. Sander, F. Bechstedt, J. Vidal, P. Olsson, S. Laribi, and J.F. Guillemoles, *Wurtzite silicon as a potential absorber in photovoltaics: Tailoring the optical absorption by applying strain.* Physical Review B, 2015. **92**(4): p. 045207. https://doi.org/10.1103/PhysRevB.92.045207

Schmidt, V., J.V. Wittemann, S. Senz, and U. Gösele, *Silicon Nanowires: A Review on Aspects of their Growth and their Electrical Properties.* Advanced Materials, 2009. **21**(25-26): p. 2681-2702. https://doi.org/10.1002/adma.200803754

Tan, T.Y., N. Li, and U. Gösele, *Is there a thermodynamic size limit of nanowires grown by the vapor-liquid-solid process?* Applied Physics Letters, 2003. **83**(6): p. 1199-1201. https://doi.org/10.1063/1.1599984

Tang, J., J.L. Maurice, F. Fossard, I. Florea, W. Chen, E.V. Johnson, M. Foldyna, L. Yu, and I.C.P. Roca, *Natural occurrence of the diamond hexagonal structure in silicon nanowires grown by a plasma-*

assisted vapour-liquid-solid method. Nanoscale, 2017b. **9**(24): p. 8113-8118. https://doi.org/10.1039/c7nr01299c
Wikipedia. *Critical radius*. 2020a 2020 Oct 19; Available from: https://en.wikipedia.org/w/index.php?title=Critical_radius&oldid=984376437.
Zhao, B., R. Zhang, Z. Huang, and B. Wang, *Effect of the size of Cu clusters on selectivity and activity of acetylene selective hydrogenation.* Applied Catalysis A: General, 2017. **546**: p. 111-121. https://doi.org/10.1016/j.apcata.2017.08.001

Chapter 6. Silicon nanowire growth with other Cu-based mixed catalysts

In Chapter 5, we have successfully obtained small and dense SiNWs with hexagonal structure (with a yield of about 5 %) using a co-catalyst of SnCu and (100) Si substrates. In this section, we look into other possibilities of growing SiNW with Cu-based mixed catalysts. On the basis of our previous experience with SnCu co-catalysts with the special core-shell structure, we will explore the use of Cu as the core catalyst, while we use other metals as catalysts instead of Sn for NW nucleation and growth. We choose two metals to make mixed catalysts with Cu respectively: Indium (In) and gold (Au). The reasons are as follows:

i) In can be used as a catalyst for SiNW growth [Wang, 2009, Yu, 2009, Zardo, 2010] and it can form a eutectic alloy with Cu like Sn, but at a lower temperature of 153 °C [Subramanian, 1989]. Therefore, it is natural to assume that In might act like Sn when it makes a mixed catalyst during SiNW growth.

ii) Au has been widely used to catalyze SiNW growth [Cui, 2001a, Hofmann, 2003, Wu, 2004, Hannon, 2006, Tian, 2007] and can form a eutectic alloy with Si at 363 °C [Okamoto, 1983], while it can also form compounds with Cu [Fedorov, 2016]. Thus, we assume that the Au-Si eutectic alloy may also perform as a liquid shell during SiNWs growth when Au is mixed with Cu.

Because of the reasons above, it is interesting to investigate SiNW growth with the two novel Cu-based mixed catalysts. In this chapter, we fabricate SiNWs with InCu (Section 6.1) and AuCu (Section 6.12) mixed catalysts and study their individual structural properties as well as the statistical distribution of key geometric parameters and their correlations to the deposited catalyst distribution. The SiNW distribution, diameter and morphology will be studied by SEM and NW crystalline structures will be characterized by TEM.

6.1. **SiNW growth with InCu mixed catalysts**

Indium has an atomic number of 49, on the left of Sn in the periodic table of elements. It is most notably used in the semiconductor industry to make low-melting-point metal alloys such as solders, and in

the production of transparent conductive coatings of indium tin oxide (ITO) on glass [Darveaux, 1990, Alfantazi, 2003, Liu, 2006, Park, 2008]. Indium has a low melting point of 156.6 °C and has the same density as Sn (7.31 g/cm^3). Indium has been reported as a catalyst for SiNW growth [Wang, 2009, Yu, 2009, Zardo, 2010]. The Si-In phase diagram is shown in Figure 6.1 [Olesinski, 1985]. Indium not only resembles Sn in density and low melting point, but also its binary phase diagram with Si looks similar to that of Si-Sn [Olesinski, 1984]. Both In and Sn can form eutectic alloys with Si, and the solubilities of Si in the two metals are very low (0.25% at 707 °C in Sn [Olesinski, 1984] and 0.095% at 495 °C in In [Olesinski, 1985]). In addition, according to the Cu-In phase diagram in Figure 6.2 [Subramanian, 1989], Cu can form an eutectic alloy with In at 153 °C with a composition of 98.4 at% In, similar to Sn (at 227 °C with a composition of 98.7 at% Sn). Therefore, considering the growth dynamics using SnCu mixed catalysts, it is reasonable to expect that the InCu alloy will behave similarly as a co-catalyst for SiNW growth. In this sub-chapter, we will introduce SiNW growth using InCu mixed catalysts.

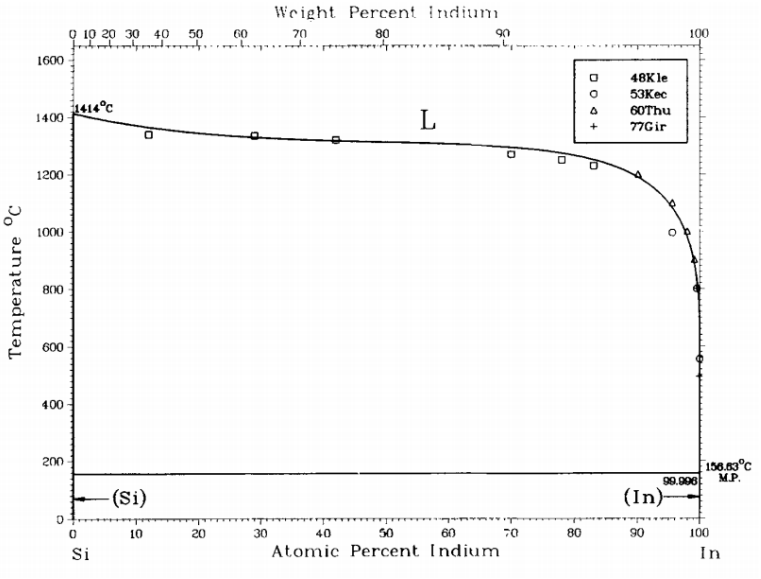

Figure 6.1. Si-In binary phase diagram [Olesinski, 1985].

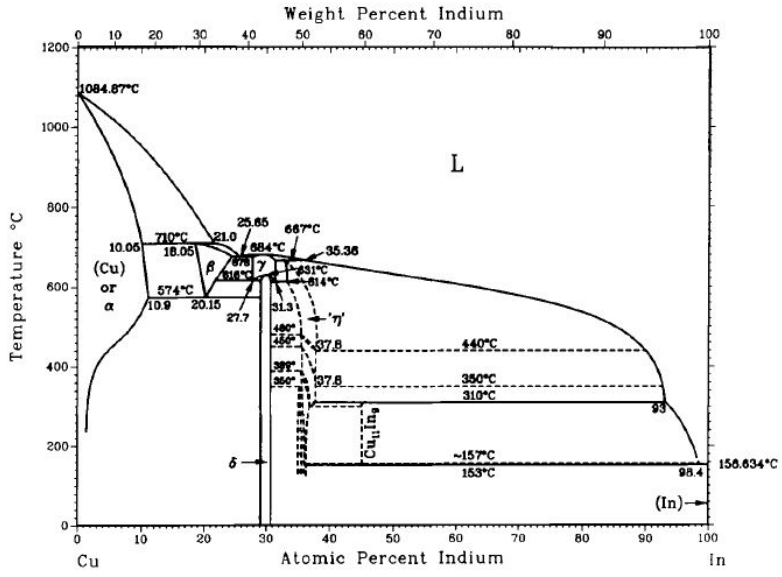

Figure 6.2. Cu-In binary phase diagram. [Subramanian, 1989].

6.1.1. **Structure of InCu mixed catalyst nanoparticles**

Firstly, we investigate the crystalline structure of InCu mixed catalyst NPs at each step of the experiments by using TEM. To prepare InCu mixed catalysts, Cu was firstly evaporated directly on the

amorphous carbon membrane of carbon-coated gold TEM grids for the convenience of TEM observation, and then In was evaporated on the top of Cu, which is similar to the preparation of SnCu co-catalysts.

As-deposited NPs

The as-deposited mixed catalyst of 1 nm In/1 nm Cu (30 at.% In) have formed NPs after thermal evaporation, as shown in Figure 6.3. The NPs have diameters around 4 to 8 nm. No dots or patterns are found in its FFT image.

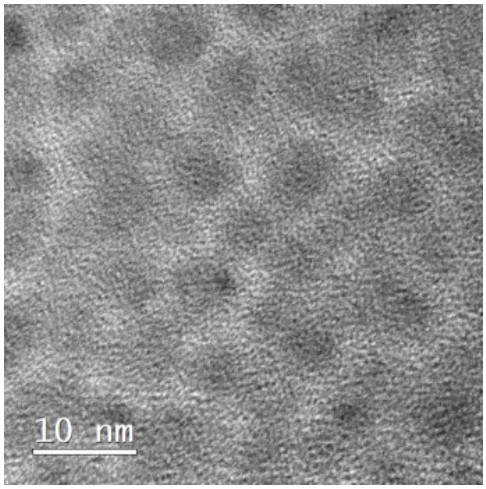

Figure 6.3. As-deposited mixed catalyst NPs of 1 nm In/1 nm Cu after thermal evaporation.

Catalyst NPs after hydrogen plasma treatment at 200 °C

Next, the substrates with the as-deposited NPs above were loaded into the PECVD reactor Plasfil for a hydrogen plasma treatment at 200 °C following the first step of the typical process as introduced in Chapter 3. The catalyst NPs after the treatment become larger, with diameters around 6 to 13 nm, as shown in Figure 6.4. We can see some atomic planes in some catalyst NPs. The FFT result in the inset of the figure shows that there is only one group of atomic planes with an interplanar spacing of 0.21 nm with different orientations, corresponding to the (111) planes of Cu. This spacing is also present in Cu_2In and Cu_7In_3 compounds, but it corresponds to secondary spots in these compounds. Thus, the present spots most likely come from pure Cu. This indicates that Cu would have crystalized and formed an ordered structure during

the hydrogen plasma treatment, similarly to what we observed for Cu in SnCu co-catalysts during the plasma treatment (see chapter 4.2).

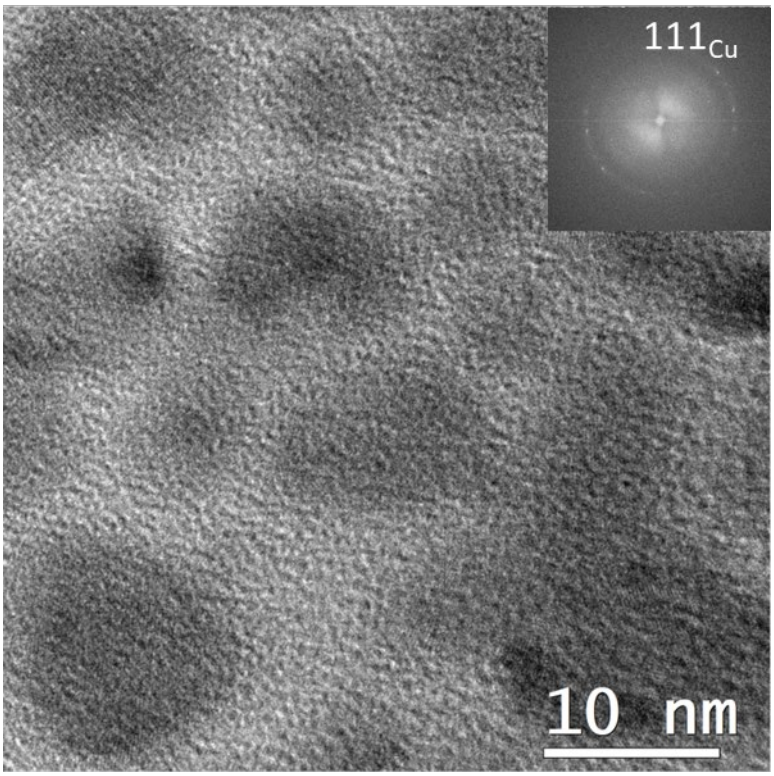

Figure 6.4. Mixed catalyst NPs of 1 nm In/1 nm Cu after a hydrogen plasma treatment at 200 °C for 2 minutes, FFT in inset.

SiNW growth with InCu catalysts

Let us now observe the SiNW growth with InCu catalysts. We prepared two catalyst compositions: a Cu-rich catalyst of 1 nm In/1 nm Cu (30 at.% In/70 at.% Cu), and an In-rich catalyst of 2 nm In/0.4 nm Cu (68 at.% In/32 at.% Cu). SiNWs have been grown successfully at 416 °C for 3 minutes following the typical conditions on (100) Si substrates. SiNWs grown with the Cu-rich mixed catalyst show a bi-modal distribution in diameter: both thin NWs (≤ 10 nm) and thick (≥ 25 nm) NWs are present as shown in the SEM image (Figure 6.5a), which is similar to the SiNWs synthesized with SnCu co-catalyst of about the same amount (see Figure 5.3). Meanwhile, the SiNWs grown with the In-rich catalyst do not show an

obvious bi-modal distribution in diameter (see Figure 6.5b); most SiNWs have diameters around 20-25 nm. Then the SiNWs were transferred to gold grids for TEM observation and EDX analysis.

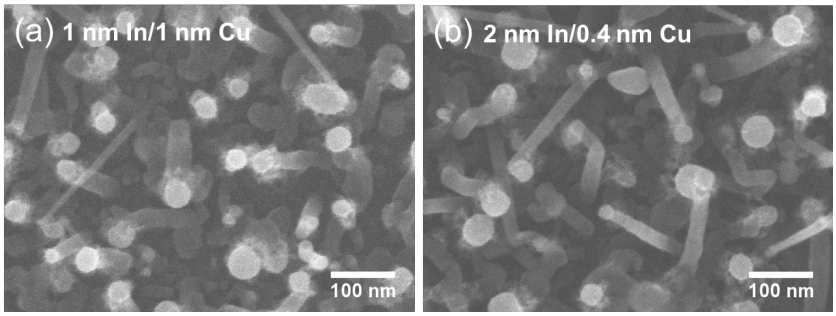

Figure 6.5. SEM images of SiNWs grown with a mixed catalyst of (a) 1 nm In/1 nm Cu and (b) 2 nm In/0.4 nm Cu following the typical PECVD conditions on (100) Si substrates.

Structure of catalyst NPs after SiNW growth

Next, we observe the crystalline structure of the mixed catalyst NPs after SiNW growth. First, let us study the crystalline structure of the Cu-rich mixed catalyst NPs. A TEM image of the catalyst NPs of 1 nm In/1 nm Cu after SiNW growth is shown in Figure 6.6. The mixed catalyst NPs have diameters ranging from 15 nm to 30 nm, which are about twice the size of the NPs obtained after the hydrogen plasma treatment (see Figure 6.4). Unlike the Cu-rich SnCu co-catalyst NPs, which usually have a typical shape (crystalline bottom with facets plus a hemispherical top with a darker contrast, see Figure 4.23) that is due to the phase separation; the Cu-rich InCu mixed catalyst NPs do not have a typical shape. And there is no regular pattern that would indicate a phase separation phenomenon.

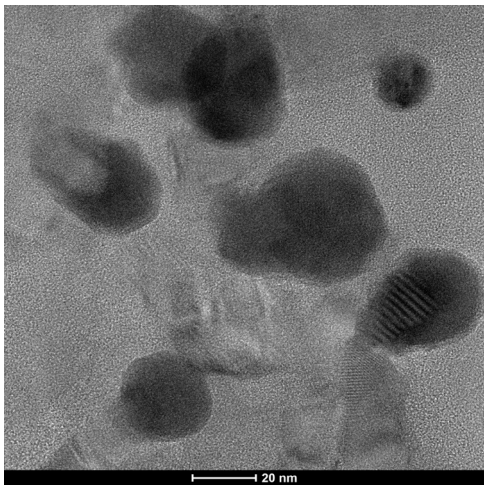

Figure 6.6. SiNWs grown with 1 nm In/1 nm Cu (30 at.% In/70 at.% Cu) mixed catalyst that have been transferred to a gold TEM grid.

In order to verify the composition of the mixed catalyst NPs of 1 nm In/1 nm Cu, we made EDX analysis in three catalyst NPs of the SiNWs (see Figure 6.7). The three spectrums show the presence of In, Cu, Si and O. The atomic ratio of In:Cu is nearly 1:3 in the three catalyst NPs. Thus, we have confirmed that both In and Cu remain present in the catalyst during NW growth.

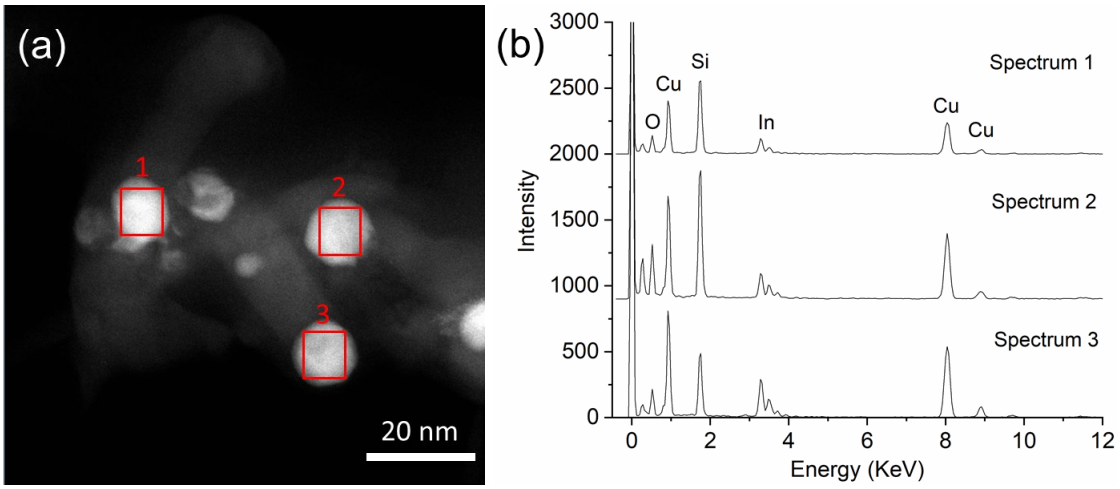

Figure 6.7. (a) HAADF image of the SiNWs grown with 1 nm In/1 nm Cu mixed catalyst; (b) EDX spectra recorded in the squared areas in (a), showing the presence of In, Cu, Si and O in the three catalyst NPs in (a).

Figure 6.8a shows a HRTEM image of a catalyst NP of 1 nm In/1 nm Cu. We selected two areas to make FFT analysis and the results are shown in Figure 6.8b and c. Figure 6.8b shows the FFT spots of (100), (200), (300) and (400) atomic planes of Cu_7In_3 (δ) phase, which correspond to interplanar distances of 0.96 nm, 0.48 nm, 0.32 nm and 0.24 nm [Koster, 1980]. It has been reported that soldering at 290 °C results in alloys consisting of $Cu_{11}In_9$, Cu_2In (η) and Cu_7In_3 (δ) intermetallic phases when using pure In as a filler to fabricate durable Cu/Cu joints for the interconnections of electronic devices [Wojewoda, 2004]. And soldering at 430 °C leads to the presence of a single Cu_7In_3 phase in the joint. Therefore, there is no surprise to find that Cu_7In_3 (δ) phase has formed during SiNW growth with a highest temperature of 416 °C. And Cu_7In_3 (30 at.% In) has the same atomic ratio as that of our evaporated catalyst with the nominal of 1 nm In/1 nm Cu. No evidence of Cu_3Si, Cu, or In phase has been found in the FFT patterns. Thus, it is reasonable to assume that the intermetallic Cu_7In_3 (δ) phase has played a role in catalyzing SiNWs.

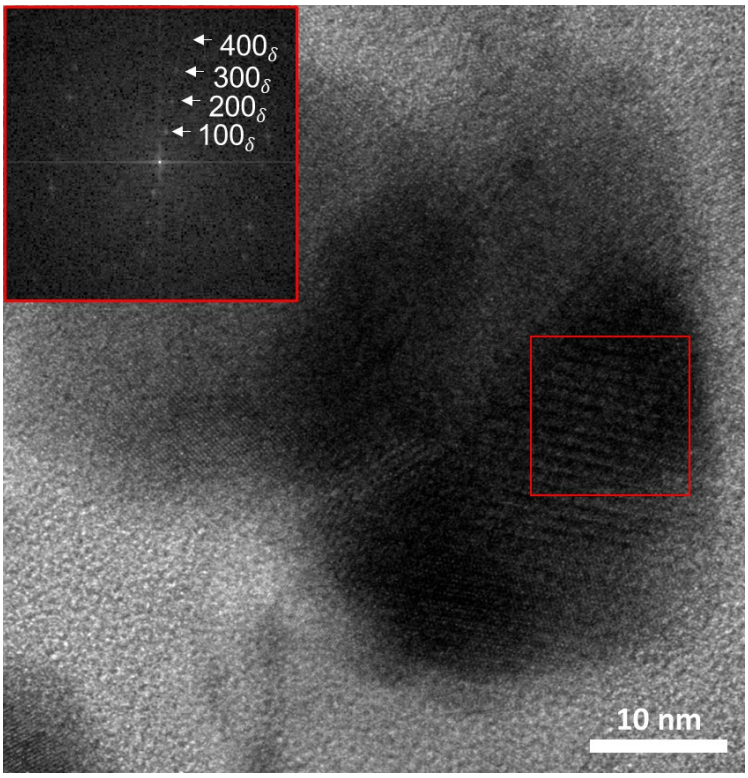

Figure 6.8. HRTEM image of a catalyst NP of 1 nm In/1 nm Cu with its FFT image of the selected area.

Figure 6.9 shows a HRTEM image of another catalyst NP obtained from 1 nm In/1 nm Cu and its FFT image. The "outer shell" of the NP with a darker contrast shows crystalline atomic planes. The FFT pattern indicates the presence of interplanar distances of 0.26 nm, 0.13 nm and 0.19 nm, which are compatible with intermetallics Cu_7In_3 (δ) and Cu_2In (η) [Che, 2013], and also Cu_3Si.

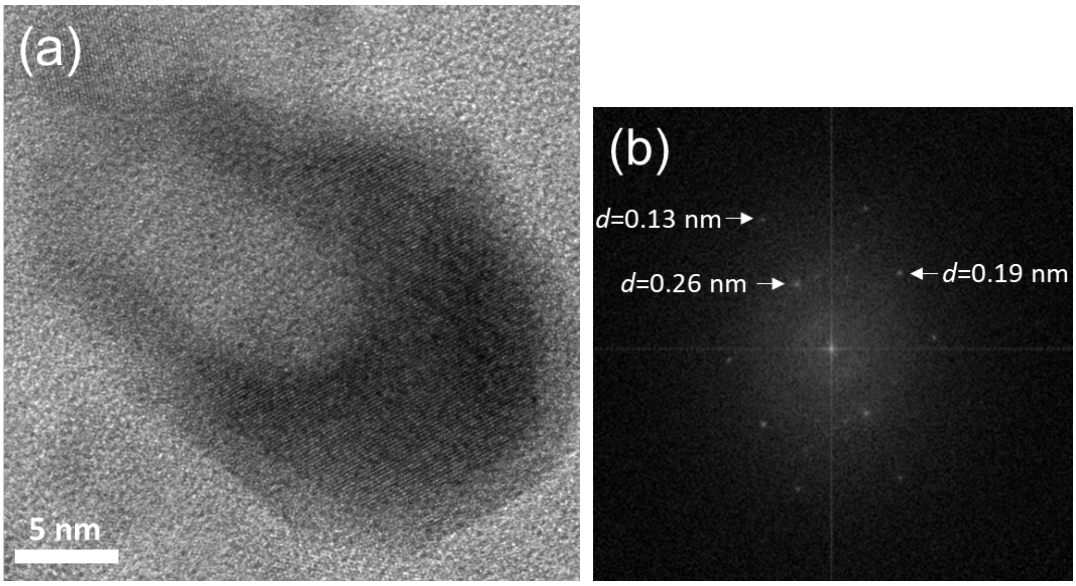

Figure 6.9. HRTEM image of a catalyst NP obtained from 1 nm In/1 nm Cu with its FFT pattern.

We have also observed the catalyst NPs of SiNWs synthesized with an In-rich catalyst of 2 nm In/0.4 nm, for example as shown in Figure 6.10. However, due to the lack of enough information of plane groups, we are not able to determine the phase of the NPs.

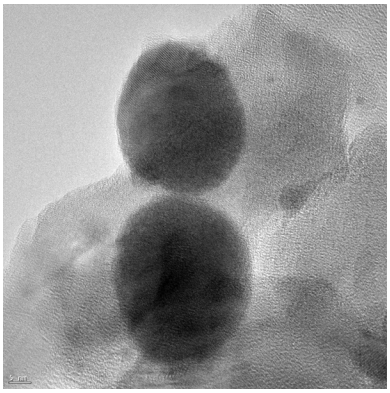

Figure 6.10. Catalyst NPs of SiNWs grown from 2 nm In/0.4 nm Cu following the typical PECVD conditions from 0 (b).

Figure 6.11 depicts the evolution of the structure of InCu mixed catalysts during the PECVD experiment. Cu is firstly evaporated on the substrate and then In is evaporated on top of Cu. The as-deposited InCu mixed catalyst NPs are amorphous like according to TEM observations (see Figure 6.3).

After a hydrogen plasma treatment at 200 °C, Cu has crystallized (see Figure 6.4). Considering this temperature is higher than the melting point of pure In (156.63 °C), In should be melted and is likely to form an In-rich liquid layer (including InCu eutectic alloy and pure In, depending on the evaporated compositions of mixed catalysts) outside the Cu crystal core according to the In-Cu phase diagram (see Figure 6.2). Then the substrate temperature is increased to 416 °C for SiNW growth. Intermetallic phase Cu_7In_3 (δ) and, probably, Cu_2In (η) have formed at elevated temperatures and served as catalysts for NW growth. We do not exclude that there might be more species of catalysts, however.

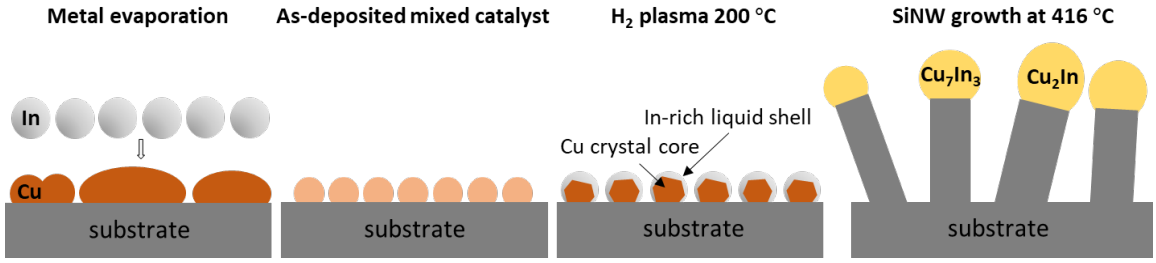

Figure 6.11. Evolution of the structure of InCu mixed catalysts during the PECVD experiment.

6.1.2. **Influence of the amount of InCu catalyst on SiNW growth**

In this section, we study the influence of catalyst amount on SiNW growth (diameter distribution and density). As before, to prepare InCu mixed catalysts, Cu was firstly evaporated on (100) substrates, and then In was evaporated on the top of Cu. InCu mixed catalysts with an increasing amount have been prepared: 0.08 nm In/0.08 nm Cu (30 at.% In/ 70 at.% Cu), 0.1 nm In/0.1 nm Cu, and 1 nm In/1 nm Cu. Then the substrates were transferred to the PECVD reactor for SiNW growth. The growth conditions here were the same as the typical PECVD conditions used for SiNW growth with SnCu co-catalyst (see Table 3.1). SiNWs have also been grown with pure In catalyst (with nominal thickness of 0.1 nm and 1 nm respectively) as control groups. Since we have already known that SiNWs cannot be catalyzed by pure Cu catalyst under the typical conditions from Chapter 4.2, we did not make a control group with Cu catalyst here.

SiNWs have been successfully synthesized with both InCu mixed catalysts and pure In catalysts; the SEM images of the obtained SiNWs with the catalysts mentioned above are shown in Figure 6.12.When SiNWs are grown with 0.08 nm In/0.08 nm Cu, the NW density is low and their average diameter is 10.5 nm (Figure 6.12a); with a catalyst amount increasing to 0.1 nm In/0.1 nm Cu (Figure 6.12b), the NW density has increased while there is no obvious change in NW diameter (average diameter: 10.7 nm). The longest NWs have lengths around 300 nm. By comparing these SiNWs with the NWs grown with 0.1 nm In (Figure 6.12d), we find that the SiNWs grown with InCu mixed catalyst are much denser. When the catalyst amount is increased to and 1 nm In/1 nm Cu (Figure 6.12c), the NW diameter shows broad distribution: from about 10 nm to 30 nm. Whereas the SiNWs grown with pure In catalyst of 1 nm nominal thickness are more homogenous in diameter distribution with an average diameter of 12.0 nm (Figure 6.12e). The longest SiNWs are about 300 nm, which is similar to the NWs in Figure 6.12b. The NW density has increased compared with that of the NWs grown with 0.1 nm In catalyst.

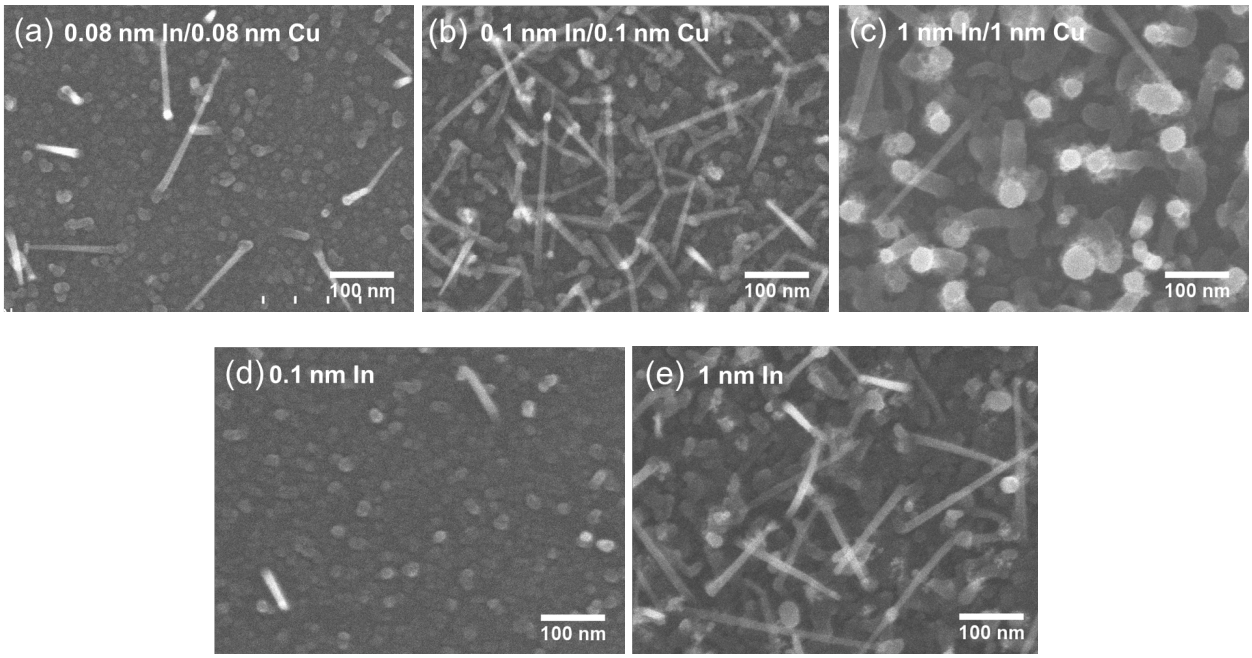

Figure 6.12. SEM images of SiNWs grown with mixed catalysts of (a) 0.08 nm In/0.08 nm Cu; (b) 0.1 nm In/0.1 nm Cu; (c) 1 nm In/1 nm Cu; (d) 0.1 nm In and (e) 1 nm In.

6.1.3. **Crystalline structure of SiNWs grown with InCu catalyst**

We characterize the crystalline structures of the SiNWs synthesized with InCu co-catalysts by TEM in this section. Firstly, we observe the SiNWs grown with a Cu-rich co-catalyst (1 nm In/1 nm Cu) and an In-rich catalyst (2 nm In/0.4 nm Cu) from Figure 6.5. Most of the observed SiNWs have diameters larger than 20 nm. They all have cubic structure.

We have also observed the SiNWs grown with 0.1 nm In/0.1 nm Cu, which have smaller diameters compared with the two samples above. More than 50 SiNWs have been observed by TEM, among these, 11 SiNWs were in the $[110]_C/[1\text{-}210]_H$ zone axis. Ten of them had cubic structures, while one of them contained hexagonal phase. The SiNW with hexagonal structure (see Figure 6.13) has a crystalline diameter around 5 nm, and a total diameter of 7.5 nm with an amorphous shell. We found there is a catalyst separation phenomenon in this SiNW, as has been reported in SnCu catalyzed SiNWs (Chapter 4.3.3). In addition to the catalyst NP connecting to the SiNW crystalline core, there's still an amorphous part above it, on top of

which lies another nanoparticle (Figure 6.4a). Catalyst separation exists not only in the hexagonal NW, but also in small-diameter cubic SiNWs synthesized with InCu catalyst. With the experience of thin SiNWs catalyzed by SnCu co-catalysts, we assume that a similar catalyst separation phenomenon has happened after SiNW growth, in the air ambient due to the use of Cu as a catalyst. An HRTEM image with higher magnification of the selected area in Figure 6.13a is shown in Figure 6.13b. The crystalline structure consists of two parts: above the yellow dash line (which is parallel to the SiNW growth direction) there is a cubic twinning with the twining plane indicated by the white dash line; below the yellow dash line, there is a hexagonal phase, which has been confirmed by the FFT pattern shown in Figure 6.4c, with $d_{(0002)} = 0.314$ nm and $d_{(10-10)} = 0.336$ nm. The co-existence of cubic twinning and hexagonal Si does extend to the top of the crystalline core. This phenomenon has not been observed in SiNWs synthesized by SnCu co-catalysts in this thesis, where cubic and hexagonal Si have appeared alternating in the direction perpendicular to NW growth direction (see Figure 5.12, Figure 5.14, Figure 5.16 and Figure 5.18).

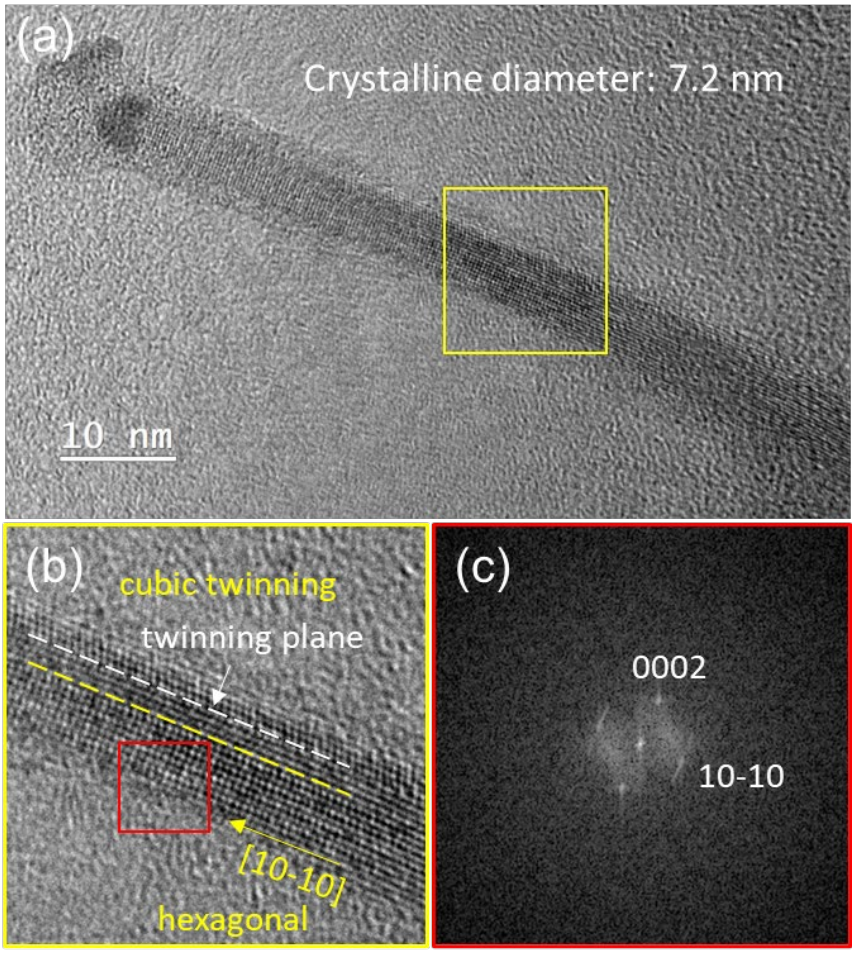

Figure 6.13. HRTEM image of a SiNW synthesized with 0.1 nm In/0.1 nm Cu co-catalyst; SiNWs are transferred from (100) Si substrates; (b) co-existence of cubic twinning and hexagonal Si along the NW growth direction; (c) FFT image of the selected area in (b) shows a pattern of hexagonal Si.

We have also characterized the crystalline structure of SiNWs grown with 1 nm In catalyst as a comparison. Figure 6.14 shows an example of these SiNWs. It has a diameter around 9 nm and has diamond cubic structure. We have observed more than 20 SiNWs and all of them had a single catalyst on top of the NWs. No catalyst separation phenomenon has been observed. Five NWs were in the <110> zone axis, all of which showed cubic phase.

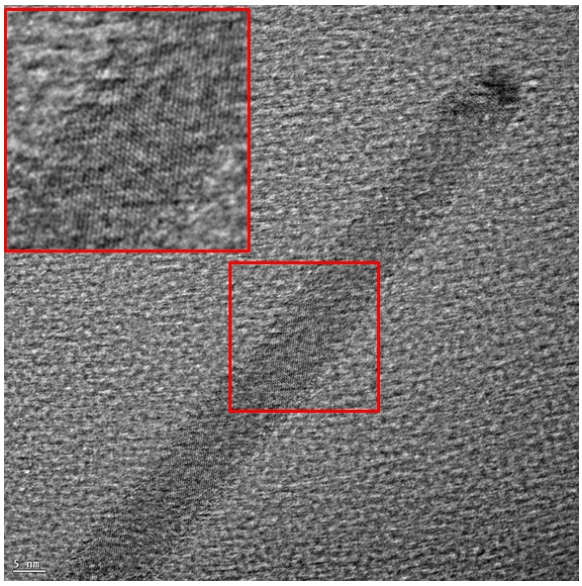

Figure 6.14. A SiNW grown with 1 nm In catalyst from (100) Si substrate.

6.1.4. **Comparison between SnCu catalyzed and InCu catalyzed SiNWs**

In this sub-section, we make a direct comparison between the SiNWs catalyzed by SnCu and InCu co-catalysts. Firstly, let us compare the size and distribution of the two kinds of SiNWs. SEM images of the SiNWs grown with SnCu co-catalysts of 0.1 nm Sn/0.1 nm Cu, and 1 nm Sn/1 nm Cu are shown in Figure 6.15a and b; while SEM images of the SiNWs grown with InCu co-catalysts of the same amount (but with In replacing Sn) are shown in Figure 6.15c and d. All the SiNWs are fabricated with the typical conditions on (100) Si substrates. In Figure 6.15a and c, we find that SiNWs grown with SnCu co-catalyst are thinner (average diameter: 7.5 nm, measure based on SEM images) and much denser than the SiNWs grown with InCu co-catalyst (average diameter: 10.5 nm) of the same amount. The InCu catalyzed SiNWs have about twice the lengths of the SnCu catalyzed SiNWs. With co-catalyst amount increasing, both SiNWs show a bi-modal distribution of thin and thick SiNWs (Figure 6.15c and d).

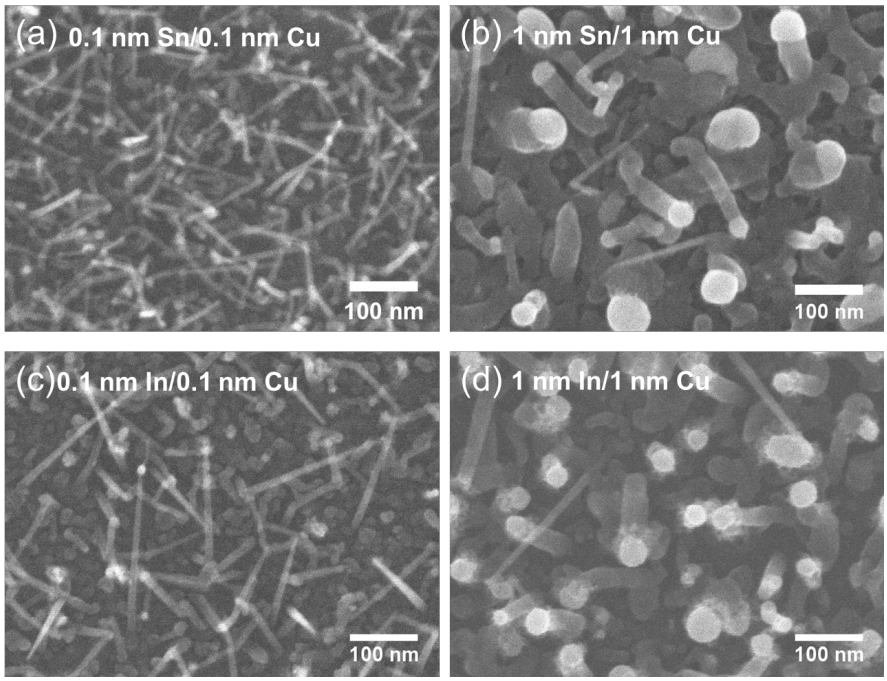

Figure 6.15. SiNWs grown with (a) 0.1 nm Sn/0.1 nm Cu, and with (b) 1 nm Sn/1 nm Cu co-catalysts on (100) Si; SiNWs grown with (c) 0.1 nm In/0.1 nm Cu, and with (d) 1 nm In/1 nm Cu co-catalysts on (100) Si.

Secondly, let us compare the crystalline structures of the two mixed catalsyts. Both as-deposited mixed catalyst NPs are amorphous and have formed a core-shell structure (crystalline Cu core plus a liquid shell) after a hydrogen plasma treatment at 200 °C. During SiNW growth, Si has reacted with Cu and formed solid Cu_3Si in the SnCu catalyst NPs, while Sn has remained liquid; thus, the SiNW growth is actually a liquid-assisted VSS process. In addition, no evidence of SnCu alloys has been found in the catalyst NPs. In the InCu mixed catalyst NPs, we have found intermetallic phases in different NPs, which are very likely to catalyze SiNW growth; however, we have no clear evidence of the presence of Cu or Cu_3Si phase in the catalyst NPs for the moment.

Finally, let us compare the crystalline structures of the SiNWs grown with the two mixed catalysts.

i) Hexagonal phase of Si has been observed in small-diameter SiNWs in both samples. The hexagonal SiNWs grown with SnCu catalyst have crystalline diameters ranging from 4 nm to

7.2 nm, with a yield around 5% - 6%. While in the only TEM sample of thin InCu catalyzed SiNWs, we have found 1 hexagonal SiNW out of 11 in <110> zone axis, (which, if repeatable on a larger scale, would make a yield of 9%), which has a small crystalline diameter of 5 nm. The SnCu catalyzed hexagonal SiNWs have growth directions along [0001]; whereas the InCu catalyzed hexagonal SiNW grew along the [10-10] direction.

ii) The catalyst separation phenomenon has been observed in thin SiNWs in both samples fabricated with SnCu and InCu catalysts. For SnCu catalyzed SiNWs, we have proven that it is due to the oxidation of Cu_3Si and formation of SiO_2 in the air after NW growth; Although we do not have solid proof of this reaction in InCu catalyzed SiNWs, we assume that it is also associated with using Cu as a co-catalyst material, since no catalyst separation phenomenon has been observed in the SiNWs catalyzed by pure In.

In brief, SiNWs have been successfully made with InCu co-catalysts by PECVD. SiNWs grown with 0.1 nm In/0.1 nm Cu have an average diameter of 10.5 nm. One SiNW with 2H structure has been found among these NWs. The Cu_7In_3 (δ) intermetallic phase has been found in the catalyst NPs after SiNW growth. Other phases were also present.

6.2. **SiNW growth with AuCu co-catalyst**

In this sub-chapter, we study SiNWs obtained with AuCu mixed catalysts. Au-Si and Au-Cu binary phase diagrams are shown in Figure 6.16a and b respectively. Au and Si can form a eutectic liquid at 363 °C at 19 at% Si. For the Au-Cu binary system, Au and Cu solids are miscible below the liquidus and above 410 °C. Below 410 °C, they can form three types of compounds: Au_3Cu, AuCu and $AuCu_3$. Au–Cu bimetallic nanomaterials have attracted tremendous attention in the field of catalysis, water splitting, biosensing and biotherapy [Liu, 2011, Jiang, 2012, Kim, 2015, Liu, 2016, Wang, 2017, Wang, 2018, Zhu, 2018, Hofmann, 2019]. There is no liquid Au-Cu phase within the range of SiNW growth temperature (around 327 – 447 °C). When Au and Cu are used as mixed catalysts, if they do not form an alloy, there will be liquid Au-Si droplet and solid Cu or Cu_3Si during SiNW growth; if they alloy with each other, the

catalyst can be: Au and Au_3Cu, $AuCu_3$ and Cu, Au_3Cu, AuCu, and $AuCu_3$ or their combinations. Using AuCu mixed catalysts may lead to different SiNW growth kinetics compared with pure Au catalyzed or SnCu catalyst SiNWs and thus different morphologies and structures. In this section, we firstly investigate the influence of Au/Cu ratio on SiNW growth (section 6.2.1), then we study the crystalline structure of the SiNWs synthesized with AuCu mixed catalysts (section 6.2.2).

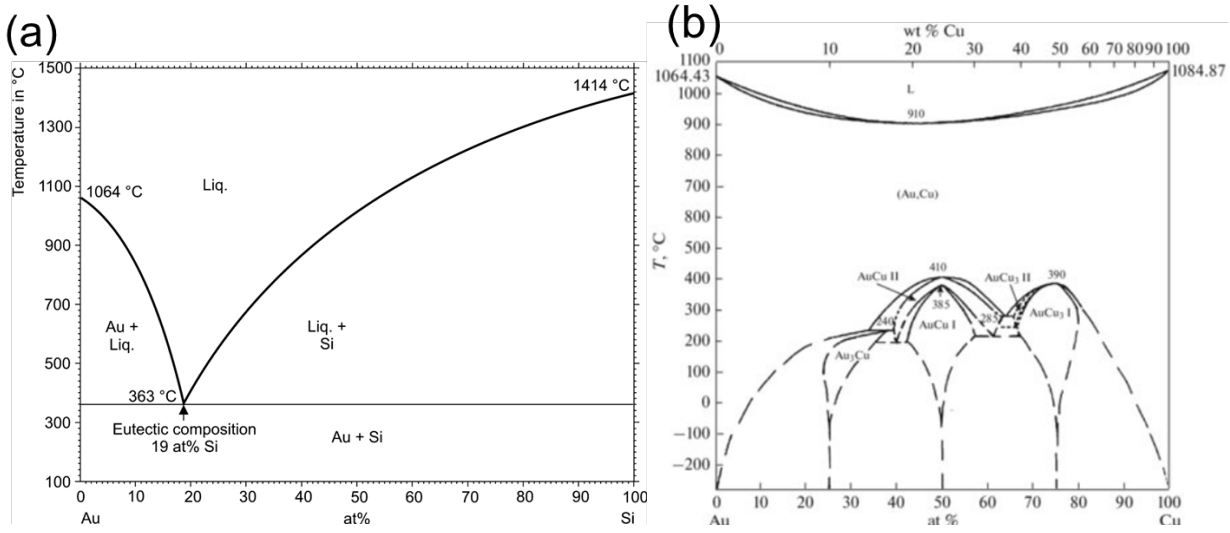

Figure 6.16. (a) Au-Si binary phase diagram [Overmeyer, 2014]; (b) Au-Cu binary phase diagram [Fedorov, 2016].

6.2.1. **Influence of Au/Cu ratio on SiNW growth**

To prepare the mixed catalysts, Cu was firstly evaporated on (100) Si substrates as before, then Au was evaporated on top of Cu. Four kinds of catalysts with different compositions were preparedf, with nominal thicknesses of: 1 nm pure Au, 1 nm pure Cu, 0.4 nm Au/0.6 nm Cu (22 at% Au/78 at% Cu), and 0.8 nm Au/0.3 nm Cu (86 at% Au/14 at% Cu). We tried SiNW growth with these catalysts using the typical conditions, however, we did not obtain any SiNWs. Therefore, we modified the PECVD settings and adopted conditions established earlier [Chen, 2016], which are listed in Table 6.1. Compared with the typical process in Table 3.1, for the H_2 plasma treatment process, we increased substrate temperature, H_2 flux, gas pressure and time duration, while we decreased plasma power; for SiNW growth, we increased

substrate temperature, ratio of SiH_4/H_2 flux and time duration, while we decreased gas pressure and RF power.

Table 6.1. Conditions of the typical PECVD process for SiNW growth with AuCu catalysts

	Substrate temperature (°C)	Flux of H_2/SiH_4 (sccm)	Gas pressure (mbar)	RF power (W)	Time duration (min)
H_2 plasma treatment	385	200/0	2	2.5	10
SiNW growth	447	50/10	1.33	1	5

SEM images of SiNWs fabricated with the above conditions are shown in Figure 6.17. All the obtained SiNWs have a low density on (100) Si substrates. The SiNWs grown with 1 nm pure Au are straight but tapered, with diameters ranging from 10 to 20 nm at the middle of the NWs, and length up to 500 nm (Figure 6.17a). When using 1 nm pure Cu as catalyst, SiNWs can barely grow; instead, we obtain some short "nano stones" (Figure 6.17b). When SiNWs are grown with a Cu-rich mixed catalyst (0.4 nm Au/0.6 nm Cu) as shown in Figure 6.17c, they have similar diameters (mostly around 10 – 20 nm) with SiNWs grown with pure Au, but the NW length has increased; the longest ones reaching about 800 nm. Finally, when SiNWs are grown with a Au-rich mixed catalyst (0.8 nm Au/0.3 nm Cu), the NW diameter remains similar (10 – 20 nm) with the other samples, while the NW length increases furthermore. The longest NW has a length around 1 μm. That is, by adding Cu into Au catalyst has an influence in SiNW length, the less Cu is added, the longer the SiNWs are. However, pure Cu catalyst cannot lead to SiNW growth under this process conditions. Next, the SiNWs from Figure 6.17are transferred to TEM grids for further structure characterizations.

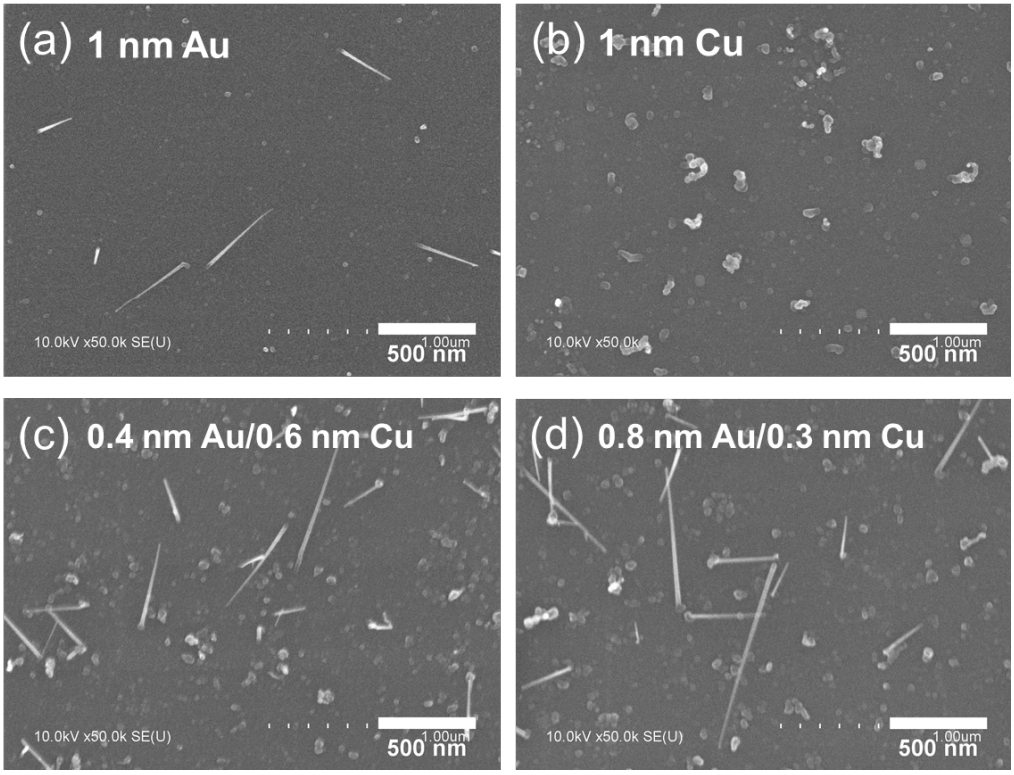

Figure 6.17. SiNWs grown with (a) 1 nm pure Au; (b) 1 nm pure Cu; (c) 0.4 nm Au/0.6 nm Cu and (d) 0.8 nm Au/0.3 nm Cu on (100) Si substrates.

6.2.2. **Crystalline structure of SiNWs obtained with AuCu catalysts**

Firstly, let us consider TEM observations of SiNWs grown with 1 nm Au catalyst. Most observed SiNWs have a single catalyst NP on top (Figure 6.18a). Catalyst separation phenomenon has not been observed among Au catalyzed SiNWs, which reinforces our previous conclusion that Cu_3Si was at the origin of this phenomenon by catalyzing the oxidation of the NWs. The image of the selected area in Figure 6.18a with a higher magnification is shown in Figure 6.18b. It can be seen that the SiNW is a bicrystal (probably a twinned crystal) with little amorphous oxide. This is common in gold catalyzed SiNWs [Wu, 2004]. We have observed more than 50 SiNWs, and found 11 SiNWs in the <110> zone axis. These SiNWs have diameters ranging from 6 nm to 25 nm, and all of them are cubic SiNWs. No hexagonal structure is found.

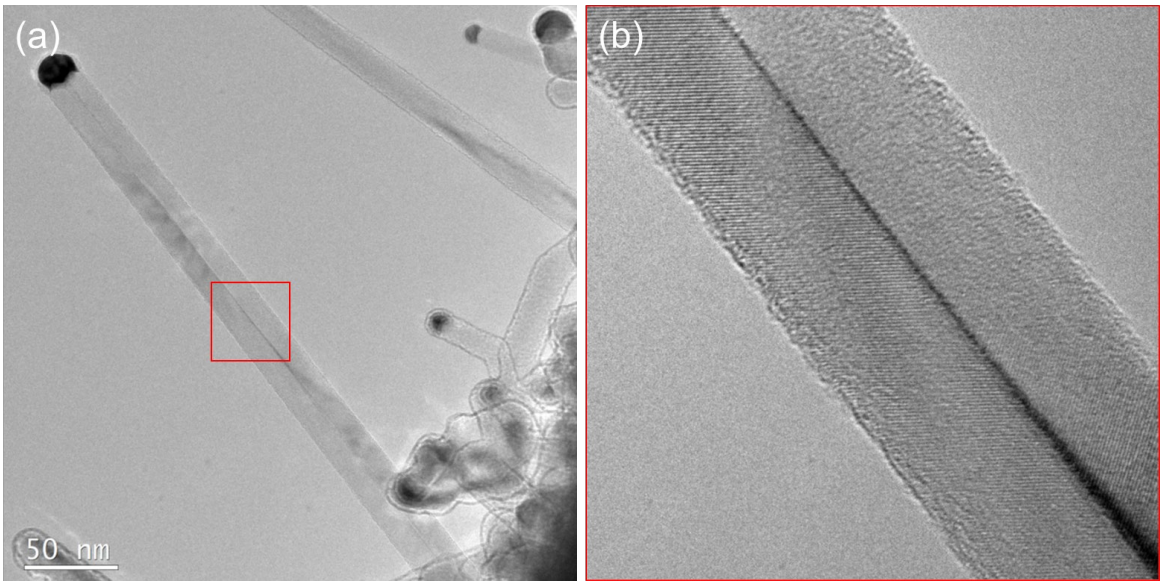

Figure 6.18. (a) SiNWs grown with 1 nm Au catalyst and (b) a magnified image of the selected area.

In the case of NWs catalyzed by 1 nm Au catalyst, in addition to well-crystallized SiNWs, we have also found a SiNW with some small branches on it. Figure 6.19a and b show different parts of a such a SiNW. On some of the branches, we found catalyst NPs, which suggested that the SiNW branches have an epitaxial relationship with the NW trunk. The SiNW branches could come from the diffusion of gold atoms from the top catalyst and with the presence of SiH_4 during the PECVD process.

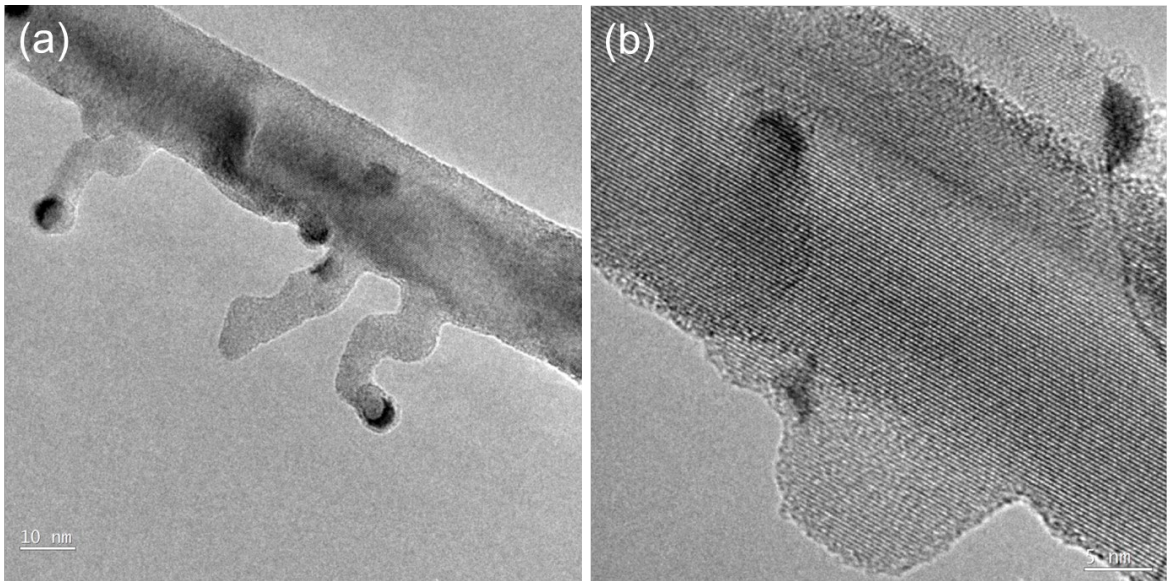

Figure 6.19. HRTEM images of different parts of a SiNW with branches catalyzed by leaking Au-Si droplets.

Next, we observed the SiNWs grown with the gold-rich mixed catalyst and the copper-rich mixed catalyst by TEM. For the former, we have observed 30 SiNWs with diameters ranging from 5.0 nm to 20.7 nm. No hexagonal phase has been found among these NWs; for the latter, we have observed 30 SiNWs with diameters ranging from 5.4 nm to 16.0 nm and we found 6 cubic SiNWs.

Figure 6.20a shows a SiNW grown with 0.8 nm Au/0.3 nm Cu (86 at% Au/14 at% Cu). There are separated catalyst NPs in this NW. We are able to observe one group of atomic planes in the top NP. Its FFT pattern shows that the interplanar spacing of this set of planes is 0.230 nm, corresponding to the (111) planes of the face-centered cubic (fcc) AuCu alloy [Khanal, 2014, Huang, 2015]. This value does not match atomic planes of Cu or Cu_3Si. Nevertheless, when taking into account the error on magnification calibration, this value can correspond to the (111) planes of Au (0.235 nm) [Zhan, 2017], or the (111) planes of Au_3Cu (0.2355 nm) [Li, 2020]. Figure 6.20b shows a SiNW grown with 0.4 nm Au/0.6 nm Cu (22 at% Au/78 at% Cu). It also has two separated catalyst NPs. We made a FFT of the top catalyst NP and found that the displayed atomic plane group has an interplanar spacing of 0.23 nm, the same as in Figure 6.20a. According to the Au-Cu binary phase diagram (see Figure 6.16b), Au can form a disordered solid solution $Au_{1-x}Cu_x$

with Cu at the growth temperature 416 °C in any ratio. The lattice constants of the solid solution $Au_{1-x}Cu_x$ with fcc structure should be close to those of Cu and Au and vary within a small range as a function of the composition. Therefore, 0.230 nm can also correspond to the (111) planes of $Au_{1-x}Cu_x$ phase. With temperature decreasing (before opening the chamber), the Au-rich mixed catalyst (86 at% Au) will become a mixture of ordered and disordered $Au_{1-x}Cu_x$ solid solutions according to the phase diagram, if we trust the nominal ratio of the evaporated metals; the Cu-rich mixed catalyst (22 at% Au) will become a mixture of $AuCu_3$ and another $Au_{1-x}Cu_x$ solid solution.

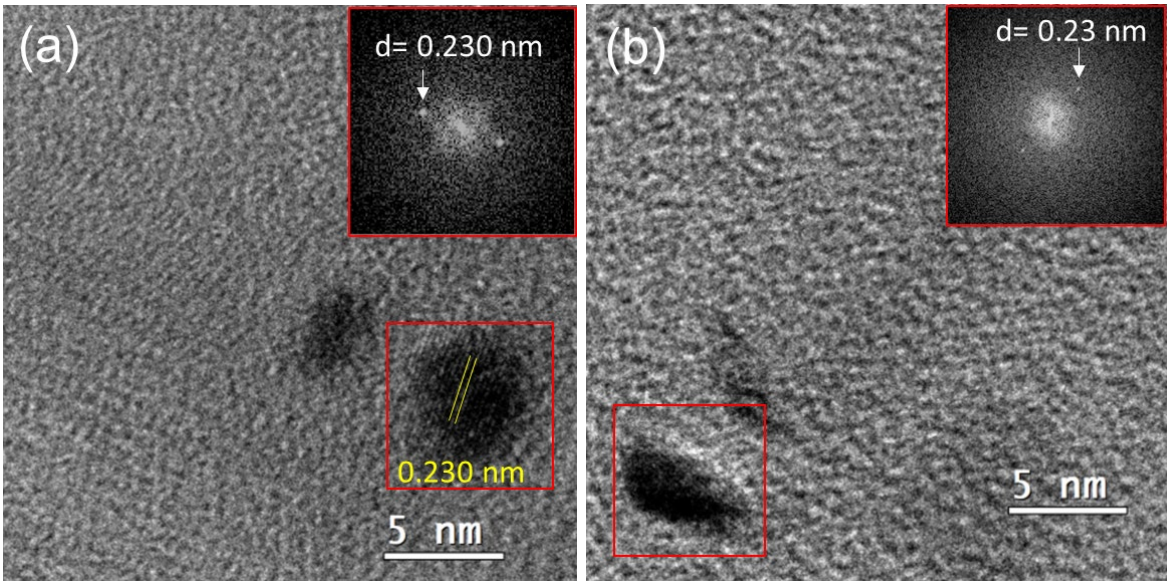

Figure 6.20. (a) HRTEM image of a SiNW with separated catalyst NPs synthesized with 0.8 nm Au/0.3 nm Cu (86 at% Au/14 at% Cu) with the FFT pattern of the top NP; (b) HRTEM image of a SiNW fabricated with 0.4 nm Au/0.6 nm Cu (22 at% Au/78 at% Cu) mixed catalyst with the FFT pattern of the top NP.

We have no evidence of Cu_3Si in the bottom catalyst NPs of the two SiNWs since we do not see any atomic planes. It is often very difficult to observe crystalline structures of catalyst NPs with such a small size (3 - 4 nm) based on our experience in this thesis. However, since the catalyst separation phenomenon has never been observed in Au-catalyzed SiNWs, we think using Cu as a co-catalyst material

is still responsible for this phenomenon. Thus, the compositions of the top catalyst NPs should be the evaporated compositions minus the one that migrated to the bottom catalyst NPs.

6.3. **Chapter conclusions**

In this chapter, we have fabricated SiNWs with two mixed catalysts: InCu and AuCu.

The as-deposited InCu mixed catalysts are amorphous. After a hydrogen plasma treatment at 200 °C, Cu is crystallized and In melted. They should form a core-shell structure: a Cu crystal core plus an In-rich liquid shell. We have found two intermetallic alloys – Cu_7In_3 (δ) with a clear signature and Cu_2In (η) with a significant probability – after SiNW growth in the catalyst NPs. With InCu mixed catalysts, SiNWs have been successfully fabricated at the typical PECVD conditions (Table 3.1). SiNWs grown with 0.1 nm In/0.1 nm Cu co-catalyst have a narrow diameter distribution and an average diameter of 10.5 nm. One SiNW including a large hexagonal domain has been found out of 10 fully cubic SiNWs, which also has a thin crystalline diameter of 5 nm. The catalyst separation phenomenon occurring after NW growth is common in this sample. SiNWs grown with 1 nm In/1 nm Cu co-catalyst show a wide distribution where both thin and thick NWs are present.

With AuCu mixed catalysts, SiNWs have been successfully fabricated using the PECVD process exposed in Table 6.1. Again, SiNWs cannot grow with pure Cu catalyst under those conditions. Using AuCu mixed catalysts can increase the SiNW length with respect to pure Au. TEM results show that SiNWs grown with pure Au catalyst have a single catalyst NP on top; while we can always find separated catalyst NPs in AuCu catalyzed SiNWs. The top NP of the SiNWs grown with AuCu mixed catalysts have an interplanar spacing of 0.230 nm, which is likely to be 111 $Au_{1-x}Cu_x$ solid solution with fcc structure, 111 AuCu, or 111 Au_3Cu. SiNWs with diameters as small as 5 nm have been observed, but we only found cubic phase.

In comparison with SiNWs grown with pure catalysts, using mixed catalysts can change SiNW diameter, length, morphology, distribution, and even crystalline structure, which can provide effective

control and adjustment over SiNW growth. This is beneficial for the applications of SiNW based devices. In the next chapter, we will fabricate solar cells with SiNWs synthesized with SnCu and InCu mixed catalysts to explore their opportunities in photovoltaic devices.

References

Alfantazi, A.M. and R.R. Moskalyk, *Processing of indium: a review.* Minerals Engineering, 2003. **16**(8): p. 687-694. https://doi.org/10.1016/s0892-6875(03)00168-7

Che, G.C. and M. Ellner, *Powder Crystal Data for the High-Temperature Phases Cu4In, Cu9In4(h) and Cu2In(h).* Powder Diffraction, 2013. **7**(2): p. 107-108. https://doi.org/10.1017/s0885715600018340

Chen, W. and P. Roca i Cabarrocas, *Insights into gold-catalyzed plasma-assisted CVD growth of silicon nanowires.* Applied Physics Letters, 2016. **109**(4): p. 043108. https://doi.org/10.1063/1.4960106

Cui, Y., L.J. Lauhon, M.S. Gudiksen, J. Wang, and C.M. Lieber, *Diameter-controlled synthesis of single-crystal silicon nanowires.* Applied Physics Letters, 2001a. **78**(15): p. 2214-2216. https://doi.org/10.1063/1.1363692

Darveaux, R. and I. Turlik, *Shear deformation of indium solder joints.* IEEE Transactions on Components, Hybrids, and Manufacturing Technology, 1990. **13**(4): p. 929-939. https://doi.org/10.1109/33.62558

Fedorov, P.P. and S.N. Volkov, *Au–Cu Phase Diagram.* Russian Journal of Inorganic Chemistry, 2016. **61**(6): p. 772-775. https://doi.org/10.1134/s0036023616060061

Hannon, J.B., S. Kodambaka, F.M. Ross, and R.M. Tromp, *The influence of the surface migration of gold on the growth of silicon nanowires.* Nature, 2006. **440**(7080): p. 69-71. https://doi.org/10.1038/nature04574

Hofmann, D.M., D.H. Fairbrother, R.J. Hamers, and C.J. Murphy, *Two-Phase Synthesis of Gold–Copper Bimetallic Nanoparticles of Tunable Composition: Toward Optimized Catalytic CO2 Reduction.* ACS Applied Nano Materials, 2019. **2**(6): p. 3989-3998. https://doi.org/10.1021/acsanm.9b00904

Hofmann, S., C. Ducati, R.J. Neill, S. Piscanec, A.C. Ferrari, J. Geng, R.E. Dunin-Borkowski, and J. Robertson, *Gold catalyzed growth of silicon nanowires by plasma enhanced chemical vapor deposition.* Journal of Applied Physics, 2003. **94**(9): p. 6005-6012. https://doi.org/10.1063/1.1614432

Huang, S.-S., L. Liu, L.-P. Mei, J.-Y. Zhou, F.-Y. Guo, A.-J. Wang, and J.-J. Feng, *Electrochemical sensor for nitrite using a glassy carbon electrode modified with gold-copper nanochain networks.* Microchimica Acta, 2015. **183**(2): p. 791-797. https://doi.org/10.1007/s00604-015-1717-z

Jiang, Z., Q. Zhang, C. Zong, B.-J. Liu, B. Ren, Z. Xie, and L. Zheng, *Cu–Au alloy nanotubes with five-fold twinned structure and their application in surface-enhanced Raman scattering.* Journal of Materials Chemistry, 2012. **22**(35): p. 18192-18197. https://doi.org/10.1039/c2jm33863g

Khanal, S., N. Bhattarai, D. McMaster, D. Bahena, J.J. Velazquez-Salazar, and M. Jose-Yacaman, *Highly monodisperse multiple twinned AuCu-Pt trimetallic nanoparticles with high index surfaces.* Phys Chem Chem Phys, 2014. **16**(30): p. 16278-83. https://doi.org/10.1039/c4cp02208d

Kim, S.I., G. Eom, M. Kang, T. Kang, H. Lee, A. Hwang, H. Yang, and B. Kim, *Composition-selective fabrication of ordered intermetallic Au-Cu nanowires and their application to nano-size electrochemical glucose detection.* Nanotechnology, 2015. **26**(24): p. 245702. https://doi.org/10.1088/0957-4484/26/24/245702

Koster, A.S., L.R. Wolff, and G.J. Visser, *Structure of copper–indium Cu7In3.* Acta Crystallographica Section B Structural Crystallography and Crystal Chemistry, 1980. **36**(12): p. 3094-3096. https://doi.org/10.1107/s0567740880010886

Li, P. and X. Peng, *Au3Cu nanosquares and frames for glucose sensor and CO oxidation catalyst.* Applied Physics A, 2020. **126**(7): p. 521. https://doi.org/10.1007/s00339-020-03707-y

Liu, M., W. Zhou, T. Wang, D. Wang, L. Liu, and J. Ye, *High performance Au-Cu alloy for enhanced visible-light water splitting driven by coinage metals.* Chem Commun (Camb), 2016. **52**(25): p. 4694-7. https://doi.org/10.1039/c6cc00717a

Liu, X., R.W. Davis, L.C. Hughes, M.H. Rasmussen, R. Bhat, C.-E. Zah, and J. Stradling, *A study on the reliability of indium solder die bonding of high power semiconductor lasers.* Journal of Applied Physics, 2006. **100**(1): p. 013104. https://doi.org/10.1063/1.2209194

Liu, X., A. Wang, L. Li, T. Zhang, C.-Y. Mou, and J.-F. Lee, *Structural changes of Au–Cu bimetallic catalysts in CO oxidation: In situ XRD, EPR, XANES, and FT-IR characterizations.* Journal of Catalysis, 2011. **278**(2): p. 288-296. https://doi.org/10.1016/j.jcat.2010.12.016

Okamoto, H. and T.B. Massalski, *The Au−Si (Gold-Silicon) system.* Bulletin of Alloy Phase Diagrams, 1983. **4**(2): p. 190-198. https://doi.org/10.1007/bf02884878

Olesinski, R., N. Kanani, and G. Abbaschian, *The I□ Si (Indium-Silicon) system.* Bulletin of Alloy Phase Diagrams, 1985. **6**: p. 128-130.

Olesinski, R.W. and G.J. Abbaschian, *The Si−Sn (Silicon−Tin) system.* Bulletin of Alloy Phase Diagrams, 1984. **5**(3): p. 273-276. https://doi.org/10.1007/bf02868552

Overmeyer, L., Y. Wang, and T. Wolfer, *Eutectic Bonding*, in *CIRP Encyclopedia of Production Engineering*, L. Laperrière and G. Reinhart, Editors. 2014, Springer Berlin Heidelberg: Berlin, Heidelberg. p. 488-492. https://doi.org/10.1007/978-3-642-20617-7_6483

Park, J.-S., J.K. Jeong, H.-J. Chung, Y.-G. Mo, and H.D. Kim, *Electronic transport properties of amorphous indium-gallium-zinc oxide semiconductor upon exposure to water.* Applied Physics Letters, 2008. **92**(7): p. 072104. https://doi.org/10.1063/1.2838380

Subramanian, P.R. and D.E. Laughlin, *The Cu−In (Copper-Indium) system.* Bulletin of Alloy Phase Diagrams, 1989. **10**(5): p. 554-568. https://doi.org/10.1007/bf02882415

Tian, B., X. Zheng, T.J. Kempa, Y. Fang, N. Yu, G. Yu, J. Huang, and C.M. Lieber, *Coaxial silicon nanowires as solar cells and nanoelectronic power sources.* Nature, 2007. **449**(7164): p. 885-9. https://doi.org/10.1038/nature06181

Wang, J., H. Zhu, D. Yu, J. Chen, J. Chen, M. Zhang, L. Wang, and M. Du, *Engineering the Composition and Structure of Bimetallic Au-Cu Alloy Nanoparticles in Carbon Nanofibers: Self-Supported Electrode Materials for Electrocatalytic Water Splitting.* ACS Appl Mater Interfaces, 2017. **9**(23): p. 19756-19765. https://doi.org/10.1021/acsami.7b01418

Wang, Z., Y. Ju, S. Tong, H. Zhang, J. Lin, B. Wang, and Y. Hou, *Au3Cu tetrapod nanocrystals: highly efficient and metabolizable multimodality imaging-guided NIR-II photothermal agents.* Nanoscale Horiz, 2018. **3**(6): p. 624-631. https://doi.org/10.1039/c8nh00135a

Wang, Z.W. and Z.Y. Li, *Structures and energetics of indium-catalyzed silicon nanowires.* Nano Lett, 2009. **9**(4): p. 1467-71. https://doi.org/10.1021/nl803345u

Wojewoda, J., P. Zieba, M. Faryna, W. Gust, E.J. Mittemeijer, and L. Litynska, *Characterization of Interfacial Reactions in Cu/In/Cu Joints.* Microchimica Acta, 2004. **145**(1-4): p. 107-110. https://doi.org/10.1007/s00604-003-0138-6

Wu, Y., Y. Cui, L. Huynh, C.J. Barrelet, D.C. Bell, and C.M. Lieber, *Controlled Growth and Structures of Molecular-Scale Silicon Nanowires.* Nano Letters, 2004. **4**(3): p. 433-436. https://doi.org/10.1021/nl035162i

Yu, L., B. O'Donnell, P.J. Alet, S. Conesa-Boj, F. Peiro, J. Arbiol, and P.R. Cabarrocas, *Plasma-enhanced low temperature growth of silicon nanowires and hierarchical structures by using tin and indium catalysts.* Nanotechnology, 2009. **20**(22): p. 225604. https://doi.org/10.1088/0957-4484/20/22/225604

Zardo, I., S. Conesa-Boj, S. Estradé, L. Yu, F. Peiro, P. Roca i Cabarrocas, J.R. Morante, J. Arbiol, and A. Fontcuberta i Morral, *Growth study of indium-catalyzed silicon nanowires by plasma enhanced chemical vapor deposition.* Applied Physics A, 2010. **100**(1): p. 287-296. https://doi.org/10.1007/s00339-010-5802-1

Zhan, W., J. Wang, H. Wang, J. Zhang, X. Liu, P. Zhang, M. Chi, Y. Guo, Y. Guo, G. Lu, S. Sun, S. Dai, and H. Zhu, *Crystal Structural Effect of AuCu Alloy Nanoparticles on Catalytic CO Oxidation.* J Am Chem Soc, 2017. **139**(26): p. 8846-8854. https://doi.org/10.1021/jacs.7b01784

Zhu, W., L. Zhang, P. Yang, C. Hu, H. Dong, Z.-J. Zhao, R. Mu, and J. Gong, *Formation of Enriched Vacancies for Enhanced CO2 Electrocatalytic Reduction over AuCu Alloys.* ACS Energy Letters, 2018. **3**(9): p. 2144-2149. https://doi.org/10.1021/acsenergylett.8b01286

Chapter 7. Radial junction solar cells based on high density thin silicon nanowire arrays

7.1. **Introduction**

Radial junction (RJ) solar cells based on SiNWs are attractive for high-performance photovoltaic devices at low cost [Kuang, 2013, Misra, 2014]. Their unique geometry allows for low material consumption while preserving the strong light absorption due to their efficient light trapping over the broad solar spectrum range and of angles of incidence when compared to planar thin film solar cells [Kayes, 2005, Adachi, 2010, Garnett, 2010]. In addition, the unique geometry of PIN RJs separates the light absorption from the carrier collection, as shown in Figure 7.1. The decoupled light absorption and carrier collection allow to increase the light absorption by making the radial junctions longer, while keeping a thin intrinsic absorber which preserves the efficient carrier collection. In the past, efforts to develop efficient PIN RJ platform at LPICM have been dedicated to the study of low cost approaches based on PECVD and low temperature VLS and an efficiency as high as 9.7 % has been realized using a Sn catalyst and the radial PIN junction with a structure of p-type SiNW/p-type a-Si:H/intrinsic a-Si:H/n-type μc-SiO_x:H [Misra, 2015].

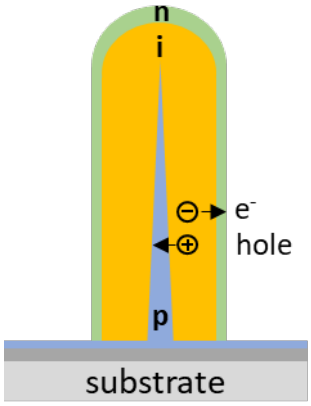

Figure 7.1. Schematic of a PIN radial junction based on a SiNW.

In this thesis, we have achieved a growth of ultra-thin and ultra-dense SiNW arrays using SnCu and InCu co-catalysts. The obtained SiNWs have single crystalline structure and averaged crystalline diameters as small as 4-5 nm. Furthermore, small-diameter SiNWs are also advantageous for the application requiring increased level of the mechanical flexibility due to their reduced diameter and increased density.

In the past, first demonstrations using low-cost and flexible substrates, such as stainless steel or aluminum foils, have been performed based on the nanowires with larger diameters [Cervenka, 2010, Xie, 2012, Wikipedia, 2020a]. In our case, SiNWs have exceptional density of 5.7×10^{10} cm^{-2} and surface to volume ratio of 5×10^{8} m^{-1}. Such a high surface to volume ratio is beneficial for applications requiring surface functionalization or catalysis such as sensors [Zhou, 2003, Peng, 2009] or water splitting artificial leaves [Zhang, 2011, Liu, 2013, Peng, 2013, Liu, 2015]. Here, we show a demonstration of the first devices based on the exceptionally dense and thin SiNW arrays grown using CuSn catalyst by LAVSS method with minimized amount of absorbing material making the radial junctions ten times denser and with diameter three times smaller than the previous devices.

7.2. **Radial junction solar cells based on SiNWs catalyzed by SnCu mixed catalyst**

We have chosen the ultra-dense thin SiNWs synthesized with SnCu mixed catalyst described in Chapter 5.2 to fabricate RJ solar cells. We tilt the substrate by 20 ° during thermal evaporation of nominal thicknesses of 0.09 nm Sn/0.09 nm Cu to slightly reduce the NW density (from 5.7×10^{10} cm^{-2} to 1.3×10^{10} cm^{-2}) and provide enough space to deposit PIN junction and top contacts (Figure 7.2).

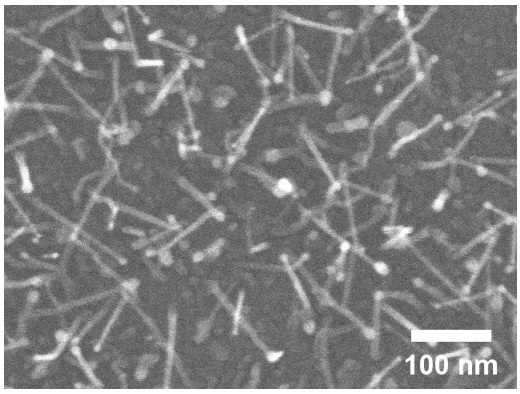

Figure 7.2. SiNWs are grown with input thicknesses of 0.1 nm Sn/0.1 nm Cu co-catalyst at the typical PECVD conditions on Si substrate, but with the substrate tilted by 20 ° during thermal evaporation. The calculated of nominal thicknesses on the tilted substrate are 0.09 nm Sn/0.09 nm Cu.

After the thermal evaporation, the substrates were transferred to the PECVD reactor for PIN junction fabrication. At first, we carry out a hydrogen plasma treatment on the catalyst NPs at 200 °C for 2 minutes to remove the oxide at the NP surface. The PECVD conditions has been given in Table 3.1 in Chapter 3. Then we fabricate PIN junctions using the parameters listed in Table 7.1. Note that the doping level inside NWs and top a-Si:H layer can be controlled by diluting doping gasses (TMB for p-type and PH_3 for n-type) in the silane hydrogen mixture. We have prepared two types of RJ solar cell samples, with the changing parameters marked in bold in Table 7.1. Compared with Sample 1, Sample two has longer NWs, thicker intrinsic absorber layer and higher doping level. The SiNWs have been grown for 4 minutes and 6 minutes based on the typical conditions to prevent them to get tapered and thicker because of the a-Si deposition on NW sidewalls (see Figure 5.20 in Chapter 5.3). Next, we decrease the bottom substrate temperature to 180 °C to deposit a conformal amorphous intrinsic absorber with 10 sccm SiH_4 for 15 and 20 minutes, respectively. Then we deposit an amorphous n-doped layer at the same temperature with 9 sccm of H_2, 2 sccm of SiH_4 and 1 and 1.5 sccm of PH_3 (1 % diluted in H_2), respectively, immediately after the i-layer deposition. The SEM images of the obtained PIN radial junctions for both samples are shown in Figure 7.3a and b. In both samples, most radial junctions are distinctly separated from the neighboring units. Radial junctions have diameters around 80 – 90 nm and are rather uniform in diameter from the bottom to

the top with the six-minute NW growth (Sample 2) bringing longer RJs than the four-minute one. After RJ fabrication, we deposit of an ITO layer (using an Alliance Concept DP 650 RF magnetron sputtering machine) as top contacts for solar cells, following the sputtering process introduced in Chapter 2. The SEM images of the two RJ samples with ITO contacts are shown in Figure 7.3c and d. The thickness of the ITO top contact is nominally 250 nm to ensure a good conductivity without the need for a silver grid on the top of the small area samples.

Table 7.1. Conditions of PIN junction fabrication by PECVD.

Sample		T (°C)	Gas flux (sccm)	Gas pressure (mbar)	RF power (W)	Growth time (min)
	p-doped SiNW	416	100 H_2/5 SiH_4/**1 TMB**	1.42	1.5	**4**
1	intrinsic layer	180	10 SiH_4	0.17	1	**15**
	n-doped layer	180	9 H_2/2 SiH_4/**1 PH_3**	0.32	1	4.5
	p-doped SiNW	416	100 H_2/5 SiH_4/**1.5 TMB**	1.42	1.5	**6**
2	intrinsic layer	180	10 SiH_4	0.17	1	**20**
	n-doped layer	180	9 H_2/2 SiH_4/**1.5 PH_3**	0.32	1	4.5

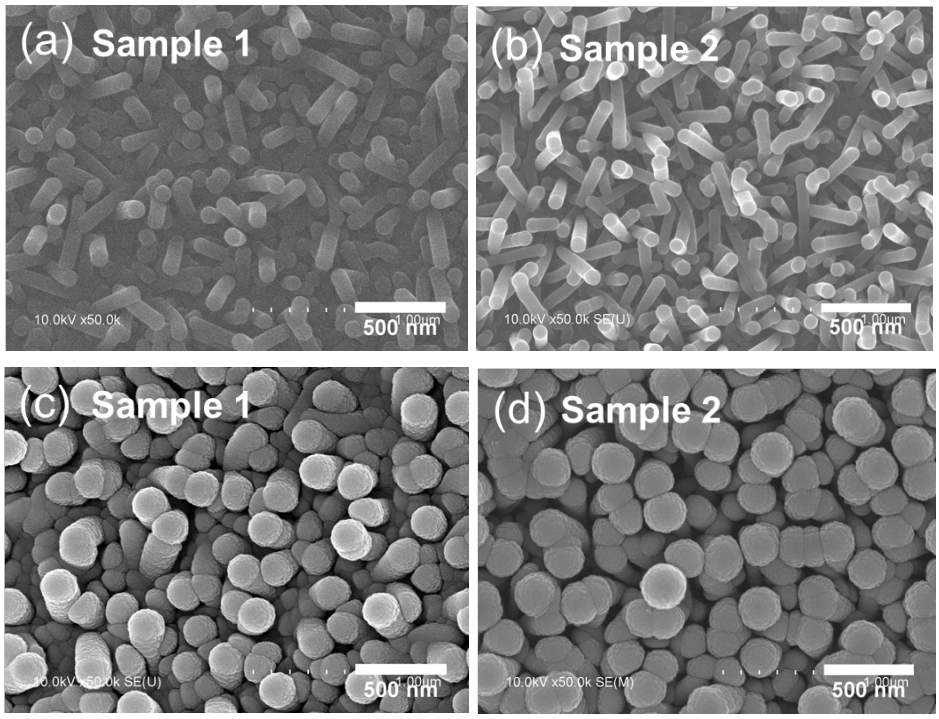

Figure 7.3. SEM images of PIN radial junctions of (a) sample 1 and (b) sample 2 fabricated following the PECVD conditions in Table 7.1 without top contact. SEM images with top ITO contact are shown in (c) for Sample 1 and (d) for Sample 2.

For a better understanding of the radial junctions deposited on ultra-dense and thin SiNWs, we make a comparison of the size and density of the RJs from Figure 7.3a in this thesis and an optimized PIN RJ sample from S. Misra's thesis [Misra, 2015] in Figure 7.4. The two images have the same scale bar. RJs in this work, based on the SiNWs with crystalline diameters of around 5 nm, have diameters around 80 – 90 nm and the density of $2.2 \times 10^9/cm^2$ (Figure 7.4a); while the RJs from [Misra, 2015] have diameters around 300 nm and the density of $2.6 \times 10^8/cm^2$ (Figure 7.4b). Solar cells demonstrated in this work have RJs with diameter about 1/4 of the value in [Misra, 2015] and about 10 times higher density, leading to a much higher surface to volume ratio.

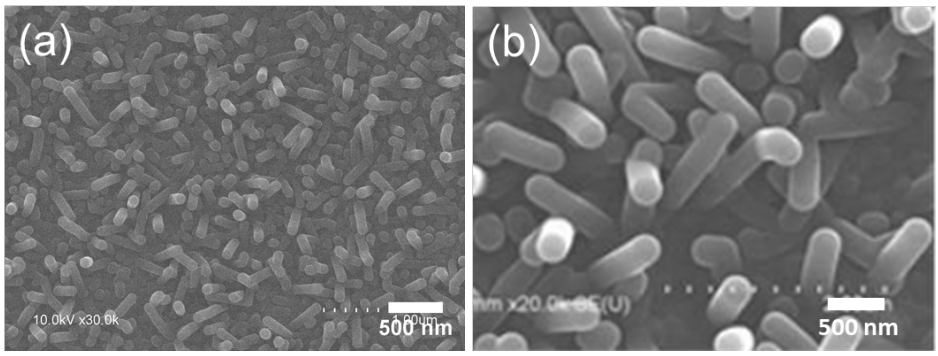

Figure 7.4. Comparison of size and density of PIN radial junctions: (a) RJs fabricated based on SiNWs synthesized with a co-catalyst of 0.1 nm Sn/0.1 nm Cu; (b) RJs fabricated based on SiNWs synthesized with Sn catalyst by S. Misra [Misra, 2015]. Note that scale is the same in both images.

We measured the J–V characteristics of the radial junction solar cells from Table 7.1 under standard AM1.5G illumination conditions using a solar simulator Newport Oriel Sol3A. The J-V curves corresponding to the cells with the highest efficiencies of the two samples are presented in Figure 7.5a corresponding to a cell area of 0.0314 cm^2. Sample 1 has the best efficiency (η) of 3.42 %, with a V_{oc} (open-circuit voltage) of 0.54 V, a J_{sc} (short-circuit current density) of 11.6 mA cm^{-2}, and a FF (fill factor) of 0.543. For sample 2 with longer and thicker RJs with higher doping levels, it has a higher efficiency of 3.73 %, with an increased V_{oc} of 0.61 V, a similar J_{sc} of 11.4 mA.cm^{-2}, and a similar FF of 0.541.

In comparison to the performance of very dense RJ based devices in Figure 7.5a, we plot in Figure 7.5b the efficiency of a-Si:H RJ solar cells as a function of the SiNW density obtained before by S. Misra *et. al.* [Misra, 2013b]. We can see that with the high NW density, η decreases and the solar cell with a highest NW density of $7 \times 10^8/cm^2$ correspond to an η of around 4 %, which is comparable to that obtained here with three times higher density. This demonstration shows that the ultra-high density RJ solar cell devices can have competitive performance while achieving much large surface to volume ratio and a better mechanical flexibility.

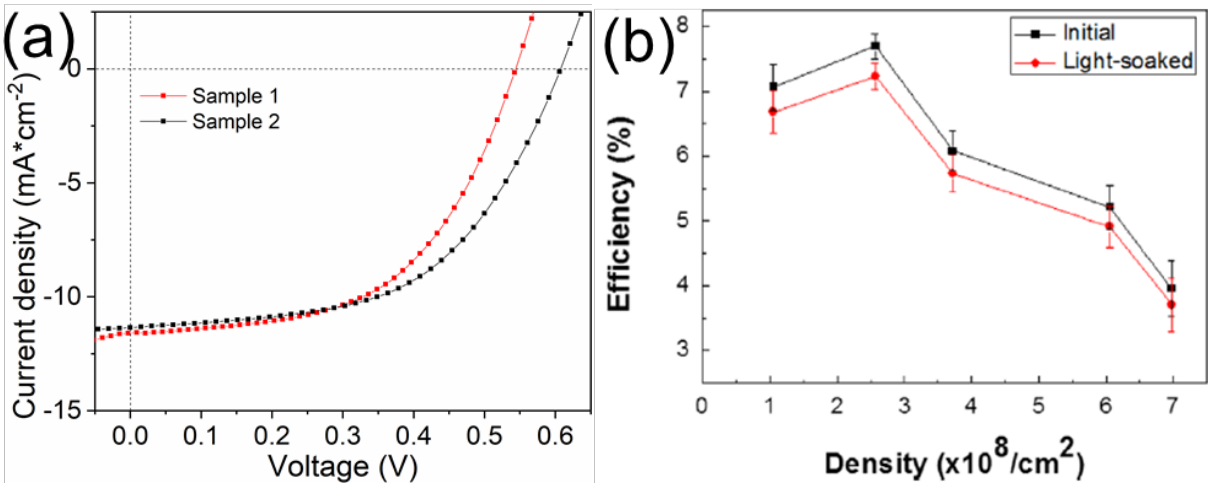

Figure 7.5. Power conversion efficiency comparison (η): (a) J-V characteristics of radial junction solar cell sample 1 and sample 2 from this thesis; and (b) η of the a-Si:H radial junction solar cells as a function of the SiNW density adapted from [Misra, 2013b].

In order to identify potential problems with such thin RJs at nanoscale, an electron beam induced current mapping (EBIC) was carried out on Sample 2 in a Hitachi SU8000 SEM system. The RJ solar cell was fixed on a sample holder, with two probes connected to the bottom contact and the Ag dot on ITO, respectively. The measurement was performed under an acceleration voltage of 25 kV, the beam current of 5 μA and a zero bias. Figure 7.6 shows an EBIC mapping of the RJ cells. Even though RJs are very dense, they seem to all perform very well without an obvious defect with the highest collected current found inside RJs as is expected from the sample geometry. This confirms that while high RJ density represents a complex challenge, the functional devices are possible and more efforts to increase their performance could lead to significant performance improvements in the future.

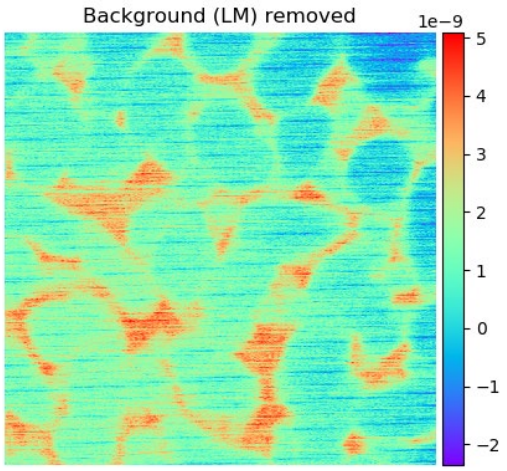

Figure 7.6. EBIC mapping on radial junction solar cell Sample 2 performed at the acceleration voltage of 25 kV with color scale highlighting the collected current.

Measured external quantum efficiency (EQE) on solar cell sample 2 using Newport system (Oriel Instruments QEPVSI-b) is shown in Figure 7.7. The EQE response was recorded within the spectral range of 350 - 850 nm. It explained a relatively low J_{sc} obtained in the devices. While the losses in the blue part of the spectrum are in line with similar devices based on a thin n-type doped a-Si:H top layer, the values of EQE are in overall smaller than in the devices achieving 15 or more mA/cm^2[Misra, 2013b]. This is mainly caused by the reduced absorber thickness, which was selected for the device demonstration. In the future, if one is to maximize the performance of such devices, an increase of the absorption layer thickness followed by an appropriate NW density adjustment would be necessary. Nevertheless, the optimization of the performance beyond the first demonstration is out of the scope of this thesis and was not fully addressed in this work.

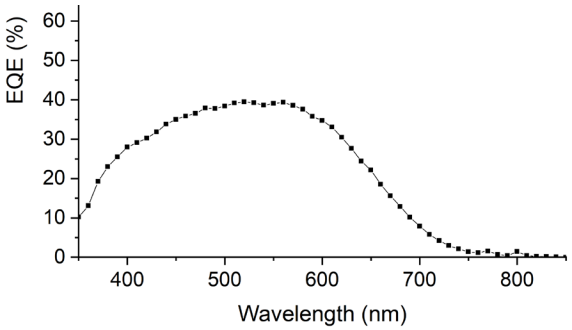

Figure 7.7. External quantum efficiency of radial junction solar cell sample 2.

7.3. **Radial junction solar cells based on SiNWs catalyzed by InCu mixed catalyst**

In this section, we fabricate radial junction solar cells based on thin SiNWs catalyzed by InCu mixed catalyst. We use a co-catalyst of 0.1 nm In/0.1 nm Cu to synthesize SiNWs. The SiNWs mostly have single crystalline structure and crystalline diameters from 5 - 8 nm as reported in 0. Hexagonal phase has been found in those SiNWs before and it is reported in 0. Compared with the SiNWs synthesized with SnCu co-catalysts at the same PECVD conditions, the SiNWs catalyzed by InCu co-catalysts have larger diameters (by about 2 – 3 nm) and twice the lengths (see Chapter 6.1.3). This means that for the same amount of the material deposited, NWs are twice as long as the previous ones with less tapering and thinner amorphous shell present on the surface.

The used solar cell fabrication process after the NW growth is the same as used before for SnCu catalyzed SiNWs. We have fabricated three radial junction samples in the PECVD reactor following the conditions detailed in Table 7.2. Before PIN junction deposition, we always perform hydrogen plasma treatment on catalyst NPs to remove the oxide at the surface. We choose a SiNW growth time of 6 minutes, similar to the experiments with SnCu catalyzed RJs in the previous section. Conditions to grow RJ are very similar to those in Table 7.1, except changing the p and n type doping to study the influence of doping levels on solar cell performance. Thickness of the intrinsic layer is the same for all samples. The variable parameters are marked bold in Table 7.2.

Table 7.2. Conditions of PIN junction fabrication by PECVD.

Sample		T (°C)	Gas flux (sccm)	Gas pressure (mbar)	RF power (W)	Growth time (min)
1	p-doped SiNW	416	100 H_2/5 SiH_4/**1.5 TMB**	1.42	1.5	6
	intrinsic layer	180	10 SiH_4	0.17	1	15
	n-doped layer	180	9 H_2/2 SiH_4/**2 PH_3**	0.32	1	4.5
2	p-doped SiNW	416	100 H_2/5 SiH_4/**2 TMB**	1.42	1.5	6
	intrinsic layer	180	10 SiH_4	0.17	1	15
	n-doped layer	180	9 H_2/2 SiH_4/**2.5 PH_3**	0.32	1	4.5
3	p-doped SiNW	416	100 H_2/5 SiH_4/**2.5 TMB**	1.42	1.5	6
	intrinsic layer	180	10 SiH_4	0.17	1	15
	n-doped layer	180	9 H_2/2 SiH_4/**3 PH_3**	0.32	1	4.5

The SEM images of the PIN radial junctions of sample 1, 2 and 3 are shown in 0a, b and c, respectively. The RJs have diameters again ranging from 80 nm to 95 nm. The RJs synthesized with InCu co-catalyst have similar diameter and density with the SnCu co-catalyzed RJs, but are much longer (see Figure 7.4a and Figure 7.8a). The RJs in sample 2 and sample 3 with higher doping levels have slightly larger diameters (about 10 nm) than the RJs in Sample 1, with all of them mostly straight and uniform along the growth directions. Next, the RJs were coated with an ITO layer in the sputtering machine as top contacts. The SEM images of the complete solar cells of the three samples are shown in Figure 7.8d, e and f. The solar cell units are again very closely packed with the density of $1.8 \times 10^9/cm^2$.

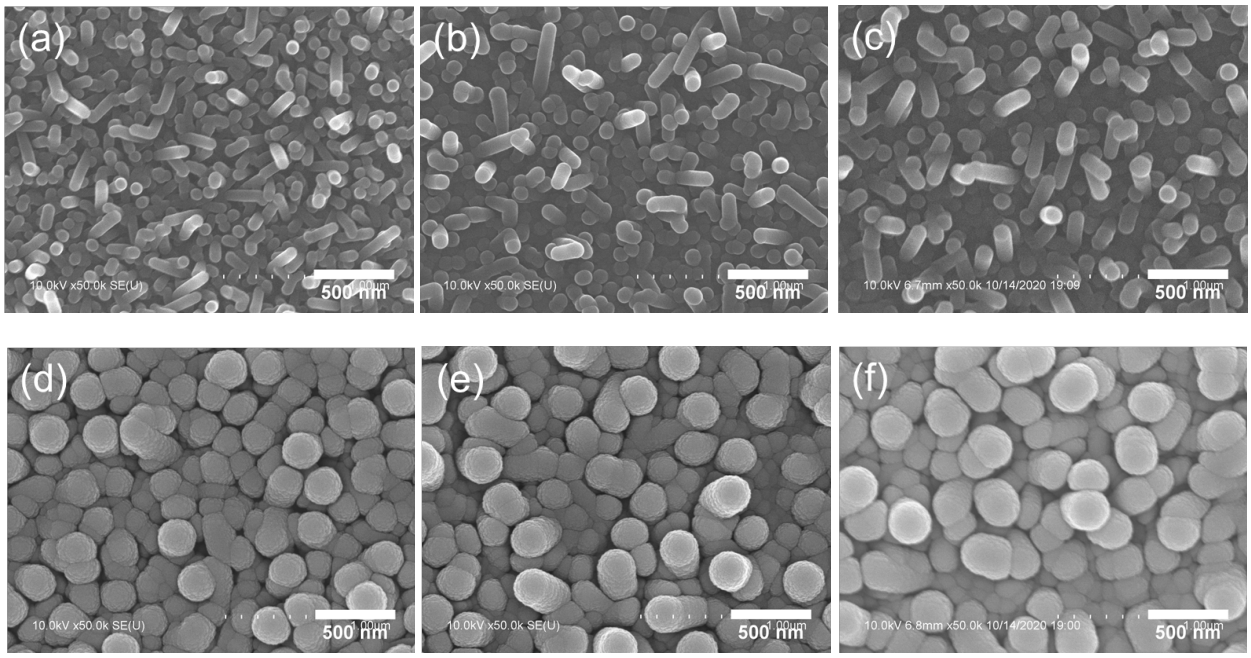

Figure 7.8. (a), (b) and (c): PIN radial junctions of Sample 1, 2 and 3, respectively, based on SiNWs synthesized with 0.1 nm In/0.1 nm Cu with increased p and n type doping levels as listed in 0; (d) (e) and (f) the same solar cells after the ITO front contact deposition.

We measured the J–V characteristics of the radial junction solar cells under standard AM1.5G illumination conditions using the same solar simulator as before. The J-V curves corresponding to the highest efficiencies of the three samples are presented in Figure 7.9. They all have a cell area of 0.0314 cm^2. Samples 1, 2 and 3 have best efficiencies of 3.41%, 4.55%, and 4.21% respectively. We can observe that V_{oc} and J_{sc} increases with increased doping in NWs and n layer.

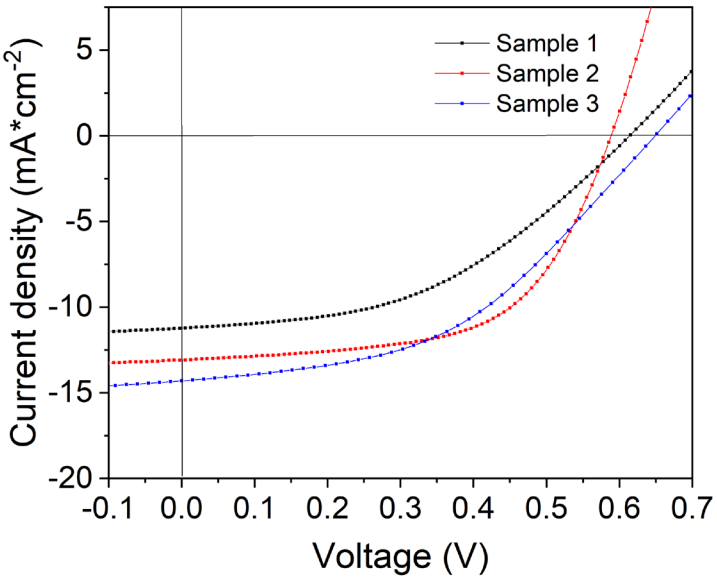

Figure 7.9. J-V characteristics of radial junction solar cells of Sample 1, 2 and 3 with increasing doping levels.

Table 7.3 summarizes the statistics of V_{oc}, J_{sc}, FF and efficiency (η) of 10 cells from Sample 1, 2 and 3 respectively. We found that with p and n doping levels increasing, V_{oc}, J_{sc}, and η have increased, whereas FF first increases and then decreases. In general, the most heavily doped sample has the best performance, thus showing that the initial doping level in Sample 1 was not enough for the higher performance of the solar cells. The highest V_{oc} and J_{sc} of Sample 3 are 0.682 V and 14.30 mA cm^{-2}, respectively.

Table 7.3. Average statistics of V_{oc}, J_{sc}, FF and η of solar cells from Sample 1, 2 and 3, respectively, acquired from 10 devices.

Samples	V_{oc} (V)	J_{sc} (mA*cm^{-2})	FF (%)	η (%)
1	0.582 ± 0.041	10.80 ± 0.37	43.08 ± 4.69	2.72 ± 0.50
2	0.587 ± 0.021	12.04 ± 0.97	52.27 ± 6.27	3.72 ± 0.69
3	0.663 ± 0.015	12.62 ± 0.81	46.28 ± 2.40	3.87 ± 0.26

7.4. **Chapter conclusions**

We have successfully demonstrated radial junction solar cells based on ultra-dense and ultra-thin SiNWs synthesized with SnCu and InCu co-catalysts for the first time. The highest solar cell efficiency of 3.7 % and 4.6 % for SnCu and InCu NW based devices has been achieved, respectively. In both cases, increasing p and n doping levels has led to the increase of V_{oc}, J_{sc}, and thus also η. The highest V_{oc} and J_{sc} of 0.68 V and 14.30 mA cm^{-2} have been achieved, which overcomes values achieved previously on less dense NW arrays in [Misra, 2013b]. The highest solar cell efficiency we have achieved is 4.55%. This demonstration of very high density ($2.2 \times 10^9/cm^2$ and $1.8 \times 10^9/cm^2$) of RJ devices with very high surface to volume ratio shows a promise for future devices on flexible substrate or surface functionalized for solar fuel and sensing applications.

References

Adachi, M.M., M.P. Anantram, and K.S. Karim, *Optical properties of crystalline-amorphous core-shell silicon nanowires.* Nano Lett, 2010. **10**(10): p. 4093-8. https://doi.org/10.1021/nl102183x

Cervenka, J., M. Ledinsky, J. Stuchlik, H. Stuchlikova, S. Bakardjieva, K. Hruska, A. Fejfar, and J. Kocka, *The structure and growth mechanism of Si nanoneedles prepared by plasma-enhanced chemical vapor deposition.* Nanotechnology, 2010. **21**(41): p. 415604. https://doi.org/10.1088/0957-4484/21/41/415604

Garnett, E. and P. Yang, *Light trapping in silicon nanowire solar cells.* Nano Lett, 2010. **10**(3): p. 1082-7. https://doi.org/10.1021/nl100161z

Kayes, B.M., H.A. Atwater, and N.S. Lewis, *Comparison of the device physics principles of planar and radial p-n junction nanorod solar cells.* Journal of Applied Physics, 2005. **97**(11): p. 114302. https://doi.org/10.1063/1.1901835

Kuang, Y., M.D. Vece, J.K. Rath, L. Dijk, and R.E. Schropp, *Elongated nanostructures for radial junction solar cells.* Rep Prog Phys, 2013. **76**(10): p. 106502. https://doi.org/10.1088/0034-4885/76/10/106502

Liu, C., J. Tang, H.M. Chen, B. Liu, and P. Yang, *A fully integrated nanosystem of semiconductor nanowires for direct solar water splitting.* Nano Lett, 2013. **13**(6): p. 2989-92. https://doi.org/10.1021/nl401615t

Liu, D., L. Li, Y. Gao, C. Wang, J. Jiang, and Y. Xiong, *The nature of photocatalytic "water splitting" on silicon nanowires.* Angew Chem Int Ed Engl, 2015. **54**(10): p. 2980-5. https://doi.org/10.1002/anie.201411200

Misra, S., *Single and tandem radial junction silicon thin film solar cells based on PECVD grown crystalline silicon nanowire arrays*. 2015, Ecole polytechnique: France.

Misra, S., L. Yu, W. Chen, M. Foldyna, and P.R.i. Cabarrocas, *A review on plasma-assisted VLS synthesis of silicon nanowires and radial junction solar cells.* Journal of Physics D: Applied Physics, 2014. **47**(39): p. 393001. https://doi.org/10.1088/0022-3727/47/39/393001

Misra, S., L. Yu, M. Foldyna, and P. Roca i Cabarrocas, *High efficiency and stable hydrogenated amorphous silicon radial junction solar cells built on VLS-grown silicon nanowires.* Solar Energy Materials and Solar Cells, 2013b. **118**: p. 90-95. https://doi.org/10.1016/j.solmat.2013.07.036

Peng, K.-Q., X. Wang, and S.-T. Lee, *Gas sensing properties of single crystalline porous silicon nanowires.* Applied Physics Letters, 2009. **95**(24): p. 243112. https://doi.org/10.1063/1.3275794

Peng, K.-Q., X. Wang, L. Li, Y. Hu, and S.-T. Lee, *Silicon nanowires for advanced energy conversion and storage.* Nano Today, 2013. **8**(1): p. 75-97. https://doi.org/10.1016/j.nantod.2012.12.009

Wikipedia. *Critical radius*. 2020a 2020 Oct 19; Available from: https://en.wikipedia.org/w/index.php?title=Critical_radius&oldid=984376437.

Xie, X., X. Zeng, P. Yang, C. Wang, and Q. Wang, *In situ formation of indium catalysts to synthesize crystalline silicon nanowires on flexible stainless steel substrates by PECVD.* Journal of Crystal Growth, 2012. **347**(1): p. 7-10. https://doi.org/10.1016/j.jcrysgro.2012.03.011

Zhang, R.Q., X.M. Liu, Z. Wen, and Q. Jiang, *Prediction of Silicon Nanowires as Photocatalysts for Water Splitting: Band Structures Calculated Using Density Functional Theory.* The Journal of Physical Chemistry C, 2011. **115**(8): p. 3425-3428. https://doi.org/10.1021/jp111182c

Zhou, X.T., J.Q. Hu, C.P. Li, D.D.D. Ma, C.S. Lee, and S.T. Lee, *Silicon nanowires as chemical sensors.* Chemical Physics Letters, 2003. **369**(1-2): p. 220-224. https://doi.org/10.1016/s0009-2614(02)02008-0

Conclusions

On the growth of quantum size silicon nanowires

Ultra-dense and ultra-thin silicon quantum nanowire arrays have been synthesized using a low-cost PECVD method with a co-catalyst composed of 0.1 nm Sn and 0.1 nm Cu nominal thickness of evaporated materials. By investigating the influence of substrate temperature, gas partial pressure and plasma power on SiNW diameter systematically, a minimum average crystalline diameter of around 4 nm has been achieved, with no NW thicker than 9 nm. The SiNWs have a high surface to volume ratio of 5×10^8 /m with a density of 5.7×10^{10} /cm^2, two orders of magnitude higher than the SiNWs synthesized with pure Sn catalyst using the same PECVD growth conditions and deposition time. The thin SiNWs benefited from the small-size SnCu co-catalyst NPs, which presented a core-shell structure (crystalline Cu_3Si core plus a Sn-rich liquid shell) during SiNW growth. The SiNWs have been grown through a unique combination of VSS and VLS growth process. A catalyst separation phenomenon including the formation of SiO_2 has been found, which we propose has taken place in the air after the growth due to the oxidation of Cu_3Si.

On SiNWs with hexagonal phase

A detailed TEM analysis has allowed to detect the presence of the diamond hexagonal phase in SiNWs with crystalline diameters ranging from 4.0 to 7.2 nm. SnCu mixed catalysts allowed us to obtain the 2H polytype structure using different catalyst compositions, at 385 and 416 °C on Cu TEM grids, and at 416 and 447 °C, with a SiH_4 partial pressure of 0.026 and 0.068 mbar on (100) Si wafer substrates. We determined the yield of the hexagonal phase to be around 5 – 6%. With InCu mixed catalyst we also obtained a 2H SiNWs with a crystalline diameter of 5 nm under the typical PECVD conditions. Hexagonal phase appeared statistically rarely, with no particular growth condition except for the small diameter.

On SiNW growth with mixed catalysts

We have developed a simple, rapid, and inexpensive method to prepare mixed catalysts with flexible compositions in a thermal evaporator for SiNW growth. SiNWs have been successfully synthesized

with SnCu, InCu and AuCu mixed catalysts. Using mixed catalysts allows us to achieve a control over SiNW diameter distribution, growth rate, and density that cannot be obtained by using evaporated pure metal catalysts. With InCu mixed catalysts we obtained denser SiNW arrays compared to the use of pure In. The catalysts of SiNWs were often – always for Sn-rich SnCu ones – made of two phases, liquid (amorphous after growth) and solid; the solid part was an intermetallic compound: a copper silicide in the case of SnCu, a more complex mix of alloys in the case of InCu and AuCu. The use of AuCu mixed catalysts gave rise to faster SiNW growth rates compared to the use of pure Au catalyst. SiNWs synthesized with 14 at% of Cu grew faster than the SiNWs synthesized with 78 at% of Cu.

On radial junction solar cells

We have demonstrated for the first time the fabrication of radial junction solar cells based on ultra-dense and thin SiNWs synthesized with SnCu and InCu co-catalysts. Both kinds of radial junctions have densities at an order of magnitude of $10^9/cm^2$. Efficiencies of 3.73%, with a V_{oc} of 0.606 V, a J_{sc} of 11.36 $mA*cm^{-2}$, and a FF of 0.541 have been achieved based on SiNWs with an average diameter of 7.2 nm (measurement based on SEM images) with different p-type doping fabricated with SnCu co-catalysts. For solar cells based on InCu catalyzed SiNWs, the highest efficiency that has been achieved is 4.55%, with the highest obtained V_{oc} and J_{sc} being 0.682 V and 14.30 $mA*cm^{-2}$, respectively.

Perspectives

On obtaining smaller-diameter NWs

As the 2H structure appeared only in NWs with diameters smaller than 8 nm, and following the DFT calculations of Béjaud stating that the stability of that structure increases as NW diameter decreases [Béjaud, 2021], we tend to think that future work on further decreasing the diameter would definitely benefit to the development of hexagonal SiNWs. In addition to SnCu and InCu, more combinations of mixed catalysts can be explored for producing smaller catalyst NPs thus smaller-diameter SiNWs. In addition to Cu-based mixed catalysts, one can further try Sn-based mixed catalysts, *e.g.*, SnAg, SnZn, and SnBi alloys. They are promising candidates because they are also common nano-solder materials with melting temperatures below 230 °C like SnCu, which may behave similarly to SnCu during SiNW growth. It will be interesting to try GeNW growth with SnCu mixed catalyst to see if it also works for Ge in obtaining small-diameter NWs with hexagonal structure. One may notice, however, that the predicted stability of Ge 2H would occur at lower NW diameter than with Si [Béjaud, 2021], so that, such studies will probably be more difficult than those proposed above.

On opto-electronic characterizations of small diameter SiNWs

In this thesis, we mainly used TEM method to characterize the crystalline structures of the small-diameter SiNWs. Since the electrical and optical properties of SiNWs are strongly size dependent, it will be interesting to characterize the opto-electronic properties of the thin SiNWs, for example, by photoluminescence (PL), cathodoluminescence (CL), absorption spectroscopy *etc*., especially if one has managed to realize an even smaller diameter and a higher yield of hexagonal phase. Preliminary PL and CL measurements have not been successful so far, probably due to the small size and the absence of surface passivation, and, in the case of PL, the small absorption of the green laser (the only one available at the time of the experiments). One can carry out surface passivation before PL and CL measurements. It will be interesting to use Si quantum wires to fabricate quantum devices in the future.

On understanding the mechanism of SiNWs growth with mixed catalysts

Although we have characterized the phases and the structures of the three mixed catalyst NPs, more questions with regard to SiNW growth mechanism are to be answered: the diffusion of Si atoms, the formation of Cu_3Si, and its role in SnCu co-catalyst NPs; the solubility, the diffusion and the precipitation of Si, and the coexistence of Si with the corresponding intermetallic alloys in InCu and AuCu co-catalyst NPs and so on. More TEM characterization including *in-situ* observation, and in-depth analysis are required for a better understanding of the SiNW growth mechanism with those mixed catalysts. *In-Situ* experiments of SiNW PECVD growth with SnCu catalyst in NanoMAX TEM can be found in Eric Ngo's thesis.

On vertical SiNW growth at temperatures below 300 °C

Using SnCu co-catalyst allows one to realize non-deformed SiNW growth at substrate temperature of 327 °C using PECVD, which cannot be achieved with pure Sn catalyst. It will be interesting to continue to explore the process parameters for SiNW growth at lower temperatures, thus for SiNW growth on flexible and low-cost polymer substrates.

References

Béjaud, R. and O. Hardouin Duparc, *Stabilizing the hexagonal diamond metastable phase in silicon nanowires.* Computational Materials Science, 2021. **188**: p. 110180. https://doi.org/10.1016/j.commatsci.2020.110180

ECOLE DOCTORALE

Titre : Croissance PECVD de nanofils de silicium cubique et hexagonal-diamant avec des catalyseurs mixtes liquides-solides pour des applications photovoltaïques

Mots clés : nanofils de silicium de petit diamètre, PECVD, TEM, Si hexagonal, catalyseur composé

Résumé : Les nanofils de silicium ont des applications prometteuses en optoélectronique. Leur petit diamètre leur donne des propriétés spécifiques. De plus, la structure metastable hexagonale diamant a été trouvée dans des petits exemplaires de ces nanofils, ajoutant de nouvelles possibilités. Nous nous sommes interessés dans cette thèse à la croissance de ce type de nanofils par dépôt chimique en phase vapeur assisté par plasma (PECVD). Nous avons étudié la croissance catalysée par des nanoparticules d'alliages (SnCu, InCu), et avons mis au jour un procédé unique vapeur-solid-solide assisté par liquide. Nous avons ainsi obtenu des tapis ultra-denses de nanofils de diamètre moyen 5 nm (avec SnCu) et 10 nm (avec InCu). La phase hexagonale est apparue statistiquement dans environ 5% des nanofils, sans conditions de croissance particulières en dehors du petit diamètre. Des cellules solaires à jonction radiale, utilisant ces nanofils, ont été fabriquées avec succès.

Title : Plasma-enhanced CVD growth of cubic and hexagonal diamond silicon nanowires with liquid-solid mixed catalysts for photovoltaic applications

Keywords : small diameter SiNWs, PECVD, TEM, hexagonal phase, mixed catalyst

Abstract : Silicon nanowires (SiNWs) have promising applications in optoelectronics. Their band gap increases with decreasing diameter, which gives them specific interesting properties. Moreover, the metastable diamond hexagonal phase has been found in small SiNWs, where the bandgap is predicted direct, which adds up new interesting possibilities. This thesis is dedicated to fabricating small diameter SiNWs using Plasma-enhanced chemical vapor deposition (PECVD). We have investigated the use of mixed particles to catalyze SiNWs (SnCu, InCu), which provide growth through a unique liquid assisted vapor-solid-solid process. We thus obtained ultra-dense and ultra-thin SiNWs with average crystalline diameter of 5 nm with SnCu, 10 nm with InCu. The hexagonal phase appeared statistically in about 5% of SiNWs, with no particular growth condition except for the small diameter. Radial junction solar cells based on those SiNWs have been fabricated successfully.